Exploring the Carbon Isotopic Ratio and Chemistry of Coccoliths and Coccolith Associated Polysaccharides as a Proxy for CO_2



Louis Michael Claxton
St Johns College
University of Oxford

A Thesis submitted for the degree of
Doctor of Philiosophy
January 23, 2022

To the few that never believed in me
and the many that always did.

Declaration

All work presented here is my own and has been conducted over the course of the past four years (2017-2021). Any contribution by other individuals has been explicitly stated and all information derived from other publications are referenced throughout.

Chapter 2: Louis Claxton and Rosalind Rickaby conceived the study. Louis Claxton conducted the sedimentary analysis with guidance from Michael Hermoso. Harry McClelland designed the original cellular isotopic flux model with Harry McClelland and Louis Claxton writing the optimisation and Monte Carlo procedures. Louis Claxton interpreted the results and wrote the paper with comments and guidance from Harry McClelland, Michael Hermoso and Rosalind Rickaby.

Chapter 3: Louis Claxton conceived the study with guidance from Rosalind Rickaby and Harry McClelland. Louis Claxton conducted the lab work and wrote the optimisation procedure based on the original cellular isotopic flux model developed by Harry McClelland. Rosalind Rickaby and Harry McClelland provided comments and guidance on the manuscript.

Chapters 4 and 5: Louis Claxton, Rosalind Rickaby and Renee Lee conceived the studies. Louis Claxton conducted the lab work and interpreted the results with guidance from Rosalind Rickaby and Renee Lee. Louis Claxton wrote the manuscripts with comments from Rosalind Rickaby and Renee Lee.

Acknowledgements

I would like to thank my supervisors for guiding me through the past four years. Thank you Renee Lee for always being upbeat about the polysaccharide work and helping me to understand all things biological. Thank you to Harry for joining my supervision team late in the day; without your guidance and meticulous eye this work would not have been possible. Your time and patience whilst showing me the intricacies of the isotopic flux model were greatly appreciated. Our discussions on the robustness of the model led to my development as a better scientist. Ros, I thank you for your encouragement and the freedom you gave me to explore and develop my own project. I always left our thought provoking meetings feeling inspired and ready to tackle the next problem. Your unwavering support and confidence in my ability gave me the strength to continue when things looked bleakest. Thank you to Christopher Day for always running my carbon isotopes so efficiently and to the highest standard. Thank you Helen Prescott in plant sciences for always accommodating me and for the lively conversations. Thank you Peter Ditchfield for running my samples in archaeology even though they clogged up your machine. Thank you Ann Pearson for running the isotopic analysis on my polysaccharide samples and providing such detailed analysis. Thank you Debbie Salmon for meticulously running the chemical analysis of my polysaccharide samples and your help in understanding the results.

Thank you to St Johns College who gave me the financial support to facilitate conference attendance and book buying. Thank you to Ruth Ogden and the SJC library team. Working as an invigilator during the evenings helped support my time at University and gave me fond memories. Thank you to OURLFC, Jamesy and Quez. Your love for rugby league and fitness reignited my passion for the sport. Thank you to all my team mates. Playing for OURLFC was one of the highlights of my time at Oxford. Thank you to Nick for encouraging me to play rugby league and being my friend throughout 8 years of University. Thank you to Henry, our lunches, pints, chats about sport and conversations about life helped me through the difficult patches. Thank you to my house mates Ella, Hamish and Oscar for putting up with me and being there for me through thick and thin. Thank you to Charlie, Donald, George and Nathan. You boys kept me grounded and reminded me that there was a world outside of Oxford. Thank you to my friends from Bristol, Joe, Mattie, Henry, Dom and Will who provided well needed respite from Oxford.

Thank you to my sister Sophie and parents Julie and Mike. Thank you to my grandparents Yvonne & Derek and Peter & Joyce. Thank you for all you have done for me and all you continue to do. You supported my decision to do a PhD and my studies throughout. I'm not sure I can ever repay your unwavering love and support without which I know I would not have gotten to where I am today. Sorry I didn't finish in time for you Grandma, I'll keep a copy with your name on it. Finally, thank you to Hannah, to whom I owe a great deal. Thank you for listening to me moan. Thank you for your support through the hard times and your company during the good times. Thank you for asking questions even though you didn't know what I was talking about and thank you for putting up with me when I was stressed, grumpy and poor. Without the help of those listed here and numerous others, this work would not have been possible.

Impact of the Coronavirus (COVID-19) Public Health Emergency

The COVID-19 pandemic enforced closure of the Department of Earth Sciences, University of Oxford from the 21/03/2020 to the 10/07/2020. During the closure I was unable to access the lab to conduct culture based experiments. The pandemic therefore forced myself to shift focus from a predominantly lab based thesis, whereby I aimed to culture several species of coccolithophore under varying carbon conditions, to a model based thesis. I originally intended to perform the culture calibration first and then apply the knowledge from the calibration to the modelling based chapter (e.g. perform chapter 3 first then apply the updated parameters to chapter 2). However, as I had to conduct the modelling chapter first due to the lockdown, it became a chapter focused on assessing the current state of coccolithophore isotopic flux models and applying them to the fossil data I had. I reconcile the re-calibrated model and the original application in chapter 3. The departmental closure also pushed back the work of chapters 4 and 5, with the data not received until late spring 2021. The data was delayed due to the international collaboration required and lab/analytical staff absences. The delayed data meant that I was unable to repeat any experiments.

Abstract

Our planet is habitable, in part, due to the carbon dioxide (CO_2) that resides in our atmosphere. Whilst the presence of CO_2 ensures that ambient surface temperatures remain above freezing, additional inputs of CO_2 drive global temperatures higher. The long-term increase in temperature associated with an increase in the mixing ratio of CO_2 in the atmosphere (pCO_2) is, however, not certain. In order to understand how much our planet's temperature rises given an increase pCO_2, we look to the sedimentary record to reconstruct coupled changes in past temperature and pCO_2. Yet, reconstructing pCO_2 is marred by inaccurate proxies, which often require numerous assumptions and only provide snapshots of past change. Recent work has linked chemical signals recorded in coccolithophores, unicellular phytoplankton, to changes in the CO_2 concentration of seawater ($[CO_{2(aq)}]$), which reflects pCO_2 in certain ocean settings. Such signals manifest in calcium carbonate plates, know as coccoliths, that coccolithophores produce and their associated polysaccharides, which assist with coccolith calcification. This thesis set out to investigate the use of coccoliths and coccolith associated polysaccharides (CAPs) as a proxy for pCO_2. I first invert an existing coccolithophore cellular carbon isotopic flux model to reconstruct pCO_2 given novel carbon isotopic data from size separated coccoliths dating to the Eocene period (56-34 million years ago). This work takes advantage of the understanding that the external concentration of CO_2 in seawater, in part, controls the carbon isotopic composition of coccolith calcite. I find that pCO_2 declined over the Eocene period with a corresponding shift to less calcified coccolithophore species. Second, I recalibrate an existing cellular carbon isotopic flux model with novel isotopic data measured from culture experiments to derive insight into modern day species carbon acquisition strategies. I find that two modern coccolithophore species, *Gephyrocapsa Oceanica* and *Coccolithus pelagicus*, have differing responses to $CO_{2(aq)}$ limitation. Whilst *G. Oceanica* likely upregulates HCO_3^- transporters under carbon limitation, *Coccolithus pelagicus* utilises HCO_3^- over all carbonate parameter space. Finally, I investigate the chemical and isotopic response of CAPs trapped within coccoliths from both culture and the sedimentary record to changes in $CO_{2(aq)}$. I find that both the monosaccharide composition and carbon isotopic ratio of CAPs vary over $CO_{2(aq)}$ space. Whilst species specific behaviour is apparent, collective changes observed across species point towards the potential development of a CAP based pCO_2 proxy. Taken together the work presented in this thesis lays the foundation for a suite of novel pCO_2 proxies that may, with supplementary work, reconstruct pCO_2 back to the Triassic period when coccoliths first appeared in the fossil record.

Contents

List of Figures x

List of Tables xii

1 Introduction 1
- 1.1 Carbon and the Carbon Cycle . . . 1
- 1.2 The Carbonate System . . . 3
- 1.3 Carbon Isotopes . . . 6
- 1.4 The carbonate pump . . . 6
- 1.5 Coccolithophores . . . 8
- 1.6 Existing Atmospheric CO_2 Proxies . . . 13
- 1.7 Thesis Aims and Objectives . . . 16
  - 1.7.1 Thesis Outline . . . 16

2 The Eocene emergence of highly calcifying coccolithophores with declining pCO_2 19
- 2.1 Introduction . . . 20
- 2.2 Discussion . . . 23
  - 2.2.1 Calcification across the Eocene . . . 23
  - 2.2.2 Implications of temperature and light on growth rate and calcification 27
  - 2.2.3 Eocene CO_2 levels . . . 28
  - 2.2.4 Conclusion . . . 31
- 2.3 Methods . . . 31
  - 2.3.1 Sample selection and preparation . . . 31
  - 2.3.2 Age model . . . 32
  - 2.3.3 Isotopic measurements . . . 32
  - 2.3.4 Development of the forward model . . . 33
  - 2.3.5 Optimization . . . 37
  - 2.3.6 Selecting initial CO_2 and R_{calc}:R_{fix} . . . 38
  - 2.3.7 Monte Carlo exploration of model output . . . 39
- 2.4 Supporting Information . . . 41
  - 2.4.1 Purity of size separated samples . . . 41
  - 2.4.2 Explanation of CIVE's . . . 43
  - 2.4.3 Ancient Cell physiology estimates . . . 43
  - 2.4.4 Calculation of calcite produced per cell . . . 46
  - 2.4.5 Growth Rate . . . 46
  - 2.4.6 Strontium to Calcium ratios . . . 47
  - 2.4.7 Carbon Speciation . . . 48
  - 2.4.8 CIVEs relative to $\delta^{13}C_{DIC}$ derived from Foraminifera . . . 50
  - 2.4.9 Monte Carlo Sensitivity Analysis . . . 53
- 2.5 Additional Section - Unpublished . . . 58

2.5.1 A note on oxygen isotopes . . . 58
2.5.2 Trends in Nannofossil Assemblage . . . 59
2.5.3 Closing Summary . . . 63

3 The carbon isotopic response of coccolithophores to variable carbon availability and its implications for carbon acquisition strategies 65
3.1 Introduction . . . 66
3.1.1 Organic carbon isotopes in Coccolithophores . . . 66
3.1.2 Inorganic carbon isotopes in Coccolithophores . . . 67
3.1.3 Carbonate system constraints in culture . . . 69
3.1.4 Chapter plan . . . 71
3.2 Methods . . . 71
3.2.1 Culture set up . . . 71
3.2.2 Carbonate Chemistry Determination . . . 73
3.2.3 SEM sample preparation . . . 73
3.2.4 Isotopic Analysis . . . 74
3.2.5 Particulate Organic Carbon and Particulate Inorganic Carbon Analysis . . . 76
3.2.6 Re-calibration of existing isotopic flux model . . . 76
3.2.7 Monte Carlo Sensitivity Analysis . . . 81
3.3 Results . . . 82
3.3.1 Culture conditions . . . 82
3.3.2 Cellular growth rates . . . 84
3.3.3 Coccolith Counts, Size and Malformation . . . 84
3.3.4 Particulate organic Carbon (POC) and Particulate Inorganic Carbon (PIC) . . . 88
3.3.5 Coccolith isotopes . . . 89
3.3.6 Organic carbon isotopes . . . 90
3.3.7 Re-calibration of existing isotopic flux model . . . 90
3.3.8 Sensitivity Analysis to refitting of Model . . . 95
3.4 Discussion . . . 98
3.4.1 $\delta^{13}C_{lith}$ response in *C. pelagicus* to changes in carbonate chemistry . . . 98
3.4.2 $\delta^{13}C_{lith}$ response in *G. oceanica* to changes in carbonate chemistry . . . 99
3.4.3 Modelled $\delta^{13}C_{org}$ and ε_p . . . 101
3.4.4 Inter study comparison of cellular parameters . . . 104
3.4.5 A note on oxygen isotopes . . . 105
3.4.6 Implications for carbon concentrating mechanisms . . . 108
3.4.7 A note on coccolith malformation and implications for cellular physiology . . . 109
3.4.8 Implications for paleoclimatology and updated presentation of Eocene data . . . 110
3.5 Conclusion . . . 113

4 Exploring the chemistry of CAPs as a proxy for pCO_2 116
4.1 Introduction . . . 117
4.1.1 The Biochemical signal of Ancient Life . . . 117
4.1.2 The Role of coccolith associated polysaccharides in coccolithophore calcification . . . 118
4.1.3 The chemical composition of CAPs as a proxy for pCO_2 . . . 119
4.1.4 Aims, objectives and hypotheses . . . 119
4.2 Methods . . . 121
4.2.1 Culture Conditions . . . 121

4.2.2 Sediment Samples . . . 121
4.2.3 CAP extraction . . . 122
4.2.4 CAP quantification . . . 123
4.2.5 Blanks and Standards . . . 123
4.2.6 CAP TFA Hydrolysis and Sample Derivatisation . . . 124
4.2.7 Gas Chromatography-Mass Spectrometry (GC-MS) . . . 124
4.3 Results . . . 125
4.3.1 CAP quantification and GC-MS analysis . . . 125
4.4 Discussion . . . 128
4.4.1 On the presence of glycerol . . . 128
4.4.2 CAP chemistry . . . 131
4.4.3 Response of CAP chemistry to elevated CO_2 in culture . . . 132
4.4.4 Implications of a low UAC on calcification . . . 134
4.4.5 Chemical composition of CAPs as a DIC proxy . . . 136
4.5 Conclusion . . . 140

5 Exploring the carbon isotopic composition of CAPs as a proxy for pCO_2 143
5.1 Introduction . . . 144
5.1.1 The carbon isotopic signal of CAPS . . . 145
5.1.2 Aims, objectives and hypotheses . . . 146
5.2 Methods . . . 147
5.2.1 Sample selection . . . 147
5.2.2 CAP extraction . . . 147
5.2.3 Blanks and Standards . . . 147
5.2.4 Isotopic analysis of CAPS . . . 148
5.3 Results . . . 149
5.3.1 Culture conditions . . . 149
5.3.2 CAP quantification . . . 151
5.3.3 CAP Carbon isotopes . . . 151
5.3.4 Sediment CAP Carbon isotopes . . . 152
5.4 Discussion . . . 153
5.4.1 Culture CAP Isotopes . . . 153
5.4.2 Relative changes in isotopic offsets . . . 155
5.4.3 Sediment $\delta^{13}C_{CAP}$ . . . 157
5.5 Conclusion and future directions . . . 159

6 Concluding remarks and future directions 162
6.1 The Isotopic Composition of Coccoliths . . . 163
6.2 Coccolithus pelagicus: A comparison of then and now . . . 166
6.3 On the use of coccolith associated polysaccharides (CAPS) . . . 167
6.3.1 CAP Chemistry . . . 167
6.3.2 CAP isotopic signal . . . 168
6.4 Concluding Remarks . . . 169

A Appendix 172

Bibliography 185

List of Figures

1.1 The carbon Cycle . . . 2
1.2 A Bjerrum plot for carbon speciation in seawater as a function of pH . . . 4
1.3 $\delta^{13}C$ of dissolved carbon species with pH . . . 7
1.4 The Global Carbonate Cycle . . . 9
1.5 *Coccolithus pelagicus* . . . 11

2.1 Measured and modelled CIVEs . . . 24
2.2 The Evolution of Genus Size and R_{calc}:R_{fix} . . . 26
2.3 Relative CO_2 across the Eocene. . . . 30
2.4 Model schematic . . . 34
2.5 SEM sediment images . . . 42
2.6 D_{Sr} values . . . 49
2.7 Model output given variations to assumed $\Omega_{calcite}$ . . . 51
2.8 CO_2 output given variations to initial CO_2 . . . 52
2.9 Explored $CO_{2(aq)}$ and R_{calc}:R_{fix} parameter space DIC calibrations . . . 54
2.10 Monte Carlo Sensitivity Analysis . . . 55
2.11 Monte Carlo Assumption Testing . . . 57
2.12 Measured Eocene sediment size fraction $\delta^{18}O$ . . . 59
2.13 Sediment $\delta^{18}O$ vs $\delta^{13}C$ . . . 60
2.14 Nannofossil Distribution across the Eocene . . . 62

3.1 Comparison of Carbonate Manipulation Methods . . . 70
3.2 Cellular isotopic flux model schematic . . . 78
3.3 Cellular Parameter affects on $\delta^{13}C_{lith}$ . . . 79
3.4 Culture Growth Rates . . . 85
3.5 SEM of *C. pelagicus* under different DIC conditions . . . 86
3.6 SEM of *G. oceanica* under different DIC conditions . . . 87
3.7 Measured PIC, POC and PIC:POC for cultures . . . 89
3.8 Culture $\delta^{13}C_{lith}$ . . . 90
3.9 $\delta^{18}O_{lith}$ vs $\delta^{13}C_{lith}$ . . . 91
3.10 Culture ε_p . . . 92
3.11 Optimisation procedure results . . . 93
3.12 Modelled $\delta^{13}C$ values . . . 94
3.13 Interstudy $\delta^{13}C$ data . . . 96
3.14 Model sensitivity analysis . . . 97
3.15 Modelled Carbon Species Ratios in Compartments . . . 100
3.16 Isotopic flux model schematic with other possible mechanisms . . . 103
3.17 $\delta^{18}O$ of carbon species vs pH . . . 106
3.18 Oxygen isotope equilibration time . . . 107
3.19 Eocene isotopic data refit with updated cellular parameters . . . 112

4.1 Variation of CAP uronic acid content through time . . . 120

4.2 CAP extraction schematic . . . 123
4.3 Monosaccharide Sugar Structures . . . 126
4.4 Monosaccharide composition of modern day CAPs . . . 126
4.5 Chemical composition of ancient CAPs excluding glycerol . . . 127
4.6 Normalised peak area of glycerol in samples . . . 128
4.7 % peak area of CAP chemistry under standard conditions . . . 132
4.8 UAC production Pathway Schematic . . . 133
4.9 6C/5C in modern day CAPs . . . 138
4.10 6C/5C in Sediments samples with Species Compositional Change . . . 138
4.11 6C/5C in Sediments samples with relative CO_2 . . . 139
4.12 Relative CO_2 vs C6/C5 monosaccharides . . . 140

5.1 $\delta^{13}C_{CAP}$ data for *Emiliania Huxleyi* . . . 146
5.2 $\delta^{13}C_{CAP}$ measured in culture . . . 152
5.3 $\delta^{13}C_{CAP}$ through the Eocene . . . 152
5.4 $\Delta\delta^{13}C_{CAP-DIC}$ measured in culture . . . 154
5.5 Culture $\delta^{13}C_{CAP}$ offset from cellular components . . . 156
5.6 $\delta^{13}C_{CAP}$ offsets through the Eocene . . . 158

A.1 Comparison of PIC calculations . . . 175
A.2 Modelled $\delta^{13}C$ values . . . 176
A.3 Optimisation sensitivity test to half assumed carbonic anhydrase . . . 177
A.4 Optimisation sensitivity test to twice assumed carbonic anhydrase . . . 178
A.5 Optimisation sensitivity test to half assumed P_{Ccell} . . . 179
A.6 Optimisation sensitivity test to twice assumed P_{Ccell} . . . 180
A.7 Optimisation sensitivity test to half assumed G value . . . 181
A.8 Optimisation sensitivity test to 2.7 times assumed G value . . . 182
A.9 Normalised peak area of Arabinose in samples . . . 183

List of Tables

2.1 Summary of inter-study changes in calcification 21
2.2 Model input parameters and associated uncertainty 45

3.1 Target Culture parameters 72
3.2 Final Measured Carbonate Parameters 83
3.3 Percentage Coccolith Malformation 85
3.4 Optimisation results 95
3.5 Updated cellular parameters 95
3.6 Inter-study Culture Conditions Comparison 109

4.1 CAP Culture parameters 121
4.2 IODP Leg 208, Site 1263 CAP sediment samples 122

5.1 $\delta^{13}C_{CAP}$ Culture data 150

A.1 IODP Leg 208, Site 1263 Sample List 172
A.2 Measured Culture Isotopic Data 173
A.3 Measured Particulate Inorganic Carbon (PIC) and Particulate Organic Carbon (POC) 174
A.4 OLS CO_2 and species vs 6C/5C statistical summary 183

Chapter 1

Introduction

1.1. Carbon and the Carbon Cycle

Without carbon, life as we know it would not exist. Carbon contributes to our molecular structure and accounts for approximately 18.5% of our total body mass. In the atmosphere, carbon combined with two oxygen atoms is known as carbon dioxide, CO_2. The presence of CO_2 and other greenhouse gases in the atmosphere keeps our planet habitable due to a chemical structure that helps to trap heat within the earth system [Mitchell et al., 1995]. Changes to the concentration of CO_2 in the atmosphere therefore adjusts our planetary thermostat [Falkowski et al., 2000, Roe and Baker, 2007].

CO_2 does not remain in the atmosphere permanently. The carbon within CO_2 is continuously cycled between reservoirs over long timescales (10^6 years) through a suite of processes known as the carbon cycle (Fig. 1.1). The largest reservoir, after that of mantle rocks (approximately 10^6Gt of carbon; 1Gt = 10^{15}grams), is the ocean, containing 38,240 Gt of carbon [Dasgupta and Hirschmann, 2010, Brovkin et al., 2002]. For comparison, the size of the terrestrial biomass reservoir is on the order of 550Gt and the atmosphere contained approximately 600Gt in 2002 [Bar-On et al., 2018, Brovkin et al., 2002]. Over million year time scales, volcanism acts as the dominant source of carbon to the atmosphere. Silicate weathering and the subsequent burial of organic and inorganic carbon in the oceans acts as the dominant sink [Berner, 2003]. The feedback between volcanism and silicate weathering ensures no runaway accumulation or loss of atmospheric CO_2 on million year time scales.

Since the industrial revolution the anthropogenic release of CO_2 has been unlike any

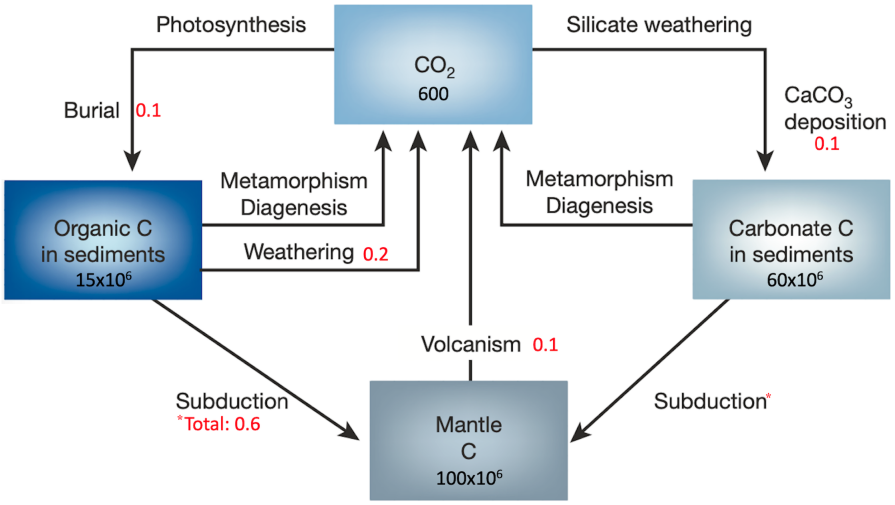

Figure 1.1: A simple box model of the long term carbon cycle subdivided into processes involving organic matter (left) and inorganic matter (right). Numbers in black represent carbon reservoir size in Gt and numbers in red represent fluxes in Gt yr^{-1}. Image originally from [Berner, 2003] modified with flux data from [Hedges and Keil, 1995].

naturally occurring event in earth's history [Falkowski et al., 2000]. The 800,000 years preceding the industrial revolution saw atmospheric concentrations of CO_2 varying within narrow bounds from 180 parts per million (ppm) to 300ppm [Lüthi et al., 2008]. At the time of writing the atmospheric concentration of CO_2 stands at 417ppm (http://www.esrl.noaa.gov/gmd/ccgg/trends). The current atmospheric concentration of CO_2 is likely the highest the planet has seen in 17 million years, making the current level of CO_2 the highest Homo Sapiens have experienced [Beerling and Royer, 2011, Foster et al., 2017].

Exactly how much the temperature of the planet varies given changes in the concentration of CO_2 is known as climate sensitivity ($S = \Delta T/\Delta R$, where S is the sensitivity parameter for a given change in temperature (ΔT) and observed radiative perturbation (ΔR), which varies given changes in factors such as atmospheric CO_2; e.g. [Palaeosens Project Members, 2012]). Climate sensitivity is estimated through earth system models coupled with reconstructions of past temperature and atmospheric CO_2 concentrations [Palaeosens Project Members, 2012, Edwards et al., 2007, Inglis et al., 2020]. Through better understanding variations in past atmospheric CO_2 and temperature we are able to better understand the earth system's response to changes in a greenhouse gas that, as a species, we are rapidly adding to the atmosphere.

The ongoing increase in atmospheric CO_2 brings with it a host of changes to our planetary system. For example, around a quarter of anthropogenic carbon released to the

atmosphere since the industrial revolution is thought to have been absorbed by the ocean [Friedlingstein et al., 2019]. The exchange of CO_2 between the atmosphere and the ocean is rapid, resulting in a near equilibrium between the surface ocean and the atmosphere. The increase in atmospheric CO_2 followed by the subsequent ocean uptake has resulted in ocean acidification, sometimes referred to as 'the other CO_2 problem' [Doney et al., 2009]. Ocean acidification may have substantial implications for marine life, particularly those that produce calcium carbonate ($CaCO_3$) shells [Doney et al., 2009]. Whilst these and other phenomena are currently being studied, we are far from a holistic understanding of the interconnectedness of our planetary system and of the changes we may expect on decadal, millennial and million year time scales.

1.2. The Carbonate System

$CO_{2(g)}$ from the atmosphere will, in part, dissolve in water to produce $CO_{2(aq)}$, which reacts with H_2O to form carbonic acid, H_2CO_3. However, the rate constant of hydration for $CO_{2(aq)}$ is slow resulting in the majority of dissolved CO_2 remaining in the form of $CO_{2(aq)}$ [Zeebe and Wolf-Gladrow, 2001]. Moreover, $CO_{2(aq)}$ and H_2CO_3 are chemically inseparable and thus here and throughout I consider $CO_{2(aq)}$ and H_2CO_3 as a single inseparable pool [Zeebe and Wolf-Gladrow, 2001]. The concentration of $CO_{2(aq)}$ in seawater ($[CO_{2(aq)}]$) is related to the partial pressure of CO_2 in the atmosphere, assuming equilibrium exists with the surface ocean, through Henrys law:

$$[CO_{2(aq)}] = K_0(T, S) \cdot pCO_2 \tag{1.1}$$

where pCO_2 is the partial pressure of CO_2 in the atmosphere and K_0 is the solubility constant of CO_2, which varies as a function of temperature (T) and salinity (S). Upon dissolution in water $CO_{2(aq)}$ reacts with water to produce a proton and a bicarbonate ion, HCO_3^-, however, it is impossible to determine whether this is by way of H_2CO_3 production or directly to HCO_3^- [Zeebe and Wolf-Gladrow, 2001]. Nonetheless, HCO_3^- subsequently dissociates to form a carbonate ion, CO_3^{2-}, through the release of a further proton [Zeebe and Wolf-Gladrow, 2001]. The species $CO_{2(aq)}$, HCO_3^- and CO_3^{2-} summed together are referred to as total dissolved inorganic carbon (DIC):

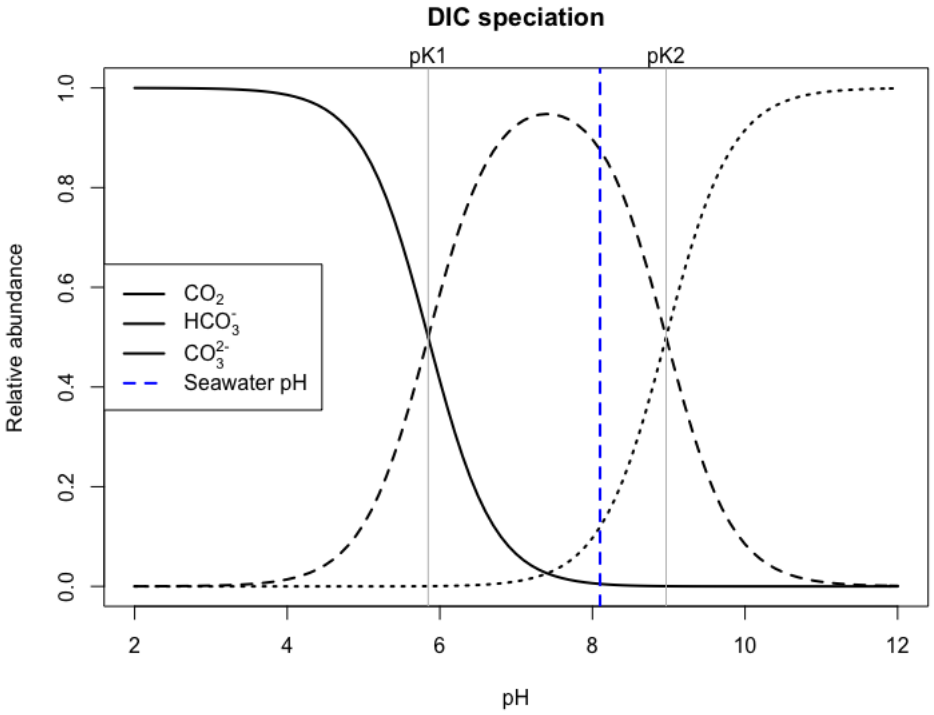

Figure 1.2: A Bjerrum plot for carbon speciation in water as a function of pH. pK1 (=5.86) and pK2 (=8.92) represent the location of the dissociation constants for $CO_{2(aq)} \rightleftharpoons HCO_3^-$ and $HCO_3^- \rightleftharpoons {CO_3}^{-2}$ respectively. At standard ocean conditions (approximately pH 8.1 represented by the vertical dashed blue line) HCO_3^- is the dominant form of dissolved inorganic carbon in the oceans.

$$\mathrm{DIC} = [CO_2] + [{HCO_3}^-] + [{CO_3}^{2-}] \tag{1.2}$$

The carbon species distribution of DIC in seawater is governed by pH and can be represented graphically as a Bjerrum plot (Fig.1.2). Under modern day conditions (ocean water pH approximately = 8.1) HCO_3^- is the dominant ion (86.5%), followed by CO_3^{2-} (13%) and $CO_{2(aq)}$ (0.5%).

The carbonate system is further described by alkalinity, a conservative quantity (not affected by changes in pressure or temperature and is constant when two bodies of water are mixed) within the ocean that relates to the overall charge balance of the system. Total alkalinity (TA) is a measure of the excess of proton acceptors over proton donors:

$$\mathrm{TA} = [{HCO_3}^-] + 2\,[{CO_3}^{2-}] + [{B(OH)_4}^-] + [{OH}^-] - {H}^+ + \text{minor components} \tag{1.3}$$

where TA refers to total alkalinity and the carbonate ion is counted twice due to its double-negative charge [Wolf-Gladrow et al., 2007]. In this thesis the minor components of alkalinity are not considered given that at the pH of seawater the carbonate, borate, hydroxide and hydrogen ions account for >99% of total alkalinity (for review of alkalinity concepts see [Zeebe and Wolf-Gladrow, 2001, Wolf-Gladrow et al., 2007, Middelburg et al., 2020]). With respect to carbon, TA describes the capacity of the ocean to store DIC in the form of either HCO_3^- or CO_3^{2-} and is referred to as carbonate alkalinity. A reduction in alkalinity shifts the surface ocean carbonate equilibria and results in an increased storage of DIC in the form of HCO_3^- or $CO_{2(aq)}$. The governing equations of the carbonate system results in two degrees of freedom across six components [Zeebe and Wolf-Gladrow, 2001]. If any two of TA, DIC, HCO_3^-, $CO_{2(aq)}$, CO_3^{2-} and pH are known, the remaining four components can be calculated.

Calcium carbonate ($CaCO_3$) formation in the surface ocean consumes Ca^{2+} and CO_3^{2-} (equation 1.4). Calcium carbonate exists in two forms, calcite, the trigonal form, and aragonite, the orthorhombic form. The net effect of calcification is to remove one mole of DIC and two moles of alkalinity from the surface ocean (two moles of alkalinity are removed due to the +2 charge of the associated ions):

$$Ca^{2+} + {CO_3}^{2-} \rightarrow CaCO_3 \tag{1.4}$$

Calcification drives a reduction in TA and thus CO_3^{2-} ions and therefore reduces the ocean's ability to buffer changes in atmospheric CO_2 due, amongst others, to the reaction of $CO_{2(aq)}$ with CO_3^{2-}.

The formation of organic matter through photosynthesis also affects the carbonate chemistry of the oceans. Nitrate-based primary production removes one mole of carbon from the surface ocean and adds 17/106 moles of alkalinity (nitrate based primary production; equation 1.5):

$$CO_2 + \frac{16}{106}NHO_3 + \frac{1}{106}H_3PO_4 + \frac{61}{53}H_2O \rightarrow (CH_2O)(NH_3)_{\frac{16}{106}}(H_3PO_4)_{\frac{1}{106}} + \frac{69}{53}O_2 \tag{1.5}$$

Aerobic respiration of organic matter opposes primary production through the addition of one mole of carbon and contributes to the removal of alkalinity when coupled with

nitrification.

1.3. Carbon Isotopes

The most abundant isotope of carbon on earth contains six neutrons and six protons and is referred to as ^{12}C. A further stable arrangement is possible containing six protons and seven neutrons, ^{13}C. Most carbon on the planet is in the form of ^{12}C, with ^{13}C making up approximately 1% of total carbon [Zeebe and Wolf-Gladrow, 2001]. The carbon isotopic composition of a system containing carbon is given relative to an international standard:

$$\delta^{13}C_{sample}(‰) = 1000 \times \frac{R_{sample} - R_{standard}}{R_{standard}} \tag{1.6}$$

where R is equal to the ratio of ^{13}C to ^{12}C in either the sample or the standard. In this thesis the reference standard is the Vienna Pee Dee Belemnite (VPDB).

All organic matter contains carbon atoms and thus has an associated value of $\delta^{13}C$. Organic matter with more positive values of $\delta^{13}C$ contain a higher proportion of ^{13}C than matter with a more negative value (or less positive). Photosynthesising plants and marine algae use the enzyme ribulose-1,5-biphosphate oxygenase-carboxylase (RuBisCO) to convert CO_2 into organic matter. The reaction is faster for $^{12}CO_2$ than $^{13}CO_2$ and thus organic matter is depleted in ^{13}C relative to the $CO_{2(aq)}$ substrate. Indeed, the process of photosynthesis imparts a fractionation on organic matter from -11 to -28‰ [Boller et al., 2011, Hayes, 2001].

The inorganic carbon species in water also have a distinct isotopic signature due to hydration and dehydration reactions occurring at different rates for ^{12}C and ^{13}C [Zeebe and Wolf-Gladrow, 2001]. For example, the hydration of CO_2 results in HCO_3^- that is approximately 13‰ depleted in ^{13}C, subsequent dehydration of HCO_3^- forms CO_2 that is approximately 22‰ more ^{13}C depleted. The combined effect is the establishment of CO_2 that is approximately 9‰ depleted than HCO_3^- in seawater at equilibrium, with the absolute offset from DIC varying as a function of pH (Fig. 1.3).

1.4. The carbonate pump

The process by which pelagic carbonate is formed and sequestered within the sediment is referred to as the carbonate pump. The proportion of $CaCO_3$ formed relative to organic

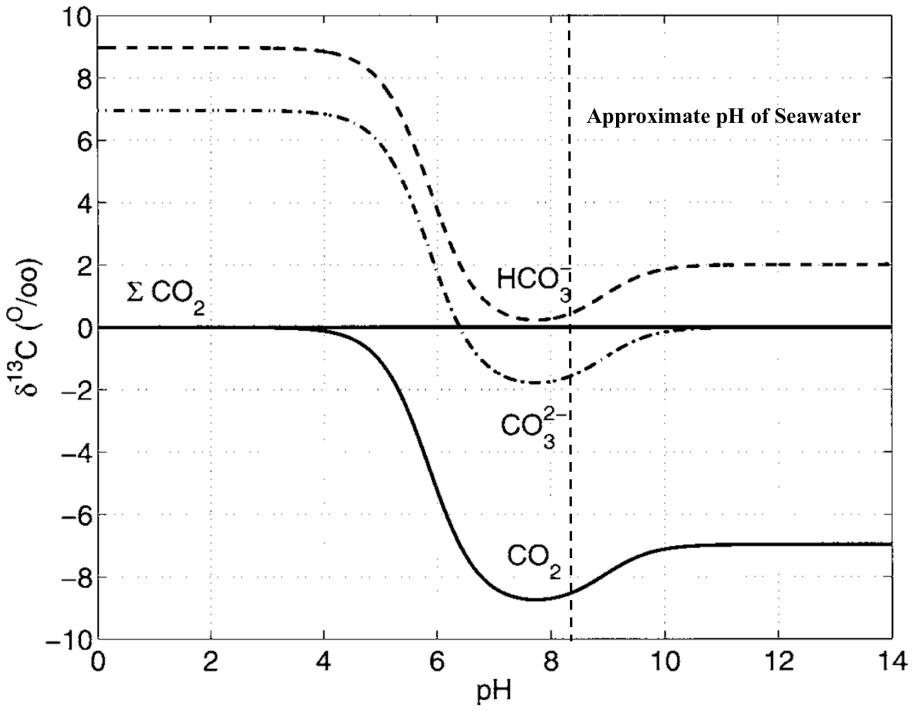

Figure 1.3: Carbon isotopic ratios of dissolved carbon species in water as a function of pH. ΣCO_2 represents the sum of dissolved carbon species in water. $\delta^{13}C_{\Sigma CO_2}$ is equal to 0‰, temperature is equal to 25°C and salinity is 35‰. Also show is the approximate pH of modern seawater (dashed vertical black line). Figure modified from original published in Zeebe and Wolf-Gladrow [2001].

matter in the surface ocean and its subsequent flux to the sea floor is known as the rain rate ratio. A decrease in the rain rate ratio results in a reduced export of $CaCO_3$ per unit of organic matter to the seafloor and, all things being equal, a reduced export of alkalinity from the surface ocean [Archer and Maier-Reimer, 1994]. Organisms such as coccolithophores, unicellular phytoplankton, both calcify and photosynthesise and are thus crucial to the rain rate ratio. Estimates suggest that coccolithophores contribute 1-10% of total global organic carbon fixation, but 50% of carbonate production making them a crucial component of alkalinity export and the rain rate ratio [Poulton et al., 2007, Broecker and Clark, 2009].

The stability of carbonate in the ocean is governed by the concentrations of its two constituent ions, $[Ca^{2+}]$ and $[CO_3^{2-}]$ and its corresponding solubility constant, K_{sp}, which varies as a function of temperature and pressure. The stability of carbonate is quantified via the calculation of its carbonate saturation state:

$$\Omega = \frac{[Ca^{2+}][{CO_3}^{2-}]}{K_{sp}} \tag{1.7}$$

Ω is defined for both calcite and aragonite, Ω_{calcite} and $\Omega_{\text{aragonite}}$ respectively (aragonite $K_{sp} \geq$ calcite K_{sp} making aragonite more soluble). Locations in the ocean where Ω_{calcite} is less than one lead to calcite dissolution and locations where Ω_{calcite} is greater than one are supersaturated and calcite is stable. K_{sp} increases as temperature declines and pressure increases making ocean depth an important control over the stability of carbonate.

The depth in the ocean at which Ω_{calcite} equals one is termed the calcite saturation horizon, below which at higher pressure calcite dissolution occurs. Dissolution occurs slowly and calcite exists below the calcite saturation horizon with the rate of dissolution proportional to the depth below the horizon [Walter and Morse, 1985]. The depth in the ocean where dissolution matches the delivery rate of carbonate is termed the carbonate compensation depth (CCD). Below the CCD the contribution of carbonate to total sediment weight is usually less than 10%. Any carbonate that survives dissolution and is locked up in sediments is ultimately recycled through volcanism on long time scales (Fig. 1.4).

The CCD is neither constant spatially or temporally due to variations in ocean circulation, biological productivity and global weathering [Greene et al., 2019, Ridgwell and Zeebe, 2005]. The variable nature of the CCD reflects the long term balance of the weathering and volcanic out-gassing feedbacks [Ridgwell, 2005]. Changes in the amount of calcification, or rate of calcification, by marine organisms can also affect the depth of the CCD. Past declines in the rate of calcification by marine organisms has been suggested to have caused a build up of alkalinity in the ocean and a subsequent deepening of the CCD [Boudreau et al., 2018]. How the amount, or rate, of calcification in marine phytoplankton that use both CO_2 for photosynthesis and CO_3^{2-} for calcification responds to variations in DIC is therefore important to quantify as changes will drive shifts in the ability of the ocean to buffer future increases in anthropogenically released CO_2.

1.5. Coccolithophores

Coccolithophores are single celled phytoplankton belonging to the division Haptophyta. Coccolithophores first appeared around 200 million years ago [Bown et al., 2004] and have been major contributors to the ocean phytoplankton community ever since [Katz et al., 2004]. Coccolithophores exist in either a haploid or diploid cell life-cycle phase, with both phases able to reproduce asexually [Houdan et al., 2004]. Coccolithophores,

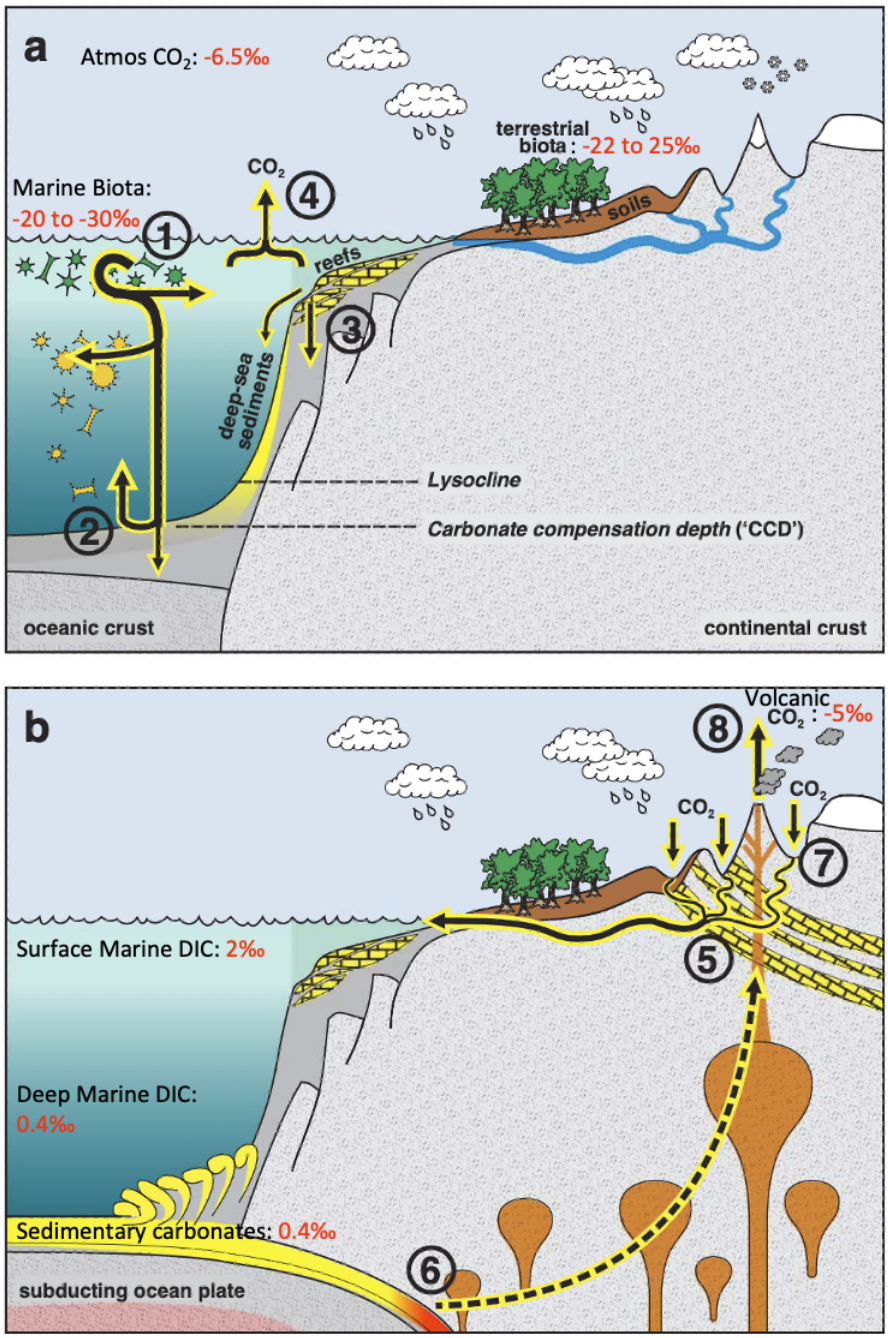

Figure 1.4: The global carbonate cycle documents the moving of calcium carbonate through reservoirs. Figure 1.4 is a more detailed depiction of the right hand side of figure 1.1. (**a**) shows the carbonate system within the ocean. **1** details the formation of carbonate through marine calcifiers in the open ocean. **2** details the carbonate reaching the sea floor. **3** details carbonate formation via coral reefs with **4** depicting the formation and release of CO_2 to the atmosphere from carbonate formation. Also shown are the lysocline, where carbonate dissolution increases dramatically and the CCD. (**b**) shows the transfer of carbonate from sediments back into the atmosphere. **5** some of the carbonate laid down on the ocean floor is rifted and undergoes mountain building and is directly recycled. **6** subducted carbonates are thermally decomposed and reacts with silicates, transforming $CaCO_3$ into $CaSiO_3$ and producing CO_2. **7** Silicate rocks ($CaSiO_3$) react with CO_2 and water to form Ca^{2+}, $2HCO_3^-$ and SiO_2. Finally, **8** shows the emission of CO_2 back into the atmosphere, derived from the break down of carbonate in **6**. Image modified from Ridgwell and Zeebe [2005] with isotopic values shown in red taken from [Vervoort et al., 2019].

during their motile haploid cell phase, produce simple rhombohedral calcite crystals on the surface of their cells [Young et al., 1999]. During the more prevalent diploid cell phase, coccolithophores produce intricate calcite plates known as coccoliths at a rate of 1-2 per hour [Houdan et al., 2004, Monteiro et al., 2016]. There are around 200 extant species of coccolithophores known to produce coccoliths [Young et al., 2003].

Despite decades of study and extensive reviews, the process of coccolith formation, or coccolithogensis, is still not fully understood [Paasche, 1968, Young et al., 1999, Young, 2003, Taylor et al., 2017, Brownlee et al., 2020]. Coccolithogenesis is thought to be initiated intracellularly within a Golgi-derived vesicle, often referred to as the coccolith vesicle (CV) (Fig. 1.5; [Young, 2003]). A system of anastomosing tubules, known as the reticular body, is thought to be key in delivering the organic and inorganic components to the CV and subsequently determining the calcite crystalline structure [Taylor et al., 2007, 2017].

Coccolithophores require DIC and Ca^{2+} to be transported to the site of calcification to form their calcite coccoliths. Coccolithophores are assumed to be mostly impermeable to CO_3^{2-}, hence carbon used for calcification likely derives from HCO_3^- or $CO_{2(aq)}$ [Buitenhuis et al., 1999, Paasche, 2001, Bach et al., 2013]. HCO_3^- transport to the site of calcification is likely coupled with the transport of Na^+ or Cl^- via the use of membrane bound anion exchange transporters of the SLC4 family, which have been shown to be up-regulated during periods of carbon limitation [Bach et al., 2013, Taylor et al., 2017]. The use of HCO_3^-, and subsequent conversion to CO_3^{2-} prior to calcite formation, within the CV necessitates the removal of a H^+ via voltage gated channels to maintain intracellular charge and pH homeostasis [Taylor et al., 2011].

The mechanistic acquisition of Ca^{2+} and its transport to the CV is less well understood. Moreover, coccolithophores face the challenge of requiring a high flux of Ca^{2+} to the CV in order to maintain calcification, yet require a low cystolic concentration of Ca^{2+} to avoid poisoning [Taylor et al., 2017]. Studies suggest that Ca^{2+} likely diffuses into the cell down electrochemical gradients via permeable channels and is removed via Ca^{2+}-ATPases and/or cation exchanges [Mackinder et al., 2010]. Gene expression and nanoscale spectroscopy studies have suggested that Ca^{2+} is transported and stored in a precursor vacuole-like compartment prior to its delivery to the CV [Mackinder et al., 2010, 2011, Sviben et al., 2016]. Storage within a precursor compartment may help to maintain calcification and prevent cellular poisoning [Sviben et al., 2016].

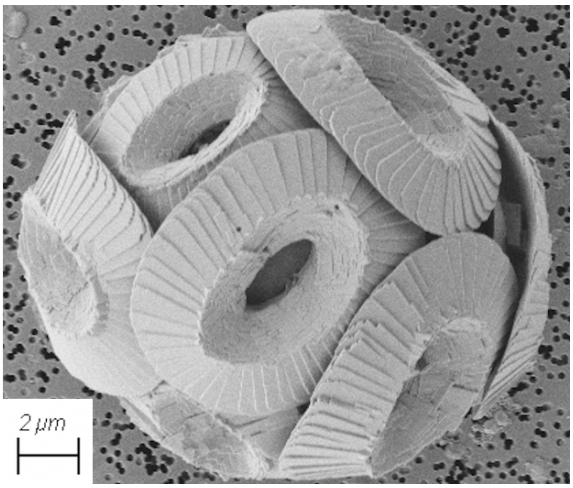

(a)

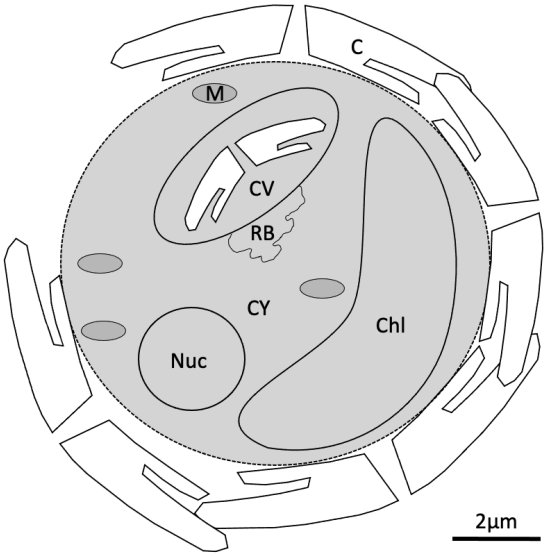

(b)

Figure 1.5: (**a**) is a SEM image of the coccolithophore *Coccolithus pelagicus* grown under standard conditions in the laboratory. (**b**) is a cartoon cross section of *Coccolithus pelagicus*. **C** represents the Coccolith, **M**: Mitochondria, **CV**: Coccolith vesicle, **RB**: Reticular Body, **CY**: Cytoplasm, **Chl**: Chloroplast and **Nuc**: Nucleus. Cartoon redrawn after Taylor et al. [2007].

Within the CV, coccolith formation begins with the nucleation of calcite crystals on the rim of an organic, insoluble baseplate made of a glucose rich polymer to form a protococcolith [Gal et al., 2016, Marsh et al., 2002]. The protococcolith undergoes further crystal growth to form a mature coccolith. Once fully formed, coccoliths are extruded to the exterior of the cell during a single exocytotic event. Once extruded to the exterior of the cell, the newly formed coccolith attaches to existing coccoliths forming an elaborate disk of interlocking anvil-shaped crystals known as a coccosphere ([Marsh et al., 2002]; Fig. 1.5). The reason, or indeed reasons, for calcification within coccolithophores remains to be fully understood. Suggestions include coccoliths playing a role in focusing light into the cell, protecting the cell from photodamage, buoyancy control, protection from predation and assisting with the prevention of calcium poisoning [Monteiro et al., 2016].

Coccolith formation is thought to be facilitated through utilisation of water-soluble coccolith-associated polysaccharides (CAPs) that provide binding sites for the mineral components of calcification such as Ca^{2+} (e.g. Borman et al. [1982], Henriksen and Stipp [2009]). CAPs bind to the periphery of the baseplate and form a microenvironment enriched in Ca^{2+} that becomes the preferred site for crystallisation [Gal et al., 2016, 2017]. Crystal precipitation is restricted to the top edge of the baseplate and results in the formation of two layers, one layer of particles projecting towards the centre, the other narrower layer projecting outward [Gal et al., 2016]. CAPs appear to promote calcite growth in crystal shapes other than that of the typical inorganic rhombohedral crystals resulting in vast morphological differences between species [Kayano et al., 2011].

Given the low affinity of RuBisCO for CO_2, lack of specificity for CO_2 over O_2 and sluggish kinetics of diffusion, most phytoplankton require a carbon concentrating mechanism (CCM; [Reinfelder, 2011]). CCM's may consist of multiple mechanisms and include the use of carbonic anhydrases (CAs), the enzyme that catalyses the dehydration and hydration of HCO_3^- and $CO_{2(aq)}$, HCO_3^- transporters and pH gradients to ensure CO_2 is concentrated at the site of RuBisCO [Reinfelder, 2011]. When external $CO_{2(aq)}$ is high, most carbon supplied to the cell likely derives from diffusion of $CO_{2(aq)}$.

The work presented in this thesis focuses on two species of coccolithophore; *Coccolithus pelagicus* and *Gephyrocapsa oceanica*. *Coccolithus pelagicus* evolved around 66 Ma and has been an important contributor to ocean carbonate production ever since [Gibbs et al., 2018, Daniels et al., 2018, Young and Bown, 2020]. Coccoliths from *Gephyrocapsa oceanica*

meanwhile were first identified during the Messinian stage (5.33-7.25 Ma) [Young and Bown, 2020]. Although geologically younger than *Coccolithus pelagicus*, *Gephyrocapsa oceanica* is closely related to the Reticulofenestra genus, which evolved around 57 Ma [Young and Bown, 2020]. Both species are therefore important to study in culture if we wish to understand the physiology of ancient coccolithophores.

1.6. Existing Atmospheric CO_2 Proxies

Quantifying pCO_2 with the view to better understanding the climate's sensitivity has long been a goal of the paleoclimate community. In order to better understand current and future change, geologists have long looked towards past events. Indeed, before we can fully understand the interconnectedness of the earth system we must first have a continuous, precise and reliable record of CO_2 for at least the Cenozoic (65 million years ago to present). However, producing a continuous record of pCO_2 becomes increasingly harder to achieve the further back in time one looks.

For the past 800,000 years of earth's history we are able to measure atmospheric mixing ratios through investigating trapped air in ice cores [Lüthi et al., 2008]. However, direct measurements from ice cores incorporate a mere 0.02% of earth's history and 1.5% of the Cenozoic. Beyond ice cores, estimates for CO_2 are derived from proxies. Several CO_2 proxies have been widely used in literature, yet these all come with caveats, assumptions and pitfalls.

Coccolithophore bulk organic carbon isotopic ratio, $\delta^{13}C_{org}$, varies, in part, as a function of $CO_{2(aq)}$ and can therefore be used to infer contemporaneous values of $CO_{2(aq)}$ (see [Laws et al., 2002] and references therein). $\delta^{13}C_{org}$ is inferred through the use of alkenones (alkenones are usually taken to be 4‰ depleted relative to bulk biomass; [Bidigare Robert R. et al., 1997, Freeman and Pagani, 2005, Pagani, 2002, Seki et al., 2010, Wilkes et al., 2018, Zhang et al., 2019]). Alkenones are unsaturated methyl and ethyl ketones produced by the Noëlaerhabdaceae family of coccolithophores and can be, under certain conditions, well preserved in sediments [Prahl et al., 1989]. However, reconstructing $\delta^{13}C_{org}$ from the sedimentary record is difficult given degradation and contamination of organic matter over time. Moreover, whilst alkenones have been found as far back as approximately 120Ma [Brassell et al., 2004], good preservation is rare in sediments older than approximately 40 million years [Pagani, 2002, Seki et al., 2010]. Further, given the only known producers

of alkenones are the Noëlaerhabdaceae, estimates of pCO_2 have only been made for the past 40 Ma [Pagani, 2002, Freeman and Pagani, 2005]. Finally, alkenones are found loose within sediments and may therefore not be directly produced by the coccoliths found in the same sediment. Given the higher transportability of alkenones relative to the coccoliths themselves, alkenones may travel substantially further and may therefore represent a different oceanographic regime [Nooteboom et al., 2019].

Inverting measurements of $\delta^{13}C_{org}$ to predict $CO_{2(aq)}$ is further complicated due to additional factors such as the cells morphometry and growth rate also exerting a control over $\delta^{13}C_{org}$ [Popp et al., 1998]. Freeman and Pagani [2005] provide a generalised equation to determine $CO_{2(aq)}$ after Rau et al. [1996] and Bidigare Robert R. et al. [1997]:

$$\varepsilon_p = \varepsilon_f - \frac{(\varepsilon_f - \varepsilon_t)C\mu}{PC_e} \tag{1.8}$$

where ε_f is the isotopic fractionation associated with the formation of organic matter via the enzyme RubisCO, ε_p is the offset observed between organic matter and $CO_{2(aq)}$, ε_t is the fractionation associated with transport of CO_2 to the site of organic matter fixation, C is the quantity of total cellular carbon, P is the cellular permeability to CO_2, μ is growth rate and C_e is the external concentration of $CO_{2(aq)}$. Equation 1.8 assumes carbon is purely acquired by diffusion driven by concentration gradients [Freeman and Pagani, 2005]. Producing estimates regarding an ancient cells physiology from alkenones alone is, however, difficult. Current methodology for estimating $CO_{2(aq)}$ from $\delta^{13}C_{org}$ therefore involves utilising the term, b, which encompasses the influence of all other factors besides $CO_{2(aq)}$ on the isotopic composition of organic matter via the equations proposed by Rau et al. [1996] and Bidigare Robert R. et al. [1997]:

$$C_e = \frac{b}{\varepsilon_f - \varepsilon_p} \tag{1.9}$$

Variations in b therefore reflects changes to a cell's morphometry, growth rate, membrane permeability to, and diffusion rate of, CO_2 [Rau et al., 1996, Freeman and Pagani, 2005]. In the sedimentary record b is estimated from assumed phosphate concentrations. If the requirement to employ the b parameter derived from phosphate concentrations can be circumnavigated, errors associated with reconstructing $CO_{2(aq)}$ can be reduced.

Recently, focus within the paleoclimate community has shifted to utilising the boron

isotopic composition of foraminifera as a proxy for pCO_2. Indeed, studies utilising the boron isotopic composition of foraminifera dominate recent estimates of atmospheric CO_2 (see https://www.p-co2.org/). Boron exists in two distinct forms within the oceans, boric acid ($B(OH_3)$) and borate ($B(OH)_4^-$). The isotopic ratio of boric acid and borate are distinct, and importantly, along with their concentrations, vary as a function of pH [Klochko et al., 2006]. Given only borate is thought to be incorporated into foraminiferal calcium carbonate, the boron isotopic ratio of any carbonate formed by foraminifera varies as a function of pH [Hemming and Hanson, 1992]. Given reasonable assumptions on another carbonate parameter and of the boron isotopic composition of seawater, measurements of $\delta^{11}B$ can provide estimates for pCO_2 [Lemarchand et al., 2002, Anagnostou et al., 2016, 2020]. However, deviations to the expected boron isotopic distribution of foraminifera at a given pH occur due to species specific biological mechanisms referred to as 'vital effects', which must be corrected before inferring pCO_2 [Henehan et al., 2016]. Additional pCO_2 proxies include leaf stomatal indices [Beerling et al., 1998] and the isotopic composition pedogenic carbonate (paleosols; Ekart et al. [1999]).

Given the sparsity and error associated with current pCO_2 proxies, the paleoclimate community is still working to find the silver bullet for reconstructing pCO_2. The development of a novel pCO_2 proxy that stretches further back into Earth's history and has a wide spatial and temporal distribution is crucial to furthering our knowledge of paleoclimates.

Additional work has suggested using the isotopic composition of coccolith calcite to reconstruct past CO_2 [Ziveri et al., 2003, Rickaby et al., 2010, Hermoso, 2014]. Indeed, McClelland et al. [2017] developed a cellular carbon isotopic flux model, which given measurements on $CO_{2(aq)}$ and measured cellular parameters is able to recreate the carbon isotopic signature of coccoliths. However, whilst qualitative inferences have been drawn between the isotopic composition of coccoliths and CO_2 [Bolton and Stoll, 2013a], studies are yet to quantitatively reconstruct CO_2 through inverting existing models. Moreover, CAPs extracted from coccoliths may also play a role in the development of a multifaceted coccolith based proxy. Studies have suggested that both the chemical composition and isotopic composition of CAPs are sensitive to $CO_{2(aq)}$ [Lee et al., 2016, Wilkes et al., 2018]. Combined measurements on the carbon isotopic composition of coccolith calcite and extracted CAPs in tandem with measuring CAP chemical composition may lead to a proxy that circumnavigates the need to constrain contemporaneous seawater isotopic

values, or estimate the b parameter needed for other proxies.

1.7. Thesis Aims and Objectives

In life, coccolithophores photosynthesise and calcify and, in doing so, record signals from their ambient environment. In death, their coccoliths are preserved in the sedimentary record and preserve associated environmental signals. Through analysing changes in coccolith abundance over time, coccolith isotopic ratios and the chemistry of organic molecules trapped within, we stand to advance our knowledge of both ancient coccolithophores and their environment. The fundamental motivation for this thesis is to advance our ability to reconstruct past variations in atmospheric CO_2 concentration using a range of signals captured by, and preserved within, coccoliths. More specifically, this thesis aims to:

1. Invert existing coccolith isotopic flux models, and using novel sedimentary data, reconstruct CO_2 levels during the warmest period of the Cenozoic, the Eocene (54 - 34 millions years ago).

2. Increase the granularity of existing coccolith isotopic flux models through the provision of additional culture data in geologically abundant species and to further elucidate individual species carbon acquisition strategies.

3. Investigate the response of $\delta^{13}C_{CAP}$ and CAP chemistry in cultures and in sediments to changes in carbon availability.

1.7.1. Thesis Outline

Chapter two attempts to answer whether it is possible to reconstruct Eocene pCO_2 based on the current knowledge of the carbon isotopic variation within coccolithophores and existing models. Chapter two reconciles the carbon isotopic composition of coccoliths from samples across the Eocene with an existing coccolithophore isotopic flux model, which is used to estimate $[CO_{2(aq)}]$. The offset between data and model $\delta^{13}C_{lith}$ is minimised through selecting optimal values for $[CO_{2(aq)}]$ and the ratio of calcification and photosynthesis, two fundamental controls on $\delta^{13}C_{lith}$. Additional data is presented for the species percentage change over the Eocene to further assist in providing an overview of past environmental conditions.

Chapter three is a culture based investigation into the response of $\delta^{13}C_{lith}$ and $\delta^{13}C_{org}$ in *Coccolithus pelagicus* and *Gephyrocapsa oceanica* to changes in pCO_2. Chapter three attempts to increase the granularity of the model applied in chapter two to a species specific level and provides updated, species specific, cellular fitted parameters. Chapter three further attempts to better understand the drivers behind the contrasting isotopic response of the species *C. pelagicus* and *G. oceanica* and to further elucidate carbon acquisitions strategies.

Chapter four investigates the changing chemistry of CAPs as a function of changing DIC conditions. CAPs are also extracted from fossil coccoliths from the sedimentary record in order to investigate how CAP chemistry changes through time and whether changes can be linked to changing carbon availability. Physiological mechanisms driving changes in CAP chemistry are explored and proposed.

Chapter five investigates the response of $\delta^{13}C_{CAP}$ for *Coccolithus pelagicus* and *Gephyrocapsa oceanica* as a function of external CO_2 concentration in controlled batch culture experiments. The physiological mechanisms driving changes in $\delta^{13}C_{CAP}$ across species are discussed in relation to previously published work. CAPs are also extracted from Eocene sediment samples. The $\delta^{13}C_{CAP}$ trend of the sediment samples are interpreted with regards to environmental change.

Chapter 2

The Eocene emergence of highly calcifying coccolithophores with declining pCO_2

Foreword

Sections 2.1 through 2.2 are, at the time of writing, under review in Nature Geoscience. Section 2.4 is the associated submitted supplementary information. The full authorship list includes Louis M Claxton, Harry L. O. McClelland, Michael Hermoso and Rosalind E. M. Rickaby. Section 2.5 is neither published nor submitted, however, contributed to the motivation of the study conducted in this chapter. Section 2.5 provides additional evidence for conclusions drawn from this study.

Abstract[1]

Coccolithophores are a group of unicellular calcifying phytoplankton and have been major contributors to marine carbonate production [Poulton et al., 2006] since their calcite plates (coccoliths) first appeared in the fossil record ~220 million years ago (Ma)[Bown, 1998]. Despite their central role in regulating the global carbon cycle, their adaptive calcification response to changes in pCO_2 remains poorly understood, particularly in warm climates. Here we use carbon isotope ratios of size-separated coccolith calcite in conjunction with a cell-scale model to interrogate cellular carbon fluxes and pCO_2 through the Eocene

[1]This abstract is as it appears in the manuscript currently under review.

(∼55-34 Ma); Earth's hottest period of the last 100 million years. We show that the large coccolithophores that rose to dominate the oceans through the Eocene have higher calcification to organic matter fixation ratios than their predecessors whilst the opposite is true for smaller coccolithophores. The rising pH and deepening carbonate compensation depth of the ocean during the Eocene implies that any change in calcite production rates are coincident with an increase in ocean alkalinity. Our novel approach also provides an independent confirmation of multiproxy based changes for pCO_2 through the Eocene [Beerling and Royer, 2011, Foster et al., 2017], supporting a decrease in pCO_2 through time in step with temperature. Together, this challenges the prevailing view that a decline in pCO_2 universally reduces calcification on evolutionary timescales [Bolton et al., 2016, Duchamp-Alphonse et al., 2018, McClelland et al., 2016, Meier et al., 2014, Si and Rosenthal, 2019, Suchéras-Marx and Henderiks, 2014].

2.1. Introduction

On short timescales sinking coccoliths remove alkalinity from the surface ocean, reducing its capacity to buffer changes in CO_2 [Zeebe and Wolf-Gladrow, 2001]. On long time scales coccolith burial in deep sea sediments removes carbon from the ocean-atmosphere system [Ridgwell and Zeebe, 2005]. The amount of calcite produced by coccolithophores varies between species and thus, changes in coccolithophore species composition through time can alter the amount of carbon transported to the deep ocean [Aloisi, 2015, Beaufort et al., 2011, Boudreau et al., 2018, Gibbs et al., 2018, Suchéras-Marx and Henderiks, 2014]. Recent observations based on the morphometry and weight of fossil coccoliths, a proxy for calcification, suggest reduced calcification during periods of low pCO_2 in the icehouse Neogene and glacial periods [Bolton et al., 2016, Duchamp-Alphonse et al., 2018, McClelland et al., 2016, Meier et al., 2014, Si and Rosenthal, 2019, Suchéras-Marx and Henderiks, 2014], although there are counter-examples [Beaufort et al., 2011, Meier et al., 2014, Su et al., 2020] (See supplementary table 2.1). The long-term adaptive response of coccolithophore calcification in a greenhouse world may be essential to understanding selective pressures in an anthropogenically altered future ocean, but is beyond the reach of short-term laboratory experiments. The Eocene, characterised by hot, yet declining temperature [Zachos et al., 2008] and pCO_2 [Anagnostou et al., 2020, Foster et al., 2017] provides a unique opportunity to gain this insight.

Period	CO_2 values	Metric used	Notes on calcification	Calcification	CO_2	weathering	Alkalinity	HCO_3^-	CO_3^{2-}	$\Omega_{calcite}$	pH	Temperature	DIC	Reference
Neogene	<500ppm	MARcoccolith	MAR change linked to productivity	↓	↓	↓			↓		↑			[Si and Rosenthal, 2019]
Glacial-Interglacial	<300ppm	Coccolith Mass	Also presents data for a species that decreases calcification with increased CO_2	↑	↓		↑	↓	↑	↑	↑	↑	↓	[Beaufort et al., 2011]
Glacial-Interglacial	<300ppm	Coccolith Mass	Also presents data for a species of G. Oceanica with calcification showing no correlation to any carbonate parameter	↑	↓			↓	↑		↑	↓		[Su et al., 2020]
Miocene	<500ppm	Size-normalised thickness		↑	↑		↑		↑		↑			[Bolton et al., 2016]
Glacial-Interglacial	<300ppm	Coccolith Mass		↑	↑									[Duchamp-Alphonse et al., 2018]
Glacial-Interglacial	<300ppm	Aspect Ratio		↑	↑							↑		[McClelland et al., 2016]
Glacial-Interglacial	<300ppm	coccolith weight		↑	↑			↑	↓	↓	↓	↓		[Meier et al., 2014]
Holocene	<300ppm	coccolith weight	Two sites, one increases with carbonate concentration, one decreases.	↑↓					↓			↓		[Berger et al., 2014]
Eocene	>750ppm	Coccolith Isotopes		↑	↓	↑		↑	↑		↑	↓		This Study

Table 2.1: Summary of changes in calcification with carbonate parameters from previously published work. The CO_2 estimates provided here are taken from the minimum and maximum values from Boron, Paleosols and Alkenone estimates of CO_2 as provided in a previous compilation of CO_2 data [Foster et al., 2017]. Estimated temperature range is the range of reconstructed mean deep water temperatures [Westerhold et al., 2020]. Metrics used to infer calcification rates include: $MAR_{coccolith}$ – Mass accumulation rate of coccoliths, the individual mass of coccoliths, their size normalised thickness and other morphometric relationships such as the coccolith aspect ratio. An increase in any of these metrics have previously been used to infer an increase in coccolithophore calcification via bulk calcite produced. Here we define an increase in calcification through a rise in the rate of calcification relative to the rate of organic matter fixation.

Organic carbon fixation by coccolithophores is a function of nutrient availability [Klausmeier et al., 2004, Moore et al., 2013], temperature [Krumhardt et al., 2017] and light levels [Zondervan, 2007]. The rate at which calcite is produced by coccolithophores relative to the rate of organic carbon fixation (R_{calc}:R_{fix}) differs by around a factor of four in modern species. R_{calc}:R_{fix} is approximately 0.5 in Emiliania huxleyi and 2 in Calcidiscus leptoporus [Aloisi, 2015]. R_{calc}:R_{fix} can potentially be constrained by measuring stable carbon isotope ratios of coccoliths [McClelland et al., 2017]. The deviation in carbon isotope ratios of coccolith calcite relative to equilibrium calcite is termed a carbon isotope vital effect (CIVE). CIVEs are a function of coccolithophore physiology and ambient carbonate chemistry [Bolton et al., 2016, Holtz et al., 2017, McClelland et al., 2017]. Coccolith calcite enriched (/depleted) in ^{13}C compared to equilibrium calcite possess a positive (/negative) CIVE [Hermoso, 2014, Rickaby et al., 2010, Ziveri et al., 2003]. CIVE expression is driven by the molar ratio of carbon demand to carbon supply and the partitioning of carbon between calcification and carbon fixation [McClelland et al., 2017]. The direction of the CIVE is largely set by R_{calc}:R_{fix}. A high R_{calc}:R_{fix} (typically greater than 1) produces a negative CIVE, while a low R_{calc}:R_{fix} (typically less than 1) a positive CIVE [McClelland et al., 2017]. This difference is largely driven by the effect of photosynthesis, which discriminates against ^{13}C, leaving the residual intracellular pool enriched in ^{13}C [McClelland et al., 2017]. The magnitude of the CIVE is set by the molar ratio of carbon demand to supply (carbon utilisation), which increases with cell size and growth rate, and decreases with ambient $CO_{2(aq)}$. Intracellular allocation of HCO_3^- [Bolton and Stoll, 2013a] and variations associated with changing light conditions [Holtz et al., 2017] impose secondary controls.

Cells of different sizes, or cells characterised by a different R_{calc}:R_{fix}, express distinct CIVEs under the same $CO_{2(aq)}$ regime. Given measured CIVEs from a record of size separated coccoliths, we can place constraints on R_{calc}:R_{fix} and $CO_{2(aq)}$, two key drivers of CIVEs. Here, we present a new coccolith calcite isotope dataset comprising isotope measurements from five size fractions of coccoliths across 37 depths from the Eocene section of ODP leg 208, Site 1263, 1300 km off the coast of southern Namibia. The size fractions generally track the isotopic composition of the bulk carbonate record but diverge at points through the interval in a size-dependent way (Fig. 2.1A). To explore the data, we used an existing cell-scale carbon isotopic flux model to find the optimal combination

of R_{calc}:R_{fix} and $CO_{2(aq)}$ that provides the best fit to measured isotopic CIVEs. Our isotopic data for the Eocene follows the independent bulk isotopic record closely with large deviations at approximately 46 Ma (Fig. 2.1A). After optimising for values of R_{calc}:R_{fix} and $CO_{2(aq)}$, we were successfully able to model the distribution of measured CIVEs (Fig. 2.1B).

2.2. Discussion

2.2.1. Calcification across the Eocene

Compared with modern, glacial and Miocene time periods, Eocene coccolithophores grew under higher temperatures and higher pCO_2 [Anagnostou et al., 2020, Foster et al., 2017], which appears to have been conducive to large size [Reinfelder, 2011]. Indeed, Eocene coccolithophores were some of the largest of the entire Cenozoic [Gibbs et al., 2018, Henderiks, 2008]. In our study we identified four dominant genera across the Eocene: *Coccolithus*, *Chiasmolithus*, *Discoaster* and *Reticulofenestra* (Fig. 2.2). We found that R_{calc}:R_{fix} across size ranges and genera were not substantially different to those of modern day coccolithophores [Aloisi, 2015], however the existence of substantially larger cells, as inferred from their correspondingly larger coccoliths [Henderiks, 2008, Sheward et al., 2017], mean that more calcite was produced per cell [Gibbs et al., 2018, Henderiks, 2008, Sheward et al., 2017, Young and Ziveri, 2000] (Fig. 2.2). Based on our values of R_{calc}:R_{fix} we infer that a cell belonging to the Eocene Coccolithus genus (radius $\sim 10\mu$m) would have produced $\sim$2.9x more calcite per cell than a large modern day *Coccolithus braarudii* (radius of $\sim 8\mu$m). The extinct genus *Discoaster* may have produced 5.4x more calcite per cell than modern day *Coccolithus braarudii* (see supplementary information). Given R_{calc}:R_{fix} for *Discoaster* was less than that of *Coccolithus*, a *Discoaster* cell would have produced less calcite per unit of organic matter fixed in the Eocene ocean. Until now, attempts to reconstruct R_{calc}:R_{fix} for *Discoaster* with morphometric approaches have been limited because of the unique star-shaped morphology of these coccoliths (Fig. S2.5). Moreover, a lack of intact coccospheres in the fossil record has made it impossible to make assumptions regarding the number of liths per cell in this lineage and thus determine R_{calc}:R_{fix} morphometrically. Isotopic compositions are determined by cellular chemical and isotopic disequilibrium that depends on relative rates of calcification to photosynthesis and thus

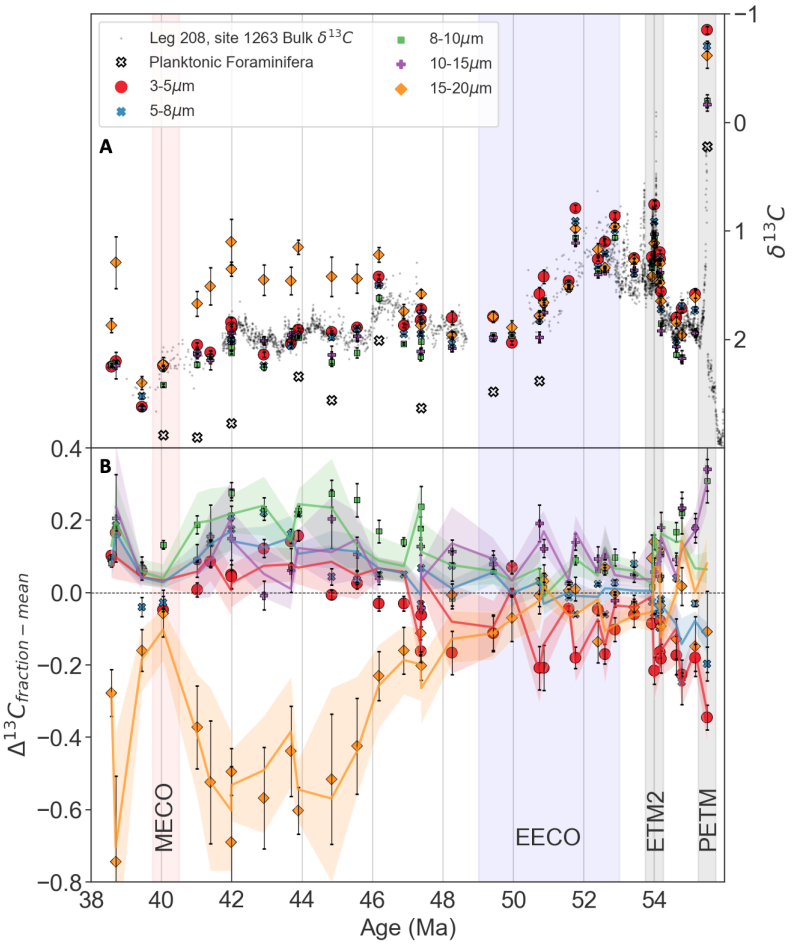

Figure 2.1: **(A)** Measured δ^{13}C across all five size fractions and coeval foraminifera measurements. Also shown are contemporaneous bulk sediment δ^{13}C values. **(B)** δ^{13}C values of each sediment size fraction relative to their age interval mean (CIVEs). Points are measurements, lines are fitted model values. The error bars in the points represent uncertainty introduced through contamination of neighbouring size fractions (see methods). The coloured envelope surrounding each line represents 95% of model runs over 10,000 Monte-Carlo simulations. The coloured vertical regions represents significant periods during the Eocene including the Paleocene-Eocene thermal maximum (PETM), Eocene thermal maximum 2 (ETM2), early Eocene climatic optimum (EECO) and the middle Eocene climatic optimum (MECO).

circumvents these difficulties.

Curiously, from 56-50 Ma the 3-5μm size fraction shows a continuous negative CIVE relative to the larger size fractions. Previous studies also noted the presence of the largest negative CIVE in the smallest size fraction during the Eocene [Bolton and Stoll, 2013a], however, this behaviour has previously proved difficult to interpret. In laboratory cultures, smaller species tend to show more positive CIVEs in comparison to larger species, owing to their lower carbon demand and generally lower R_{calc}:R_{fix} [Hermoso et al., 2016a, McClelland et al., 2017, Rickaby et al., 2010]. Our results suggest that from 56-50 Ma the smallest size fraction consisted mostly of *Coccolithus* whilst the largest size fraction was dominated by the genus *Discoaster* (Fig. 2.2). Given our genera distribution and modelled R_{calc}:R_{fix} values, we conclude that the CIVE pattern displayed during the early Eocene is consistent with the smallest size fraction having the largest R_{calc}:R_{fix}.

Our results suggest that a reorganisation of the coccolithophore community occurred during the transition from the early to middle Eocene. During the early Eocene, *Discoaster*, a warm water dwelling genus, by Eocene standards [Bralower, 2002, Bukry, 1971, Wei and Wise, 1990], was abundant in the surface ocean. From 47 Ma we find relative $CO_{2(aq)}$ declined contemporaneously with global temperatures [Westerhold et al., 2020] (see later results) and, with the transition to cooler surface waters, *Discoaster* was replaced by genera better adapted to cooler and oligotrophic conditions: *Coccolithus* and *Chiasmolithus* [Bralower, 2002, Bukry, 1971, Wei and Wise, 1990] (Fig. 2.2). Our inverse modelling efforts suggest that the community shift corresponded to a change from coccolithophores with a low apparent R_{calc}:R_{fix} to those with a higher apparent R_{calc}:R_{fix} in the largest size fraction. Yet, in the smallest size fraction, the community shift corresponds to a change from coccolithophores with a high apparent R_{calc}:R_{fix} to those with a lower apparent R_{calc}:R_{fix}

Few existing studies focus on reconstructing R_{calc}:R_{fix} for the Eocene period. Those that are available focus on morphometric reconstructions, which require assumptions about cell size and the number of coccoliths per cell and usually target short term warming events [Gibbs et al., 2018]. One such study suggests that community level R_{calc}:R_{fix} during the Paleocene-Eocene thermal maximum were similar to modern values with species such as *Coccolithus pelagicus* possessing ratios of $\sim$2, similar to our findings [Gibbs et al., 2018].

Evidence suggests that across the Eocene the CCD deepened [Pälike et al., 2012], ocean

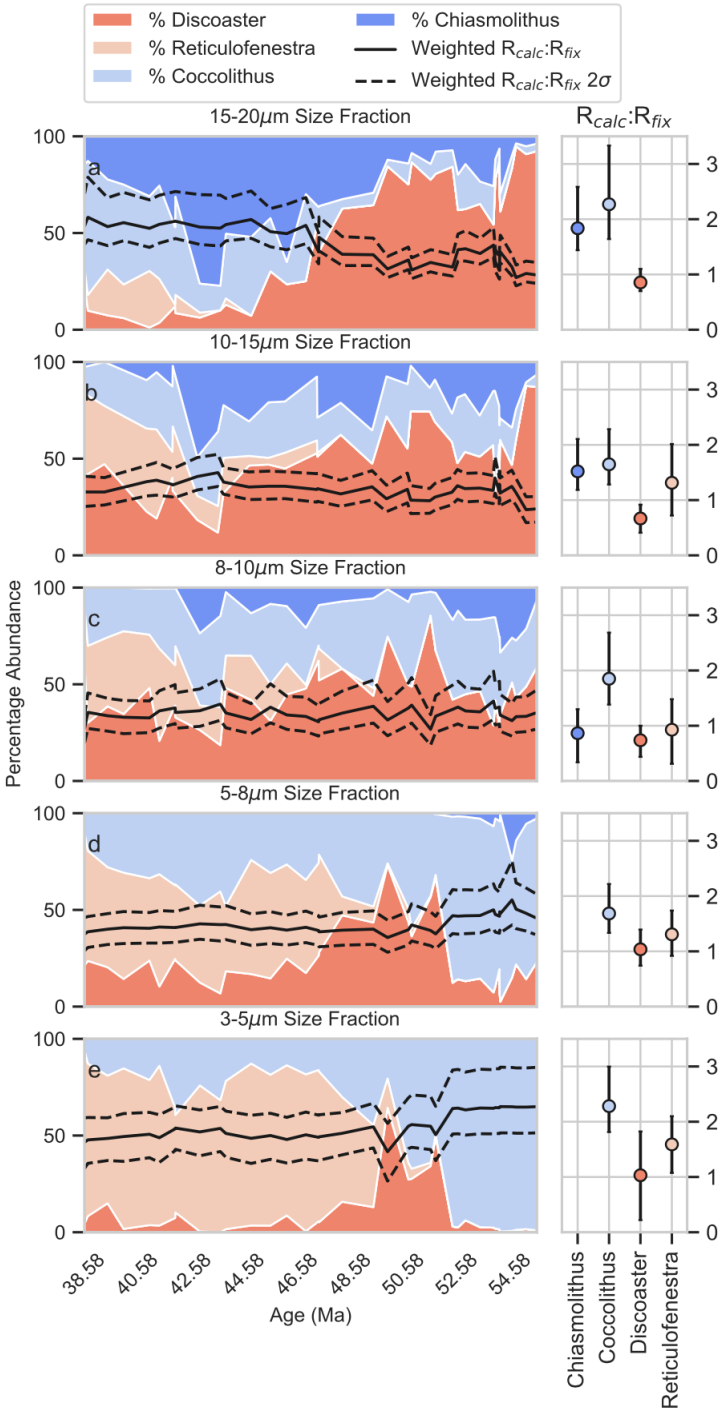

Figure 2.2: Stack plots represent coccolith counts for the (a) 15-20μm, (b) 10-15μm, (c) 8-10μm, (d) 5-8μm (e) and 3-5μm size fractions. Each stack plot represents a normalized closed sum of the four genera. Also shown to the right of each plot is the distribution of associated R_{calc}:R_{fix} values (for full species percentage abundance counts please see extended data). Reconstructed R_{calc}:R_{fix} values are shown for each of the four dominant genera across all sediment size fractions. Presented R_{calc}:R_{fix} represent the values that minimise the error between measured and modelled CIVEs. Error bars represent 95% of Monte Carlo realizations. The solid black line associated with each stack plot represents the abundance weighted average of each size fraction R_{calc}:R_{fix}. Dashed lines bound 95% of calculated weighted R_{calc}:R_{fix} values. The weighted R_{calc}:R_{fix} values are on an equivalent scale to the subplots on the right hand side.

pH rose [Anagnostou et al., 2020] and an increase in global weathering [McArthur et al., 2001, Misra and Froelich, 2012, Pegram et al., 1992, Ravizza and Zachos, 2003] likely drove an increased flux of alkalinity to the oceans. Carbonate mass accumulation rates (CMAR) at Site 1263 and at other sites across the ocean appear to have declined [Brummer and van Eijden, 1992, Zachos et al., 2004] (see supplementary table 2.1). Across the Eocene, our results suggest R_{calc}:R_{fix} increased within the largest coccolithophores from approximately 1 to 2, but decreased in the smallest coccolithophores from around 2.1 to 1.5. Taken together these data could suggest that the smaller and larger coccolithophores have different optima for calcification. Determining the weighted change in R_{calc}:R_{fix} across the whole coccolithophore community is not possible based on abundances in sediment alone due to likely systematic differences in dissolution potential between the smallest and largest species. The putative deepening of the CCD implies an increase in the saturation state of the deep ocean, which suggests that either there was a whole ocean decrease in calcite production rates, or an increase in delivery of alkalinity to the deep ocean reservoir, possibly via increased respiration driven dissolution of exported carbonate. Our data suggest that a decrease in carbonate export from the surface ocean could be explained by a shift in surface ocean coccolithophore community composition from larger (increasingly heavily calcifying) to smaller (decreasingly heavily calcifying) coccolithophore species. Resolving the intensity of respiration dissolution during the Eocene could be addressed in future work by assessing the history of decoupling between the lysocline and CCD.

2.2.2. Implications of temperature and light on growth rate and calcification

Growth rate is a key parameter in all phytoplankton d13C based investigations of paleo-CO_2, but is notoriously difficult to constrain [Ziveri et al., 2003, Rickaby et al., 2010, Hermoso et al., 2016a, Holtz et al., 2017, McClelland et al., 2017]. In our model, growth rate was assumed to scale allometrically and was therefore set constant for individual cell sizes across genera. However, over million-year timescales variations in nutrient conditions, light and temperature may result in variations to cellular growth rate and calcification. Moreover, inter-species and genus variations likely exist. Yet, without a reliable growth rate proxy for ancient coccolithophores, constraining growth rates for cells during the Eocene is difficult. Lab based studies have shown that coccolithophores likely exhibit a species-specific optimum-like response to variations in temperature [Krumhardt et al.,

2017]. Qualitatively, the long term decline in temperature across the Eocene [Westerhold et al., 2020] may therefore result in variations to growth for different species. For an observed CIVE a net decrease (/increase) in the growth rate of a size fraction would require a correspondingly lower (/higher) predicted ambient CO_2 concentration. Similar reasoning exists for changes in growth rate manifesting from variations in nutrient and light conditions. Future improvements may be made with an allometric formulation of growth rate relationship that includes coefficients for temperature, light and nutrient conditions, which would allow for such variations to be quantitatively investigated within our model. We investigated uncertainty on our results deriving from variations to growth rate within our sensitivity analysis (see SI and Supplementary Fig 2.10).

In laboratory based studies R_{calc}:R_{fix} ratios, or the measurable particulate inorganic to particulate organic carbon ratio (PIC:POC), has been shown to decline below a threshold temperature, which likely varies between species [Krumhardt et al., 2017]. In our study predicted R_{calc}:R_{fix} was assumed to be constant for each genus within each size fraction throughout our record. Predicted R_{calc}:R_{fix} values therefore reflect the best fit for the entire Eocene period. Predicting R_{calc}:R_{fix} for each time step would result in an under constrained problem. The long term decline in temperature, or indeed any driver of calcification, across the Eocene may therefore result in variations to R_{calc}:R_{fix}, which due to our experimental approach cannot be captured.

2.2.3. Eocene CO_2 levels

Our model implies that $CO_{2(aq)}$ was higher in the early Eocene and decreased across the Epoch as CIVEs emerge and increase in magnitude, in line with previous data [Foster et al., 2017] (Fig. 2.3). Given Site 1263 was likely close to equilibrium with the atmosphere (see methods), modelled $CO_{2(aq)}$ can be assumed to reflect atmospheric pCO_2. The temperature change across the Eocene was taken into consideration when calculating pCO_{2atm} across the interval via Henry's law (Supplementary Fig. 2.9). Proxies show that the sea surface temperature may have reached 30 °C at site 1263 during the middle Eocene; roughly 20 °C warmer than modern day [Boscolo Galazzo et al., 2014, Inglis et al., 2020, Lunt et al., 2021]. Estimates of Eocene pCO_2 vary between ~500 and 2000 ppm [Anagnostou et al., 2020, Beerling and Royer, 2011, Foster et al., 2017, Henehan et al., 2020, Zachos et al., 2001, 2008], but agree on the presence of a long term decline, with

substantial departures at 40 Ma and 54 Ma [Anagnostou et al., 2020, Foster et al., 2017], in line with our results (Fig. 2.3).

Qualitatively the convergence of CIVEs at 53.5-54 Ma indicates higher pCO_2, given reduced CIVEs are observed at higher $[CO_{2(aq)}]$ [McClelland et al., 2017], which is supported by our modelled predictions (Fig 2.1 and 2.3). Our predicted peak in relative $CO_{2(aq)}$ during the early Eocene approximately 53.5-54 Ma may be attributed to Eocene thermal maximum 2 (ETM2), a rapid period of warming [Sluijs et al., 2009, Stap et al., 2009, 2010]. High relative $CO_{2(aq)}$ at ∼40 Ma is likely associated with the middle Eocene Climatic Optimum (MECO [Bohaty and Zachos, 2003]). The MECO is believed to represent a period of elevated volcanic outgassing, decreased silicate weathering [van der Ploeg et al., 2018], and rapid shallowing of the CCD [Pälike et al., 2012]. Prior to the MECO our relative $CO_{2(aq)}$ curve shows a highly significant (p-value ≤ 0.001) negative correlation with global $\delta^{18}O_{benthic}$ data (Fig. 2.3b), a widely accepted proxy for deep sea temperature (in the absence of ice sheets) in the Eocene that reflects longer term climatic change. The observed covariance between reconstructed $CO_{2(aq)}$ and this independent proxy for temperature lends strong support to the robustness of our findings. From 41.5 Ma to 38.5 Ma, we find that the relative $CO_{2(aq)}$ curve shows no correlation to global $\delta^{18}O_{benthic}$. Data from 41.5 Ma to 38.5 Ma (four of 37 data points) were excluded from the regression analysis. The exclusion is justified given the potential decoupling between $\delta^{18}O_{benthic}$, atmospheric CO_2 and carbonate storage within the ocean during the MECO owing to an unstable nascent cryosphere [Henehan et al., 2020]. Variations in ice volume at high latitudes and altitudes from 41.5-38.5 Ma rather than temperature could cause a deviation to the relationship between $\delta^{18}O_{benthic}$ and CO_2.

Unlike other carbon isotope-based pCO_2 proxies [Freeman and Pagani, 2005, Pagani, 2002, Zhang et al., 2019] the use of mean-normalized model predictions fitted to mean-normalized measurements makes our approach internally dependent on coccolith calcite and independent of seawater carbon isotopic values. Independence comes at the cost of one degree of freedom per depth interval (total of 37) and results in a solution that is non-unique in absolute $CO_{2(aq)}$ and R_{calc}:R_{fix}, but robust with respect to relative change in $CO_{2(aq)}$ and R_{calc}:R_{fix}. Loose constraints on the absolute value and change in pCO_2 are provided by estimates of seawater carbon isotopic values from foraminiferal calcite (Supplementary Fig. 2.9). When carbon utilisation is low (particularly at high external

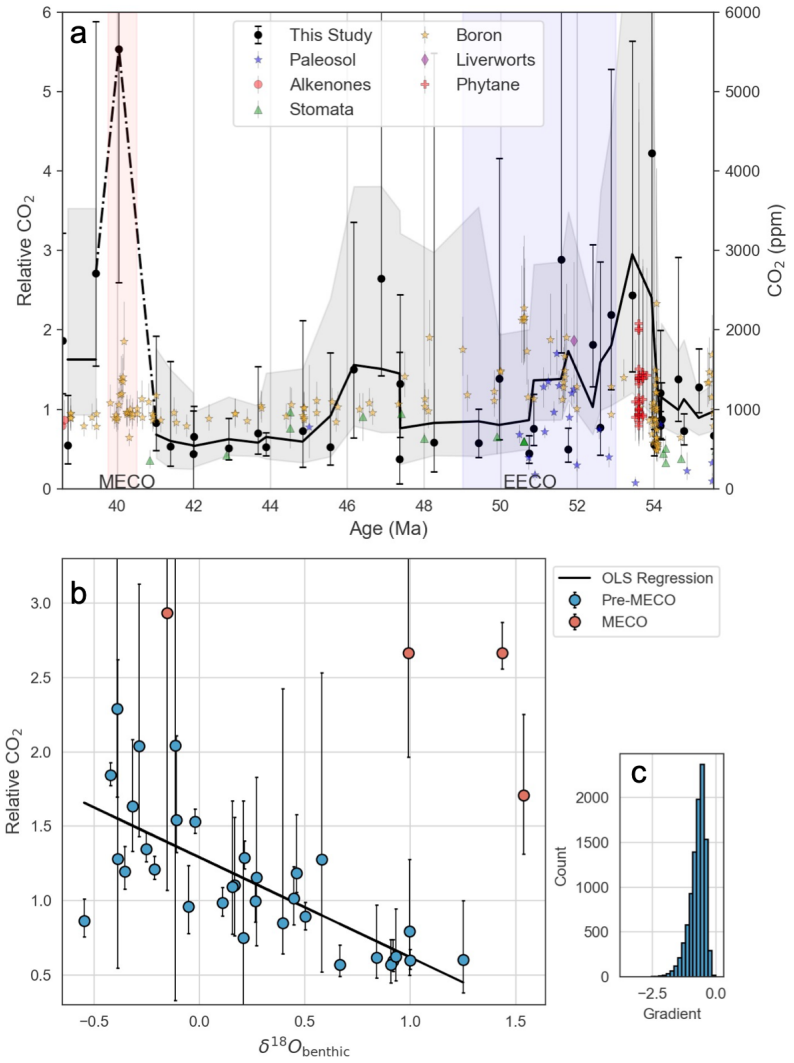

Figure 2.3: Relative CO_2 is derived from our optimized model with new size differentiated isotopic constraints. The coloured markers represent previously published pCO_2 data [Anagnostou et al., 2020, Foster et al., 2017] across the Eocene (right hand y-axis). The black circles represent the median relative $CO_{2(aq)}$) over 10,000 iterations of our Monte-Carlo optimization (left hand y-axis). The black line represents a 3-point moving average of our output, with the grey shaded region representing 95% of realizations. Our modelled low in relative $CO_{2(aq)}$) during the middle Eocene coincides with a step wise increase in proxies linked to an increase in the rate of chemical weathering and therefore CO_2 draw-down [McArthur et al., 2001, Misra and Froelich, 2012, Pegram et al., 1992, Ravizza and Zachos, 2003]. b) The five point moving average of relative $CO_{2(aq)}$) is plotted against the five point moving average of $\delta^{18}O_{benthic}$. The five point moving average was used to avoid noise in the data and evaluate the longer term trend. Error bars represent one sigma uncertainty on reconstructed $CO_{2(aq)}$) values. The four points in red represent the points from the MECO and younger, which have been excluded from the p-value calculation (p-value ≤ 0.005). Without the MECO data included, our relative $CO_{2(aq)}$) and $\delta^{18}O_{benthic}$ show a robust negative correlation. The warmer early Eocene characterised by more negative values of $\delta^{18}O_{benthic}$ has on average higher values of relative $CO_{2(aq)}$). c) The slope of relative $CO_{2(aq)}$) with $\delta^{18}O_{benthic}$ for each of the 10,000 Monte-Carlo simulations was calculated and plotted as a histogram. Only one value was greater than 0.

$CO_{2(aq)}$) the effect of $CO_{2(aq)}$ on CIVE expression is small. During the hyperthermals (e.g. ∼40 Ma) the model therefore results in a greater spread of possible $CO_{2(aq)}$ values.

2.2.4. Conclusion

The question thus remains, what parameters drive long term adaptive changes in calcification? In addition to declining temperature and $CO_{2(aq)}$, the Eocene was likely characterised by an increase in ocean alkalinity [Misra and Froelich, 2012, Pegram et al., 1992, Ravizza and Zachos, 2003] and pH [Anagnostou et al., 2020]. These conditions appear to correlate with an increase in calcification relative to organic matter fixation in the largest cells, and the inverse in the smallest cells, in the greenhouse world of the Eocene. For the largest cells, whose small surface area to volume ratios may make them particularly vulnerable to self-acidification of the cytosol by calcification, increasing surface ocean pH [Anagnostou et al., 2020] may have resulted in a more favourable gradient for the efflux of H^+ ions and thus enabled the emergence of large, more heavily calcified coccolithophores [Bach, 2015, Monteiro et al., 2016]. Without fully understanding why coccolithophores calcify, the exact drivers of change remain elusive.

2.3. Methods

2.3.1. Sample selection and preparation

The sediment samples were from Ocean Drilling Program (ODP) leg 208, Site 1263. Site 1263 has remained at a relatively constant latitude for most of the Cenozoic [Zachos et al., 2004]. Ocean general circulation models suggest reduced Atlantic upwelling during the Eocene, with the Walvis ridge likely outside of any significant zones of upwelling [Bice et al., 2000, Handoh et al., 2003]. We thus posit that Site 1263 was in equilibrium with the atmosphere. Site 1263 was drilled from a current water depth of 2717m, with the paleodepth during the Eocene believed to be around 1500m [Zachos et al., 2004]. 37 samples were selected at approximately 0.5 Ma intervals through the Early and middle Eocene.

Sediment samples were placed in 100ml of pH neutral de-ionised water and placed on an orbital shaker overnight for disaggregation. Samples were then filtered through 64μm, 38μm and 20μm sieves to remove large particles such as foraminifera and their fragments.

The $\leq$20μm fraction was separated into four smaller fractions with microfiltration: 3-5μm, 5-8μm, 8-10μm and 10-20μm. The 10-20μm fraction was further separated into a 10-15μm and a 15-20μm fraction via the settling method [Zhang et al., 2018]. Through size separation and microscopic analysis, we constrained the average coccolith length for each genus across all size fractions. The coccolith length was subsequently used to determine cell size through established morphometric relationships (see supplementary information)[Gibbs et al., 2018, Henderiks, 2008]. Nannofossil counts were conducted over a gridded 400μm2 area. Nannofossil relative abundance is presented as % contribution of coccoliths to total counted and averaged across two counts. The microfiltration technique was assumed to be imperfect; we therefore ascribed an uncertainty to the measured coccolith carbon isotopic values relative to an international standard (δ^{13}C) assuming contamination from neighbouring size fractions. The 15-20μm fraction and the 3-5μm fraction were assumed to have a 25% contamination from the 10-15μm fraction and the 5-8μm fraction respectively in line with previous studies [Hermoso et al., 2020]. The remaining size fractions were assumed to have a 12.5% contamination from the bounding size fractions. SEM images show good preservation of coccolith material; however, we address the possibility of slight overgrowth on individual coccoliths/nannoliths within the supplementary information.

2.3.2. Age model

The age of each sample has been calculated based on three astronomically tuned age models for Site 1263 that best represent the mid and late Eocene [Lauretano et al., 2016, Westerhold et al., 2017, 2015]. The age model from 56Ma to 50Ma is based on a regression model of the biostratigraphic datums to best fit the data around the PETM with our oldest point believed to be during peak PETM given its isotopic signature.

2.3.3. Isotopic measurements

$\delta^{13}C_{lith}$ was determined from approximately 150μg of size separated sedimentary material. In total 182 samples were processed (5 size fractions x 37 depths =185, minus seven lost samples due to machine error). Material was analysed via a Delta V Advantage isotope mass spectrometer fitted with a Gas Bench II in the department of Earth Sciences at the University of Oxford. An isotopic measurement was made for each of the five size fractions from each time interval. Samples were calibrated to Pee-Dee-belemnite (PDB)

via the international NBS-19 standard. All measurements are expressed relative to the V-PDB standard and the analytical precision on the standard was better 0.04‰ across repeat measurements for $\delta^{13}C$ (1σ). Reproducibility of sample replicates were within 0.04‰. The final error on isotopic measurements encompasses both analytical error and error introduced from the microfiltration technique (Fig. 2.1).

2.3.4. Development of the forward model

We developed a forward model that used coccolithophore taxonomic abundance (resolved to genus-level) and a previously published cellular isotopic flux model [McClelland et al., 2017] to generate abundance-weighted predictions of size fraction-specific CIVEs, with individual taxon-specific CIVEs calculated as a function of R_{calc}:R_{fix} and $CO_{2(aq)}$. Our approach separates the dependence of the CIVE from the isotopic composition of DIC by subtracting the mean CIVE for each depth (/age point) from both the modelled predictions and the data. We use an iterative optimization approach to search parameter space for 20 size and genus-specific values of R_{calc}:R_{fix} (five size fractions within the four dominant genera) and 37 (age or depth-specific) values of $CO_{2(aq)}$, to maximize the fit of model predictions to the mean-normalized CIVE record (See figure 2.4 for full work flow). Our approach allowed changes in relative $CO_{2(aq)}$ to be constrained independent of $\delta^{13}C_{DIC}$. However, we also used a foraminiferal record of $\delta^{13}C_{DIC}$ to place additional constraints on absolute pCO_2 (see supplementary information). We used a Monte Carlo approach to explore the sensitivity of constrained values to model inputs (see methods and supplementary information).

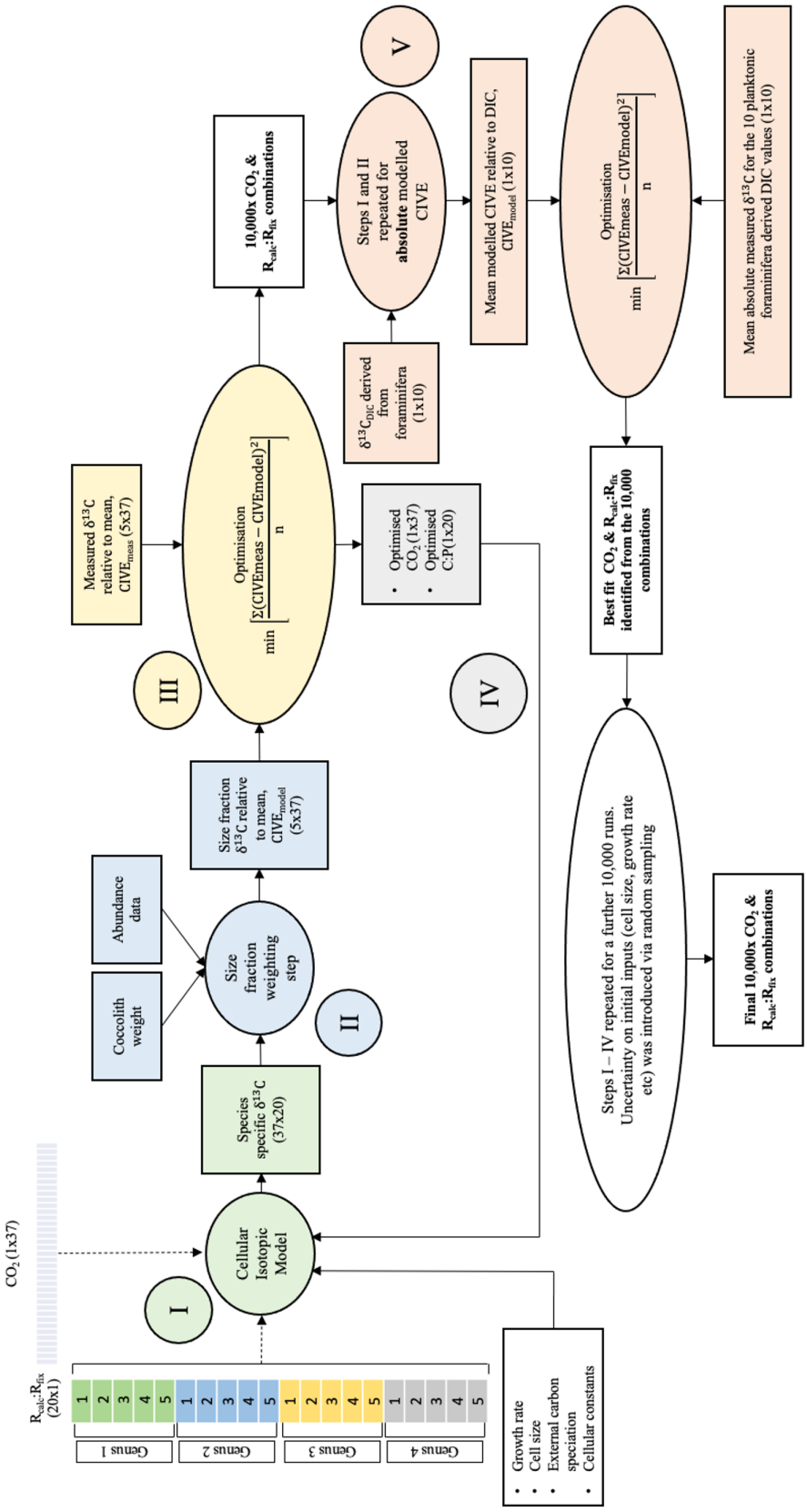

Figure 2.4: Caption on following page.

Figure 2.4: Modelling processes such as the isotopic model and the optimisation step are denoted by ovals. Input and output parameters are represented by rectangles. The process is as follows; (I) Input parameters are fed into the isotopic cellular model including growth rate, cell size, the external carbon speciation parameter space and the cellular constants. The initial CO_2 values are fed into the model in a 1x37 matrix, representing a value of CO_2 for each of the 37-time intervals. An original matrix of cellular R_{calc}:R_{fix} is also fed into the model, representing all four species and the five size fractions. The original 1x37 CO_2 matrix and the 20x1 R_{calc}:R_{fix} matrix is only utilised on the first iteration of the optimisation procedure. 10,000 initial values of R_{calc}:R_{fix} were selected from a log-uniform distribution between 0.5 and 10, whilst an initial 10,000 $CO_{2(aq)}$ values were selected from a uniform distribution between 20 and 150 μmols kg^{-1}, with external carbon conditions allowed to reach concentrations as low as 5 μmols kg^{-1}. (II) The output of the cellular model produces a 37x20 matrix representing the $\delta^{13}C$ of every size fraction across all four species at every time interval. This data is then fed into the size fraction weighting step, whereby the percentage abundance data and coccolith weight is used to calculate a mass fraction weighting of the species-specific contribution to each size fraction (see methods). The mean $\delta^{13}C$ for each age interval is then subtracted to determine the CIVE relative to the mean. The output is a 5x37 Matrix of size fraction specific $\delta^{13}C$ relative to the mean at each time interval. (III) The size fraction specific CIVE relative to the mean is fed into the optimisation step with the difference from the measured CIVE relative to their mean values used as the target minimisation function. R_{calc}:R_{fix} is optimised first, then using those values of R_{calc}:R_{fix}, CO_2 is optimised to further reduce the offset of measured and modelled CIVEs. (IV) The output values of R_{calc}:R_{fix} and CO_2 are fed back into the cellular model to recalculate the species specific $\delta^{13}C$ values combined with the other inputs. The method was repeated until the values of CO_2 and R_{calc}:R_{fix} remained consistent given the initial conditions. The steps I-IV were repeated 10,000 times to get a series of 10,000 optimised R_{calc}:R_{fix} and CO_2 values. (V) Steps I and II were repeated, however the CIVE was given relative to DIC rather than to the mean value. The offset from the measured absolute CIVE was then calculated. The run with the lowest was used as the starting point for a further 10,000 runs and uncertainty analysis based on Monte Carlo resampling (stages I-IV repeated). The mean of the final set of 10,000 runs was taken and is presented in the main manuscript.

The forward model predicts the $\delta^{13}C$ of each size fraction as a weighted sum of the predicted $\delta^{13}C$ for taxa that contribute to each size fraction and their observed relative abundances. Predicted $\delta^{13}C$ values for each size and taxon specific unit (STU; four genera across five size fractions giving 20 in total) were calculated from a previously published model as a function of ambient carbonate chemistry (all STUs are assumed to experience the same ambient environment at each time point) and STU-specific parameters: R_{calc}:R_{fix}, cell size and growth rate (assumed constant for each STU throughout the studied interval). Growth rate was assumed to follow an allometric scaling relationship with cell size [Aloisi, 2015]; cell size was determined from coccolith size [Gibbs et al., 2018, Henderiks, 2008, Young and Ziveri, 2000]; and abundances were counted directly (model inputs found in table S2). The assumption of constant growth rate for each STU is supported by Sr/Ca data (supplementary Fig. 2.6). Parameters fitted to culture data in the original paper remain unchanged [McClelland et al., 2017]. Carbon speciation in ambient seawater was calculated via the Seacarb package for R with an assumed constant calcite saturation state. The remaining parameters, $CO_{2(aq)}$ and R_{calc}:R_{fix} (referred to as RR in the below mathematical representation), defined the parameter space to be explored. Initial values for $CO_{2(aq)}$ and R_{calc}:R_{fix} were initialised from a random uniform distribution (see section on selecting initial CO_2 and R_{calc}:R_{fix} below).

For each STU-specific RR_i (i $\in \{1 : I\}$, I = 20 STUs) and each age-specific $CO_{2(aq)}$j (k $\in \{1 : K\}$, K=37 depths), the isotopic flux model was used to calculate a $\delta^{13}C$ value, D_{ik} (I x K = 740 in total). Modelled estimates of size-fraction-specific $\delta^{13}C$, E_{jk} (j$\in \{1 : J\}$, J=5 size fractions) then involved weighting each age and STU combination by its relative contribution to the analysed calcite for each size fraction. To do this, D was combined with a matrix of the fractional abundance of each genus in each size fraction (B, with elements B_{ik}) based on data from microscope counts, a matrix of genus coccolith weight (C, with elements C_{ik}) calculated from previously published morphometric relationships [Gibbs et al., 2018, Young and Ziveri, 2000], and a sorting matrix to produce a J x K (5 x 37) matrix of age and size-fraction-specific $\delta^{13}C$ values (E):

$$E = [A(B \otimes C \otimes D)]\emptyset[A(B \otimes C)] \tag{2.1}$$

A, B, C, D and E are all matrices. $\otimes$ represents the mathematical operation of element

wise multiplication and ∅ element wise division, and A is given by:

$$A = \begin{bmatrix} 1 & 1 & 1 & 1 & 0 & 0 & 0 & 0 & 0 & 0 & 0 & 0 & 0 & 0 & 0 & 0 & 0 & 0 & 0 & 0 \\ 0 & 0 & 0 & 0 & 1 & 1 & 1 & 1 & 0 & 0 & 0 & 0 & 0 & 0 & 0 & 0 & 0 & 0 & 0 & 0 \\ 0 & 0 & 0 & 0 & 0 & 0 & 0 & 0 & 1 & 1 & 1 & 1 & 0 & 0 & 0 & 0 & 0 & 0 & 0 & 0 \\ 0 & 0 & 0 & 0 & 0 & 0 & 0 & 0 & 0 & 0 & 0 & 0 & 1 & 1 & 1 & 1 & 0 & 0 & 0 & 0 \\ 0 & 0 & 0 & 0 & 0 & 0 & 0 & 0 & 0 & 0 & 0 & 0 & 0 & 0 & 0 & 0 & 1 & 1 & 1 & 1 \end{bmatrix}$$

The overall result is to transform D (STU-specific δ^{13}C I x K matrix) to E (a J x K matrix that represents the weighted δ^{13}C values for each size fraction that would have been measured at each time interval).

The modelled δ^{13}C mean for each time interval was then subtracted from each size fraction δ^{13}C at the corresponding time interval to remove the dependence on absolute isotopic compositions and generate a mean-centred value of CIVE (F) for each size fraction:

$$F_{j,k} = E_{j,k} - \overline{E_{1:J,K}} \tag{2.2}$$

Where $\overline{E_{1:J,K}}$ is the mean for modelled δ^{13}C across all five size fractions at each age point. F represents a J x K matrix of mean centred model-predicted δ^{13}C values subsequently used for the fitting of R_{calc}:R_{fix} and CO_2.

2.3.5. Optimization

The measured data were treated similarly to remove the dependence on $\delta^{13}C_{DIC}$ and generate a mean corrected measured isotope matrix, H:

$$H_{j,k} = G_{j,k} - \overline{G_{1:J,K}} \tag{2.3}$$

Where G is the absolute $\delta^{13}C_{calcite}$ measured for each size fraction at each depth and $\overline{G_{1:J,K}}$ is the mean $\delta^{13}C_{calcite}$ across all five size fractions at each age point. The misfit function between the mean-corrected data (H) and the mean-corrected model-predicted values (F) is given by:

$$\min \left[\frac{\sum_{j=1}^{J} \sum_{k=1}^{K} (H_{j,k} - F_{j,k})^2}{n} \right] \tag{2.4}$$

Where n is the total number of measured and modelled pairs (J x K minus any missing values). There were 7 missing values across 185 size and depth combinations, giving a total of 178 data points to constrain 57 parameter values (20 R_{calc}:R_{fix} + 37 CO_2s).

An iterative optimisation approach was taken to find the best $CO_{2(aq)}$ and R_{calc}:R_{fix} combination to generate model predictions (F) that fit the measured mean centred CIVE data (H). We used a two-step iterative optimisation to minimise the offset: Step one consisted of optimising for R_{calc}:R_{fix} given an initial constant $CO_{2(aq)}$; step two consisted of optimising for $CO_{2(aq)}$ using the values of R_{calc}:R_{fix} determined in step one. Taking the fitted values of $CO_{2(aq)}$ for the new initial value, the optimisation process was repeated until R_{calc}:R_{fix} and $CO_{2(aq)}$ were stable. An unconstrained Nelder-Mead optimiser (*fminsearch*, matlab) was used to determine fitted values of $CO_{2(aq)}$ and R_{calc}:R_{fix} that reduced the misfit between the measured and modelled CIVEs (according to equation 3.11) for each iteration. Both $CO_{2(aq)}$ and R_{calc}:R_{fix} were only allowed to be positive values.

2.3.6. Selecting initial CO_2 and R_{calc}:R_{fix}

The model outputs of R_{calc}:R_{fix} and $CO_{2(aq)}$ using the mean centred CIVEs are dependent on their initial values. However, relative change is robust across depths and across STUs (Fig. 2.8). These parameters described a valley of stability in parameter space whereby the average output $CO_{2(aq)}$ trades off against the average output R_{calc}:R_{fix}. We therefore present CO_2 as a relative change where relative CO_2 is given by the optimized $CO_{2(aq)}$ output divided by the initial prescribed $CO_{2(aq)}$ value. Differences in the trends in CO_2 between different initial values were minor, however to non-arbitrarily choose initial values of CO_2 and R_{calc}:R_{fix}, we introduced an additional optimization step that used an independent estimate of $\delta^{13}C_{DIC}$ derived from coeval planktonic foraminifera (see supplementary discussion and Fig 2.9).

10,000 initial values of R_{calc}:R_{fix} were selected from a log-uniform distribution between 0.5 and 10, whilst an initial 10,000 $CO_{2(aq)}$ values were selected from a uniform distribution between 20 and 150 μmols kg^{-1}, although external carbon conditions allowed to reach

concentrations as low as 5 μmols kg^{-1}. The optimization outlined in equations 2.1-2.3 was undertaken for each of the 10,000 combinations, and a fitted array of $CO_{2(aq)}$ and R_{calc}:R_{fix} values was generated for each combination. The fitted values of CO_2 and R_{calc}:R_{fix} were then passed to the forward model to generate 10,000 E matrices of modelled absolute CIVEs.

δ^{13}C of planktonic foraminifera were analysed for 10 depths with the associated $\delta^{13}C_{DIC}$ determined assuming a constant vital effect (P; see supplementary discussion). $\delta^{13}C_{DIC}$ was added onto $E_{j:J}$ for the corresponding depths, and the misfit between the mean raw size fraction data (G) and the predicted mean of the E matrices + $\delta^{13}C_{DIC}$ were calculated:

$$\min \left[\frac{\sum_{m=1}^{M} \sum_{j=1}^{J} G_{j,m} - (E_{j,m} + P_m)^2}{N} \right] \tag{2.5}$$

where foram depths is a set where each value is the depth at which planktonic foraminifera were picked and measured (m $\in$ {foram depths}). P is the vector of $\delta^{13}C_{DIC}$ values, and N is the total number of size-fraction-specific δ^{13}C values from the 10 samples that we analysed coeval foraminifera.

Comparison of the modelled CIVEs relative to $\delta^{13}C_{DIC}$ provides constraints on the absolute magnitude of R_{calc}:R_{fix} and $CO_{2(aq)}$ (and pCO_2; Fig. 2.9). However, estimating $\delta^{13}C_{DIC}$ from planktonic foraminifera relies on poorly constrained vital effects, which compromises the elegance of our approach. We thus present relative $CO_{2(aq)}$ changes based on an internally consistent analysis of coccolith calcite (independent of $\delta^{13}C_{DIC}$), and consider estimates of absolute $CO_{2(aq)}$ to be only loosely constrained by the additional consideration of the δ^{13}C of foraminiferal calcite given the calibration on 10 data points.

2.3.7. Monte Carlo exploration of model output

A Monte Carlo approach was employed to further explore how uncertainties in growth rate, coccolith abundance data, coccolith weight and external carbonate saturation state impact the results over 10,000 runs. For each iteration, values were resampled from their uncertainties (see supplementary table 2.4.3). Additionally, the initial target value for H was selected from the uncertainty ascribed due to contamination during the filtration process (see sample selection and preparation). The distribution was assumed normal

around its mean. Initial R_{calc}:R_{fix} was fixed at 1.45 and the initial [$CO_{2(aq)}$] at 29μmol kg^{-1}, the values that provided the best fit of measured CIVEs with modelled CIVEs relative to $\delta^{13}C_{DIC}$. Assuming an average pCO_2 of 1000 ppm, pH of 7.7 and temperature of 25°celcius across our time interval [Anagnostou et al., 2020, Foster et al., 2017] the corresponding average [$CO_{2(aq)}$] calculated via Seacarb in R would be ~29μmol $kg^{-}1$, which further validates our choice. Final values of R_{calc}:R_{fix} and relative $CO_{2(aq)}$ presented in Figure 2.2 and 2.3 represent the output of R_{calc}:R_{fix} from the Monte Carlo simulation over 10,000 iterations.

We also performed a sensitivity analysis on our Monte Carlo simulation to determine the degree of uncertainty that each of our input variables had on our final predicted values of CIVE, relative $CO_{2(aq)}$ and R_{calc}:R_{fix} over 100 iterations (see supplementary discussion and supplementary figure 2.10). For each of the sensitivity analyses, uncertainty on all but the target variable was assumed to be 0, whilst the uncertainty on the target variable was ascribed as listed in supplementary table 2.4.3. We found the model similarly sensitive to all parameters within the ranges investigated. The robustness of our outputs to variations in our model assumptions such as the validity of an allometrically scaled growth rate and an assumed constant R_{calc}:R_{fix} was also investigated. Our results show that the trends in $CO_{2(aq)}$ and R_{calc}:R_{fix} were robust across growth rates and that the model is unable to fit measured CIVEs given a constant R_{calc}:R_{fix} (supplementary figure 2.11). When growth rate was fixed at one for all sizes much larger values of relative $CO_{2(aq)}$ were required to fit the modelled data. Finally, we investigated the effect of changes in carbonate chemistry parameter space given variations in Ca^{2+} concentration across the Eocene (see supplementary discussion and supplementary figure 2.11). Whilst marginal differences were apparent, the trends in $CO_{2(aq)}$ and R_{calc}:R_{fix} were robust. We opted not to include the change in Ca^{2+} over time to avoid imposing trends into our data that were not internally derived from the measured values.

The model produced a narrow range of fitted values of R_{calc}:R_{fix} when the genus contributes a large proportion to the total sediment size fraction (Fig. 2.2). If a genus is underrepresented in a specific size fraction the possible range of R_{calc}:R_{fix} is much wider since it contributes minimal carbonate within the size fraction $\delta^{13}C$ signal. The R_{calc}:R_{fix} of Chiasmolithus in the 3-5μm and the 5-8μm size fractions and Reticulofenestra in the 15-20μm size fraction are poorly constrained, and thus not presented. All code can be

found at https://github.com/lclaxton/Eocene$_V$*Es*.

2.4. Supporting Information

2.4.1. Purity of size separated samples

The percentage of nannofossils in the sediment in all size fractions was ≥90%. Calcareous dinoflagellates and juvenile foraminifera were observed in several 15-20μm size fraction samples. The juvenile foraminifera percentage contribution was never greater than 5%, whilst the calcareous dinoflagellates percentage contribution varied between 2.5-5%. The four dominant genera throughout the Eocene included *Coccolithus*, *Chiasmolithus*, *Discoaster* and *Reticulofenestra*.

Previous studies have found that the genus *Discoaster* may be prone to diagenetic calcite overgrowth during the Eocene, particularly during hyperthermal events [Dedert et al., 2014]. Diagenetic overgrowth is likely to result in bulk *Discoaster* calcite becoming ^{18}O enriched relative to pristine *Discoaster* calcite. However, whilst overgrowth is likely to affect *Discoaster* oxygen isotopic values, differences in carbon isotopic values of overgrown and pristine calcite in *Discoasters* was found to be minimal [Dedert et al., 2014]. SEM images taken here suggest good preservation, however we cannot rule out minor overgrowth in the form of fattening *Discoaster* nannoliths (Fig. 2.5). As previously found, fattening of *Discoaster* nannoliths would result in their calcite becoming more similar to bulk calcite carbon isotope measurements [Dedert et al., 2014]. Overgrowth would therefore act to minimise any true vital effects within nannoliths. In our study, CIVEs are minimal during the early Eocene when *Discoaster* is the dominant genera. If *Discoaster* is overgrown, our predicted R_{calc}:R_{fix} and CO_2 may be an overestimate since larger CIVEs are associated with R_{calc}:R_{fix} further from one or lower CO_2. Any overgrowth associated with *Discoaster* nannoliths would, therefore, unlikely change our conclusions that the lower R_{calc}:R_{fix} *Discoaster* was replaced by higher R_{calc}:R_{fix} coccolithales across the Eocene. However, we accept that the magnitude of CO_2 values during the early Eocene may be lower than those presented in Figure 2.3 of the main manuscript if overgrowth is significant.

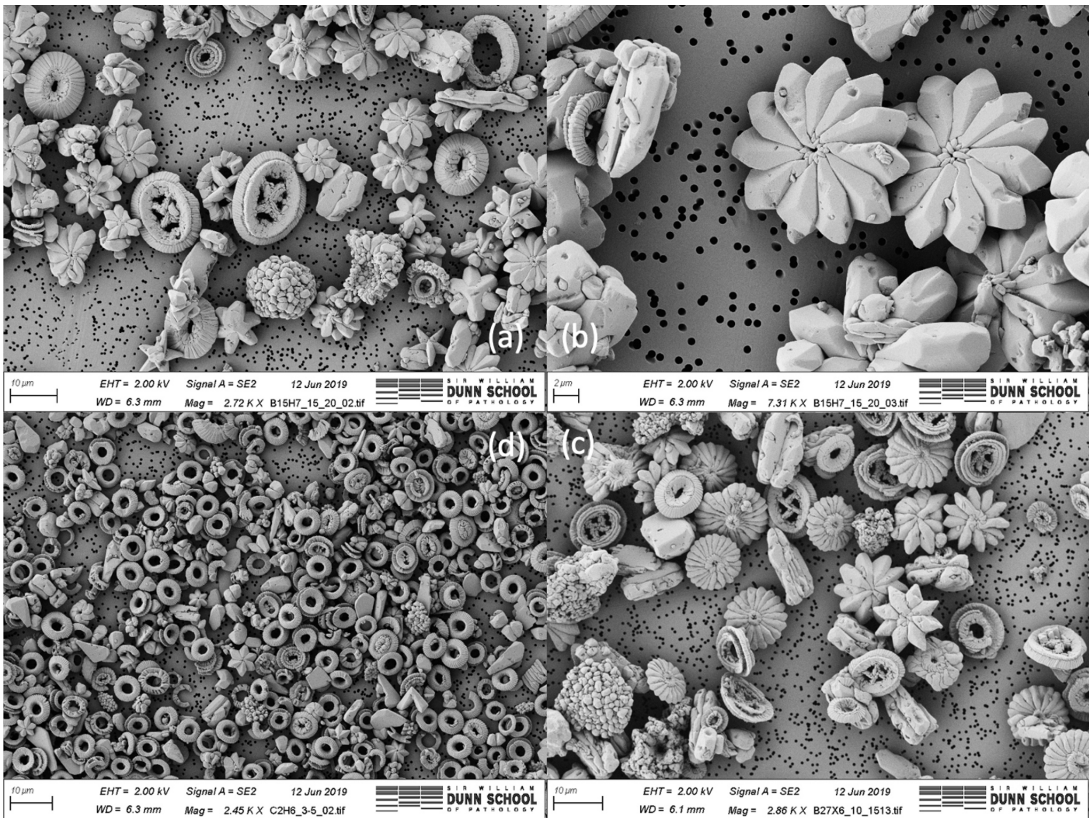

Figure 2.5: SEM images of nannofossils are shown. (a) Nannofossils dating to 47.36 million years ago from the 15-20μm size fraction, with a closer view of *Discoasters* in (b). (c) 10-15μm nannofossils from 55.16 million years ago, and (d) 3-5μm nannofossils from 38.5 Ma. Whilst some overgrowth in the form of fattening may be present on *Discoasters*, samples were generally well preserved across our time interval. *Discoaster* nannoliths are the star shaped fossils in (a-c). Around 90% of coccoliths present in (d) derive from *Reticulofenestra*. The large coccolith in the centre of (a) represents a coccolith derived from the extinct *Chiasmolithus* genus.

2.4.2. Explanation of CIVE's

The CIVE amplitude is controlled by the proportion of carbon used in the cell relative to the total cellular carbon supply, referred to as the degree of carbon utilisation [McClelland et al., 2017]. The cellular carbon supply is a function of carbon availability in the proximal environment and its subsequent rate of transport to and across the cellular membrane. The amount of carbon required by the cell is a function of the cellular carbon density, cell size and the rate of inorganic and organic carbon production. CIVEs are largest when cellular carbon demand approaches the total carbon supply, driven by low $[CO_{2(aq)}]$, high growth rate (μ) or a large cellular radius (r) [Hermoso et al., 2016b, McClelland et al., 2017, Rickaby et al., 2010]. CIVEs are negligible when supply far exceeds demand and any isotopic fractionation is masked by an abundant source of carbon to the cell. The offset direction, and to a lesser degree, the amplitude of the CIVE is further controlled by the calcification to photosynthetic rate and the flux of carbon between cellular compartments [McClelland et al., 2017].

The chloroplast and the coccolith vesicle, the site of calcification, exist within the cellular cytosol and utilise carbon from a common carbon pool [McClelland et al., 2017]. Photosynthetic carbon fixation and calcification both fractionate carbon isotopes, with the photosynthetic product depleted in ^{13}C, and calcite enriched in ^{13}C relative to their respective substrates [Zeebe and Wolf-Gladrow, 2001]. The isotopic signature of the coccolith ($\delta^{13}C_{lith}$) is influenced by the rate of photosynthesis through the leakage of heavy carbon from the chloroplast to the coccolith vesicle and Rayleigh type fractionation within the coccolith vesicle. As carbon utilisation increases an additional source of heavy carbon is derived from the upregulation of uptake of bicarbonate ions [McClelland et al., 2017]. The balance of these processes within the cell controls the direction of $\delta^{13}C_{lith}$ to positive or negative values compared with a reference (negative CIVEs and positive CIVEs respectively).

2.4.3. Ancient Cell physiology estimates

Cell size was determined via established morphological relationships or via the analysis of previously published data (Table 2.4.3). For members of the *Coccolithus* genus, cell size, (D_C), was determined based on regression analysis of 1490 coccospheres from *Coccolithus*

pelagicus [Gibbs et al., 2018]. The relationship used to determine D_C for *Coccolithus* was extrapolated to the *Chiasmolithus* genus, a close relative of *Coccolithus pelagicus*. *Coccolithus* and *Chiasmolithus* were both prescribed a coccolith shape factor (K_s) of 0.06 [Gibbs et al., 2018, Young and Ziveri, 2000]. For coccoliths deriving from the extinct group *Reticulofenestra* D_C was calculated via $0.55 + 0.88C_L$ [Henderiks, 2008], whilst Ks was prescribed as 0.04 [Gibbs et al., 2018, Henderiks, 2008, Young and Ziveri, 2000], where C_L is the measured coccolith length in microns. As no intact spheres of *Discoaster* have been found in the fossil record to date, K_s and D_C have been determined via previously published equations [Gibbs et al., 2018]. Briefly, D_C was calculated via $1.93C_L$, which is based on a rosette morphology, whilst K_s was prescribed a value of 0.04, based on half that of the extant genus *Calcidiscus*. Coccolith weight was calculated via $C_w = 2.7 \times K_s \times C_L^3$, where C_w is the weight of an individual coccolith in pg and 2.7 is the density of calcite in pg μm^{-3}.

Table 2.2: Model input parameters and associated uncertainty

Variable	**Value**	**Uncertainty**	**Comments**
Growth rate (day^{-1})	$1.26V^{-0.11}$	+/- 0.1	Allometrically scaled growth rate based on empirical relationship between growth rate and cell size [Aloisi, 2015].
Cell diameter (μm)	*Coccolithus* C_L+2.38, *Discoaster* $1.93C_L$, *Chiasmolithus* C_L+2.38, *Recticulofenestra* $0.88C_L$+0.55	For size fractions 3-5μm and 5-8μm, +/- 0.15μm. For sizes fractions 8-10μm, 10-15μm and 15-20μm, +/- 0.2μm	C_L is the coccolith length. Cell size for Coccolithus and *Chiasmolithus* based off regression analysis of 1490 coccospheres [Gibbs et al., 2018]. *Discoaster* based on rosette geometry [Gibbs et al., 2018]. *Reticulofenestra* based on empirical analysis [Henderiks, 2008].
Coccolith weight (C_w)	$2.7K_s\ C_L^3$	$C_W(\sigma_{K_s}/K_S + 3\sigma_{C_L}/C_L)$	C_w from empirical analysis [Young and Ziveri, 2000]. K_s from previous estimations [Gibbs et al., 2018, Young and Ziveri, 2000]. C_L from size separation.
Measured CIVE	$\delta^{13}C_{size-fraction}$ - $\delta^{13}C_{mean}$	3-5μm and 15-20μm size fractions assumed 25% contamination from neighbouring size fraction. For 5-8μm, 8-10μm and 10-15μm size fractions assumed 12.5% contamination from each neighbouring size fraction	
R_{calc}:R_{fix}	Uniform distribution between 0.5 and 3		Starting R_{calc}:R_{fix} assumed to be between 0.5 and 3 for initial calibration with $\delta^{13}C_{DIC}$. 1.45 provided the best fit from the 10,000 runs calibrated to $\delta^{13}C_{DIC}$

2.4.4. Calculation of calcite produced per cell

In order to compare relative amounts of calcite produced per cell equation 2.6 was used:

$$\frac{R_{calcA}}{R_{calcB}} = \frac{R_{calcA} : R_{fixA}}{R_{calcB} : R_{fixB}} \times \left(\frac{r_A}{r_B}\right)^3 \tag{2.6}$$

Where subscript A and B refer to a cell A or B and r refers to the radius of each cell. Cell size was determined from equations presented in table 2.4.3. Cells in the 15-20μm size fraction were assumed to have an average coccolith length of 17.5μm. Modern day *Coccolithus pelagicus ssp braarudii* produces coccoliths up to 15μm in length [Young et al., 2003]. The largest coccoliths observed belonging to the *Coccolithus* genus during the Eocene were up to approximately 22μm (microscopic analysis). Given the difference in cell size calculated from coccolith length, even the average sized *Coccolithus* from the 15-20μm size fraction produced approximately 2.9x more calcite per cell (assuming modern day C. pelagicus has a R_{calc}:R_{fix} of 1.5, cell radius of 8μm and Eocene *Coccolithus* has a R_{calc}:R_{fix} of 2.2 and cell radius of 10μm). Similarly, *Discoaster* cells possessing an average radius of 17μm and a R_{calc}:R_{fix} of 0.85, likely produced 5.4x more calcite per cell than modern day *Coccolithus*. *Discoaster* thus produced 1.9x more calcite per cell than Eocene *Coccolithus* (assuming morphometric relationships presented in Supplementary Table 2.4.3).

2.4.5. Growth Rate

If we assumed ambient carbon availability remains constant and growth rate (μ; specific growth rate day^{-1}) is not fixed for each cell size, an increased μ would result in higher carbon utilisation and contribute to a greater amplitude of CIVE expression [McClelland et al., 2017]. In nature, several factors may contribute to variations in μ including irradiance, temperature, NO_3^{2-}, PO_4^{3-} and Fe [Aloisi, 2015]. In the open oceans μ varies both spatially, temporally and in a species specific manner. On the order of months, μ can increase from approximately 0.2 in winter to approximately 1 during springtime blooms [Lessard and Murrell, 1998, Mayers et al., 2019]. However, μ determined from the sedimentary record will reflect longer term averages, and will most likely be less variable except during periods of large environmental perturbations such as during the Paleocene Eocene Thermal Maximum (PETM; [Gibbs et al., 2018]). The application of an allometrically scaled growth rate for each size fraction is therefore, valid and reflects longer term

averages. We opted to use an allometrically scaled growth rate based on pre-existing data [Aloisi, 2015]:

$$\mu = 1.26V^{-0.11} \tag{2.7}$$

Where μ is the cell growth rate and V is the cell volume in μm^3. The cell volume is derived from the cell radius, in turn derived from the coccolith length, measured in the sediment size fractions. Equation 2.7 represents the optimum growth rate with cell size. Our Monte-Carlo simulation samples calculated values of μ assuming a 0.1 uncertainty. Changes to growth rate affect the degree of carbon utilisation within the cell whilst R_{calc}:R_{fix} controls the direction and to an extent the scale of the CIVEs expressed.

2.4.6. Strontium to Calcium ratios

The ratio of strontium to calcium (Sr/Ca) in coccoliths is believed to reflect biogeochemical processes, namely coccolithophorid calcification [Stoll and Schrag, 2000]. Whilst other factors such as species composition, post depositional alteration and seawater Sr/Ca may also affect the measured value of coccolith Sr/Ca, studies suggest that paleoproductivity is the main driver of variation within coccoliths [Billups et al., 2004, Stoll and Bains, 2003, Stoll and Schrag, 2000]. The Sr/Ca ratio in seawater has not remained constant over time and varies on million year timescales [Lear et al., 2003]. Previous work reconstructed Cenozoic Sr/Ca seawater values using foraminifera and shows that whilst large variations have occurred in geological history, seawater Sr/Ca remained low and consistent during the Eocene [Lear et al., 2003].

Samples of coccolith material were taken for Sr/Ca analysis after size separation. Although the size separation process does not remove all of the clay material and detritus, it contributes to significantly reducing the presence of both. Moreover, the concentration of Al and Fe were measured to determine the possible abundance of clay material. Approximately 125μg of calcite was dissolved in 5ml of 2% HNO_3 before being run on a PerkinElmer NexION 350D ICP-MS. The strontium partition coefficient D_{Sr} was calculated to account for changes to contemporaneous changes to the seawater Sr/Ca value (equation 2.8). Seawater values can be determined from coeval foraminifera [Lear et al., 2003].

$$D_{sr} = \frac{(Sr/Ca)_{coccolith}}{(Sr/Ca)_{seawater}} \tag{2.8}$$

Our D_{sr} data show consistent values across the Eocene (Fig. 2.6). Whilst no calibrations exist to produce quantifiable growth rates for each point, consistent values allude to coccolithophore growth rate remaining constant throughout the Eocene. A consistent D_{sr} ratio implies that inferred vital effects exhibited in the late Eocene are not as a result of significant variations in growth rates. Moreover, the oceanographic setting of site 1263 is, and was for most of the Eocene, outside major upwelling zones, further supporting our hypothesis that growth rate was most likely low and consistent throughout the Eocene. We therefore assume that whilst small scale fluctuations to productivity cannot be ruled out, long term variations to growth rate are not the key driver of observed vital effects. Whilst species composition varied throughout the Eocene, there is no correlation between D_{sr} and species variation, in agreement with previous findings [Stoll and Schrag, 2000, Stoll and Bains, 2003]. We therefore interpret the measured values for Sr/Ca presented here as an accurate reflection of coccolithophore productivity throughout the Eocene.

2.4.7. Carbon Speciation

The original isotope flux model [McClelland et al., 2017] calculated external carbon speciation with pH held constant, reflective of the culture experiments in which the model was calibrated. Over the geologic record it is likely that the pH was not constant [Halevy and Bachan, 2017]. Over the Cenozoic the calcite saturation state ($\Omega_{\text{calcite}} = [Ca^{2+}][CO_3^{2-}]/K_{sp}$, where K_{sp} is the saturation constant) in the surface ocean is thought to have remained relatively constant [Tyrrell and Zeebe, 2004]. In our study the original model has therefore been updated to search carbonate parameter space in which carbon speciation is defined by a constant Ω_{calcite}. Ω_{calcite} is chosen from a value between 5 and 6 [Tyrrell and Zeebe, 2004] with the exact value chosen at random for each iteration of our Monte-Carlo method. The changing external CO_2/HCO_3^- results in a shift in carbon availability for the cell at low $[CO_{2(aq)}]$ and thus results in a change to the average carbon isotopic signature of the carbon entering the cell [Bach et al., 2015, McClelland et al., 2017, Zeebe and Wolf-Gladrow, 2001].

Our model has the added capability to calculate carbonate parameters in the scenario

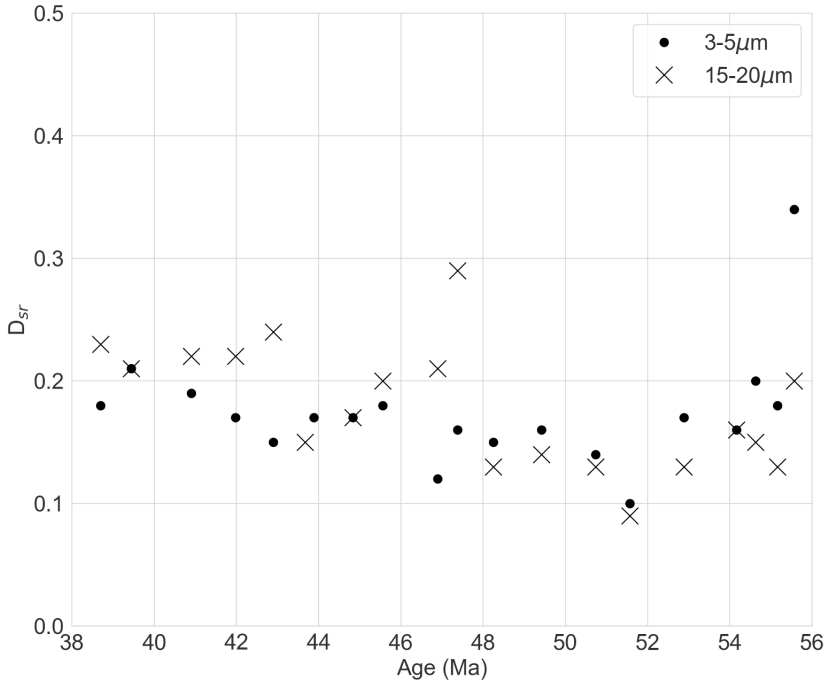

Figure 2.6: The values of D_{Sr}, or the ratio of strontium to calcium in a sample relative to the contemporaneous seawater is consistent overtime with a gradual trend to higher values. The 15-20μm size fraction (black crosses) show a greater variation in values when compared to the 3-5μm size fraction. A large deviation is measured in the 3-5μm size fraction at 55.5Ma, believed to be during the peak PETM. The same peak is not observed in the 15-20μm size fraction. The consistent values of D_{Sr} supports a stable growth rate over the course of the Eocene.

whereby Ω is not held constant. In such a scenario, either pH or DIC must be held constant to allow calculation of the remaining carbonate parameters over parameter space. Such a scenario would change the ratio of $CO_{2(aq)}$ to HCO_3^- available at all values of $CO_{2(aq)}$. By changing this ratio, variations to the overall isotopic composition of carbon entering the cell would vary at higher carbon utilisation given $CO_{2(aq)}$ and HCO_3^- have distinctive isotopic compositions [Zeebe and Wolf-Gladrow, 2001]. Whilst, here we assume Ω was constant through time given the evidence available [Tyrrell and Zeebe, 2004], future studies may wish to rerun the model with either pH or DIC held constant. Given the original implementation of the model was conducted under constant pH we believe the affect on the final results to be minimal, however, future work should confirm this [McClelland et al., 2017]. Moreover, without sufficient experimental data to constrain the model under constant DIC but with variations to pH we accept that we cannot confirm how our results may vary.

We also investigated the output of the model given a $\Omega_{calcite}$ of 1, 5 and 20 with an initial $CO_{2(aq)}$ of 30μmol KgSw^{-1}, R_{calc}:R_{fix} of 1 and optimal allometric growth rate (Fig. 2.7). Results show that as the value of $\Omega_{calcite}$ increases, the peaks of $CO_{2(aq)}$ predicted generally increase in magnitude. Moreover, the values returned for R_{calc}:R_{fix} generally become more variable. The peaks in $CO_{2(aq)}$ represent periods where there is minimal expression of CIVEs. When $\Omega_{calcite}$ is larger DIC increases and the ratio of CO_2/HCO_3^- becomes smaller at all pH ranges. When there is a greater availability of carbon, as under a higher $\Omega_{calcite}$ (assuming a constant $[Ca^{2+}]$), carbon utilisation of cells decreases. Hence, in order to achieve the same magnitude of CIVEs as those measured in the sediments across the Eocene, R_{calc}:R_{fix} must be more variable to overcome the lower utilisation. The final predicted $CO_{2(aq)}$ must similarly be higher when there are minimal CIVEs to ensure that even with larger R_{calc}:R_{fix} predicted, minimal vital effects are observed. Future work should calibrate the model to changes in DIC and pH in the lab with $\Omega_{calcite}$ held constant.

2.4.8. CIVEs relative to $\delta^{13}C_{DIC}$ derived from Foraminifera

Our data shows that the mean initial prescribed value of $CO_{2(aq)}$ scales with the geometric mean of the outputted $CO_{2(aq)}$, with the trend of change consistent across parameter space (Fig. 2.8). In the main manuscript we therefore report our $CO_{2(aq)}$ values as relative change across the Eocene.

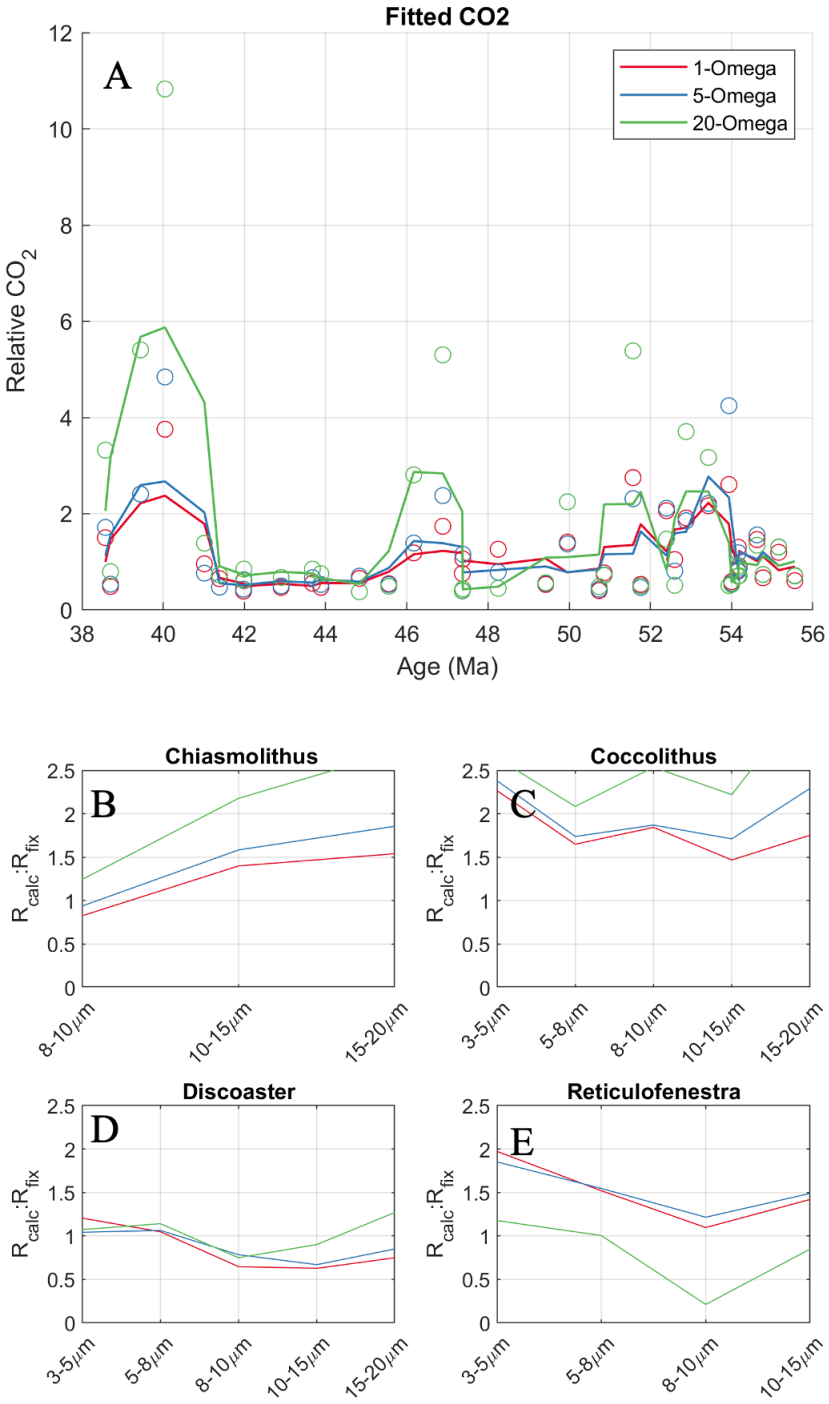

Figure 2.7: (A) The final values of $CO_{2(aq)}$ calculated depend on the value of $\Omega_{calcite}$ prescribed. $\Omega_{calcite}$ is believed to have been constant through geological time. Whilst dramatic shifts on the order of 5 to 20 are unlikely to have occurred during the Cenozoic, we investigated $CO_{2(aq)}$ returned resulting from changes in $\Omega_{calcite}$ from 1 to 20. **B-E)** Model output for corresponding R_{calc}:R_{fix} values returned by the model given variations to prescribed $\Omega_{calcite}$ for our four dominant species. The value of $\Omega_{calcite}$ prescribed changes the ratio of HCO_3^- to $CO_{2(aq)}$ in the external environment and hence the overall isotopic value of carbon available to the cell and subsequently of the carbon taken up by the cell.

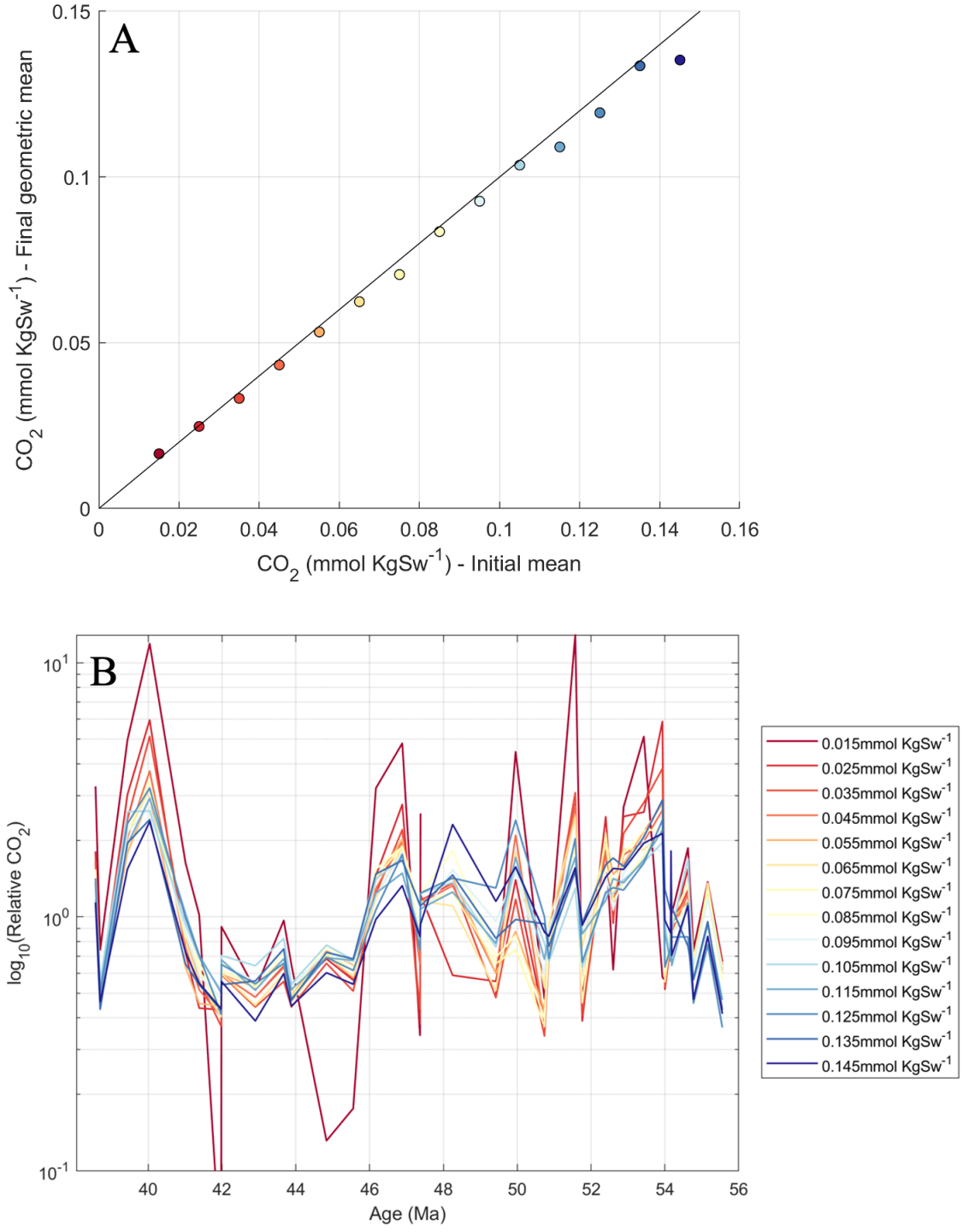

Figure 2.8: The final $CO_{2(aq)}$ values returned by the optimization procedure varies as a function of the initial $CO_{2(aq)}$ prescribed. **A)** Represents the relationship between the outputted geometric mean of $CO_{2(aq)}$ and the initial prescribed value of $CO_{2(aq)}$. **B)** Shows the trends for the final outputted log relative $CO_{2(aq)}$ values over time. The trend across outputted values is consistent across initial prescribed CO2((aq) except when the model predicts low values of $CO_{2(aq)}$ from a low initial starting $CO_{2(aq)}$ and the model breaks down (e.g. initial $[CO_{2(aq)}] = 15\mu$Mol kg Sw^{-1}).

In order to provide an additional constraint on absolute values of $CO_{2(aq)}$ we compared the CIVEs to the $\delta^{13}C$ of dissolved inorganic carbon (DIC). The isotopic flux model was adapted to directly calculate modelled CIVEs relative to DIC, whilst the isotopic composition of the planktonic foraminifera genus, *Acarinina*, was used to derive the $\delta^{13}C$ of contemporaneous DIC. The $\delta^{13}C$ of contemporaneous DIC then permitted the calculation of measured CIVEs relative to DIC. Given there is no reliable calibration, we tested the sensitivity of the final fitted values to various foraminifera vital effects ranging from no offset from DIC to the foraminifera being 1.5‰ heavier than DIC.

The mean square error was calculated for the offset of modelled CIVEs relative to DIC from measured CIVEs relative to DIC, given varying foraminiferal-DIC vital effects, for 10,000 combinations of $CO_{2(aq)}$ and R_{calc}:R_{fix} (see methods in main manuscript, equation 2.5; Supplementary figure 2.9). The -0.5‰ vital effect provided the best fit to our data, is in line with those used in previous assumptions [Bijl et al., 2010] and is similar to laboratory based cultures [Spero, 1998]. We additionally find that the trend of declining pCO_2 is consistent across foraminiferal vital effects, further validating our use of relative $CO_{2(aq)}$ in the main manuscript.

Given a foraminifera vital effect of -0.5‰, we estimate that the true mean of $CO_{2(aq)}$ across the Eocene is approximately 30μmol $KgSw^{-1}$ (Fig. 2.9), in line with previous estimates [Anagnostou et al., 2020, Foster et al., 2012]. pCO_2 was determined using Henrys law. The solubility constants (K_0) used were determined for each age point via the Seacarb package for R. The temperature record was taken from previous work from a near, albeit more equatorward, site [Anagnostou et al., 2020]. Salinity was assumed to be 35‰.

2.4.9. Monte Carlo Sensitivity Analysis

We tested the sensitivity of the final predicted values to assumed uncertainty on growth rate, cell size, coccolith weight, measured CIVEs and external carbon speciation (Supplementary figure 2.10). The influence of assumed changes in temperature were also investigated. Temperature was used to calculate rate constants that determined the external carbon speciation of DIC and their isotopic ratios (Supplementary figure 2.10). In the temperature sensitivity analysis temperature was varied between 15 and 25 °Celsius.

The robustness of our conclusions given changes to assumptions in relationships used

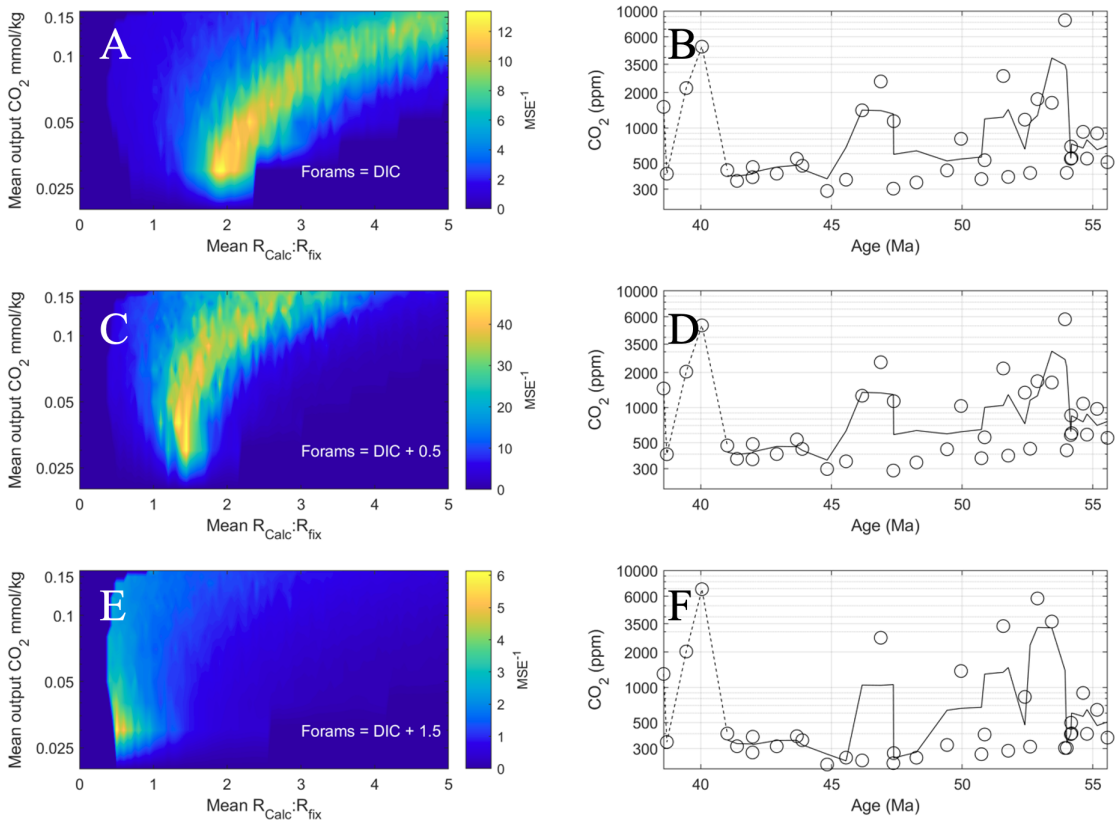

Figure 2.9: The mean $CO_{2(aq)}$ and R_{calc}:R_{fix} output of each of the 10,000 iterations are plotted with the colour scale representing goodness of fit (mean squared error^{-1}; colour bar scales are not uniform). Goodness of fit was determined based on the ability of the model recreating CIVEs relative to DIC derived from planktonic foraminifera in comparison to measured CIVEs. **(A)** Represents the goodness of fit to DIC when DIC is equal to the $\delta^{13}C$ of the planktonic foraminifera. **(B)** represents the associated best fit pCO_2 from **(A)**. **(C)** Represents the goodness of fit to DIC when DIC is 1.5‰ lighter than the $\delta^{13}C$ of the planktonic foraminifera. **(D)** represents the associated best fit pCO_2 from **(C)**. **(E)** Represents the goodness of fit to DIC when DIC is 0.5‰ lighter than the $\delta^{13}C$ of the planktonic foraminifera. **(F)** represents the associated best fit pCO_2 from **(E)**. For **(B)**, **(D)** and **(F)** the solid black line represents the three-point moving average with the dashed line showing the trend during the MECO and later Eocene where pCO_2 is less certain given the lack of CIVE expression. The pCO_2 is presented on a logarithmic scale.

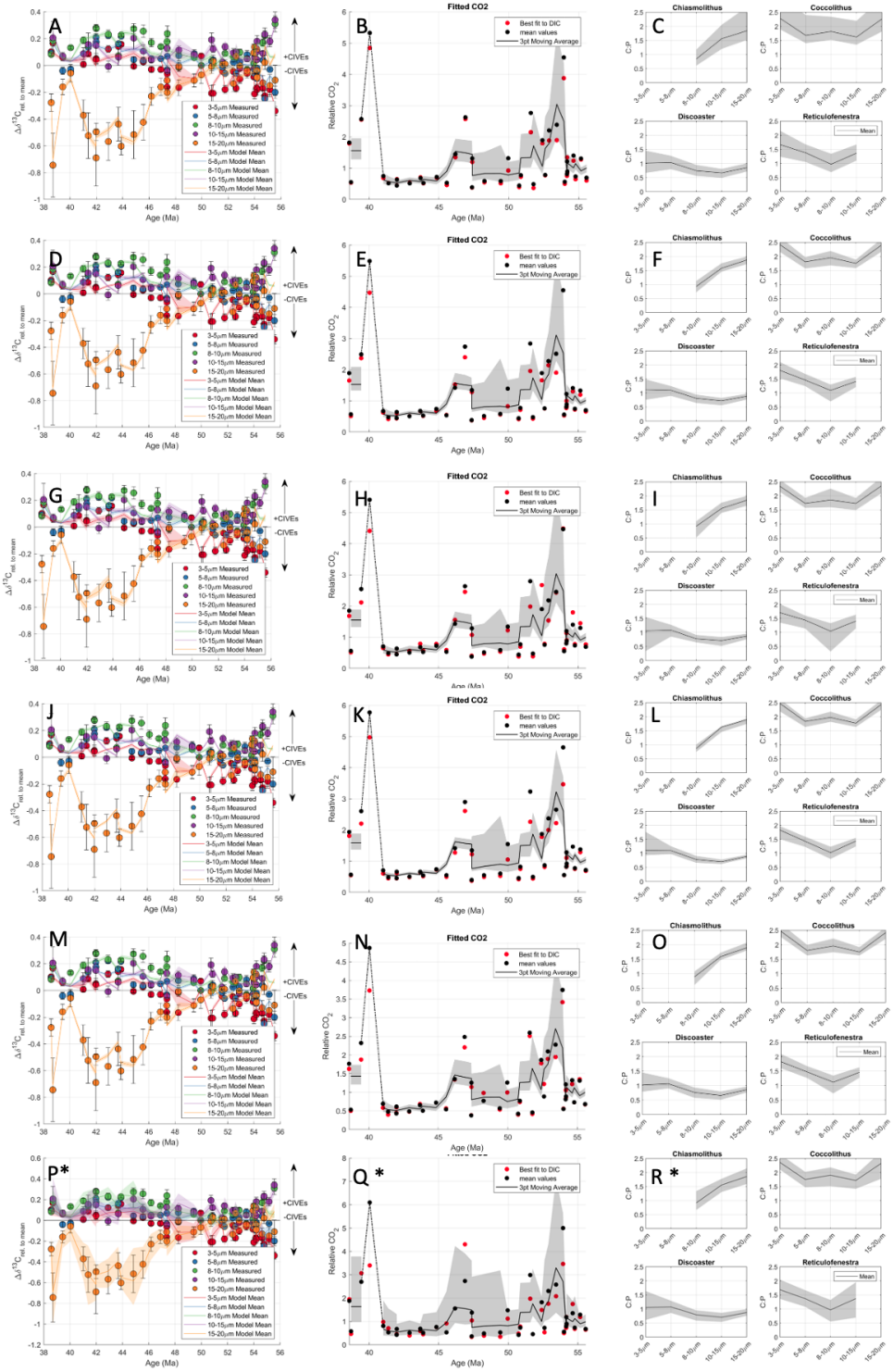

Figure 2.10: The model outputs over 100 iterations of our Monte Carlo sensitivity analysis are presented. **A-C)** represents the CIVE, relative $CO_{2(aq)}$ and R_{calc}:R_{fix} output respectively for variations in ascribed initial growth rate.**D-F)** represents the output from variations to the cell radius, **G-I)** for coccolith weight, **J-L)** variations in $\Omega_{calcite}$, **M-O)** for temperature used to calculate the external carbon speciation and **P*-R*)** for measured CIVE values. **P*-R*)** represents sensitivity to input data rather than model parameters thus resulting in a larger area of percentage realisations in P given the different target values across all runs.

to predict growth rate and calculate external carbon speciation were also tested. Changes to our assumed allometric growth rate [Aloisi, 2015] allowed us to test whether changes in growth rate drove trends in modelled R_{calc}:R_{fix}. An assumed allometric growth rate results in a decrease in growth rate with cell size. A smaller growth rate as cell size increases reduces the increase in carbon demand relative to supply that would manifest under an assumed constant growth rate for all sizes. When growth rate is held constant, the increase in carbon demand to carbon supply with cell size increases at a greater rate when compared to an allometric scaling. With a constant growth rate, cells thus require a smaller R_{calc}:R_{fix} to achieve the same magnitude CIVE than with the allometric growth rate (supplementary figure 2.11). Indeed, with growth rate fixed at one for all sizes, predicted R_{calc}:R_{fix} for *Discoaster*, *Coccolithus* and *Reticulofenestra* decreases with an increase in cell size, although the trend between sizes remains in line with the allometrically scaled growth rate. Moreover, although R_{calc}:R_{fix} for *Reticulofenestra* declines from 3-5μm to 8-10μm, R_{calc}:R_{fix} increases from 8-10μm to the 10-15μm size. We thus still observe a shift to species with larger R_{calc}:R_{fix} in the largest size fractions and a shift to larger R_{calc}:R_{fix} values into the mid to late Eocene. Our data also suggests that when the growth rate is assumed to be 1 across all sizes the corresponding values of $CO_{2(aq)}$ required to achieve the same magnitude of CIVE are much higher than with an assumed allometric growth rate (supplementary figure 2.11).

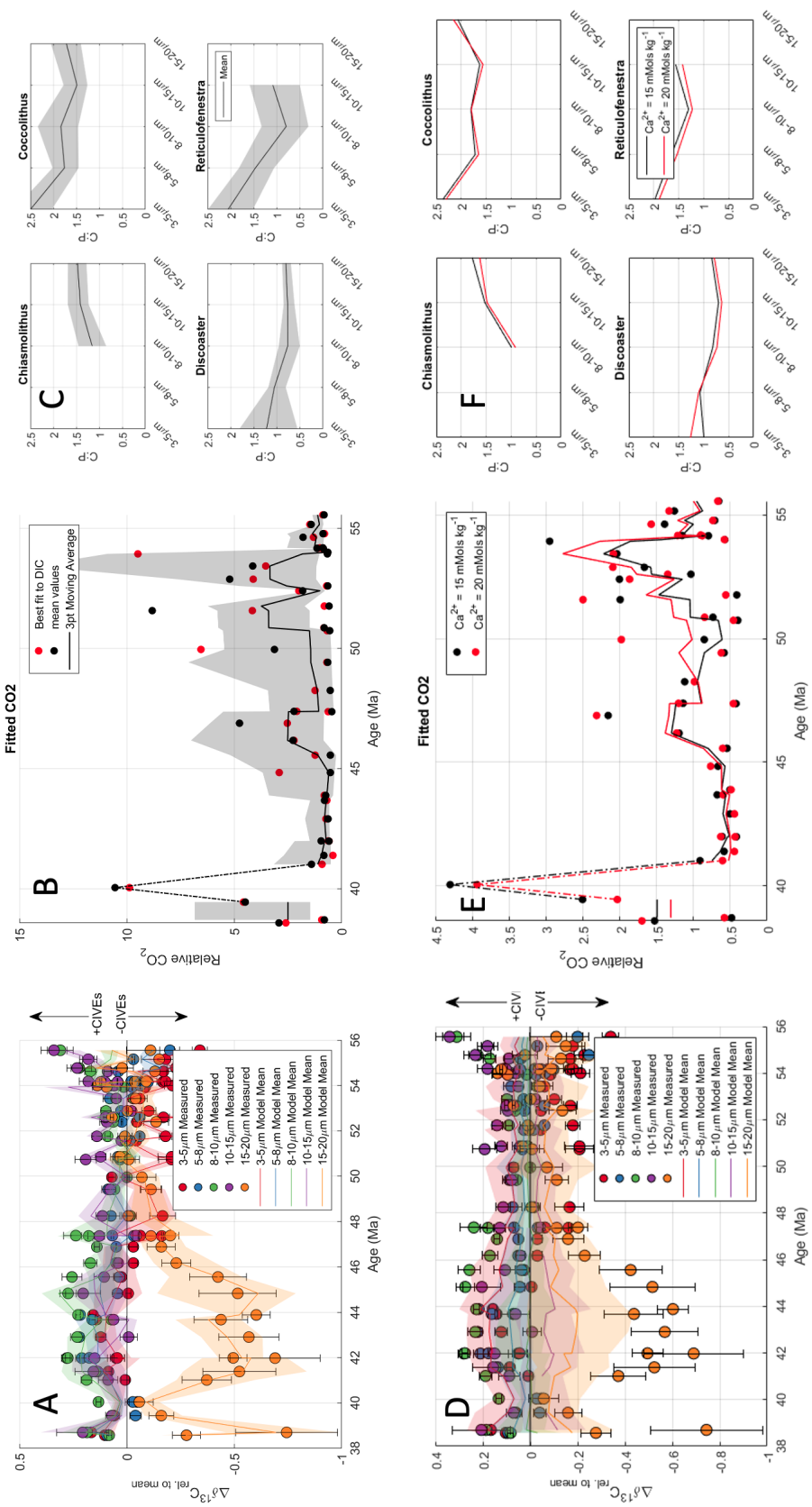

Figure 2.11: A-C) represents the CIVE, relative $CO_{2(aq)}$ and R_{calc}:R_{fix} output from 1000 iterations of the model assuming a constant growth rate of 1. Uncertainty across all other input values was kept as described in supplementary table 1. **D)** represents the CIVE output from 100 iterations with optimization for R_{calc}:R_{fix} disabled and initial R_{calc}:R_{fix} set as 1.45. **E-F)** represent the relative $CO_{2(aq)}$ and R_{calc}:R_{fix} and output for different assumed concentrations of Ca^{2+}. Although absolute values differed the overall trend was consistent, with values between concentrations well within our uncertainty presented on our Monte-Carlo simulation over 10,000 runs. **F)** represents the CIVE output from 100 iterations with optimization for R_{calc}:R_{fix} disabled and initial R_{calc}:R_{fix} set as 1.45.

We further explored the robustness of our predicted values of relative $CO_{2(aq)}$ and R_{calc}:R_{fix} to changes in the calculation of external carbon parameter space given changes to assumptions regarding ambient Ca^{2+} concentration. External carbon parameter space was calculated for each Monte Carlo run given an assumed $\Omega_{calcite}$ between five and six selected from a uniform distribution of 0.1 unit intervals. Carbonate parameter space was determined via the Seacarb package for R, which by default assumes a constant Ca^{2+} concentration and achieves variations in $\Omega_{calcite}$ through variations to the carbonate ion concentration. Over the Eocene it is likely that Ca^{2+} was not constant. Upper and lower values of 20 mMols $kgSw^{-1}$ and 15 mMols $kgSw^{-1}$ were selected, which spans the range of values determined for the Eocene [Tyrrell and Zeebe, 2004]. $\Omega_{calcite}$ for both runs was held at five and thus changes to Ca^{2+} at constant $\Omega_{calcite}$ manifests in changes to the ratio of external carbon species availability. Although marginal variations were apparent between Ca^{2+} concentrations, our trends across the Eocene for relative $CO_{2(aq)}$ and R_{calc}:R_{fix} were robust (supplementary figure 2.11).

To test whether our model could recreate the CIVE distribution through varying CO_2 independently of changes in R_{calc}:R_{fix}, we removed the R_{calc}:R_{fix} optimisation step and set the initial R_{calc}:R_{fix} to 1.45, the assumed best fit resulting from our absolute CIVE comparison with DIC. When R_{calc}:R_{fix} is fixed between sizes and across species, CIVEs diverge in a sequential manner and the large, independent CIVE in the largest size fraction is unable to be recreated (supplementary figure 2.11).

2.5. Additional Section - Unpublished

2.5.1. A note on oxygen isotopes

Coupled oxygen isotopes were measured in addition to carbon isotopes for all sediment size fractions (Fig. 2.12). Whilst investigating variations in $\delta^{18}O$ was outside the scope of this study, the $\delta^{18}O$ values help to rule out CIVEs driven by changes in the depth habitat of coccolithophores. All else being equal, coccolithophores that move to deeper habitats will exist in DIC which has a more negative $\delta^{13}C$ value. Assuming then that the negative CIVEs derive from changes in depth one would also expect the oxygen isotopes to shift to heavier values given the temperature dependence of the oxygen isotopic system. The corresponding $\delta^{18}O$ values for the largest size fraction during the middle Eocene shift

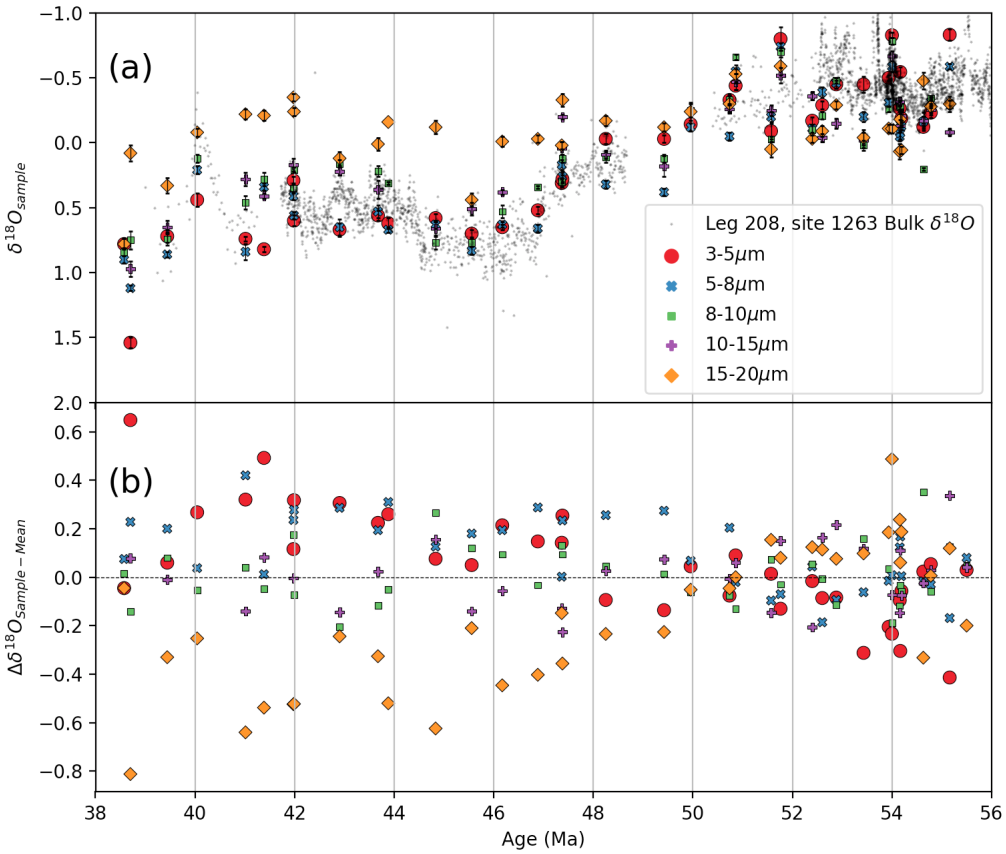

Figure 2.12: The absolute measured δ^{18}O values are presented over the Eocene time interval **(a)**. Also shown are global bulk sediment δ^{18}O values [Boscolo Galazzo et al., 2014, Westerhold et al., 2015, Luciani et al., 2017, Zachos et al., 2010, Lourens et al., 2005, Stap et al., 2009, Littler et al., 2014]. The offset of $\delta^{18}O_{size-fraction}$ relative to the mean **(b)** is also shown. Symbols represent different size fractions.

to lighter values contemporaneously with a shift to negative CIVEs. Moreover, all size fractions show a positive correlation between oxygen and carbon isotopes (Fig. 2.13). The coupled response of δ^{18}O and δ^{13}C is strong evidence to suggest that the CIVEs during the Eocene do not derive from changes to water depth habitat.

2.5.2. Trends in Nannofossil Assemblage

In the fossil record species abundance data can be combined with environmental proxies, when fortuitously available, to further correlate specific species with particular environmental niches. Given the global distribution and high preservation potential of coccoliths, such relationships can be extrapolated to cover additional sites where other environmental proxies have poor preservation. Coccolithophore species occupy a diverse range of global niches from nutrient rich coastal waters to oligotrophic open oceans [De Vargas

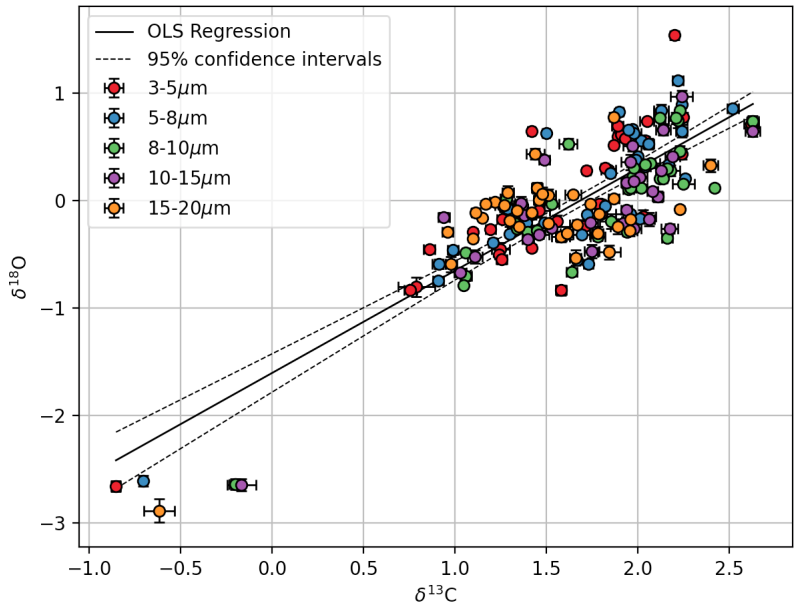

Figure 2.13: Correlation plot showing the paired $\delta^{18}O$ and $\delta^{13}C$ values for sediment size fractions (coloured markers). Also shown is a least squares regression analysis showing the relationship to be statistically significant (r^2 =0.686, p-value $\leq$ 0.001). Cluster of points located in bottom left hand quadrant of the figure are for isotopes measured during the PETM isotopic excursion.

et al., 2007, Winters et al., 1994]. In the modern ocean most species are restricted to a specific geographic distribution in which conditions are most favourable. For example, the extant species *Coccolithus pelagicus* is restricted to the arctic/subarctic, while species such as *Gephyrocapsa oceanica* are found more commonly in warmer waters [McIntyre and Be, 1967]. The richness of species diversity can also help elucidate overall climate, with warmer climates being associated with a greater diversity [Wei and Wise, 1990]. A rapid turnover of coccolithoporoid species can act as a canary in a coal mine and may indicate significant past environmental perturbation. Indeed previous studies have linked rapid turnover in coccolithophoroid species to changes in temperature, nutrient profile and ocean stratification [Gibbs et al., 2006b,a, Raffi et al., 2009].

For the analysis in this chapter species counts were conducted for all size separated samples and can hence offer further insight into the oceanic regime during the Eocene. In this study species have been grouped together to enhance trends within the data. The four dominant genera found throughout the study interval include *Discoaster*, *Reticulofenestra*, *Coccolithus* and *Chiasmolithus* (Fig. 2.14). The general, dominant trends across the Eocene represent the decline of the *Discoaster*, the rise of large Coccolithales (the order containing genera *Coccolithus* and *Chismolithus*) and the expansion and radiation

of *Reticulofenestra*.

Previous studies investigate nannofossil species variation in response to contemporaneous environmental change [Gibbs et al., 2006b, Villa et al., 2008, Wei and Wise, 1990]. Although there is inherent uncertainty in aligning extinct taxa to specific environmental conditions, an evolving consensus has been reached for several indicative taxa [Villa et al., 2008], notably the genera of *Coccolithus*, *Reticulofenestra*, *Discoaster* and *Chiasmolithus*. These genera can be grouped into temperate water (*Coccolithus* and *Reticulofenestra*), warm water (*Discoasters*) and cold water (*Chiasmolithus*) specialists [Bralower, 2002, Bukry, 1971, Wei and Wise, 1990]. Although sea surface temperature is a key driver of variations in percentage abundance, factors such as nutrient availability and water mass stratification may also contribute to short term variations. Moreover, whilst smaller scale fluctuations are present, the long term trend of nannofossil distribution corresponds to a transition from warmer sea surface temperatures in the early Eocene to cooler sea surface temperatures by the middle Eocene. During the early Eocene (56-48 Ma), the *Discoaster* genus has a high abundance in all size fractions greater than the 5-8μm size fraction. Indeed the early Eocene climatic optimum (EECO; 52.5 to 50Ma) was likely the warmest period during the Cenozoic [Zachos et al., 2008, Inglis et al., 2020, Lunt et al., 2021]. After the early Eocene *Discoaster* declines in abundance and occupies a narrower size range, existing dominantly within the 8-10μm and 10-15μm fractions. Concurrent with the decline in *Discoaster* is the increase in abundance of the *Chiasmolithus*, particularly notable with in the 15-20μm fraction. The *Coccolithus* genus, whilst declining in abundance in the smaller size fractions, fills a wider range of sizes, with an increase in the average percentage of larger size fractions. The trend of declining *Discoaster* and rising of Coccolithales follows the decline in temperature at leg 208 site 1263. *Reticulofenestra* first appears approximately 50Ma within the 3-5μm size fraction before becoming increasing more abundant in the larger size fractions. Its appearance and subsequent radiation likely fills a niche left by the *Coccolithus* genus. The decline in surface temperatures at site 1263, as inferred by changing nannofossil presence, is supported by the overall increase in benthic δ^{18}O data, a well-established proxy for the global climate, which suggests global temperatures were also declining [Zachos et al., 2008].

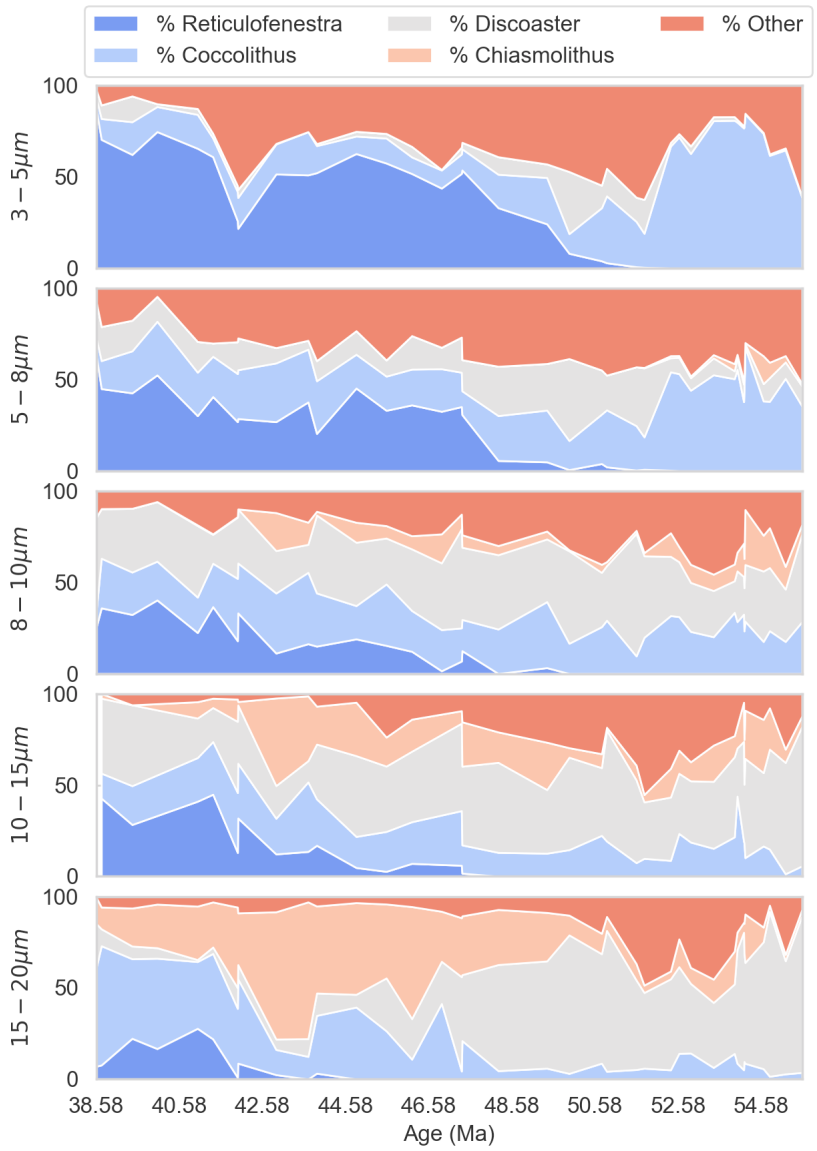

Figure 2.14: The nannofossil distribution across the Eocene is shown for all five size fractions (smallest to largest, top to bottom). The four dominant genera and all other species are grouped and labelled The y-axis represents percentage abundance of each genus or other.

2.5.3. Closing Summary

Here I have attempted to answer whether it is possible to reconstruct Eocene pCO_2 based on the current knowledge of the carbon isotopic variation within coccolithophores with existing models. I have presented a novel isotopic dataset from size separated Eocene coccoliths that has been used to constrain relative change in $[CO_{2(aq)}]$ and R_{calc}:R_{fix} via the inversion of an existing cell scale carbon isotopic flux model. The results show that large coccolithophores that rose to dominate the oceans through the Eocene exhibit increasingly high R_{calc}:R_{fix}, complicating the suggestion that a decline in pCO_2 universally reduces calcification on evolutionary timescales. The novel approach presented also provides an independent confirmation of multiproxy based changes in relative $[CO_{2(aq)}]$ through the Eocene.

Chapter 3

The carbon isotopic response of coccolithophores to variable carbon availability and its implications for carbon acquisition strategies

Abstract

Coccoliths, the calcite plates produced by coccolithophores, preserve geochemical signals from the environment in which they were formed. Of particular interest is the enigmatic variation in coccolith carbon isotopic ratios, termed 'vital effects', which respond, in part, to the external concentration of aqueous CO_2. In order to better understand coccolith carbon isotope vital effects, studies have looked to develop and calibrate cell-scale isotopic models with cultures grown under controlled variations in media CO_2 availability. However, cellular parameters within existing models are calibrated to isotopic data from several species, or a singular modern species, which limits applicability to ancient coccolithophores and the insights we can gain into species specific carbon acquisition strategies. Here, I grow the species *Gephyrocapsa oceanica* and *Coccolithus pelagicus* under elevated carbon conditions and measure their isotopic response to re-calibrate an existing cellular isotopic flux model to each species. Model parameters such as membrane permeability to

carbon species are fitted to the data. Results suggest that *C. pelagicus* acquires HCO_3^- proportional to its ambient concentration, whilst *G. oceanica* appears to be more efficient at acquiring HCO_3^- at lower $[CO_{2(aq)}]$. Changing carbon acquisition strategies under carbon limitation may explain the success of *G. oceanica* relative to *C. pelagicus* in the modern low CO_2 oceans.

3.1. Introduction

The longstanding paleoclimate goal is to invert coccolithophore isotopic models to predict CO_2 given measured $\delta^{13}C_{lith}$ from the fossil record. Whilst this has now been achieved (see chapter 2), models are only reflective of the culture data to which they are calibrated. Geologically abundant species are underrepresented in culture experiments, with fitted cellular parameters tuned to the abundant, modern species *Emiliania huxleyi* or to the isotopic response of several species [McClelland et al., 2017, Holtz et al., 2017]. In the absence of variable CO_2 at constant $\Omega_{calcite}$ experimental data, the current application of models to the geological record requires an extrapolation beyond the range of currently available culture data.

3.1.1. Organic carbon isotopes in Coccolithophores

Coccolithophores are photoautotrophs that exist in the well lit surface layer of the worlds oceans. Coccolithophores have an inherent requirement to photosynthesise whilst also producing calcite plates, known as coccoliths, during their diploid life phase [Young et al., 1999, Houdan et al., 2004]. Coccolithophores use the enzyme ribulose-1,5-biphosphate oxygenase-carboxylase (RuBisCO) to fix CO_2 and produce organic matter via photosynthesis. RuBisCO catalysed carbon fixation discriminates against the heavy isotope of carbon, ^{13}C, which results in a fractionation between the CO_2 substrate pool and the product, organic matter. Organic matter is therefore depleted in ^{13}C relative to CO_2 in the immediate vicinity of the enzyme. The estimated kinetic isotope effect associated the enzyme RuBisCO is believed to range from -11 to -30‰ relative to $CO_{2(aq)}$ and is referred to as ε_f [Boller et al., 2011, Hayes, 2001].ε_f is not always fully realised due to ongoing cellular processes and the isotopic enrichment of the internal cellular carbon pool [Burkhardt et al., 1999, Rost et al., 2002, Laws et al., 2002, Keller and Morel, 1999]. The fractionation realised during the formation of organic matter is given by ε_p (equivalent

to the difference between the isotopic composition of organic matter and media CO_2). Maximum fractionation effects are observed in organic matter (ε_p approaches ε_f) when minimal ^{13}C enrichment of the internal carbon pool occurs e.g. at low growth rate (μ) or high $[CO_{2(aq)}]$.

Early work suggested a negative linear relationship between ε_p and $\frac{\mu}{[CO_{2(aq)}]}$ based on the assumption that carbon used for organic matter fixation is derived from diffusive CO_2 alone [Laws et al., 1995, Rau et al., 1996, Bidigare Robert R. et al., 1997]. Further experimentation presented deviations from linearity inferred to derive from the additional supply of carbon to the cell in the form of HCO_3^- [Keller and Morel, 1999, Laws et al., 2002], a variable ratio of cellular carbon influx to efflux [Burkhardt et al., 1999], cell size [Popp et al., 1998], cellular carbon density and the permeability of the cellular membrane to CO_2 [Popp et al., 1998, Keller and Morel, 1999, Burkhardt et al., 1999, Laws et al., 2002]. All else being equal, an increased μ or lower $[CO_{2(aq)}]$ leads to greater proportional enrichment of ^{13}C within the cells internal carbon pool and a smaller ε_p. If μ and $[CO_{2(aq)}]$ remain unchanged, an increase in cell size will increase cellular carbon demand, but also act to increase the surface area over which carbon fluxes occur (e.g. [Popp et al., 1998]). Efforts to model isotopic fractionation of carbon into organic matter with changing carbon availability have become more complex over time. Initial efforts invoked intracellular carbon fluxes and the internal inter conversion of carbon species (e.g. Sharkey and Berry [1985]) with more recent efforts comprising a thykaloid/pyrenoid complex and a carbon concentrating mechanism (CCM) driven by light [Wilkes and Pearson, 2019].

3.1.2. Inorganic carbon isotopes in Coccolithophores

Alongside the development of organic isotopic models, studies sought to mechanistically understand the variation in coccolith carbon isotope vital effects (CIVEs) as a function of carbon availability [Holtz et al., 2017, Bolton and Stoll, 2013a, McClelland et al., 2017]. CIVEs are given here as the offset of $\delta^{13}C_{lith}$ from that of the $\delta^{13}C$ of dissolved inorganic carbon (DIC). Aforementioned factors such as cell size, cellular carbon density and membrane permeability that affect $\delta^{13}C_{org}$ also affect $\delta^{13}C_{lith}$ due to the use of carbon from a common internal carbon pool.

According to recent modelling work and all else being equal, the relative magnitude of CIVEs vary as a function of cellular carbon demand relative to carbon supplied to the

cell, referred to as carbon utilisation [McClelland et al., 2017]. According to one model developed by McClelland et al. [2017], the CIVE direction is a function of the rate of calcification relative to the rate of photosynthesis (R_{calc}:R_{fix}). The rate of photosynthesis sets the degree of ^{13}C enrichment within the chloroplast and rate of leakage to the cytosolic carbon pool. ^{13}C enrichment of the cytosolic pool subsequently affects the $\delta^{13}C$ of the carbon supplied to the coccolith vesicle. The rate of calcification meanwhile contributes to ^{13}C depletion locally within the coccolith vesicle [McClelland et al., 2017]. For a given R_{calc}:R_{fix}, CIVEs are predicted to be largest when cellular carbon demand approaches the total carbon supply, driven by a low external [$CO_{2(aq)}$] or high μ [McClelland et al., 2017, Rickaby et al., 2010, Hermoso et al., 2016b]. When cells are carbon limited they likely acquire more of their carbon in the form of HCO_3^- via Na^+/Cl^- antiport/symport exchange proteins of the SLC4 gene family [Rost et al., 2002, Mackinder et al., 2011, Bach et al., 2013, Kottmeier et al., 2014]. An increased uptake of HCO_3^- alters the average $\delta^{13}C$ of the total cellular carbon flux to the cell. As carbon utilisation increases, the leakage of ^{13}C enriched carbon from the chloroplast contributes a larger proportion of total carbon used for calcification, with the effect most pronounced in species with a low R_{calc}:R_{fix} [McClelland et al., 2017].

Other theories also exist for the explanation of variable $\delta^{13}C_{lith}$ with changing carbon conditions. The model developed by Bolton and Stoll [2013a] infers CIVE magnitude is controlled by the rate of intracellular active transport of HCO_3^- to the coccolith vesicle relative to the rate of calcification. Secondary controls include the active pumping of HCO_3^- to the chloroplast at the expense of pumping to the CV at low [$CO_{2(aq)}$]. The model by Holtz et al. [2017] meanwhile focuses on CIVE expression given variations to photon fluxes. Holtz et al. [2017] finds that CIVE magnitude varies based on the rate of photosynthesis and the accumulation of ^{13}C within the chloroplast that subsequently spreads to the surrounding cell similar to assumptions made by McClelland et al. [2017]. Regardless of the exact driver of $\delta^{13}C_{lith}$ variation, all models agree that CIVEs are minimal when carbon supply far exceeds demand (low carbon utilisation) and any processes resulting in isotopic fractionation are negligible relative to carbon fluxes.

Most models have additional cellular parameters that are either tuned to culture data or inferred from the wider literature. These cellular parameters often include: ε_{ef}, the effective fractionation associated with organic matter fixation; the permeability of the cell

to CO_2; the effective permeability to HCO_3^- through protein channels; and the internal concentration of Carbonic Anhydrase (CA), which catalyses the inter-conversion of $CO_{2(aq)}$ to HCO_3^- [McClelland et al., 2017, Zhang et al., 2021, Hopkinson, 2014, Schulz et al., 2007, Holtz et al., 2017].

3.1.3. Carbonate system constraints in culture

The governing equations of the carbonate system parameters ($CO_{2(aq)}$, HCO_3^-, CO_3^{2-}, pH, DIC and Alk) results in a system with two degrees of freedom at equilibrium, meaning that if two parameters are defined, the remaining four can be determined [Zeebe and Wolf-Gladrow, 2001]. Culture experiments of the past decade investigating variations to the carbonate system have focused on increasing $CO_{2(aq)}$ via bubbling with high CO_2 air (e.g. Laws et al. [1995]), lowering the pH to shift the speciation of dissolved carbon (e.g. [Riebesell et al., 2000, Langer et al., 2006]) or adding bicarbonate to increase total DIC while keeping pH constant (e.g. [Rickaby et al., 2010]; Figure 3.1)). Whilst these experiments have been crucial to our understanding of the drivers of $\delta^{13}C$ for coccoliths and organic matter, experiments performed under constant calcite saturation state have yet to be conducted ($\Omega_{calcite} = [Ca^{2+}][CO_3^{2-}]/K_{sp}$, where K_{sp} is the saturation constant for calcite).

In order to effectively apply CO_2 proxies based on the isotopic signature of coccolithophore components we must constrain changes in $\delta^{13}C_{org}$ and $\delta^{13}C_{lith}$ under elevated CO_2 with constant $\Omega_{calcite}$. Sedimentary evidence suggests that the calcite compensation depth (CCD), the depth in the ocean where calcite dissolution is approximately equal to its delivery, has remained relatively constant for at least the last 100 million years [Tyrrell and Zeebe, 2004]. The stability of the CCD coupled with the consistent paleolatitudinal range in shallow water ooids and absence of calcifying cyanobacteria that require $\Omega_{calcite} \geq 10$ suggest that surface ocean $\Omega_{calcite}$ has remained relatively constant over the last 100 million years [Tyrrell and Zeebe, 2004]. On million year time scales, chemical carbonate compensation (heterogeneous ocean buffering) and the negative feedback between silicate weathering and volcanic emissions likely keep $\Omega_{calcite}$ within narrow bounds (see chapter 1; [Middelburg et al., 2020]), although biological calcification can also significantly modulate the CCD [Boudreau et al., 2018].

The pH of the external media affects the ratio of $CO_{2(aq)}$ to HCO_3^- in a coccolithophores

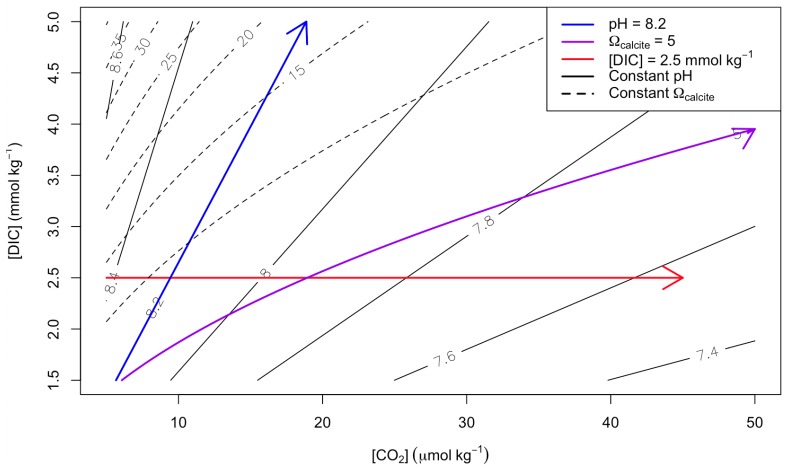

(a)

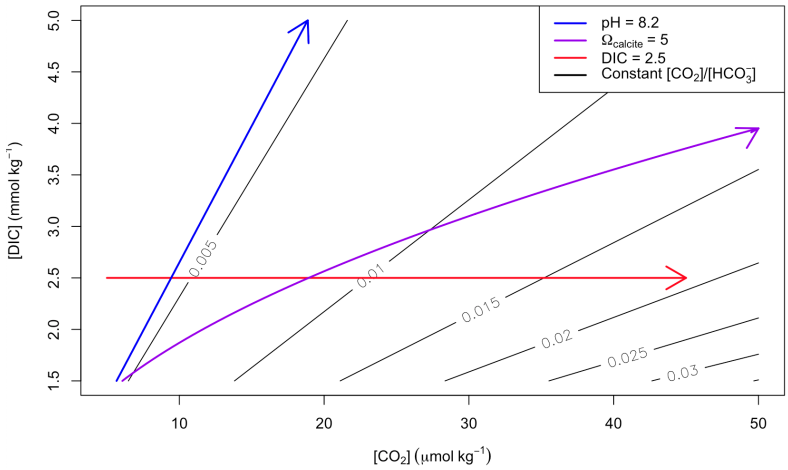

(b)

Figure 3.1: Multiple methods have been developed to manipulate carbonate chemistry in culture with each method altering carbonate parameters in subtle, but different, ways. **(a)** and **(b)** represent carbonate parameter space explored in carbonate manipulation experiments. **(a)** represents how DIC and $CO_{2(aq)}$ change with the solid contours representing constant pH and dashed contours representing constant calcite saturation state ($\Omega_{\text{calcite}} = [Ca^{2+}][CO_3^{2-}]/K_{sp}$, where K_{sp} is the saturation constant for calcite). Studies that investigate changes in DIC and $CO_{2(aq)}$ whilst keeping pH constant are represented by changes along the solid pH contours (represented by the blue arrow). Experiments that add acid and keep DIC constant are represented by shifts parallel to the red arrow. Studies that shift both DIC and pH, but keep Ω_{calcite} constant are represented by changes along the dashed contours (represented by the purple arrow, which follows the Ω_{calcite} of five contour). **(b)** represents the same parameter space and the arrows represent the same changes to carbonate chemistry, however the contours represent changes in the ratio of $CO_{2(aq)}/HCO_3^-$.

local environment and the $\delta^{13}C$ of the carbon species (Fig. 1.3). When the pH and the isotopic compostion of DIC is held constant and DIC is altered, the ratio of $CO_{2(aq)}$ to HCO_3^- remains the same, with the $\delta^{13}C$ of both $CO_{2(aq)}$ to HCO_3^- remaining constant. When the ratio of $CO_{2(aq)}$ to HCO_3^- is changed (e.g. pH is not held constant), the $\delta^{13}C$ of $CO_{2(aq)}$ and HCO_3^- changes [Zeebe and Wolf-Gladrow, 2001]. Since coccolithophore cells acquire CO_2 by diffusion and likely transport HCO_3^- into cells, changes to external carbonate chemistry will alter the overall bulk $\delta^{13}C$ of carbon entering the cell [Keller and Morel, 1999, Mackinder et al., 2011, McClelland et al., 2017].

3.1.4. Chapter plan

This study aims to grow two species of geologically relevant coccolithophores, *Coccolithus pelagicus* and *Gephyrocapsa oceanica*, at elevated DIC concentrations whilst maintaining a constant $\Omega_{calcite}$. *Coccolithus pelagicus* has existed for the majority of the Cenozoic time period (65 million years ago (Ma) - present day) [Young and Bown, 2020]. *Gephyrocapsa oceanica* evolved around 7.3 million years ago and descends from the Reticulofenestra order, the Cenozoic alkenone producers that evolved approximately 57 Ma [Young and Bown, 2020]. This study will use novel isotopic data to constrain existing isotopic flux models to a species specific level and provide insights into cellular carbon acquisition strategies. Moreover, this study provides updated, species specific, cellular parameters for geologically relevant coccolithophores enabling existing models to better recreate data from ancient coccolithophores and hence provide more reliable pCO_2 estimates.

3.2. Methods

3.2.1. Culture set up

Coccolithus pelagicus ssp braarudii (strain Roscoff Culture Collection (RCC) 1198) and *Gephyrocapsa oceanica* (strain RCC 1314) were grown under a 16:8 h light-dark cycle under 100 μmol photons m^{-2} s^{-1} at 15°C and 20°C respectively with controlled carbonate chemistry and nutrients. Salts, with the exclusion of $NaHCO_3$, were added to de-ionised milli-Q water to make synthetic ocean water after Keller et al. [1987]. The solution was then brought to pH 3 using 1M HCl, under which conditions 99% of dissolved inorganic carbon will be in the form of $CO_{2(aq)}$ [Zeebe and Wolf-Gladrow, 2001]. The solution

Table 3.1: Target carbonate conditions for the culture manipulations.

Experiment	DIC (μmol/KgSW)	pH	$CO_{2(aq)}$ (μmol/KgSW)	$\Omega_{calcite}$
1	1500	8.17	6	5
2	2370	8.09	15.4	5
3	3139	7.96	28.1	5
4	3597	7.90	37.5	5
5	4369	7.81	56.3	5
6	5023	7.75	75	5

was then bubbled over night with air removing ~99% of total dissolved inorganic carbon (DIC). The solution was filter sterilised (0.2μm) before adding $NaHCO_3$ to target DIC concentrations (Table 3.1). pH was adjusted to target $\Omega_{calcite} = 5$ across experiments via the addition of 1 M HCl. Filter sterile nutrients were added according to modified K/2 media ($NaNO_3$ modified to 4.4 x 10^{-4}mol L^- and Na_2.glycero.PO_4^{3-} to 5 x 10^{-6}mol L^-; Keller et al. [1987]). Culture vessels were stored without headspace in 2.4-L polycarbonate bottles.

Whilst a lower pH is likely to have occurred during the Eocene [Anagnostou et al., 2020], the concentration of DIC is not well constrained. Evidence exists for both a somewhat constant DIC through time (e.g. [Caves et al., 2016]) and a DIC range up to 2.5 times higher during the Eocene compared to the modern day ([Paillard and Donnadieu, 2014, Tyrrell and Zeebe, 2004]). In the experiments conducted as part of this study, DIC was raised and pH lowered to target constant $\Omega_{calcite}$ after work presented by Tyrrell and Zeebe [2004] and Paillard and Donnadieu [2014]. Moreover, Ca^{2+} was kept constant to reduce confounding factors on final results, although we accept that a constant Ca^{2+} is not a direct analogue for past conditions [Tyrrell and Zeebe, 2004] and that additional studies are needed that manipulate both DIC and Ca^{2+}. Nonetheless, conditions in this study help to mechanistically explore carbon isotopic variance over controlled carbonate chemistry parameter space.

Cultures were inoculated in triplicate after at least six generations (two separate subcultures) of acclimatising to the target conditions. Cultures were shaken daily to mix cells and minimise the establishment of any gradients within the culture. Cultures for *C. pelagicus* and *G. oceanica* were harvested when cell density reached approximately 2,500 cells ml^{-1} and 18,500 cells ml^{-1} respectively, to ensure $\leq$ 5% drift in DIC [Rickaby et al.,

2010]. Cell counts were taken on a Beckman Coulman Coulter Counter every other day two hours after the start of the light cycle (within a two hour window) to avoid changes in cell diameter that develop at different points in the light-dark cycle due to light-synchronised division [Sheward et al., 2017].

The culture growth rate (μ), which has units day^{-1}, was calculated for cultures via:

$$\mu = \frac{[\ln(c_1) - \ln(c_0)]}{\Delta t} \tag{3.1}$$

where c_0 and c_1 are the cell concentrations at each time interval and Δt is the time between cell counts. Repeat measurements were made for each culture to determine a standard deviation across cell counts.

3.2.2. Carbonate Chemistry Determination

12ml aliquots of media were taken for alkalinity analysis prior to inoculation (initial) and after experimentation (final) to monitor any drift in carbonate chemistry. Total alkalinity was measured using a 916 Ti-Touch automatic titrator (Metrohm) and a 0.01 M HCl titrant standardised using a Na_2CO_3 solution adapted from Bradshaw et al. [1981]. The seacarb program in R was used to calculate the remaining carbonate parameters from the measured alkalinity and pH. The total pH scale was used with dissociated constants, K_1 and K_2 taken after Lueker et al. [2000]. Triplicate readings were taken for initial and final aliquots.

3.2.3. SEM sample preparation

Prior to harvesting, 50ml of media was filtered onto 0.2μm polycarbonate filters for visual inspection of coccolithophores under a scanning electron microscope at the Department of Pathology, University of Oxford. Filters were rinsed with 10ml of ethanol to remove debris and ensure halite crystals did not precipitate during oven drying overnight at 40°C. Samples were then coated in gold before being loaded into the SEM for analysis. ImageJ software was used to measure the coccolith length of approximately 100 coccoliths from each DIC condition. The number of coccoliths surrounding each coccolithophore was also counted.

3.2.4. Isotopic Analysis

Cultures were collected and pelleted via centrifugation. Culture pellets were washed with 10ml 1% Triton-X100 in 0.05M $NaHCO_3$ and 6ml 12% NaOCl to remove organic matter for subsequent calcite isotopic analysis. Calcite samples were then rinsed in DI water corrected to pH 7 three times to remove the Triton and NaOCl solution. The calcite samples were then dried in an oven overnight at 40°C. Approximately 50μg of cleaned coccolith material was weighed out for $\delta^{13}C_{\text{lith}}$ analysis. Material was analysed via a Delta V Advantage isotope mass spectrometer fitted with a Gas Bench II in the department of Earth Sciences at the University of Oxford. Samples were calibrated to Pee-Dee-belemnite (PDB) via the international NBS-19 standard. The isotopic composition was calculated via:

$$\delta^{13}C_{\text{lith}} = 1000 \times \left[\frac{(^{13}C/^{12}C)_{lith} - (^{13}C/^{12}C)_{VPDB}}{(^{13}C/^{12}C)_{VPDB}} \right] \tag{3.2}$$

All measurements are expressed relative to the V-PDB standard and the analytical precision across repeat measurements of the standard was ≤ 0.04‰ ($\pm 1\sigma$, n =11). Corresponding δ^{18}O measurements were also recorded during measurements for carbon isotopes. Reproducibility across standards (n=11) was within 0.1‰ for δ^{18}O, which was also expressed on the VPDB scale.

$\delta^{13}C_{\text{DIC}}$ was determined on aliquots of culture media taken before innoculation and after harvesting. Material was analysed via a Delta V Advantage isotope mass spectrometer fitted with a Gas Bench II in the department of Earth Sciences at the University of Oxford. DIC samples were calibrated to Pee-Dee-belemnite (PDB) via the international NBS-19 standard. The analytical precision across repeat measurements of the standard was ≤ 0.05‰ (1σ). The average of initial $\delta^{13}C_{\text{DIC}}$ and final $\delta^{13}C_{\text{DIC}}$ was calculated and used as the reference $\delta^{13}C_{\text{DIC}}$ value (see appendix table A.2 for full results).

The determination of $\delta^{13}C_{\text{org}}$ was via particulate organic carbon (POC) analysis on a SERCON 20/22 Isotope ratio mass spectrometer (IRMS) coupled to a SERCON GSL elemental analyser in the School of Archaeology, University of Oxford (see section 3.2.5).

In order to calculate ε_p, $\delta^{13}C_{\text{CO2(aq)}}$ must first be determined. However, the fractionation of carbon isotopes within the DIC system varies as a function of temperature and pH. For each condition the equilibrium fractionation factors governing the carbon system were

calculated as a function of temperature after those presented in Zeebe and Wolf-Gladrow [2001] after Zhang and Quay [1995]:

$$\varepsilon_{cg} = 0.052 \times T + 7.22‰ \tag{3.3}$$

$$\varepsilon_{bg} = -0.1141 \times T + 10.78‰ \tag{3.4}$$

$$\varepsilon_{dg} = 0.0049 \times T - 1.31‰ \tag{3.5}$$

where ε_{cg} represents the fractionation between the CO_3^{2-} and $CO_{2(g)}$, ε_{bg} the fractionation between the HCO_3^- and $CO_{2(g)}$ and ε_{dg} the fractionation between the $CO_{2(aq)}$ and $CO_{2(g)}$. T is the temperature in degrees Celsius (°C). ε_{cb} and ε_{db}, the fractionation between CO_3^{2-} & HCO_3^- and $CO_{2(aq)}$ & HCO_3^- respectively were calculated via the equations presented in [Zeebe and Wolf-Gladrow, 2001]:

$$\varepsilon_{cb} = \frac{\varepsilon_{cg} - \varepsilon_{bg}}{1 + \varepsilon_{bg} \times 10^{-3}} \tag{3.6}$$

$$\varepsilon_{db} = \frac{\varepsilon_{dg} - \varepsilon_{bg}}{1 + \varepsilon_{bg} \times 10^{-3}} \tag{3.7}$$

The isotopic composition of HCO_3^- ($\delta^{13}C_{HCO_3^-}$) was then calculated via:

$$\delta^{13}C_{HCO_3^-} = \delta^{13}C_{DIC} - \frac{\varepsilon_{db} \times [CO_{2(aq)}]}{[DIC]} - \frac{\varepsilon_{cb} \times [CO_3^{2-}]}{[DIC]} \tag{3.8}$$

where $[CO_{2(aq)}]$, $[CO_3^{2-}]$ and [DIC] represent the calculated concentrations of species in solution for each experiment. At a given [DIC], $[CO_{2(aq)}]$ and $[CO_3^{2-}]$ are set by the media pH. The isotopic composition of $CO_{2(aq)}$ ($\delta^{13}C_{CO_{2(aq)}}$) was calculated from $\delta^{13}C_{HCO_3^-}$ via:

$$\delta^{13}C_{CO_{2(aq)}} = \varepsilon_{db} + \delta^{13}C_{HCO_3^-} \tag{3.9}$$

Finally, ε_p was then calculated after Freeman and Hayes [1992] via:

$$\varepsilon_p = \frac{\delta^{13}C_{CO_{2(aq)}} - \delta^{13}C_{org}}{1 + \delta^{13}C_{org} \times 10^{-3}} \tag{3.10}$$

3.2.5. Particulate Organic Carbon and Particulate Inorganic Carbon Analysis

Total particulate carbon (TPC) and particulate organic carbon (POC) samples were prepared by filtering 100ml of culture media onto pre-combusted (overnight at 500° C) GF/F filters before being dried overnight in a 40° oven and stored at -20° C prior to analysis. Inorganic carbon was removed from POC samples via treatment with 280μl of 0.1N HCL before being oven dried overnight at 40°C. TPC and POC were measured on a SERCON 20/22 Isotope ratio mass spectrometer (IRMS) coupled to a SERCON GSL elemental analyser in the School of Archaeology, University of Oxford which also provided $\delta^{13}C_{org}$. Blank GF/F filters were treated in the same way allowing the final mass and $\delta^{13}C_{org}$ to be blank corrected. The final TPC and POC values given here are the measured value minus the average measured blank mass. The final presented $\delta^{13}C_{org}$ are calculated from a mass balance equation of the sample and blank weights and isotopic values. POC and PIC measurements were averaged across triplicates, with the error representing the standard deviation across measurements. Final values of TPC and POC were divided by the number of cells per 100ml of media to determine TPC and POC per cell and compared with the data set from Aloisi [2015] for validity. Particulate inorganic carbon (PIC) was calculated as the difference between TPC and POC.

A pre-weighed Alanine standard ($C_3H_7NO_2$; ~40% carbon) was used to calibrate the SERCON GSL elemental analyser to measure POC mass and correct to the VPDB scale for the isotopic measurements. The international certified value for the Alanine standard is -27.11‰ VPDB. Across 12 repeat measurements the average value was -27.13‰ with a standard deviation of 0.06‰. Average analytical precision for mass estimates was 8.5μg across repeat measurements on the Alanine standard.

3.2.6. Re-calibration of existing isotopic flux model

Model Set Up

The isotopic flux model developed by McClelland et al. [2017] (hereafter referred to as HM17-model) was employed to model $\delta^{13}C_{lith}$ and $\delta^{13}C_{org}$ values. The HM17-model estimates the concentration of carbon species (both $CO_{2(aq)}$ and HCO_3^-) and their isotopic composition through three cellular compartments, the cytosol, coccolith vesicle and chloroplast from the external environment (Fig. 3.2). The model requires five measurable

parameters to constrain isotopic values: PIC:POC, cell size, growth rate, external pH and DIC. Growth rate, external pH, DIC and PIC:POC were measured directly, whist cell size was inferred from coccosphere diameter determined on the Beckman Coulter Counter. The cellular isotopic flux model has six additional parameters; ε_{ef} the effective fractionation factor; T_A, the background effective cellular permeability to HCO_3^-; T_B, a constant that describes the degree of HCO_3^- channel up-regulation as a function of carbon utilisation; [CA] the Carbonic Anhydrase concentration in cellular compartments; P_{Ccell} the permeability of the cells to $CO_{2(aq)}$; and G, the asymmetric flux of HCO_3^- into cells owing to the electrochemical gradient. A G value of 1 implies the membrane permeability is symmetric. ε_{ef} acts as a black box fractionation factor that accounts for total fractionation associated with the pyrenoid and thylakoid compartments, which are not explicitly accounted for in the model. Together T_A and T_B set the effective permeability to HCO_3^- via assumed anion exchange protein channels of the SLC4 gene family within the cellular membrane. Upregulation of HCO_3^- transports therefore refers to an increase in the number of SLC 4 exchange proteins on cellular/compartmental membranes. These six cellular parameters contribute to controlling the variation of $\delta^{13}C_{lith}$ and $\delta^{13}C_{org}$ with changing $CO_{2(aq)}$ (Fig. 3.3).

The HM17-model was coupled with an optimisation routine to minimise the offset between measured and modelled $\delta^{13}C_{lith}$ and $\delta^{13}C_{org}$ values. The target variables were ε_{ef}, T_A and T_B. Values for [CA], P_{Ccell} and G were selected based on previously published values Blanco-Ameijeiras et al. [2020], Zhang et al. [2021]. Fitting all cellular parameters to the data would result in an under-constrained solution. Given the variance in cellular permeability to HCO_3^- is not well understood across species, T_A and T_B along with ε_{ef} were selected as targets for optimisation. *C. pelagicus* and *G. oceanica* were treated separately allowing species specific values to be constrained.

The presence of CA has yet to be confirmed in species other than *E. huxleyi*, yet, isotopic measurements and models suggest that CA must be present in order to achieve the observed vital effects measured in cultures [McClelland et al., 2017, Holtz et al., 2017, Wilkes and Pearson, 2019]. The HM17-model assumed a fixed value of CA for all species of 1 mM. Early attempts to model CCMs within diatoms suggested CA concentrations between 0.01 and 1 mM, with the exact value scaling with pH and light availability [Hopkinson et al., 2011, Hopkinson, 2014]. Subsequent numerical models based on *E. huxleyi*

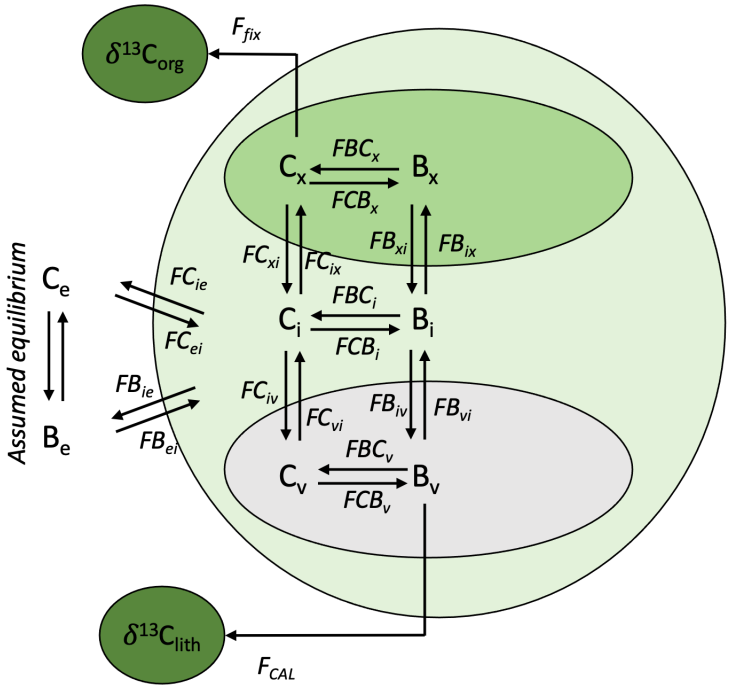

Figure 3.2: HM17 models carbon concentrations and fluxes from the external media through cellular compartments. The external concentrations of CO_2 and HCO_3^- are assumed to be in chemical and isotopic equilibrium, with the conditions of the cell boundary layer assumed to equal that of the bulk media. Fn_{jk} represents the flux of carbon species n (CO_2, C, or HCO_3^-, B) from compartment j to compartment k. Subscripts e, i, x, v represent the compartments external media, cytosol, chloroplast and coccolith vesicle respectively. Fn_{jk} is the product of the concentration of carbon species n in compartment j, the permeability of the cell to species n, and the surface area of the membrane. The units of Fn_{jk} are therefore mols $m{\cdot}s^{-1}$. The net flux of carbon species n between compartment j and compartment k is therefore set by the permeability of the cell to carbon species n and its associated concentrations in compartments j and k. The permeability of the cell to CO_2 is set by the prescribed value P_{Ccell}, whilst the net permeability to HCO_3^- is set by $T_A + T_B \times U_0$, T_A is the effective background permeability to HCO_3^-, T_B is the scaleable permeability to HCO_3^- and U_0 represents the carbon utilisation of the cell [McClelland et al., 2017]. The carbonic anhydrase concentration within each cellular compartment is constant and sets the rate of carbon species interconversion within each compartment denoted by Fnn_j. ε_{ef} sets the offset of $\delta^{13}C_{org}$ from the isotopic composition of C_x. Cell schematic adapted from McClelland et al. [2017].

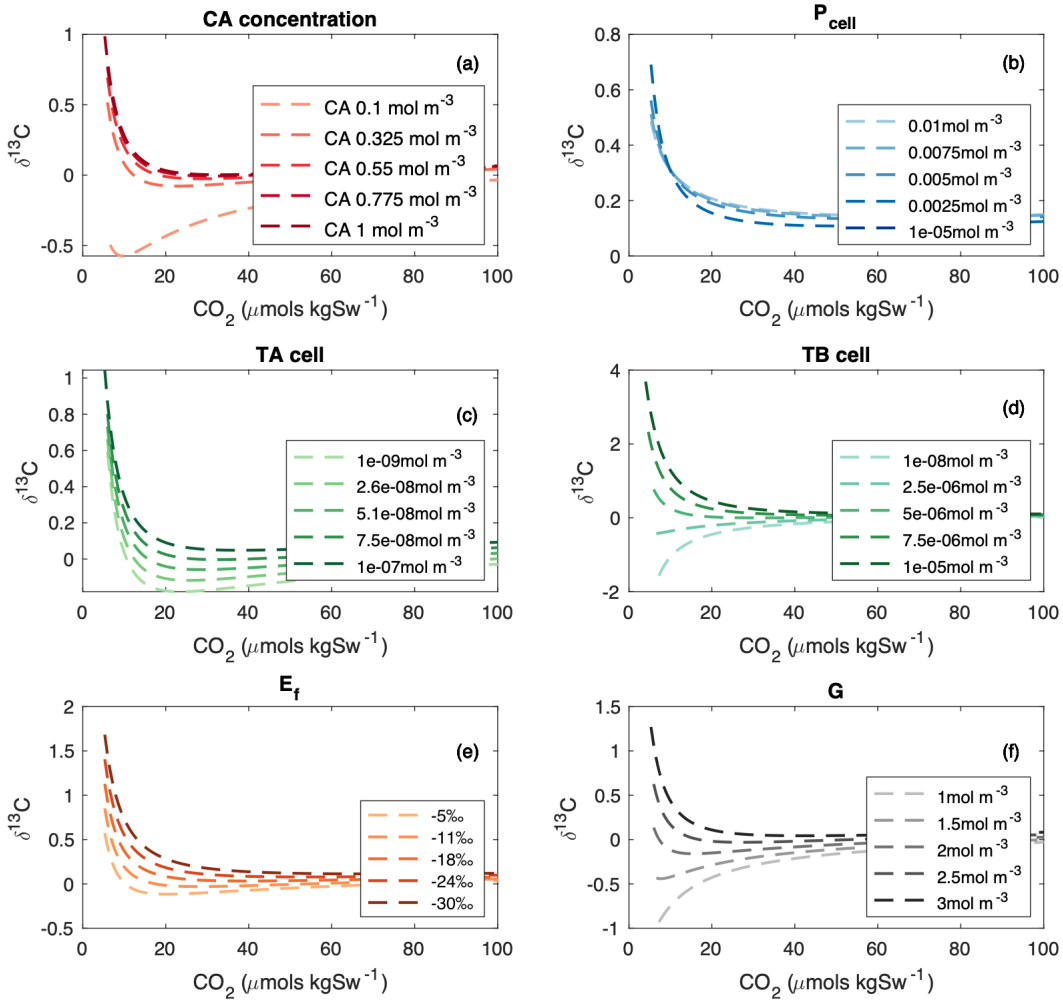

Figure 3.3: In each of the above plots the sensitivity of modelled $\delta^{13}C_{lith}$ is shown given variations in specified parameters with all other parameters are held constant as defined in McClelland et al. [2017]. Modelled values of $\delta^{13}C_{lith}$ are plotted for a cell with a PIC:POC of 0.75, cell radius of 7μm, and a growth rate of 0.7 day^{-1} as a function of $[CO_{2(aq)}]$. Changes in $\delta^{13}C_{lith}$ output is shown with variations to **(a)** [CA], **(b)** P_{Ccell}, **(c)** T_A, **(d)** T_B, **(e)** ε_{ef} and **(f)** G a unitless quantity.

suggested values of around 0.05 mM [Holtz et al., 2015]. Recent experiments utilising carbon and oxygen isotope tracer experiments suggest values between 0.3 and 0.5 for *E. huxleyi* that do not scale with pH or DIC [Zhang et al., 2021]. Here [CA] was set to 0.4 mM and is assumed to be constant across pH and DIC conditions after Zhang et al. [2021].

P_{Ccell} in the HM17-model was constrained to be 9.3 x 10^{-4} ms^{-1}, on the upper end of previous estimates. Hopkinson et al. [2011] suggests a range of P_{Ccell} values in diatoms between 1.5 x 10^{-4} ms^{-1} to 5.6 x 10^{-4} ms^{-1}. Studies on coccolithophores suggests a range of P_{Ccell} from 1 x 10^{-4} ms^{-1} to 1.2 x 10^{-4} ms^{-1} [Blanco-Ameijeiras et al., 2020]. P_{Ccell} was taken as 1.2 x 10^{-4} ms^{-1} for *C. pelagicus* which was the modelled permeability of *Calcidiscus leptoporous*, a large coccolithopore of the same order as *C. pelagicus*. P_{Ccell} for *G. oceanica* was taken as 1 x 10^{-4} ms^{-1} which was modelled for the closely related *E. huxleyi* [Blanco-Ameijeiras et al., 2020].

Optimisation Procedure

An optimisation procedure was coupled with HM17 to constrain our target variables through minimising the misfit between modelled and measured isotopic values. In order to find a global minima we varied the starting values of ε_{ef}, T_A and T_B according to a uniform random distribution spanning previous estimates of values (10^{-5} to 10^{-13} ms^{-1} for T_A and T_B and -11 to -30‰ for ε_{ef}; [McClelland et al., 2017, Blanco-Ameijeiras et al., 2020, Hopkinson et al., 2011]). In total 100,000 initial combinations of ε_{ef}, T_A and T_B were selected. For each of the 100,000 initial combinations of ε_{ef}, T_A and T_B, equation 3.11 and a constrained optimiser in Matlab (built in function *fmincon, sqp algorithm*) was employed to minimise the offset between measured and modelled $\delta^{13}C_{lith}$ and $\delta^{13}C_{org}$:

$$\min \left[\frac{\sum_{i=1}^{I} \frac{1}{\sigma_i}(A_i - B_i) + \sum_{j=1}^{J} \frac{1}{\sigma_j}(C_j - D_j)}{I + J} \right] \tag{3.11}$$

where A is a vector of mean measured $\delta^{13}C_{lith}$ values across triplicates, B is a vector of modelled $\delta^{13}C_{lith}$, C a vector of mean measured $\delta^{13}C_{org}$ across triplicates, D a vector of modelled $\delta^{13}C_{org}$, i $\in \{1 : I\}$ and j $\in \{1 : J\}$ where I and J are the number of measured/modelled isotopic values for $\delta^{13}C_{lith}$ and $\delta^{13}C_{org}$ respectively and both are equal to 6, representing the six target conditions. The misfit function was weighted by the

inverse of the standard deviation of measured values across triplicates ($1/\sigma$) to ensure that values with a large measured uncertainty contributed less to the determination of fitted parameter values. Cellular parameters including PIC:POC, cell size, growth rate, external pH and DIC were averaged across triplicates before being input into the model. For the optimisation procedure, cellular parameters were assumed equal to their mean. The combination of ε_{ef}, T_A and T_B values that provided the best fit for each species from the 100,000 initial combinations were then used as initial values for a Monte-Carlo like sensitivity analysis (see section 3.2.7).

3.2.7. Monte Carlo Sensitivity Analysis

The robustness of the best fit combination of ε_{ef}, T_A and T_B for each species was tested to the uncertainty associated with each of the seven additional input values: PIC:POC, cell size, growth rate, external pH, DIC and $\delta^{13}C_{lith}$ and $\delta^{13}C_{org}$. The sensitivity analysis involved rerunning the optimisation procedure with fixed values of ε_{ef}, T_A and T_B, but with variable input values for each of the seven additional aforementioned input values. The sensitivity analysis was run 10,000 times for each input variable with initial values of ε_{ef}, T_A and T_B fixed as the best fit for each species based on the output from the optimisation procedure. For each sensitivity test, values for the input variable were selected from a Gaussian distribution with the standard deviation equal to the standard deviation across triplicate measurements. All other input values were assumed equal to their mean so that the model sensitivity for each input variable could be investigated individually. Given there are seven input variables, a total of 70,000 runs were conducted (10,000x7).

To determine an overall uncertainty on presented best fit values an additional analysis was performed with error ascribed to all input variables over 10,000 runs. The 16th and 84th percentiles were taken as the lower and upper bounds on the best fit values from the optimisation procedure. Input variables were selected from Gaussian distributions around their mean with the standard deviation equal to that determined for the triplicate measurements. Initial values for ε_{ef}, T_A and T_B were fixed as the best fit for each species from the optimisation procedure. G, [CA] and P_{Ccell} remained unchanged throughout.

Finally an additional sensitivity analysis was performed whereby the variation in output values of T_A, T_B and ε_{ef} was investigated given changes to assumed values of P_{Ccell}, [CA] and G (see section 3.3.8).

3.3. Results

3.3.1. Culture conditions

The measured carbonate parameters prior to inoculation and prior to harvesting are given in table 3.2. Mean values of alkalinity and pH were derived from initial and final measured media values, which were then used to determine the remaining carbonate parameters for each triplicate. The percentage drift in DIC concentration between inoculation and harvest for *C. pelagicus* cultures was between -6.92% and +0.83% with an average of -2.69%. DIC drift between inoculation and harvest for *G. oceanica* cultures varied between -3.72% and +1.41% with an average drift of -1.22%. Experiments were conducted at approximately constant Ω_{calcite}. The average Ω_{calcite} for *C. pelagicus* was 5 ± 0.96 and 5.1 ± 1 for *G. oceanica*. Whilst some variance in Ω_{calcite} is observed, prior studies observe ranges from 2 to approximately 20 [Rickaby et al., 2010] and 30 [McClelland et al., 2017].

Table 3.2: Initial and final measured values for alkalinity and pH are presented (Alk_0 represents initial value whilst Alk_f represents the final measured value). The mean pH and alkalinity value is determined before calculating the remaining carbonate parameters using seacarb (see methods).

Species	Experiment	Alk_0 (mMol kg^{-1})	Alk_f (mMol kg^{-1})	pH_0	pH_f	ALK_{mean} (mMol kg^{-1})	pH_{mean}	$[CO_{2(aq)}]$ (μMol kg^{-1})	DIC (mMol kg^{-1})	$[HCO_3^-]$ (mMol kg^{-1})	$[CO_3^{2-}]$ (μMol kg^{-1})	$\Omega_{calcite}$
C. pelagicus	1	1.96	1.80	8.08	7.94	1.88	8.01	12.67	1.69	1.55	127.05	3.03
		1.96	1.82	8.08	7.98	1.89	8.03	11.97	1.69	1.55	133.18	3.18
		1.97	1.84	8.07	7.98	1.91	8.03	12.24	1.71	1.56	133.19	3.18
	2	2.68	2.63	8.16	8.22	2.65	8.19	11.03	2.31	2.04	252.78	6.03
		2.63	2.48	8.16	8.18	2.55	8.17	11.11	2.23	1.98	235.70	5.63
		2.66	2.62	8.06	8.20	2.64	8.13	12.92	2.33	2.09	226.10	5.40
	3	3.64	3.68	7.90	7.92	3.66	7.91	32.52	3.42	3.18	207.67	4.96
		3.67	3.58	7.93	7.94	3.62	7.93	30.58	3.38	3.13	213.95	5.11
		3.65	3.58	7.91	7.92	3.61	7.92	31.74	3.38	3.14	206.93	4.94
	4	3.92	3.92	7.90	7.83	3.92	7.87	39.09	3.70	3.46	204.01	4.87
		3.92	3.84	7.90	7.83	3.88	7.87	38.82	3.66	3.42	201.35	4.81
		4.00	3.89	7.80	7.84	3.95	7.82	44.57	3.75	3.52	185.74	4.43
	5	4.64	4.63	7.70	7.93	4.64	7.81	52.98	4.42	4.15	217.09	5.18
		4.72	4.71	7.80	7.93	4.71	7.86	47.34	4.46	4.17	244.79	5.84
		4.81	4.67	7.81	7.92	4.74	7.86	47.61	4.49	4.19	246.19	5.88
	6	5.18	5.30	7.72	7.90	5.24	7.81	60.36	5.00	4.70	244.14	5.83
		5.26	5.32	7.69	7.92	5.29	7.81	61.91	5.06	4.75	243.60	5.81
		5.23	5.21	7.78	7.89	5.22	7.83	56.70	4.97	4.66	255.17	6.09
G. oceanica	1	1.97	1.90	8.09	8.05	1.93	8.07	11.08	1.72	1.56	146.09	3.49
		1.96	1.89	8.08	8.03	1.92	8.05	11.46	1.71	1.56	141.57	3.38
		1.97	1.90	8.09	8.03	1.93	8.06	11.38	1.72	1.56	143.49	3.42
	2	2.82	2.80	8.02	8.00	2.81	8.01	18.99	2.56	2.35	193.67	4.62
		2.79	2.71	8.04	7.98	2.75	8.01	18.79	2.51	2.30	187.84	4.48
		2.86	2.80	8.03	7.99	2.83	8.01	19.10	2.58	2.36	195.27	4.66
	3	3.50	3.44	7.93	7.91	3.47	7.92	30.01	3.24	3.01	201.00	4.80
		3.51	3.43	7.93	7.90	3.47	7.92	30.31	3.24	3.01	199.14	4.75
		3.57	3.42	7.93	7.91	3.50	7.92	30.35	3.26	3.03	201.87	4.82
	4	4.04	3.90	7.99	7.96	3.97	7.98	29.78	3.67	3.39	256.92	6.13
		3.98	3.96	7.97	7.95	3.97	7.96	30.78	3.68	3.40	250.86	5.99
		4.02	3.93	7.97	7.95	3.98	7.96	31.06	3.69	3.41	249.51	5.95
	5	4.58	4.56	7.88	7.89	4.57	7.88	43.69	4.31	4.02	246.41	5.88
		4.57	4.55	7.88	7.88	4.56	7.88	44.01	4.30	4.02	244.39	5.83
		4.65	4.63	7.88	7.87	4.64	7.88	44.93	4.38	4.09	247.80	5.91
	6	5.27	5.28	7.84	7.85	5.27	7.84	55.87	5.01	4.69	263.05	6.28
		5.29	5.26	7.84	7.84	5.28	7.84	56.34	5.02	4.70	261.44	6.24
		5.33	5.32	7.85	7.85	5.33	7.85	56.06	5.06	4.74	267.02	6.37

3.3.2. Cellular growth rates

The aim of the experiment was to observe cells grown under stable carbonate system parameters. There was hence a requirement to harvest cells in early stage exponential growth before the growing number of cells altered the media carbonate parameters. The early exponential harvesting of cells resulted in a relatively large spread among replicates owing to the greater uncertainty in cell counts at low cellular concentrations. This was, however, necessary to avoid the drift in targeted DIC concentration and pH. The growth rate for *C. pelagicus* was between 0.83 day^{-1} and 0.4 day^{-1} with all cultures growing at all DIC concentrations (Fig 3.4). The effect of carbonate chemistry on *C. pelagicus* growth rate was not statistically significant. The growth rate for *G. oceanica* varied between 0.76 day^{-1} and 0.45 day^{-1} and appeared to show an optimum based response to changing carbonate parameters (Fig 3.4).

3.3.3. Coccolith Counts, Size and Malformation

SEM images enabled the measurement of coccolith length and determination of the number of coccoliths that surround cells. Moreover, SEM images enabled us to visually inspect the health of the coccoliths. In both *G. oceanica* and *C. pelagicus*, coccolith malformation appears to be a function of carbonate chemistry. In *C. pelagicus* malformed coccoliths were defined as blocky or incomplete coccoliths with an irregular repetition of overlapping calcite crystals. Although the growth rate for *C. pelagicus* was similar under all conditions, as DIC was increased, cells produced an increased proportion of malformed coccoliths (Fig 3.5, Table 3.3).

G. oceanica is characterised by a bridge that spans the central opening of the coccolith. At lower DIC *G. oceanica* formed complete and intact bridges (Figure 3.6). As DIC was increased, above that common of modern oceans, the only visible change was the failure to produce fully intact bridges, however, this was not consistent across all cells. I cannot say for certain if the change in bridge structure was an artefact of sample preparation or a true response to elevated DIC.

A one-way ANOVA was performed to test whether coccolith lengths (C_L) and the number of coccoliths surrounding the coccolithophore (C_N) varied significantly across conditions for each species. For both *C. pelagicus* and *G. oceanica*, C_L was found to vary

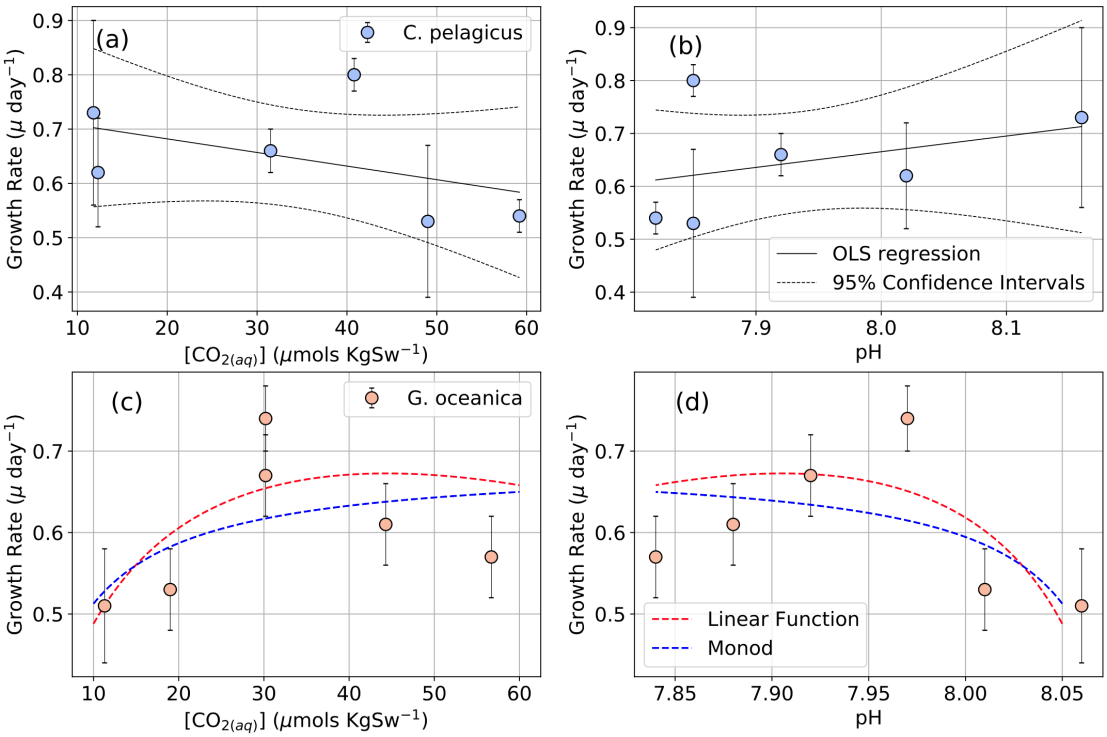

Figure 3.4: Growth rate of *C. pelagicus* across all experiments as a function of **(a)** $CO_{2(aq)}$ and **(b)** pH. Markers represent average isotopic values across triplicate measurements with the error representing standard deviation across triplicates. Also show is a ordinary least squares regression for both $CO_{2(aq)}$ and pH. Growth rate of *G. oceanica* as a function of **(c)** $CO_{2(aq)}$ and **(d)** pH is also shown. The red dotted line in **(c)** and **(d)** represents the ordinary least squares fit for growth rate as a non-linear function of both $CO_{2(aq)}$ and pH of the form $(CO_2)^a$+b·ph + c where a= 0.18, b=1.85 and c = -15.9. The blue dotted line represents a simple Monod type relationship for growth rate as a function of $CO_{2(aq)}$ and pH of the form $\frac{aCO_{2(aq)}}{b+CO_{2(aq)}} - c \cdot pH$ where a = 0.68, b=3.44 and c=-8.34 x 10−4. The blue and red lines were fit using the scipy minimise function in python.

Table 3.3: Measured number of malformed coccoliths as percentage of total counted. Coccolith length represents the values measured through SEM image analysis. Shown in brackets is the standard deviation across all measured coccoliths. Coccosphere diameter measured via the Beckman coulter counter is also shown.

Species	Experiment	Malformation % (σ)	Coccolith Length μm (σ)	Coccosphere diameter μm (σ)
C. pelagicus	1	0.67 (0.8)	10.35 (1.1)	13.8 (0.6)
	2	13.7 (3.7)	8.76 (1.0)	13.6 (1.0)
	3	28.6 (5.4)	7.52 (1.1)	11.4 (0.8)
	4	23.7 (4.9)	8.39 (1.1)	13.8 (0.4)
	5	99 (10.0)	7.15 (1.1)	13.6 (0.6)
	6	88.4 (9.4)	7.84 (0.9)	14.1 (0.7)
G. oceanica	1	4.8 (2.2)	4.93 (0.6)	6.2 (0.2)
	2	12 (3.5)	4.92 (0.46)	6.0 (0.1)
	3	9.2 (3.0)	4.92 (0.57)	5.7 (0.1)
	4	11.1 (3.3)	5.27 (0.69)	5.3 (0.1)
	5	12 (3.5)	5.54 (0.71)	5.6 (0.2)
	6	9.5 (3.1)	5.31 (0.71)	5.8 (0.1)

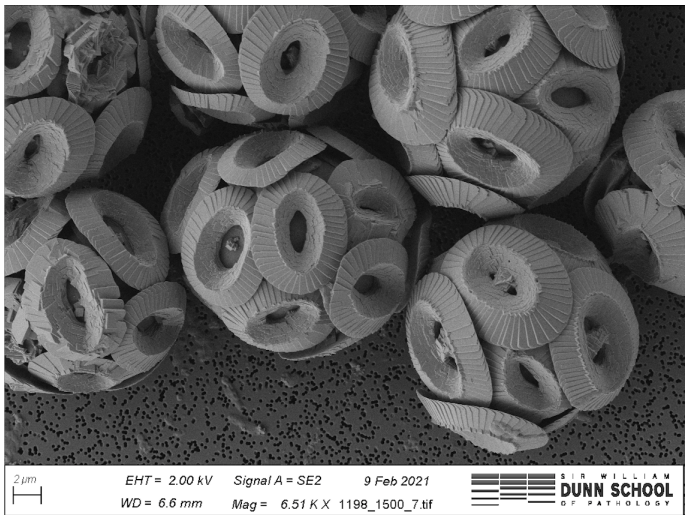

(a)

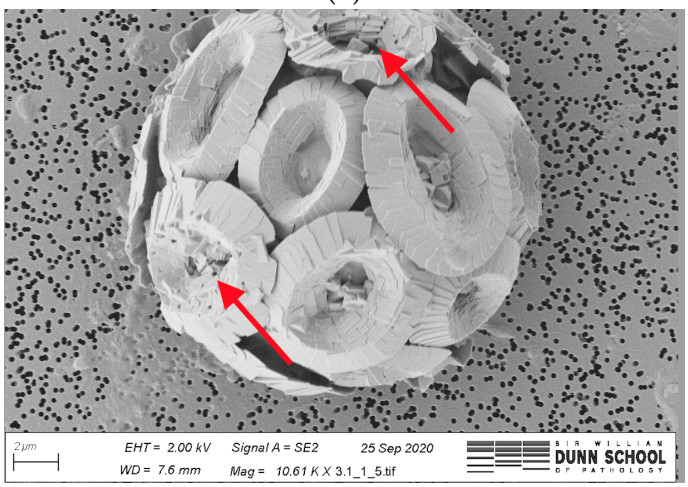

(b)

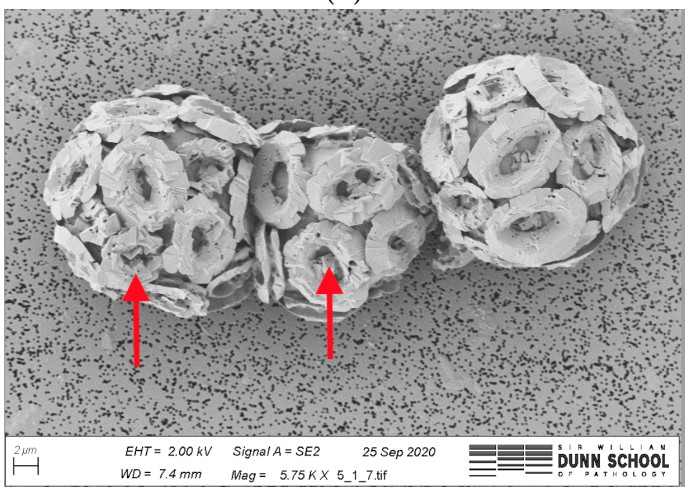

(c)

Figure 3.5: *C. pelagicus* grown under **(a)** 1.5 mMols DIC kgSw^{-1}, **(b)** 3.1 mMols DIC kgSw^{-1} **(b)** and **(c)** 5 mMols DIC kgSw^{-1}. Red arrows in **(b)** and **(c)** show typical areas of malformation.

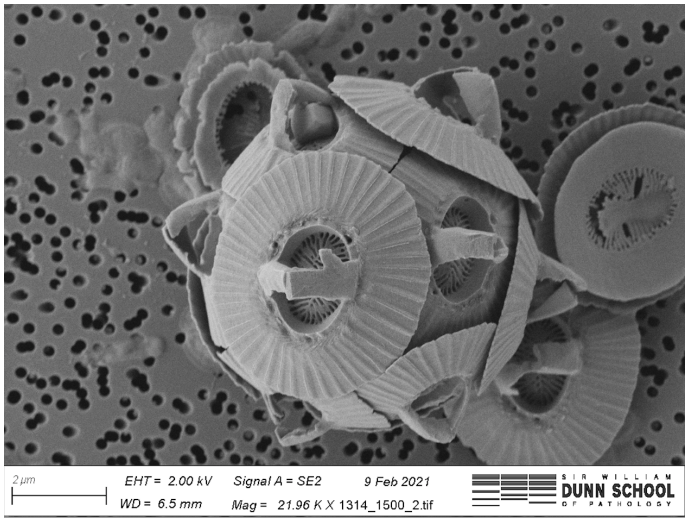

(a)

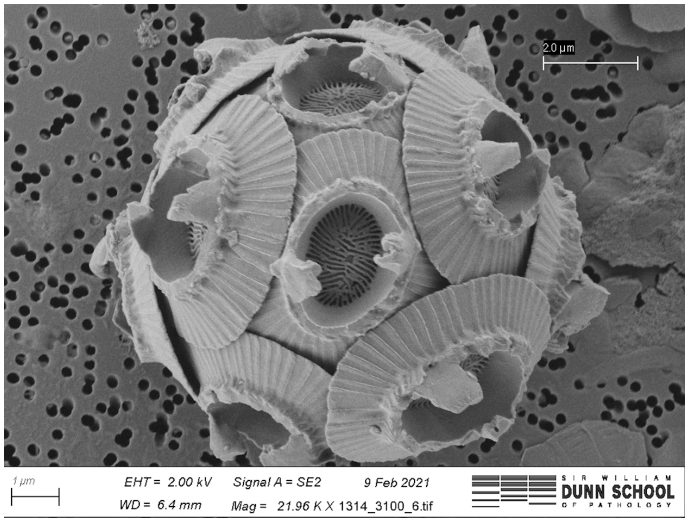

(b)

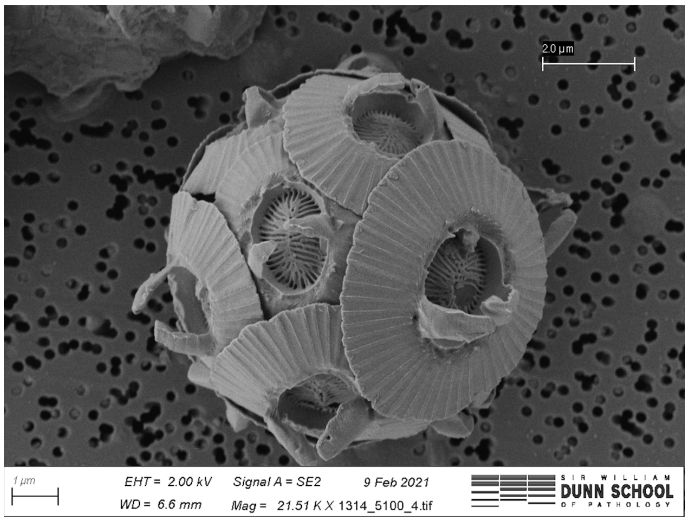

(c)

Figure 3.6: **(a)** *G. oceanica* grown under **(a)** 1.5 mMols DIC kgSw^{-1}, **(b)** 3.1 mMols DIC kgSw^{-1} **(b)** and **(c)** 5 mMols DIC kgSw^{-1}.

significantly (P-value ≤ 0.001) with DIC whilst C_N was found to not vary significantly to the 1% level (*C. pelagicus* P-value = 0.039, *G. oceanica* P-value = 0.189). The average C_N for *C. pelagicus* was 16 and 12 for *G. oceanica*.

For *C. pelagicus* coccolith length was found to be greatest under 1.5 mMol DIC $KgSw^{-1}$ (Table 3.3). For *G. oceanica* coccolith length showed an optimum type response to elevated DIC conditions with the largest observed coccoliths under 4.3 mMol DIC $KgSw^{-1}$ (Table 3.3). Whilst coccolith length was found to significantly vary across experiments, the relationship of coccosphere diameter with external $CO_{2(aq)}$ for *C. pelagicus* and *G. oceanica* was found to be non-significant in both cases (p-values were 0.74 and 0.24 respectively). The data therefore shows that although variations in coccolith length are apparent, overall coccosphere, and by inference cell size, remained similar across experiments.

3.3.4. Particulate organic Carbon (POC) and Particulate Inorganic Carbon (PIC)

POC for *C. pelagicus* appeared to increase with increasing DIC, although the relationship was not statistically significant (p value = 0.126, figure 3.7). POC for *G. oceanica* showed a negative trend with increasing DIC conditions, however, the trend was not statistically significant (p value = 0.06). The TPC methodology was found to give variable results across triplicate measurements in comparison to the variation on POC measurements. The highly variable TPC resulted in a correspondingly large uncertainty on measured value for PIC and hence PIC:POC (see Fig. 3.7). An alternative method was thus employed after Bach et al. [2015] to confirm the magnitude of measured PIC values based on the change in alkalinity measurements before inoculation and after harvesting via:

$$\text{PIC}\ (\text{pg C cell}^{-1}) = \frac{(Alk_{\text{final}} - Alk_{\text{initial}}) \times 10^6 \times 12}{-2 \times cc} \tag{3.12}$$

where $\text{Alk}_{\text{final}}$ and $\text{Alk}_{\text{initial}}$ represent the final and initial alkalinity measurements in μmol $KgSw^{-1}$ respectively and cc represents the cell count per ml. The use of 10^6 converts measurements to pg and 12 converts moles of carbon to grams of carbon. Comparison of measured PIC and calculated PIC from alkalinity change can be found in appendix A.1. Full measured POC and PIC data can be found in appendix A.3.

Given similar trends and magnitudes across methods used to determine PIC (see ap-

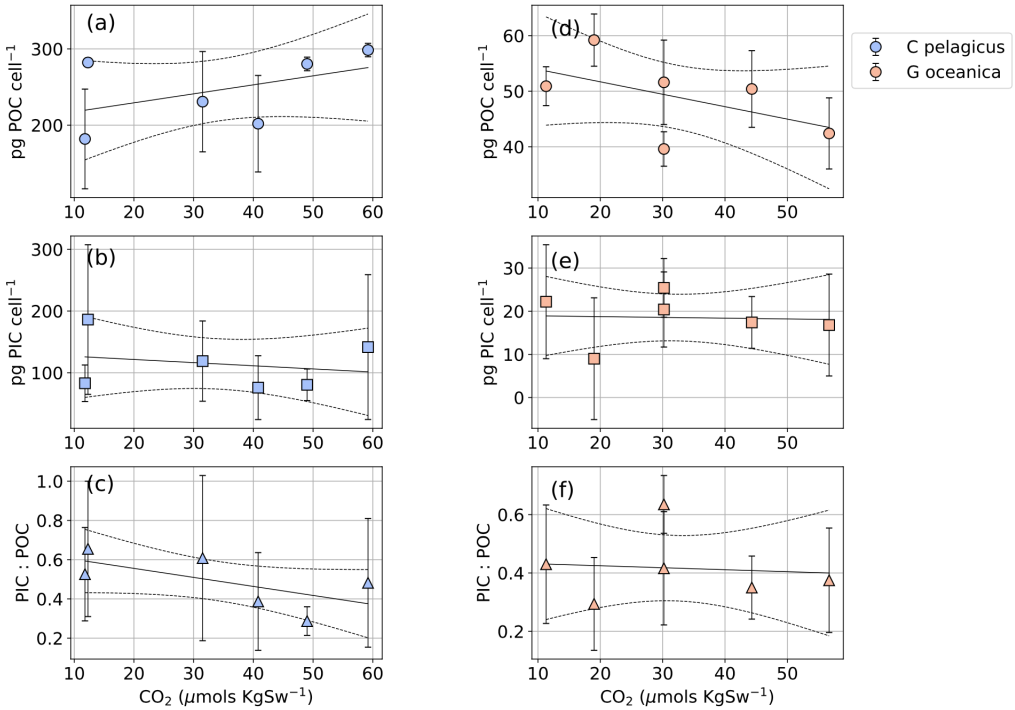

Figure 3.7: PIC **(a)**, POC **(b)** and PIC:POC **(c)** shown for both *C. pelagicus* (light blue) and *G. oceanica* (light orange **(d-f)**) as a function of $[CO_{2(aq)}]$. POC was measured directly, whilst PIC derives from the difference between TPC and POC. Y axes for each species are not constant. Error bars represent the standard deviation across triplicate measurements.

pendix A.1), the PIC calculated from TPC and POC measured on the SERCON GSL elemental analyser was assumed to be reliable. The relationship of PIC and PIC:POC with $CO_{2(aq)}$ for both *C. pelagicus* and *G. oceanica* were found to not be significant (P values = 0.66, 0.15, 0.92, 0.85 respectively).

The average blank mass was 12μg which generally accounted for $\leq$ 10% of sample mass. Given the average mass and blank isotopic value of -24.2‰, the effect on the final presented value of sample $\delta^{13}C_{org}$ was $\leq$ 0.5‰ for all samples.

3.3.5. Coccolith isotopes

Our results show that coccolith carbon isotopic behaviour with varying carbon availability was distinct for each species (Figure 3.8; full isotopic results given in appendix A.2). Indeed, CIVEs for *C. pelagicus* vary significantly with DIC. In experiment 1, $\delta^{13}C_{lith}$ was approximately 3‰ lower than coccoliths grown under higher DIC conditions. CIVEs for *G. oceanica* meanwhile appeared to be insensitive to changes in carbonate parameters with $\delta^{13}C_{lith-DIC}$ values remaining around 0‰.

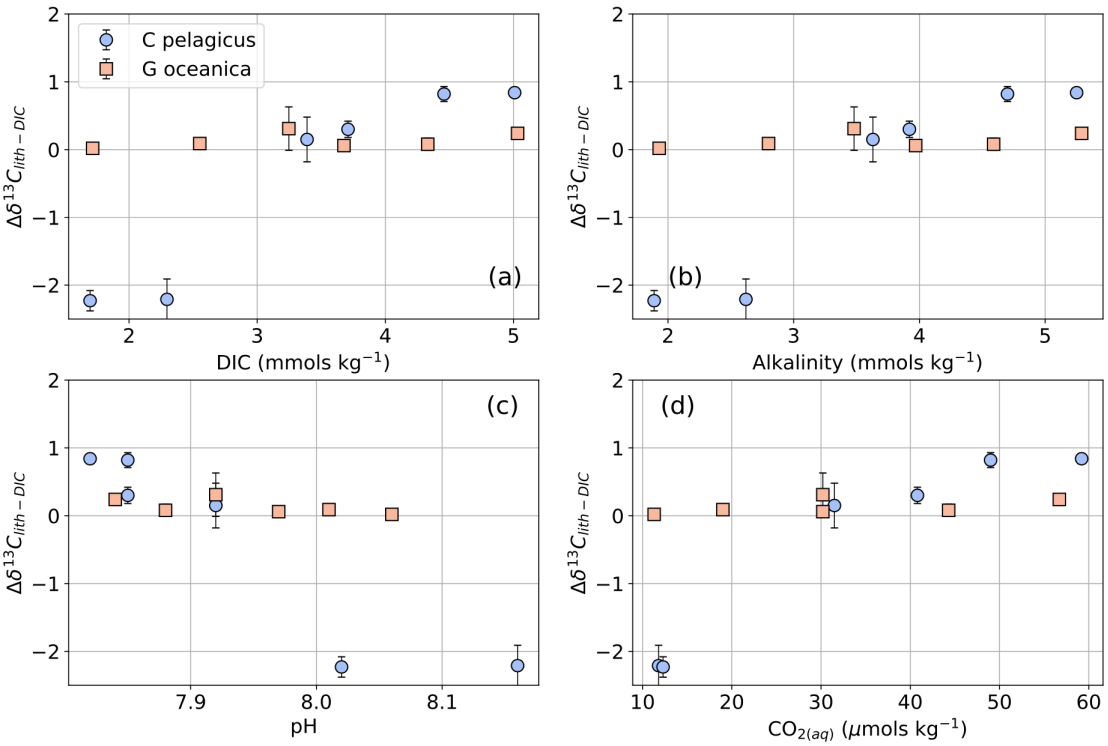

Figure 3.8: $\delta^{13}C_{lith}$ data for *C. pelagicus* (blue markers) and *G. oceanica* (red markers) against [DIC] **(a)**, alkalinity **(b)**, pH **(c)** and $CO_{2(aq)}$ **(d)**. Error bars represent the standard deviation across triplicate measurements.

The corresponding oxygen isotopic data was also measured for each experiment. At high DIC, *C. pelagicus* is characterised by more positive $\delta^{18}O_{lith}$ values, which become more negative as DIC declines (Fig. 3.9). $\delta^{18}O_{lith}$ for *G. oceanica* shows no overall trend with DIC nor $\delta^{13}C_{lith}$ (Fig. 3.9) (full oxygen isotope data can be found in appendix A.2).

3.3.6. Organic carbon isotopes

Calculated values of ε_p appeared to show a non-linear response for *C. pelagicus*, with the most positive values apparent at low values of $\frac{\mu}{[CO_{2(aq)}]}$ (Fig. 3.10). ε_p was smaller for *G. oceanica* compared with *C. pelagicus* (Fig. 3.10). For *G. oceanica*, ε_p values appeared to be at a minimum for intermediate values of $\frac{\mu}{[CO_{2(aq)}]}$.

3.3.7. Re-calibration of existing isotopic flux model

Results from the optimisation procedure suggest optimum values exist for T_A and ε_{ef} for *C. pelagicus* and T_B and ε_{ef} for *G. oceanica* (Fig. 3.11). For T_B, that is the scaleable permeability to HCO_3^-, fitted to *C. pelagicus* the model score did not increase as T_B decreased below values of 1 x $10^{-8.2}$ ms^{-1}. Within the model the overall effective perme-

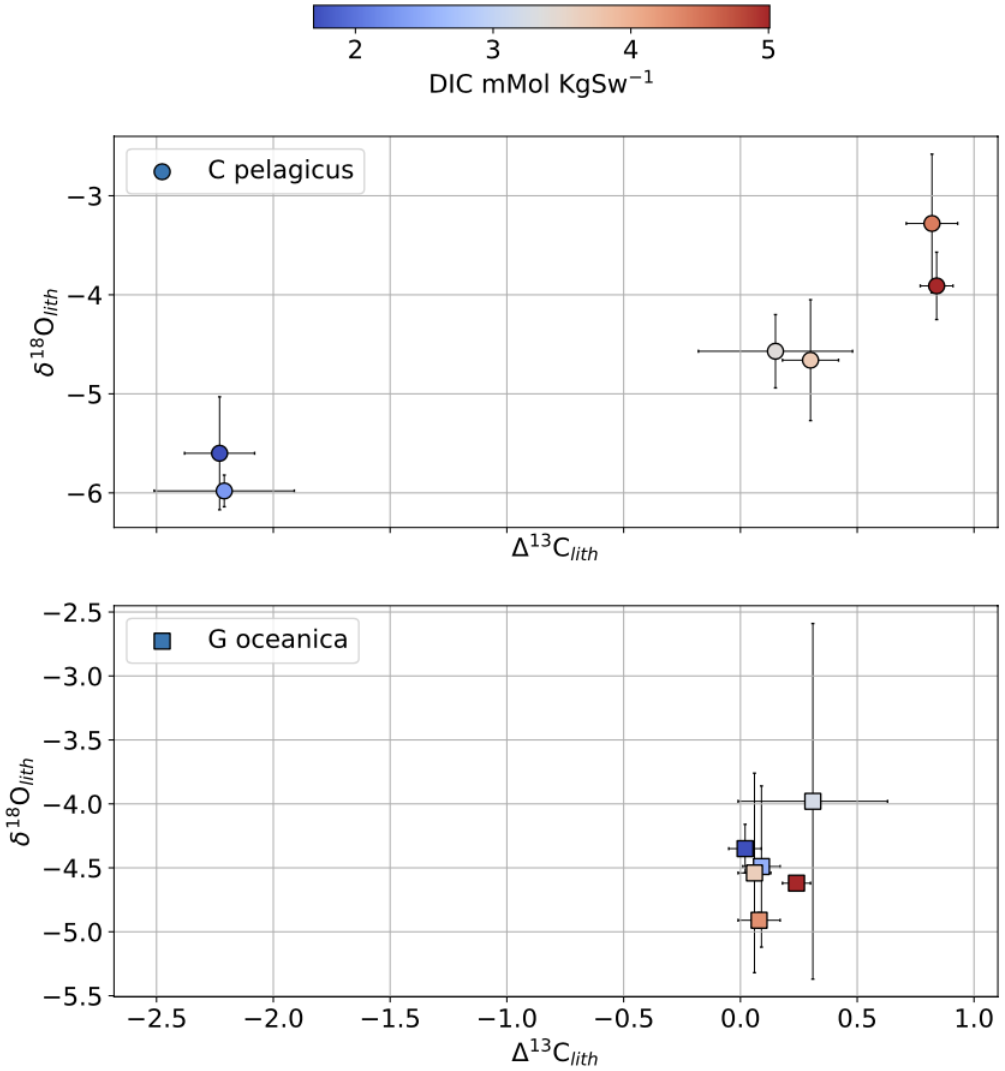

Figure 3.9: $\delta^{18}O_{lith}$ is plotted against $\delta^{13}C_{lith}$ with the colour representing measured DIC concentration in mMols C KgSw^{-1}. Error bars represent the standard deviation across triplicate cultures. The top panel is represents data from *C. pelagicus* and the bottom panel represents data for *G. oceanica*. Contrasting $\delta^{18}O_{lith}$ behaviour may reflect changes to CV pH level across DIC conditions.

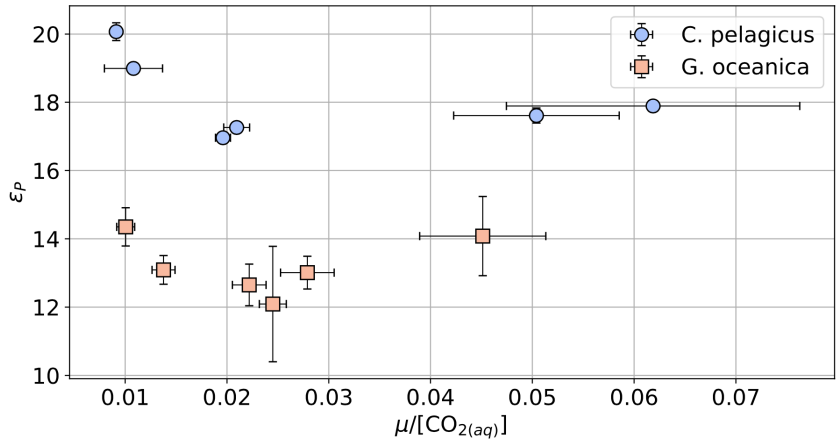

Figure 3.10: ε_p vs $\frac{\mu}{[CO_{2(aq)}]}$. Data is presented for both *C. pelagicus* (light blue) and *G. oceanica* (light orange). Error bars represent the standard deviation across triplicate measurements.

ability of the cell to HCO_3^- is equal to T_A + U_0T_B, where U_0 represents the degree of carbon utilisation of the cell [McClelland et al., 2017]. As T_B approaches 0, the effective permeability of the cell tends towards T_A at all values of U_0, which suggests that the cell does not vary its permeability to HCO_3^-. For *C. pelagicus*, T_B was therefore assumed to be equal to 0. The assumption that T_B is equal to 0 is valid based on a calculation of total cellular permeability to HCO_3^- at high carbon utilisation (low $CO_{2(aq)}$). For example if T_B is taken as 1 x $10^{-8.2}$ ms^{-1} and T_A equal to 1.3 x 10^{-7} ms^{-1} for the highest cellular carbon utilisation (U_0 approximately = 0.1 for experiment 1), the percentage change to overall permeability from experiment 6 to experiment 1 of the cell to HCO_3^- is less than one percent. The assumption of T_B equal to 0 is highlighted by the increasing model fit as T_B tends towards 0 and thus T_BxU_0 becomes negligible at which point no further decrease in T_B affects model behaviour or fit even at the highest predicted carbon utilisation values observed here (Fig. 3.11). Similar behaviour for T_A, that is the background or baseline permeability to HCO_3^-, was observed for *G. oceanica*. Model fit for T_A for *G. oceanica* improved until approximately 10^{-10} ms^{-1} below which it plateaued. T_A was therefore assumed to be 0 for *G. oceanica*. More generally it appears that the carbon isotopic response of *G. oceanica* appears to have no dependency on CO_2 system parameters.

Given the varying magnitudes of $\delta^{13}C_{org}$ measured for both species, ε_{ef} was estimated to be approximately -22.7 ‰ and -13.8 ‰ for *C. pelagicus* and *G. oceanica* respectively (Table 3.4). Given the best fit values for ε_{ef}, T_A and T_B for each species and updated values of [CA], G and P_{Ccell} the isotopic flux model was able to recreate $\delta^{13}C_{lith}$ and $\delta^{13}C_{org}$

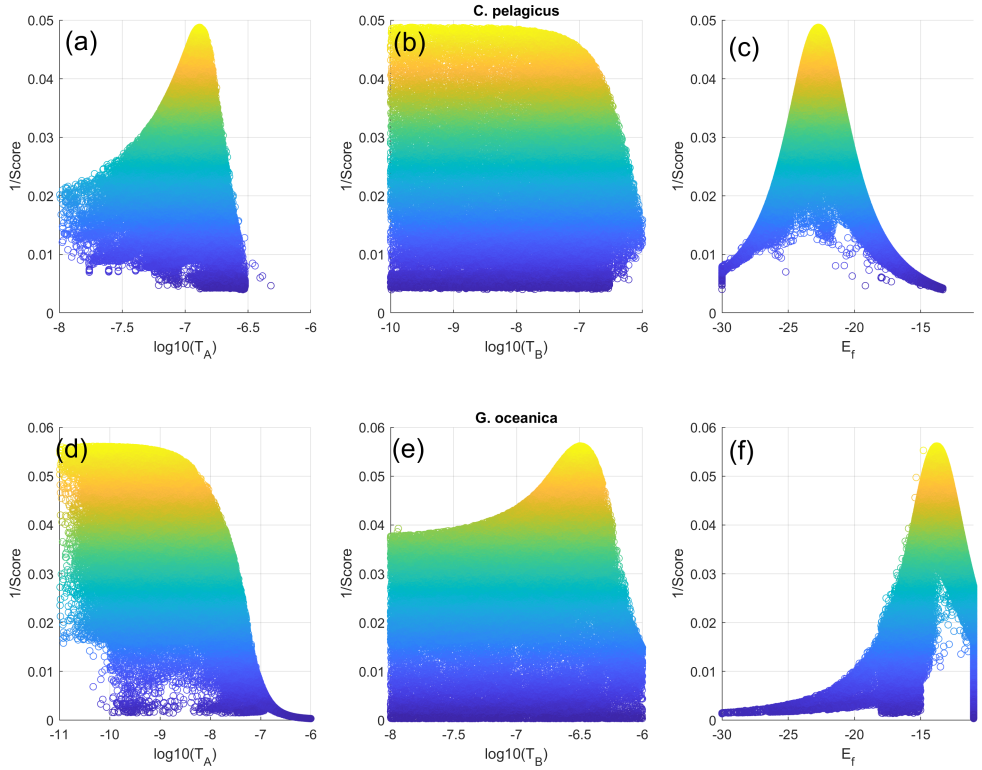

Figure 3.11: Inverted scores from the misfit function over 100,000 runs are plotted vs optimised values of T_A, T_B and ε_{ef} for *C. pelagicus* **(a-c)** and *G. oceanica* **(d-f)**. Each point represents a single optimisation run possessing a different initial combination of T_A, T_B and ε_{ef} values. Colour scales with 1/score to highlight optimums.

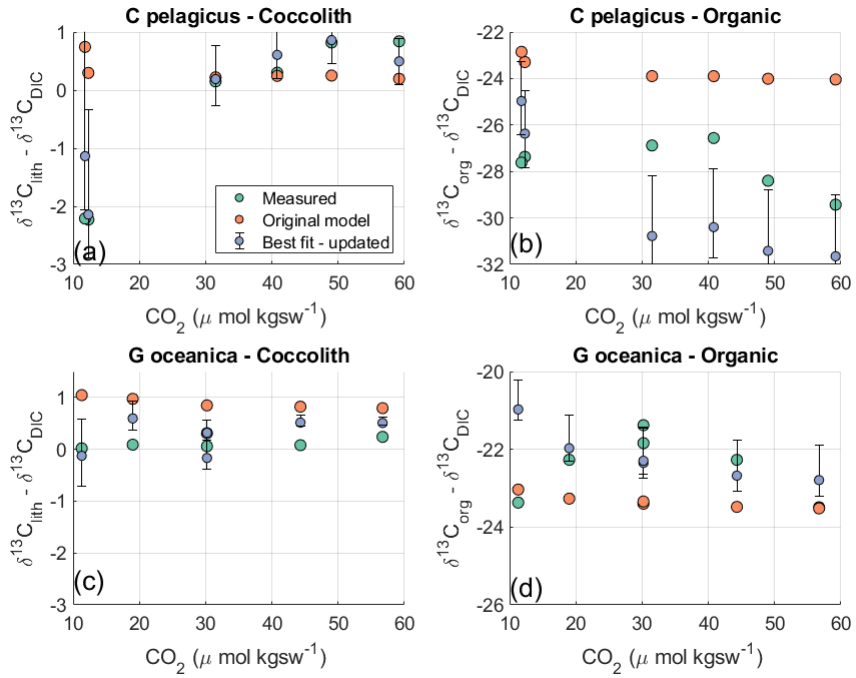

Figure 3.12: $\delta^{13}C_{lith}$ relative to $\delta^{13}C_{DIC}$, **(a)**, and $\delta^{13}C_{org}$ relative to $\delta^{13}C_{DIC}$, **(b)**, are presented for *C. pelagicus*. Green markers represent mean $\delta^{13}C$ values across triplicate measurements for each experiment. Error bars on measured values not shown for clarity. Red markers represent modelled $\delta^{13}C$ values using ε_{ef}, T_A, T_B, [CA], P_{Ccell} and G as listed in McClelland et al. [2017]. Blue markers represent modelled $\delta^{13}C$ values derived from the updated values for ε_{ef}, T_A, T_B, [CA] P_{Ccell} as listed in the tables 3.4 and 3.5. Error bars represent the 16th and 84th percentiles from the Monte-carlo sensitivity analysis over 10,000 runs with all input variables varied according to a Gaussian distribution around their mean. Corresponding measurements for $\delta^{13}C_{lith}$ relative to $\delta^{13}C_{DIC}$, **(c)**, and $\delta^{13}C_{org}$ relative to $\delta^{13}C_{DIC}$, **(d)**, are show for *G. oceanica*. Modelled $\delta^{13}C_{lith}$ values for *C. pelagicus* using cellular parameters defined by McClelland et al. [2017] fail to capture the shift to C^{13} depleted values at low $[CO_{2(aq)}]$. Using updated and constrained cellular parameters from this study (see tables 3.4 and 3.5), the carbon isotopic flux model was able to model the C^{13} enriched and C^{13} depleted $\delta^{13}C_{lith}$ values for *C. pelagicus* at high and low $[CO_{2(aq)}]$ respectively.

relative to $\delta^{13}C_{DIC}$ with a smaller offset than using values as prescribed in McClelland et al. [2017] (Fig. 3.12). Indeed the misfit value via equation 3.11 was reduced from 148 to 20 for *C. pelagicus* and 106 to 17 for *G. oceanica* respectively when the cellular parameters were updated from those presented in McClelland et al. [2017] to those presented in table 3.4.

The flux of a carbon species into the cell is calculated as the product of the permeability of the cell to the carbon species and its concentration in the external environment. The percentage contribution of HCO_3^- is therefore calculated as the proportional flux of HCO_3^- into the cell relative to total carbon flux (HCO_3^- + $CO_{2(aq)}$) supplied to the cell. Based

Table 3.4: Constrained values for ε_{ef}, T_A and T_B. The lower and upper bounds represent the 16th and 84th percentiles from the sensitivity analysis over 10,000 runs with all input variables varied according to a Gaussian distribution around their mean. The original model column represents the values presented in McClelland et al. [2017] and were constant for all species.

		C pelagicus			G. oceanica		
Variable	Original Model	Best fit	Lower	Upper	Best fit	Lower	Upper
T_A (ms^{-1})	7.8 x 10^{-8}	1.30 x 10^{-7}	4.8 x 10^{-8}	2.8 x 10^{-7}	0	0.	0
T_B (ms^{-1})	5.1 x 10^{-6}	0	0	0	3.2 x 10^{-7}	1.9 x 10^{-8}	5.8 x 10^{-7}
ε_{ef} (‰)	-14.3.	-22.7	-23.7	-20.4	-13.8	-14.2	-12.9

Table 3.5: Comparison of cellular parameters P_{Ccell}, [CA] and G with the original model developed by McClelland et al. [2017] with this study. The reference column represents where the values in this study are taken from. The value of 1 for G was inferred based on discussions with Harry McClelland and assumes the membranes are permeable to HCO_3^- to the same degree in both directions.

		This Study		
Variable	McClelland et al. [2017]	*C. pelagicus*	*G. oceanica*	Reference
P_{Ccell} (ms^{-1})	9.3 x 10^{-4}	1.2 x 10^{-4}	1 x 10^{-4}	Blanco-Ameijeiras et al. [2020]
CA (mM)	1	0.4	0.4	Zhang et al. [2021]
G (ratio)	2.7	1	1	Inferred

on values derived for T_A, HCO_3^- forms approximately 14% of the carbon flux to a *C. pelagicus* cell at low DIC and around 8% at high DIC concentrations. Although T_B is zero for *C. pelgaicus* the changing ratio of CO_2 to HCO_3^- available in the external media in different experiments results in a change in the percentage of HCO_3^- usage. For *G. oceanica* given T_A is assumed to be 0, $CO_{2(aq)}$ is the dominant source of carbon to the cell at at high DIC with $\leq 0.5\%$ of carbon acquired in the form of HCO_3^-. Given T_B is not 0, 5% of carbon supplied to the cell is in the form of HCO_3^- at low DIC for *G. oceanica* (e.g. for experiment 1).

Although $\delta^{13}C_{lith}$ values were in line with previous studies, existing data was not included in the re-calibration given the large variation in $\delta^{13}C_{org}$ values (Fig. 3.13). The large spread in absolute value of $\delta^{13}C_{org}$ resulted in poor constraints on all parameters. Future studies should aim to improve the performance of the model at fitting measured $\delta^{13}C_{org}$ values (see discussion).

3.3.8. Sensitivity Analysis to refitting of Model

The sensitivity of ε_{ef}, T_A, and T_B values derived from the optimisation procedure were tested to uncertainty on external DIC concentration, external pH, $\delta^{13}C_{lith}$, $\delta^{13}C_{org}$, cell radius, growth rate and PIC:POC (Fig. 3.14). The sensitivity analysis shows that the

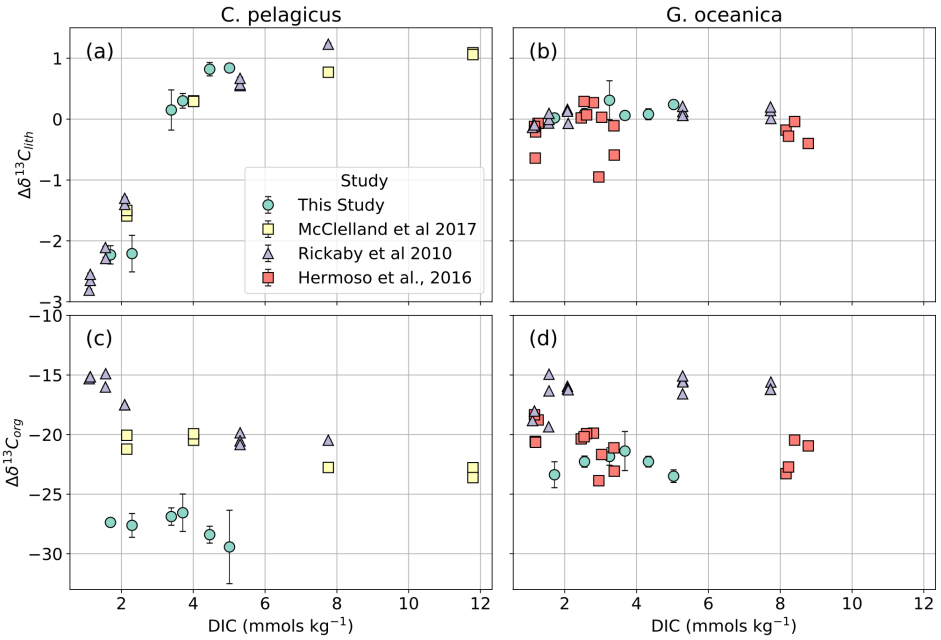

Figure 3.13: $\delta^{13}C_{lith}$ - $\delta^{13}C_{DIC}$ for *C. pelagicus* **(a)** and *G. oceanica* **(b)** as a function of [DIC] for this study, McClelland et al. [2017] and Rickaby et al. [2010]. Corresponding $\delta^{13}C_{org}$ - $\delta^{13}C_{DIC}$ is also shown **(c)** for *C. pelagicus* **(c)** and *G. oceanica* **(d)**.

greatest source of uncertainty on final predicted values of T_A, T_B and ε_{ef} derives from the uncertainty on PIC:POC. Indeed the large associated uncertainty on $\delta^{13}C_{lith}$ for *C. pelagicus* under low $CO_{2(aq)}$ is reduced when PIC:POC is excluded from the Monte-Carlo sensitivity analysis over 10,000 runs (compare figure 3.11 with appendix A.2).

An additional sensitivity analysis was performed whereby the variation in output values of T_A, T_B and ε_{ef} was investigated given a doubling or halving in assumed values of P_{Ccell}, [CA] and G (see appendix A.3 to A.8). Whilst the final results were similar under variations in [CA] and G, the sensitivity analysis shows that modelled absolute values of T_A and T_B are dependent on values of P_{Ccell} as P_{Ccell} acts to alter the availability of carbon to the cell. However, variations in P_{Ccell}, [CA] and G act to shift final values of T_A, T_B and ε_{ef} in expected ways. For example changes in P_{Ccell} led to changes in assumptions regarding T_A and T_B being equal to 0 for *G. oceanica* and *C. pelagicus* respectively. Indeed, when P_{Ccell} was halved, *C. pelagicus* was found to have a non zero value of T_B to facilitate an additional source of carbon at low $CO_{2(aq)}$. When P_{Ccell} was doubled, T_A and T_B both tended to 0 for *G. oceanica* as the diffusive supply of $CO_{2(aq)}$ was sufficient to match the carbon demand across all experiments, thus reducing the dependence of the cell on the transport of HCO_3^-. Nonetheless, a doubling or halving of P_{Ccell} represents an extreme end case scenario. Given P_{Ccell} has recently been well constrained for close relatives of

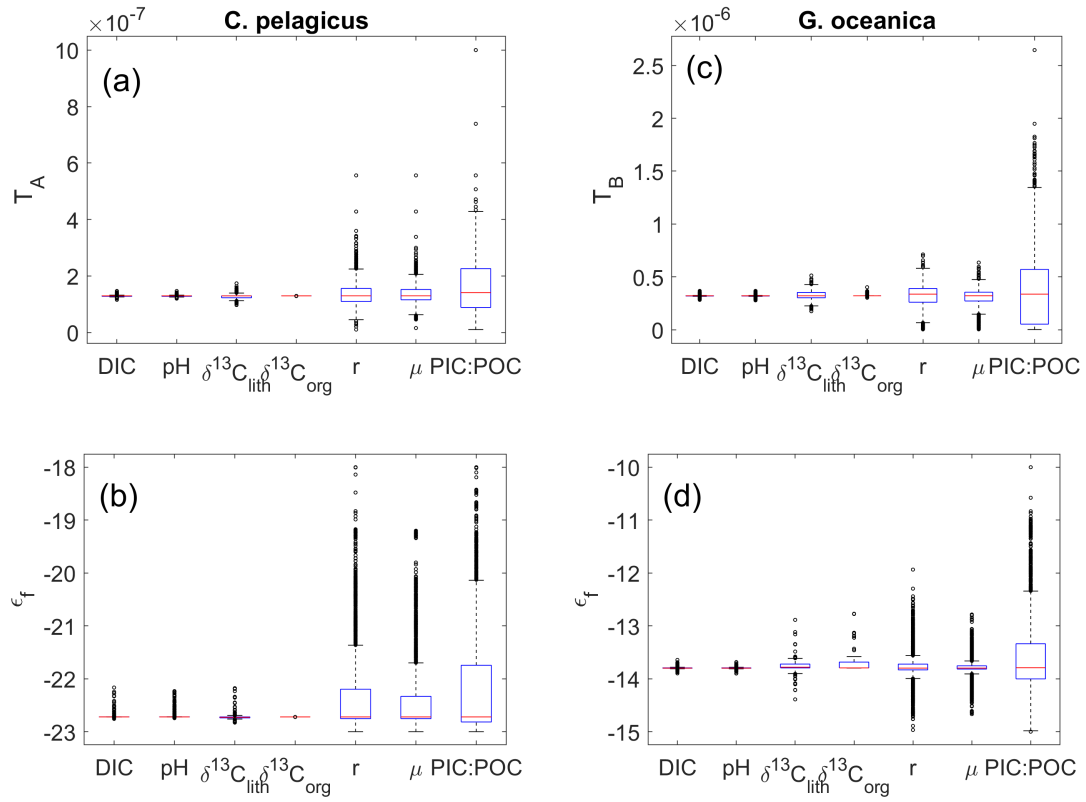

Figure 3.14: Predicted values of T_A **(a)** and ε_{ef} **(b)** for *C. pelagicus* and for *G. oceanica* **(c-d)**. Box plots represent the spread in values over 10,000 optimisations runs with error ascribed to the selected value alone, with all others variables set to the measured value. Error was introduced according to a gaussian distribution on the standard deviation of the measurement. Note the scale on figures **(a)** and **(c)**. Plots for T_B and T_A for *C. pelagicus* and *G. oceanica* respectively are not shown as values are assumed to be 0.

the species investigated here, we believe our selection of P_{Ccell} values are robust [Blanco-Ameijeiras et al., 2020]. If updated values of P_{Ccell}, [CA] and G are presented in the future, re-calibration studies should be run.

3.4. Discussion

One novel aspect of our approach is that the model is fitted to individual species of coccolithophore thus permitting novel insight to be derived regarding species specific carbon acquisition strategies. This is in contrast to existing studies that are calibrated to aggregated data for several species of coccolithophore owing to a paucity of data [McClelland et al., 2017].

3.4.1. $\delta^{13}C_{lith}$ response in *C. pelagicus* to changes in carbonate chemistry

In the species *C. pelagicus* studies have shown that as $CO_{2(aq)}$ becomes limiting, $\delta^{13}C_{lith}$ trends to more ^{13}C depleted values [Rickaby et al., 2010, Hermoso et al., 2016a]. Results from this study are consistent with existing data (Fig. 3.13). Such a large variation in $\delta^{13}C_{lith}$ values measured for *C. pelagicus* across carbonate parameter space suggests substantial changes occur with respect to the isotopic composition of the carbon pool within the coccolith vesicle (CV) as DIC declines. Under high DIC conditions, $\delta^{13}C_{lith}$ relative to $\delta^{13}C_{DIC}$ is approximately +0.8‰, which is approaching the isotopic offset achieved during abiogenic calcite precipitation (approximately +1‰ relative to DIC; [Zeebe and Wolf-Gladrow, 2001]). In order to approach the isotopic composition of abiogenic calcite, the $\delta^{13}C$ value of the carbon within the coccolith vesicle ($\delta^{13}C_{CV}$) must be approaching that of the external media. When DIC is high, carbon fixed through calcification is negligible relative to the total fluxes of carbon into and out of the CV. Moreover, the isotopic composition of the fluxes into and out of cellular compartments are thus set by the ratio of CO_2/HCO_3^- of the flux into and out of each compartment. Given the cytosol within the model is prescribed a lower pH than the CV, the isotopic flux to the CV is ^{13}C depleted relative to the isotopic flux from the CV to the cytosol due to the pH difference between the cytosol to the CV (assumed CV pH = 7.1 vs cytosol ph of 7.0 resulting in influx has a higher $CO_{2(aq)}/HCO_3^-$ ratio than the efflux) [Anning et al., 1996, McClelland et al., 2017].

As DIC declines $\delta^{13}C_{lith}$ approaches -2‰ relative to $\delta^{13}C_{DIC}$. Moreover, calcification becomes significant relative to fluxes into and out of the CV. As the removal of carbon

from the CV pool via calcification becomes an appreciable fraction of the total flux of carbon to the CV, isotopic and chemical dis-equilibrium between the cell and the ambient environment occurs. Dis-equilibrium derives from the continued ^{13}C-depletion of the CV carbon pool through ongoing calcification and through a shift in the ratio of CO_2 to HCO_3^- in the efflux and influx ratios.

Within the constraints of the model, variation to $\delta^{13}C_{CV}$ derives from ^{13}C depletion through calcification and/or a change in the δ^{13}C of the carbon supplied to the CV. Given maximum distillation of the carbon pool is limited to the 1‰ (abiogenic carbonate formation is 1‰ enriched relative to DIC), the -2‰ vital effects measured within *C. pelagicus* must also derive in part from a change in the isotopic signature of carbon supplied to the CV. As membranes are approximately 1000x more permeable to $CO_{2(aq)}$, when carbon fixation through calcification becomes significant relative to the fraction of the carbon supplied to the CV (at low $CO_{2(aq)}$ or high μ), CO_2 forms an increasing fraction of the carbon hydrated and subsequently used for carbonate formation. This behaviour likely derives from *C. pelagicus* not adjusting its number of HCO_3^- transporters and having a greater carbon demand in comparison to *G. oceanica*, which does not see an increase in the ratio of $CO_{2(aq)}/HCO_3^-$ within its CV (Fig. 3.15). $\delta^{13}C_{lith}$ therefore approaches that of the isotopic composition of the carbon flux to the CV. The relative increase in CO_2 supply and increased isotopic disequilibrium drives $\delta^{13}C_{lith}$ isotopically light.

3.4.2. $\delta^{13}C_{lith}$ response in *G. oceanica* to changes in carbonate chemistry

In contrast to *C. pelagicus*, *G. oceanica* displays remarkably consistent $\delta^{13}C_{lith}$ values with variations in external $CO_{2(aq)}$. Such consistent $\delta^{13}C_{lith}$ values measured in *G. oceanica* across experiments one to six suggests that $\delta^{13}C_{CV}$ remains constant. The isotopic behaviour likely derives from *G. oceanica* having a lower carbon demand and smaller size.

Using cellular parameters constrained by McClelland et al. [2017] the carbon isotopic flux model recreated $\delta^{13}C_{lith}$ values well for *G. oceanica* except for experiment one (Fig. 3.12). Using the HM17 model with original parameters, $\delta^{13}C_{lith}$ for experiment one was predicted to deviate to more positive values. For cells with a PIC:POC ≤ 1, as measured for *G. oceanica* here, under a low carbon availability $\delta^{13}C_{lith}$ is predicted to deviate to ^{13}C enriched values due to the increase in HCO_3^- uptake as carbon availability declines [McClelland et al., 2017]. Given $\delta^{13}C_{lith}$ measured here for *G. oceanica* shows no up-

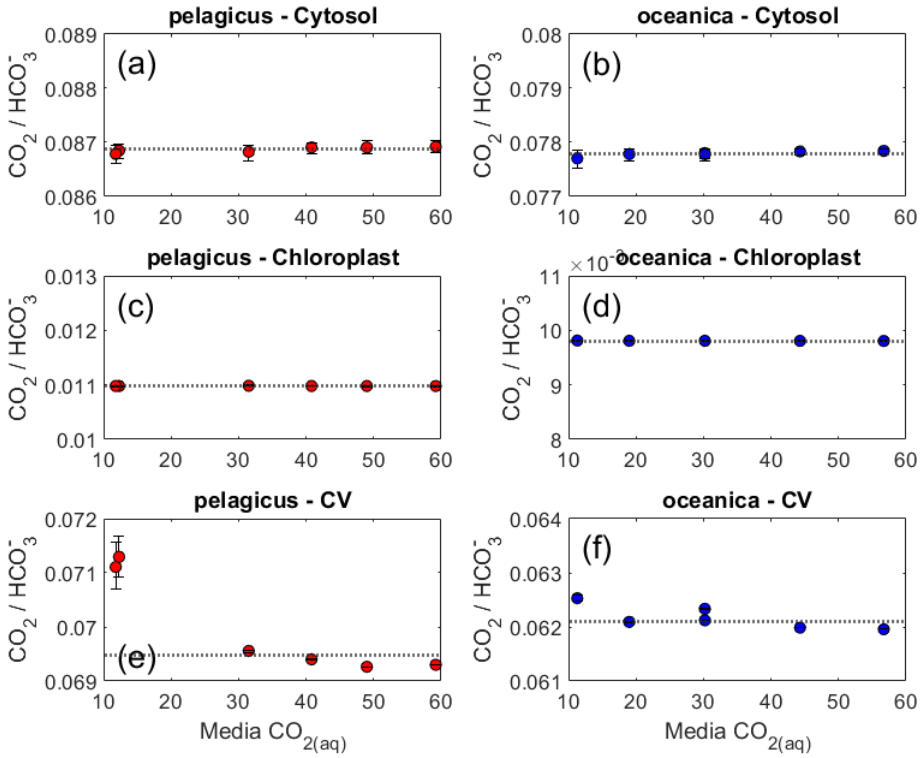

Figure 3.15: The modelled ratio of CO_2 to HCO_3^- for both *C. pelagicus* (red; left plots) and *G. oceanica* (blue; right plots) within the cytosol **(a-b)**, chloroplast **(c-d)** and CV **(e-f)** as a function of external $CO_{2(aq)}$. Data points are best fit values from the optimisation procedure with the error deriving from one standard deviation of ratios over the sensitivity analysis with error introduced to all input variables. All y-axis are across the same range to allow for comparison. The dashed horizontal line in each plot represents the approximate equilibrium ratio achieved at low carbon utilisation within each compartment.

ward inflection towards lower carbon availability, the constrained lower T_B, or ability to upregulate HCO_3^-, makes intuitive sense. (Fig. 3.3).

3.4.3. Modelled $\delta^{13}C_{org}$ and ε_p

Whilst the carbon isotopic flux model was able to recreate $\delta^{13}C_{lith}$ well for both species, it performed poorly when recreating $\delta^{13}C_{org}$. Indeed, using original cellular parameters presented by McClelland et al. [2017] the carbon isotopic flux model struggled to recreate the magnitude and behaviour of measured $\delta^{13}C_{org}$ values for both species. Whilst the model better recreated the $\delta^{13}C_{org}$ magnitudes with updated cellular parameters, the model was unable to recreate observed variations in $\delta^{13}C_{org}$ across the entire carbonate parameter space (Fig. 3.12).

Within the model $\delta^{13}C_{org}$ is determined as a combination of the isotopic composition of the substrate, CO_2, and ε_{ef}, the effective fractionation factor. At low carbon utilisation the flux of carbon across cellular membranes relative to carbon fixation is large and ^{13}C enrichment of the carbon pool within the chloroplast due to isotopic discrimination by RuBisCO is negligible. As carbon utilisation increases, the intracellular flux of carbon across membranes relative to carbon fixation is reduced and the isotopic composition of the carbon pool within the chloroplast drifts to ^{13}C-enriched isotopic values. Subsequent organic matter fixation occurs from an increasingly ^{13}C enriched pool and a curve-linear decrease of ε_p with $\frac{\mu}{[CO_{2(aq)}]}$ is traditionally observed [Keller and Morel, 1999, Schulz et al., 2007, McClelland et al., 2017]. Deviation from this traditional curve-linear form suggests mechanisms that are not accounted for within the model are affecting measured $\delta^{13}C_{org}$ values as function of carbon utilisation. Notably, $\delta^{13}C_{org}$ values for both species under experiments one and two appear to be more ^{13}C-depleted than expected (Fig. 3.12; see two lowest CO_2 values).

One possible scenario that could explain the discrepancy between modelled and measured $\delta^{13}C_{org}$ values is the influence of respiration. Previous studies have shown that significant respiration relative to photosynthesis occurs during the dark phase of the cell cycle [Schulz et al., 2007]. When carbon utilisation is low, any carbon supplied by respiration is likely small relative to the fluxes across cellular membranes, resulting in a negligible drift to the internal carbon pool. However, when utilisation of carbon is high, the flux of CO_2 from respiration may become significant relative to total cellular fluxes and would

also be more ^{13}C depleted than $CO_{2(aq)}$ from the external media with absolute values depending on the isotopic composition of the organic matter respired. At low levels of DIC it is therefore plausible that isotopically depleted carbon from respiration could be reused during subsequent organic matter fixation resulting in a more negative (/positive) signal in $\delta^{13}C_{org}$ ($/\varepsilon_p$). If ^{13}C enriched matter relative to $\delta^{13}C_{org}$ but depleted relative to external $CO_{2(aq)}$ was preferentially respired, then respiration would also act to drive the remaining organic matter $\delta^{13}C_{org}$ to more ^{13}C depleted values. Respiration would, however, additionally act to drive $\delta^{13}C_{lith}$ to more ^{13}C depleted values at high carbon utilisation. If respiration was contributing to a shift in $\delta^{13}C_{lith}$ and $\delta^{13}C_{org}$ the assumptions within this model may need to be reconsidered. Other studies suggests respiration increases the gross cellular carbon demand and thus necessitates greater HCO_3^- usage shifting $\delta^{13}C_{org}$ to more ^{13}C enriched values, opposite to that observed here [Holtz et al., 2015]. The influence of respiration on the carbon isotopic composition of cellular components remains understudied in the literature.

Alternatively it may be that an additional process is occurring within the chloroplast that is acting to shift $\delta^{13}C_{org}$ to lighter than expected values at low external $[CO_{2(aq)}]$. The carbon isotopic flux model used here employs a black box like fractionation factor, whereby $\delta^{13}C_{org}$ is a fixed offset from $\delta^{13}C_{CO_2}$ within the chloroplast. In reality the formation of the process of organic matter fixation is more complicated, involving a pyrenoid and thylakoid complex and more than one membrane as inferred here. Wilkes and Pearson [2019] invoked an additional CCM within coccolithophores, whereby CO_2 is actively transported and hydroxylated from the cytosol into the thykaloid. The thykaloid was suggested to be acidic with CA present to concentrate CO_2, which could then diffuse into the pyrenoid for use in carbon fixation. The process was suggested to be driven by light. The possibility that this process is only 'switched-on' at low utilisation was not addressed, however such a scenario would increase the flux of CO_2 available for carbon fixation and increase modelled ε_p at high carbon utilisation (Fig. 3.16). Such a mechanism would likely leave $\delta^{13}C_{lith}$ unchanged. Gene expression for such a process remains to be identified, but activation at low carbon utilisation would reconcile the data presented here.

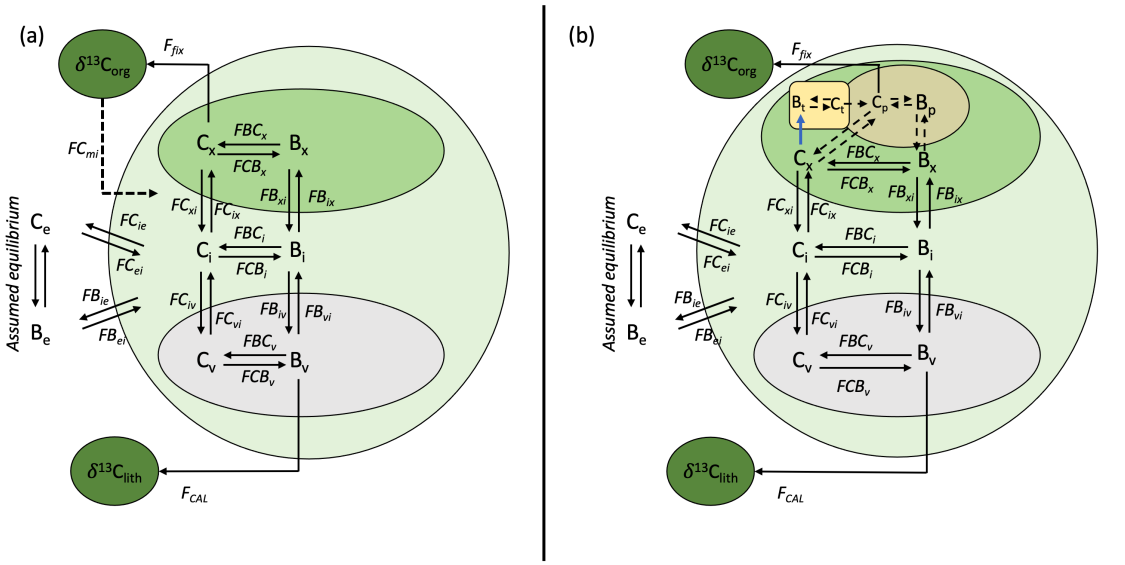

Figure 3.16: Possible mechanisms for the deviation of ε_p from the expected curve linear response include the influence of respiration **(a)** and the existence of a pyrenoid complex in cells **(b)**. **(a)** represents the cell in figure 3.2, however, an added flux exists in which isotopically depleted carbon is released to the cytoplasm via respiration of ^{13}C depleted organic matter (highlighted by the additional dashed black arrow from the fixed OM). FC_{mi} represents the flux to the cytosol from the mitochondria. **(b)** depicts a scenario in which the chloroplast consists of two additional compartments, the thykaloid and the pyrenoid. The blue arrow represents a one directional ATP powered pump and hydroxylation of CO_2 into the thykaloid (yellow rectangle) as HCO_3^-. The dotted arrows represented additional proposed fluxes of carbon species, which are not labelled due to limited space, but follow nomenclature from **(a)** and figure 3.2. The thykaloid is acidic and is assumed to contain carbonic anhydrase. The thykaloid-pyrenoid (pyrenoid is represented by the brown oval within the chloroplast) complex would add an additional layer of complexity to the model, however for a given CO_2, ε_p can be larger due to the expression of isotopic fractionation associated with the hydroxylation of CO_2. Hydroxylation of CO_2 into the thykaloid, which acts as a CCM, provides an additional flux of CO_2 into the pyrenoid for organic matter fixation. **(b)** adapted from McClelland et al. [2017] and Wilkes and Pearson [2019].

3.4.4. Inter study comparison of cellular parameters

Prior to the undertaking of this work, literature had investigated cellular parameters in marine algae through a variety of methods. Coupled *in vivo* and *in silico* studies into *E. huxleyi* suggest T_A is less than 1 x 10^{-7} m s^{-1} and studies on diatoms suggest values of 0.4 x 10^{-7} m s^{-1} to 2.5 x 10^{-8} m s^{-1} [Blanco-Ameijeiras et al., 2020, Hopkinson et al., 2011]. The value of T_A predicted here for *C. pelagicus* is therefore within the range of previous estimates. Given cellular permeabilities to HCO_3^- are often held fixed in models for diatoms and large coccolithophores the assumption of T_B equal to 0 for *C. pelagicus* also appears valid [Blanco-Ameijeiras et al., 2020, Hopkinson et al., 2011].

T_A was assumed to be 0 for *G. oceanica*, however, a non 0 value predicted for T_B suggests total permeability to bicarbonate is variable (total permeability = $T_A + T_B x U_0$). Recent work has suggested that the small *E. huxleyi* must increase its HCO_3^- pumping rate into the cell and chloroplast at low $CO_{2(aq)}$ to explain variations in isotope measurements within isotopic labelling experiments [Zhang et al., 2021]. An increase in pumping rate would have a similar affect to the increased permeability to HCO_3^- predicted here that is inferred to derive from an upregulation of HCO_3^- protein channels at high carbon utilisation [McClelland et al., 2017]. Given *G. oceanica* and *E. huxleyi* are closely related, the finding that *G. oceanica* must upregulate its HCO_3^- transporters is consistent with previous findings.

Existing literature suggests that P_{Ccell} may vary by up to two orders of magnitude given changes in the sterol content of cell membranes [Stoll et al., 2019]. Moreover, changes in temperature have also been suggested to alter P_{Ccell} in *E. huxleyi* [Blanco-Ameijeiras et al., 2020]. It is possible that prescribing scaleable values of P_{Ccell} with carbon utilisation may result in a better fit for $\delta^{13}C_{lith}$ and $\delta^{13}C_{org}$. Model scenarios in which P_{Ccell} is not fixed should be the target for future work in both *C. pelagicus* and *G. oceanica*. This study, and all model-data studies, are faced with a problem in which a large number of cellular fitted parameters are required, yet there is a lack of culture data to constrain all parameters. Model-culture studies must therefore choose which values are the target of optimisation to ensure the parameters are not over fit to the data and under-constrained.

It is important to note that alternative theories exist to explain carbon isotopic variation within coccolithophore cellular components. Relative changes in the rate of HCO_3^-

supplied to the CV relative to the rate of calcification has been invoked to explain shifts to ^{13}C depleted value of coccolith calcite at low external $CO_{2(aq)}$ [Bolton and Stoll, 2013a]. However, such a mechanism relies on the assumption that HCO_3^- can only leave the CV via calcification. Calcite vital effects are therefore almost entirely set by the proportional supply of HCO_3^- to the CV rather than CV equilibrium of carbon species and the movement of HCO_3^- out of the CV as is likely the case in reality [Bolton and Stoll, 2013a]. Moreover, the model developed by Bolton and Stoll [2013a] predicts a shift to ^{13}C depleted values in coccolith calcite at low external $CO_{2(aq)}$ driven by active pumping of HCO_3^- to the chloroplast at the expensive of the supply to the CV. The increase supply of HCO_3^- to the chloroplast at low external $CO_{2(aq)}$ would act to shift ε_p to more negative values. However, data used to calibrate the model shows a shift to more positive values at low external $CO_{2(aq)}$ with the discrepancy not discussed (see Bolton and Stoll [2013a] supplementary plot Figure S2). This study also observes a to shift to more negative ε_p values at low $CO_{2(aq)}$ with the model used here unable to replicate observations. Cellular models as a whole are therefore failing to capture behaviour controlling the organic isotopes at low $CO_{2(aq)}$ for *G. oceanica*.

3.4.5. A note on oxygen isotopes

Whilst the oxygen isotope system is not accounted for within of the isotopic flux model, investigating the oxygen isotopic composition of coccoliths ($\delta^{18}O$) can provide additional information regarding coccolithophore physiology. Whilst the suggestion that an increase in CO_2/HCO_3^- supplied to the CV with declining DIC accounts for the observed changes in $\delta^{13}C_{lith}$ for *C. pelagicus*, it cannot account for the changes in $\delta^{18}O_{lith}$ alone. Indeed, the increased supply of CO_2/HCO_3^- with declining DIC should manifest in a positive shift in $\delta^{18}O_{lith}$ given $\delta^{18}O_{CO2}$ is more positive than $\delta^{18}O_{HCO_3^-}$ (Fig. 3.17; [Zeebe and Wolf-Gladrow, 2001]). However, the oxygen isotopic system has an additional layer of complexity due to the interaction of oxygen atoms associated with H_2O and DIC.

Equilibration with regards to the oxygen isotopic system is exclusively reached through the hydration and hydroxylation of $CO_{2(aq)}$ [Zeebe and Wolf-Gladrow, 2001]. The time to reach equilibrium therefore depends on the concentration of $CO_{2(aq)}$, which is a function of pH [Zeebe and Wolf-Gladrow, 2001]. After approximately 12 hours at pH 8, and a salinity of 35‰, any isotopic signal within the DIC pool will be overwritten through

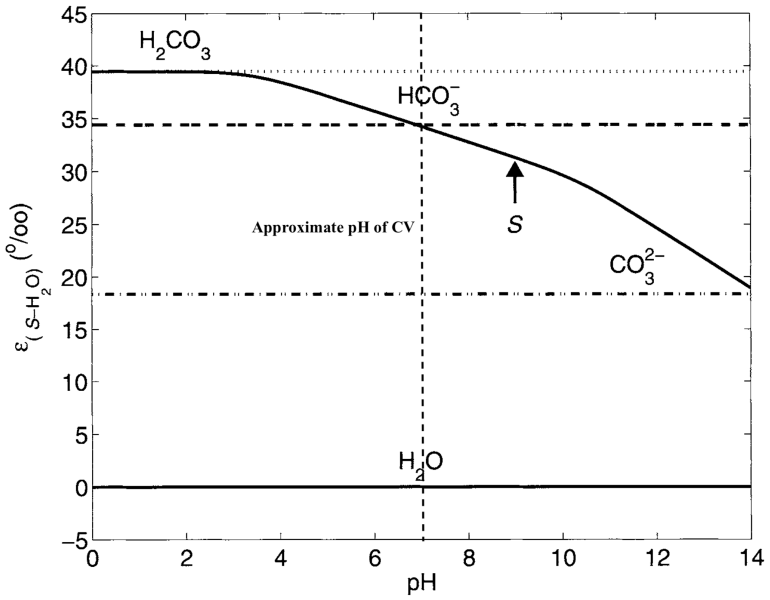

Figure 3.17: The oxygen isotopic composition of carbon species are shown as a function of pH. S = H_2CO_3 + HCO_3^- + CO_3^{2-}. The vertical dashed line represents the pH of the CV assumed within the model after [Anning et al., 1996]. Original figure modified from [Zeebe and Wolf-Gladrow, 2001].

exchange with the effectively infinite supply of oxygen attached to H_2O relative to the DIC system. However, the time required for equilibrium to be established with regards to the oxygen isotopic system can be significantly decreased in the presence of carbonic anhydrase [Uchikawa and Zeebe, 2012]. Indeed, inferred [CA] here of 0.4 mols m^{-3} is sufficient to achieve 99% equilibration within the oxygen isotopic system on the order of seconds for all experiments (Fig. 3.18; [Zeebe and Wolf-Gladrow, 2001, Uchikawa and Zeebe, 2012, Zhang et al., 2021]). The oxygen isotopic system is therefore assumed at equilibrium on the time scales of coccolith formation (approximately one every two hours).

At high DIC, *C. pelagicus* is characterised by more positive $\delta^{18}O_{lith}$ values, which become more negative as DIC declines (Fig. 3.9). In the model presented here CV pH is prescribed to be constant, however to achieve a negative $\delta^{18}O_{lith}$ at equilibrium, a change in CV pH over DIC availability is required. A change in CV pH would alter the $\delta^{18}O$ of total carbonate species (H_2CO_3 + HCO_3^- + CO_3^{2-}; denoted as $\delta^{18}O_S$ after [Zeebe and Wolf-Gladrow, 2001]; Fig. 3.17). At low $CO_{2(aq)}$ and a higher CV pH the $\delta^{18}O_S$ would shift to a more negative value resulting in a more negative $\delta^{18}O_{lith}$. Given the production of coccoliths is on the order of one every two hours, the heavy oxygen isotopic signature associated with CO_2 would be eradicated once the system reached rapid equilibrium due to the presence of [CA], whilst the carbon supplied would maintain its light carbon isotopic

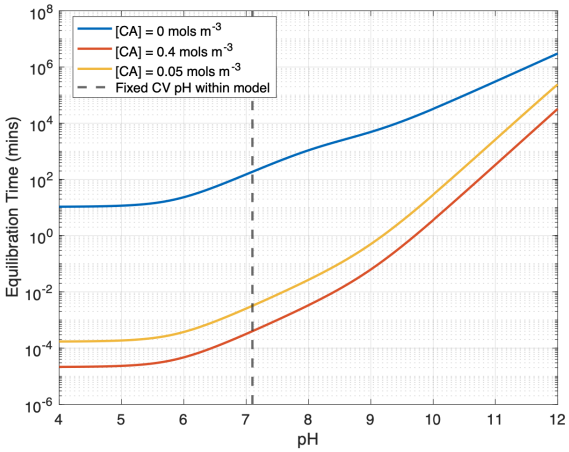

Figure 3.18: The equilibration time for the oxygen isotopic system is shown as a function of pH for a system containing differing concentrations of CA. Equilibration times were calculated after equations presented in Zeebe and Wolf-Gladrow [2001], Uchikawa and Zeebe [2012], Lueker et al. [2000].

signature thus giving a coupled light $\delta^{18}O_{lith}$ and $\delta^{13}C_{lith}$.

To achieve an approximate 2‰ shift observed within $\delta^{18}O_{lith}$ for *C. pelagicus* a corresponding change of 1.5 pH units is required. The mechanism to drive such a large shift in pH remains to be established although such large shifts have been observed [Anning et al., 1996]. A caveat is that the $\delta^{18}O_{lith}$ shift may be smaller, or indeed non existent, once the $\delta^{18}O_{DIC}$ of the ambient media is taken into account. Indeed as with the carbon isotopic system there may be some drift in $\delta^{18}O_{DIC}$ across experiments, although it is unlikely to be on the order of 3‰. Moreover, given the pH of the bulk media was altered across experiments, the distribution of $\delta^{18}O$ of the carbon species in the bulk media also changed. We were unable to measure the $\delta^{18}O_{DIC}$ of the bulk media and thus cannot correct for the offset.

Previous experiments suggest *C. pelagicus* is an equilibrium species with respect to oxygen isotopes [Hermoso et al., 2014]. However, Hermoso et al. [2014] maintained a constant pH and altered the oxygen isotopic composition of water which seems unlikely to have resulted in large changes to the CV pH. New data presented here suggests that *C. pelagicus* does exhibit oxygen isotope vital effects with changes in pH and may not be a truly equilibrium species if changes in bulk media pH occur as in this study. Other experiments in which DIC was elevated also observe a coupled shift in both $\delta^{18}O_{lith}$ and $\delta^{13}C_{lith}$ further supporting our suggestion [Rickaby et al., 2010]

Whilst it is possible to explain the variations in oxygen isotopes through variations in

CV pH, the isotopic flux model employed in this study assumes that pH is fixed. Future work should focus on better constraining the oxygen isotopic system and explore the possibility of changes in intracellular pH within the isotopic flux model.

$\delta^{18}O_{lith}$ for *G. oceanica* shows no overall trend with DIC nor $\delta^{13}C_{lith}$ (Fig 3.9). Given the growth rate measured for *G. oceanica*, the cellular compartments are likely to be approaching isotopic equilibrium with regards to the oxygen isotopic system. The CV pH is therefore likely more constant that that of *C. pelagicus* given the absolute magnitude of variations.

3.4.6. Implications for carbon concentrating mechanisms

Comparing cell permeabilities to $CO_{2(aq)}$ and the effective permeability to HCO_3^- for each coccolithophore species informs on the presence of hypothesised carbon concentrating mechanisms (CCM). Cells that are only permeable to $CO_{2(aq)}$ likely do not possess a CCM and when $CO_{2(aq)}$ becomes limiting, such cells will likely be adversely affected. Cells that are meanwhile able to supplement their diffusive supply of carbon from $CO_{2(aq)}$ with that of HCO_3^- are likely better adapted to lower $CO_{2(aq)}$ regimes. Whilst the results presented here suggest *C. pelagicus* and *G. oceanica* have differing approaches to carbon limitation, both species are predicted to have the ability to transport HCO_3^- into their cells, inline with previous studies [Kottmeier et al., 2014, Mackinder et al., 2011].

Given the larger cell size of *C. pelagicus*, the total cellular carbon demand is greater than that of *G. oceanica*. Here we predict that HCO_3^- forms an appreciable fraction of total carbon supplied to a cell of *C. pelagicus* (e.g. T_A was found to not be 0) at all values of $\frac{\mu}{[CO_{2(aq)}]}$. The elevated supply of HCO_3^- may predominantly help to facilitate the production of coccoliths, and given the presence of [CA], may also provide an additional source of CO_2 for organic matter production. Such behaviour may have evolved to help *C. pelagicus* adapt to declining $CO_{2(aq)}$ values across the Cenozoic (see chapter 2; [Foster et al., 2017]).

G. oceanica, which evolved approximately 7.3 million years ago [Young and Bown, 2020], appears to be a low CO_2 specialist given its lower carbon demand and ability to up-regulate HCO_3^- transporters (e.g. T_B is not zero) under carbon limitation. The findings for *G. oceanica* are in line with those based on disequilibrium experiments performed on *E. huxleyi* [Kottmeier et al., 2014]. *E. huxleyi* was shown to predominantly utilise $CO_{2(aq)}$

Table 3.6: Summary of different carbonate conditions and their affect on coccolith malformation for *C. pelagicus*. The Low and High columns represent the experiments in which $CO_{2(aq)}$ in μMols C $KgSw^{-1}$ was lowest and highest respectively. Values presented for this study represents the average value across triplicates in experiment 1 and 6 respectively.

Study	Carbonate Chemistry	$[CO_{2(aq)}]$		Malformation (%)	
		Low	High	Low CO_2	High CO_2
Rickaby et al. [2010]	Increased DIC, Constant pH	9.1	64	10	95
Langer et al. [2006]	Constant DIC, Decreased pH	5.4	32.8	5	18
This Study	Increased DIC, Decreased pH	12.14	41.4	10	90

via passive diffusion into the cell with the pumping of HCO_3^- only occurring under carbon limitation to supplement the diffusive $CO_{2(aq)}$ supply [Kottmeier et al., 2014]. In summary the work presented here supports the theory that both *C. pelagicus* and *G. oceanica* possess forms of CCM based on cell membrane HCO_3^- transporters.

3.4.7. A note on coccolith malformation and implications for cellular physiology

Based on SEM image analysis, coccolith malformation was found to increase from experiment one to six for *C. pelagicus* (Table 3.3). Increased malformation of coccoliths has been observed in previous laboratory culture experiments, although to varying degrees (Table 3.6). Data presented here coupled with existing data therefore suggests that the coccolith malformation response is common with an increase in $CO_{2(aq)}$. However, the degree of malformation also appears to be a function of the method of carbonate chemistry manipulation. Studies that increased total DIC in addition to $CO_{2(aq)}$ appear to increase the degree of malformation observed for coccolithophores. Given the observed change across studies, malformation of coccoliths produced by *C. pelagicus* therefore appears to be a function of both $CO_{2(aq)}$ and DIC.

Coccolithogenesis occurs within the CV, with the precipitation of calcite regulated by coccolith associated polysaccahrides (CAPs). Recent work has suggested that the ability of CAPs to control calcification is determined by the CAPs charge and $\Omega_{calcite}$ of the local environment [Giuffre et al., 2013]. A lower charge provides a lower barrier to nucleation and a higher rate of calcite nucleation, which allows coccolith growth to initiate at a lower $\Omega_{calcite}$ [Giuffre et al., 2013]. CAPs produced by *C. pelagicus* are suggested to have a low charge density and are therefore suitable for precipitating calcite in a CV

with a low saturation state (see chapter 4; [Walker et al., 2018, Giuffre et al., 2013]). Elevated $CO_{2(aq)}$ or DIC within the culture media would drive an increase in $\Omega_{calcite}$ within the CV. Increased $\Omega_{calcite}$, along with the low charge on the CAP of *C. pelagicus*, may result in the decreased control over precipitation of calcite. This hypothesis may explain the differences in degree of malformation observed across experimental conditions (Table 3.6). The moderate increase in malformation observed by Langer et al. [2006] may derive from the increased availability of carbon within the coccolithophore due to the raised concentration of $CO_{2(aq)}$ available to diffuse into the cell, even under constant DIC. In this study, and that of Rickaby et al. [2010], elevated DIC and $CO_{2(aq)}$ would have increased the availability of carbon within the cell at a greater rate than through increasing $CO_{2(aq)}$ alone, leading to the greater increase in malformation observed.

In contrast to *C. pelagicus*, *G. oceanica* showed no signs of malformation under increased DIC and $CO_{2(aq)}$. The variation in coccolith malformation across DIC conditions for *C. pelagicus* and *G. oceanica* suggests contrasting controls over their calcification process or perhaps variations in CV $\Omega_{calcite}$ due to variations in pH. Previous work has shown that the CAP produced by *G. oceanica* has a more negative charge under standard conditions than that of *C. pelagicus* (see Chapter 4; [Walker et al., 2018]). A more negative charge may therefore provide a greater barrier to nucleation at higher saturation states. However, new data suggests that the CAP charge changes with DIC concentration, which may complicate the picture further (see Chapter 4). Nonetheless, it appears *G. oceanica* exerts a greater control over intracellular calcification, and perhaps stability of its CV environment, even at higher DIC and $CO_{2(aq)}$ than *C. pelagicus*.

3.4.8. Implications for paleoclimatology and updated presentation of Eocene data

The relationships of $\delta^{13}C_{lith}$ for both *C. pelagicus* and *G. oceanica* with changes in $CO_{2(aq)}$ are in line with that of previous work [Rickaby et al., 2010, McClelland et al., 2017]. Under constant $\Omega_{calcite}$ and variable DIC, coccolithophores appear to exhibit a similar isotopic response to variable DIC under constant pH [Rickaby et al., 2010]. The updated cellular parameters of T_A, T_B and ε_{ef} for *C. pelagicus* and *G. oceanica* provide a more nuanced, species specific approach to modelling pCO_2 given measured carbon isotopic vital effects in the fossil record. Data for *C. pelagicus* is directly applicable to *C. pelagicus* sediment

samples, whilst the parameters for *G. oceanica* can be extended for sediment samples containing the abundant Reticulofenestra coccoliths.

Using updated and re-constrained cellular parameters for *C. pelagicus* and *G. oceanica*, the optimisation routine from chapter 2 was rerun to remodel pCO_2 and R_{calc}:R_{fix} (Fig. 3.19). Consistent across the original model with the updated simulation is a trend from higher relative CO_2 in the early Eocene to lower CO_2 in the middle-late Eocene. However, When cellular parameters constrained for *C. pelagicus* and *G. oceanica* were used to rerun the data from chapter 2, predicted values for R_{calc}:R_{fix} were lower for all genera than compared to the run with the original parameters. Given updated cellular parameters result in lower R_{calc}:R_{fix}, smaller and more variable CO_2 values are also required to recreate the given expression in CIVEs (e.g compare Fig. 3.19B with 3.19H), although as stated previously the overall trend remains.

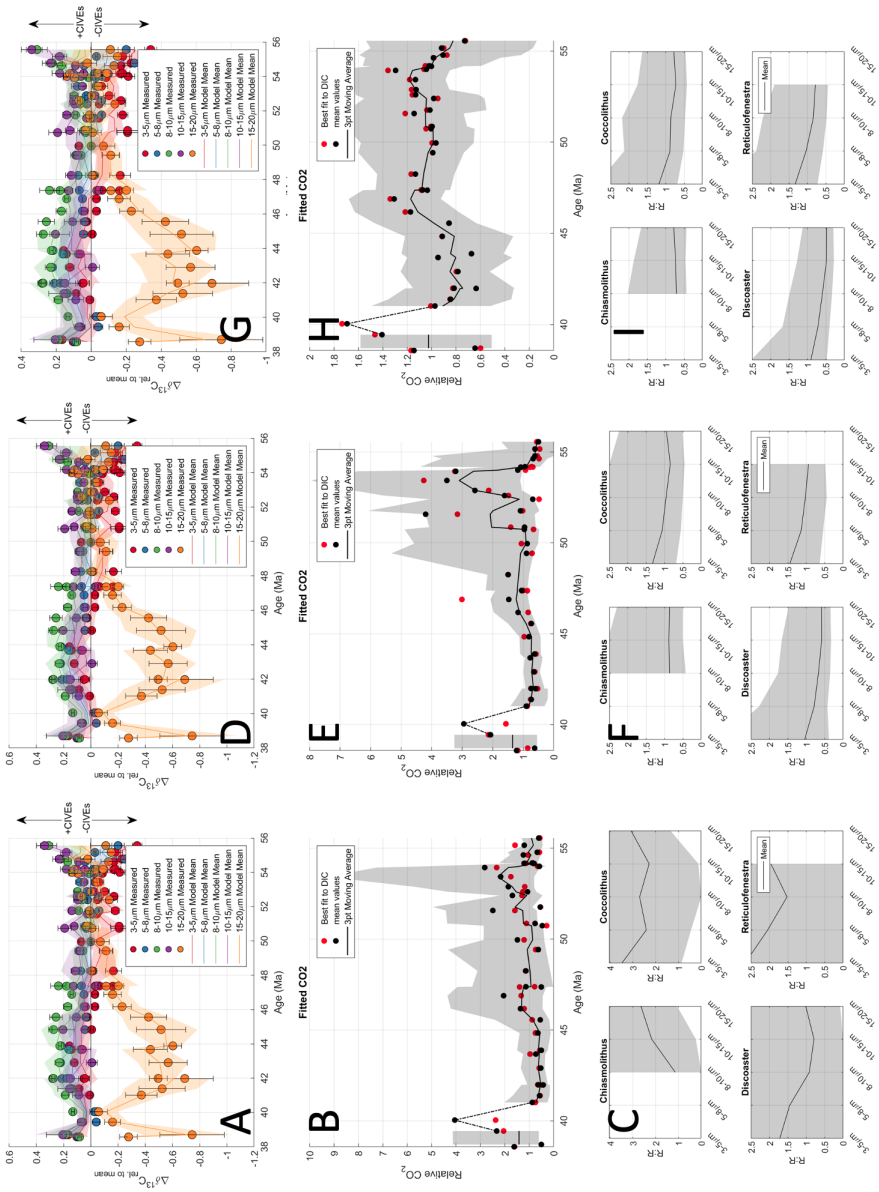

Figure 3.19: The optimisation routine from chapter 2 was rerun 1,000 times with the original cellular parameters define in McClelland et al. [2017] (**A-C**), 1,000 times with the updated cellular parameters constrained for *C. pelagicus* (**D-F**), and 1,000 times for the updated cellular parameters constrained for *G. oceanica*. Whilst CIVE figures (**A,D,G**) show similar fits, the absolute magnitudes of relative CO_2 and R_{calc}:R_{fix} are lower for the updated model parameters. Shaded regions (coloured in **A,D,G** and grey in **B,C,E,F,G,I**) encompasses 95% of all model runs across 1,000 iterations of the model.

Recalibration suggests that ancient cells had a lower R_{calc}:R_{fix} than orignally predicted. Whilst lower absolute R_{calc}:R_{fix} has implications in terms of absolute volumes of alkalinity sequestered relative to organic matter fixation, the trends between genera are robust across all model arrangements. The conclusion that there is a transition from lightly calcified coccolithophores (Discoaster) to more heavily calcified coccolithophores (Coccolithus) across the Eocene is therefore still valid. The conclusion that the increase in calcification led to a negative feedback on a declining carbonate compensation depth is also still supported by the updated model runs. A caveat is that both model reruns assign all Eocene species firstly with cellular parameters calibrated for *C. pelagicus* (e.g Fig. 3.19D-f) and subsequently for *G. oceanica* (e.g. Fig. 3.19G-I). Each rerun therefore represents an end case scenario whereby all ancient cells are assumed to be similar to *C. pelagicus* or *G. oceanica*. Future work should update the model so that each species can have individually prescribed cellular parameters.

In order to reliably recreate past pCO_2 the development of a method to reconstruct R_{calc}:R_{fix} is needed. In doing so the number of parameters to constrain will be significantly reduced and more reliable estimates of CO_2 can be made. Alternatively more reliable estimates of CO_2 will permit better constrained R_{calc}:R_{fix} values.

3.5. Conclusion

We have shown that the response of coccolith carbon isotopic values for both *C. pelagicus* and *G. oceanica* with varying DIC and pH under constant Ω_{calcite} are remarkably consistent with previous studies. The work presented here therefore validates the use of the CIVE based proxy through at least the Cenozoic where Ω_{calcite} was thought to be approximately constant. This study further suggests that species specific variations in $\delta^{13}C_{\text{lith}}$ values, whilst driven by PIC:POC and intracellular fluxes, may be further determined by variations in T_A ,T_B and ε_{ef}. Results suggest that larger *C. pelagicus* is more permeable to HCO_3^- than *G. oceanica* under all carbon conditions, likely owing to its larger carbon demand. Meanwhile, *G. oceanica* has a scaleable permeability to HCO_3^- resulting from the upregulation of HCO_3^- transporters at lower external $CO_{2(aq)}$ making it a low $CO_{2(aq)}$ specialist. *C. pelagicus* may also have a more variable CV pH, however, this is yet to be confirmed with *in vivo* measurements. Model investigations in which CV pH is not held constant should be the target of future work. Realised values of ε_{ef} also appear to be

species specific with that of *C. pelagicus* greater than that of *G. oceanica*. The ability of *G. oceanica* to upregulate its number of HCO_3^- transporters at low carbon availability in additional to its reduced carbon demand, may explain the widespread distribution during the current low CO_2 world compared to the restricted environments in which *C. pelagicus* lives.

The lack of malformation, constant $\delta^{13}C_{lith}$ and constant $\delta^{18}O_{lith}$ values observed within *G. oceanica* are in stark contrast to *C. pelagicus* and suggest that it has a more controlled CV environment in terms of pH and carbon fluxes. The mechanism that results in such a controlled CV remains to be determined and should be the target of future work, however, the controlled CV likely, in part, derives from its lower carbon demand. In this model CA was assumed to be equally distributed throughout the cell. However, in practice CA may be localised at the site of calcification or organic matter fixation. Future work should assess the possibility of localised CA activity and whether P_{Ccell} scales with carbon utilisation. Ultimately, the updated cellular parameters stated here will help to improve the reliability of future predicted CO_2 values using inverse modelling of $\delta^{13}C_{lith}$ values from species-specific sediment samples.

Chapter 4

Exploring the chemistry of CAPs as a proxy for pCO_2

Abstract

The most robust method to reconstruct past variations in the partial pressure of atmospheric CO_2 (pCO_2) is through analysing gaseous mixing ratios in air bubbles trapped in ice cores. Yet, ice core records only extend to around 800,000 years into the past. Beyond the use of ice cores we must turn to pCO_2 proxies. However, pCO_2 proxies such as those based on the isotopic composition of alkenones require constraints on the producers cellular physiology and the isotopic composition of contemporaneous seawater. Developing novel pCO_2 proxies that requires fewer assumptions is therefore the ultimate goal for paleoclimate researchers. Recent studies have suggested that the chemical composition of coccolith associated polysaccharides (CAPs), molecules that assist with coccolith formation, produced by coccolithophores may inform on pCO_2. Here I extract CAPs from *Coccolithus pelagicus* and *Gephyrocapsa oceanica* grown under variable carbon availability and investigate corresponding changes in their chemical composition. I find that both species alter their CAP chemical composition with changing carbon availability. Common amongst both species was a shift to a lower uronic acid content with increasing carbon availability, challenging the hypothesis that higher pCO_2 goes hand in hand with a higher uronic acid content. The ratio of six carbon monosaccharides to five carbon monosaccharides (6C/5C) also appeared to increase within increasing carbon availability in the species *C. pelagicus*. Changes in monosaccharide composition are suggested to be driven

by variable enzyme activities and may reflect a requirement to adapt CAP conformity to assist with calcification under changeable conditions. Variations in 6C/5C were also found in CAPs extracted from the sedimentary record that varied, in part, as a function of carbon availability. Culture and sedimentary work presented here sets the foundations for the use of 6C/5C based $p\mathrm{CO}_2$ proxy.

4.1. Introduction

4.1.1. The Biochemical signal of Ancient Life

The local environment in which an organism lives influences the biochemistry of its molecular structure and composition. If biological components that respond to environmental change are preserved within the sedimentary record then geologists can interpret their biochemical signals to reconstruct past environmental conditions. However, organic molecules are usually found dissociated within the sediment or suffer degradation over time, limiting our insight into the organism and its contemporaneous environment. Organic molecules with a tightly constrained origin that are well preserved within the sedimentary record are thus highly sought after in the geochemistry world.

Fossilised remains of ancient organisms have the potential to trap and preserve organic molecules. Identifiable fossilised remains allow for tighter constraints to be placed on the origin of associated organic molecules and enable species specific attributes to be inferred that further assists with the explanation of biochemical signals.

Coccoliths, calcite plates produced by coccolithophores, have been well preserved within the sedimentary record for at least the last 200-million years and are known to contain organic molecules within their calcite lattice [Bown et al., 2004, Henriksen et al., Lee et al., 2016]. Coccoliths are formed internally within a golgi-derived vesicle, referred to as the coccolith vesicle, before being extruded to the surface of the cell [Marsh, 2003]. To assist with calcification coccolithophores produce coccolith associated polysaccharides (CAPs), which are believed to contribute to calcite nucleation and dictate coccolith morphology [Gal et al., 2016, Kayano et al., 2011, Ozaki et al., 2004]. As the coccolith grows, the CAP becomes entombed within the calcite crystalline structure and, as a result, can be well preserved in the sediment[1]. CAPs are directly extracted from coccoliths, which have

[1] assuming the coccolith avoids dissolution

distinct geographical distributions and can be separated in to species specific size fractions. CAPs therefore have the potential to provide insight into ancient coccolithophores and their contemporaneous environment with coccolith isotopic analysis and morphometry providing further insight [Bolton and Stoll, 2013b, Tremblin et al., 2016, McClelland et al., 2017, Beaufort et al., 2011].

4.1.2. The Role of coccolith associated polysaccharides in coccolithophore calcification

Although CAPs were first identified and studied in the 1970's, how they are produced and how their chemical composition varies between species remains poorly understood [Jong et al., 1976, Borman et al., 1987, Marsh et al., 2002, Lee et al., 2016, Walker et al., 2018]. The functional role of CAPs in coccolith formation is not universal between, or even within, species. For example, *Pleurochrysis carterae* is known to produce three CAPs: PS1, PS2 and PS3. PS1 and PS2 are thought to be associated with Ca^{2+} transport and calcite nucleation, whilst PS3 is believed to control coccolith morphology through binding to steps of calcite crystals [Marsh et al., 1992, 2002, Kayano et al., 2011]. *Emiliania huxleyi* meanwhile is thought to only produce a single CAP and is believed to be functionally similar to PS3 [Ozaki et al., 2004]. More recent work by Walker et al. [2019] found that whilst CAPs extracted from *E. huxleyi* inhibited all forms of carbonate formation, CAPs extracted from *Gephyrocapsa oceanica* actively promoted the nucleation and growth of calcite crystals over the polymorphs aragonite and vaterite.

To date, the most extensively studied CAP, in terms of structure and chemistry, derives from *E. Huxleyi*. CAPs extracted from *E. huxleyi* consist of a mannose backbone with complex side-chains containing galacturonic and glucuronic acid and ester-bound sulfate groups [Fichtinger-Schepman et al., 1981, Henriksen and Stipp, 2009]. The negatively charged uronic acids are thought to be responsible for binding Ca^{2+}, which likely inhibits the deposition of calcium carbonate crystals on the growing crystal [Borman et al., 1982, Sand et al., 2014]. The uronic acid component additionally likely binds to Ca^{2+} ions in solution, thus altering the carbonate saturation state ($\Omega_{\text{calcite}} = [Ca^{2+}][CO_3^{2-}])/K_{sp}$, where K_{sp} is the solubility constant of calcite) of the coccolith vesicle, affecting crystal growth indirectly [Sand et al., 2014].

Additional *in vitro* studies have sought to elucidate the role of CAPs in controlling

calcification. Polysaccharides with regularly repeating monosaccharide backbones and simple functional groups, thought to reflect the composition of CAPs, were found to present varying barriers to calcification based on their overall charge or uronic acid content (UAC) [Giuffre et al., 2013]. More negatively charged molecules (higher UAC) created greater thermodynamic barriers to nucleation. The barrier was purported to derive from a more hydrophilic nature creating a stronger substrate-water interface and a greater barrier to forming a substrate-crystal interface [Giuffre et al., 2013]. Neutrally charged molecules provided the lowest thermodynamic barrier to forming a substrate-crystal interface.

In addition to CAP chemistry, the calcifying solution has been shown to be important in the formation of calcite. At high Ω_{calcite}, CAPs with a higher UAC were found to promote faster nucleation rates [Giuffre et al., 2013]. Other components of the media such as the Mg^{2+} concentration have also been shown to alter how CAPs bind to the growing calcite crystal [Henriksen and Stipp, 2009, Sand et al., 2017].

4.1.3. The chemical composition of CAPs as a proxy for pCO_2

Using *E. huxleyi* cells derived from open ocean locations with varying $CO_{2(aq)}$ concentrations. Lee et al. [2016] suggested that an increase in the UAC of CAPs may indicate a corresponding rise in pCO_2. Moreover, the trend in UAC through time was shown to generally track changes in pCO_2, although periods during the Cenozoic showed only trace levels of uronic acid when pCO_2 was thought to be higher than modern day ([Lee et al., 2016]; Fig. 4.1). No additional studies have investigated the applicability of a UAC based pCO_2 proxy. In order to validate the applicability of a potential UAC based pCO_2 proxy, additional *in vivo* experiments are needed on multiple, geologically relevant species. Such experiments will help to determine the control of carbonate chemistry on the UAC of CAPs and how the response varies across species.

4.1.4. Aims, objectives and hypotheses

This study seeks to determine whether the chemical composition of CAPs for the species *Coccolithus pelagicus ssp braarudii* and *Gephyrocapsa oceanica* vary under standard and high DIC conditions. Additional measurements will be made on size separated coccolith sediment samples spanning the early and middle Eocene from IODP leg 208, Site 1263. Sediment samples will be investigated in an attempt to understand any CAP chemistry

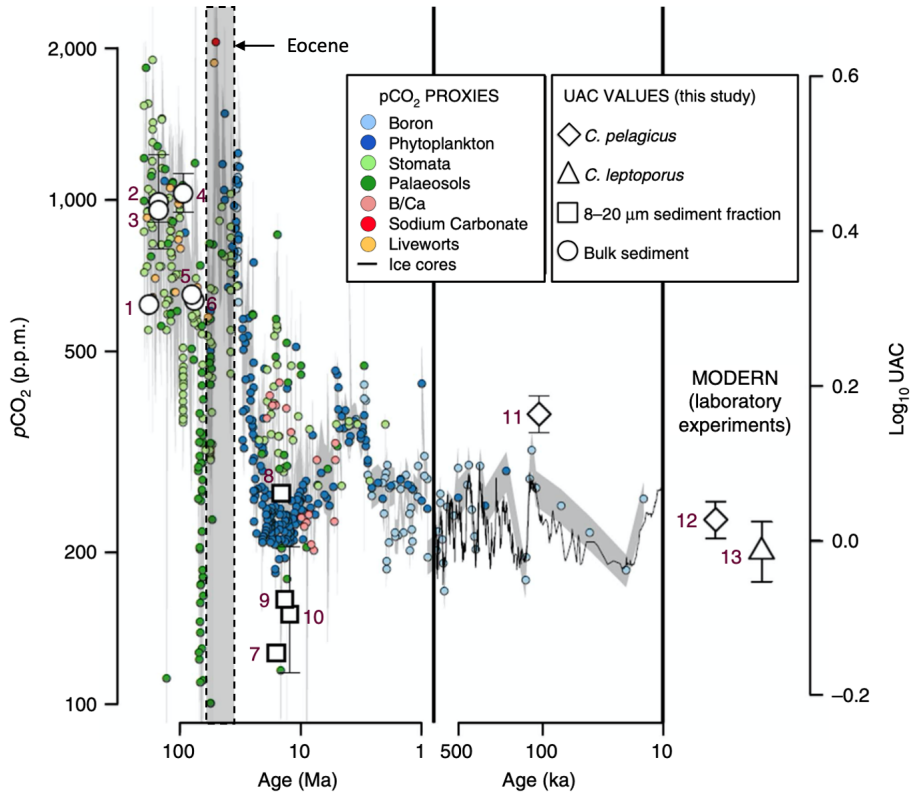

Figure 4.1: The average UAC of samples from modern Coccolithales (the order of which *C. pelagicus* belongs; points 12 and 13), C. pelagicus from the Upper Pleistocene sediments (point 11) and Neogene sediments (points 7–10). Prehistoric predecessors of the Coccolithales from bulk fossil samples are also shown (points 1–6). Established CO_2 proxy data is given by the coloured markers. The grey lines represent the range of CO_2 as estimated from proxies and ice core data (to 1σ). Highlighted in the grey box is the Eocene period (56 - 34Ma). Figure modified from [Lee et al., 2016].

variation, in particular UAC, in the context of contemporaneous environmental change and coccolithophore species variation. The Eocene epoch (approximately 56-34 million years ago (Ma)) was characterised by warmer temperatures and higher concentrations of atmospheric CO_2 than present day (the Eocene was introduced in chapter 2 and is thus not reintroduced here; Fig. 4.1). The Eocene is therefore a promising target to test the validity of a CAP chemistry based pCO_2 proxy given the abundance of the extant species *Coccolithus pelagicus* [Bordiga et al., 2015] and corresponding CO_2 reconstructions from chapter 2.

Table 4.1: Experimental carbonate conditions for cultures grown under standard DIC conditions (Experiment 1) and high DIC conditions (Experiment 2).

Experiment	DIC (μmol/KgSW)	pH	$CO_{2(aq)}$ (μmol/KgSW)
1	2300	8.10	15
2	5023	7.75	75

4.2. Methods

4.2.1. Culture Conditions

Gephyrocapsa oceanica and *Coccolithus pelagicus ssp braarudii* were grown under a 16:8 h light-dark cycle, 100 μmol photons m^{-2} s^{-1} at 15°C and 20°C respectively with controlled carbonate chemistry and nutrients. Standard dissolved inorganic carbon (DIC; experiment 1) and elevated DIC (experiment 2) conditions were targeted (Table 4.1). For experiment 1, which was in equilibrium with the atmosphere, all salts were initially added to de-ionised milli-Q water to create synthetic ocean water after Keller et al. [1987]. Filter sterile nutrients were added according to modified K/2 media ($NaNO_3$ modified to 4.4 x 10^{-4}mol L^- and Na_2.glycero.PO_4^{3-} to 5x10^{-6}mol L^-; Keller et al. [1987]). Media was stored in autoclaved culture vessels prior to inoculation. For experiment 2, salts with the exclusion of $NaHCO_3$, were added to de-ionised milli-Q water to make synthetic ocean water after Keller et al. [1987]. The media for experiment 2 was brought to pH 3 using 1M HCl, conditions under which 99% of DIC will be in the form of $CO_{2(aq)}$ [Zeebe and Wolf-Gladrow, 2001]. The solution was then bubbled over night with air to remove $\geq$ 99% of DIC. The solution was filter sterilised (0.2μm) before adding $NaHCO_3$ to target DIC concentrations (Table 4.1). pH was adjusted via the addition of 1 M HCl. Filter sterile nutrients were added according to modified K/2 media in line with experiment 1. Culture vessels from experiment 2 were stored without headspace in 2.4-L polycarbonate bottles.

4.2.2. Sediment Samples

12 size separated sediment samples from the Eocene were also prepared for CAP extraction. The sediment samples are as detailed in chapter 2 and a subset of those in appendix A.1. Sample preparation, size separation, age models and nannofossil abundance are identical to that listed in chapter 2. The 12 sediment samples were selected from the filtered 3-5μm

Table 4.2: Sediment Sample List from expedition 208, site 1263 used for CAP chemistry analysis.

Hole	Core	C-Type	Sec.	Age	Age model reference
B	7	H	3	38.701	[Rivero-Cuesta et al., 2019]
C	3	H	4	39.441	[Rivero-Cuesta et al., 2019]
A	15	H	6	41.385	[Rivero-Cuesta et al., 2019]
A	16	H	1	41.987	[Westerhold et al., 2015]
B	11	H	3	42.904	[Westerhold et al., 2015]
A	17	H	6	43.882	[Westerhold et al., 2015]
A	18	H	5	44.832	[Westerhold et al., 2015]
B	14	H	3	46.171	[Westerhold et al., 2015]
A	22	H	3	49.421	[Lauretano et al., 2016]
A	27	H	3	52.881	[Lauretano et al., 2016]
C	9	H	7	53.430	[Lauretano et al., 2016]
C	10	H	7	54.167	[Lauretano et al., 2016]

size fractions to provide a low resolution slice through the Eocene (table 4.2).

4.2.3. CAP extraction

Cultures were harvested via centrifugation at 3000g for 10 minutes to pellet the organic matter and coccoliths. Culture pellets were washed with 10ml 1% Triton-X100 in 0.05M $NaHCO_3$ and 6ml 12% NaOCl to remove organic matter. The cleaned coccolith pellet was centrifuged through a gradient of 100ml LUDOX TM-50 colloidal silica (Sigma-Aldrich) and 25ml 20% weight/volume sucrose at 23,000g for 20 minutes to remove any remaining organic matter. The denser coccolith fraction collected at the bottom whilst less dense organic matter remained in the supernatant. The resulting pellet was rinsed with 0.05M NH_4HCO_3 three times to remove any residual LUDOX. 0.5M EDTA in DI water at pH 8 was then added to the cleaned coccolith pellet to decalcifiy the coccolith overnight. The resulting solution was sonicated and then centrifuged at 31,000g for one hour to remove any insoluble residue. The supernatant, containing the soluble CAPs was then passed through a Mersk Amicon Ultra-4 centrifugal filter (10 kDa cutoff) to remove molecules $\leq$ 10 kDa and allow for buffer exchange with 20mM Tris-HCl (pH 8). The supernatant was then passed through a Hi-Trap DEAE FF (GE Healthcare) column for anion exchange liquid chromatography according to the manufacturers instructions. The CAP was eluted using 0.5M NaCl before using a further 10 kDa Amicon Ultra-4 centrifugal filter to concentrate the acidic polysaccharide into ultrapure de-ionised water. CAP samples were stored in a -20°C freezer prior to analysis.

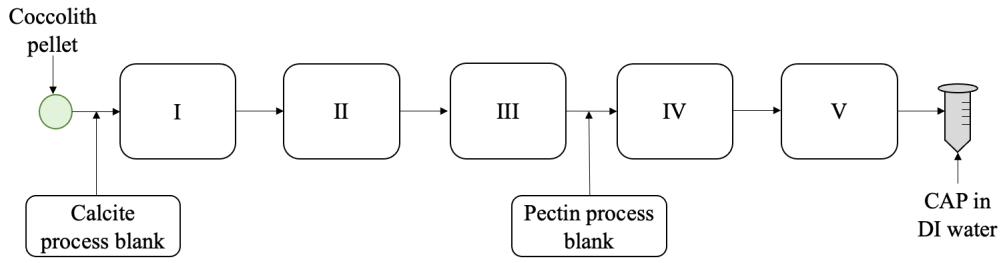

Figure 4.2: The schematic above summarises how blanks were introduced during the extraction process. The CAP pellet was first washed with Triton-X100 in $NaHCO_3$ and NaOCl (I), before passing through a centrifugal ludox gradient (II). The pellet was then decalcifed with 0.5M EDTA (III) before passing through anion-exchange columns to extract the acidic polysaccharides (IV). The CAP then underwent buffer exchange via a 10 kDa filter (V) before being stored in ultra-pure DI water. Calcite process blanks underwent steps I-V and apple pectin process blanks are introduced after step III.

4.2.4. CAP quantification

Prior to sending CAPs for GC-MS analysis, polysaccharide presence was confirmed via the use of a phenol-H_2SO_4 assay with a glucose standard. 10μl of each sample with 90μl of DI water was reacted with 500μl 4% phenol and 2.5ml 96% H_2SO_4. After 30 minutes the absorbance of the solution was measured on an ultraviolet-spectrophotometer at 490nm wavelength. Pure DI water was treated in the same way and used as a control. Absorption values for samples greater than that of DI water confirmed the presence of polysaccharides.

4.2.5. Blanks and Standards

Process blanks were run alongside samples to investigate whether contamination occurred during the CAP extraction procedure (Fig. 4.2). Powdered apple pectin (Sigma, reference number 76282-100G) was dissolved in ultra pure 18mΩ water to target concentrations of 0.1μg pectin μl^{-1}. The pectin process blank was run in parallel from the first filtration step through the Amicon Ultra-4 centrifugal filter (step III, Fig. 4.2). A pure calcite process blank ($\geq$ 99%, Sigma, reference number 239216-100G) underwent all steps. The pectin process blank was compared with an unprocessed pectin standard to determine whether the procedure altered the chemistry of the samples. The calcite process blanks acted as a true blank.

4.2.6. CAP TFA Hydrolysis and Sample Derivatisation

Extracted CAPs from culture and sediment samples were sent for chemical analysis at the University of Exeter. Prior to chemical analysis, CAP samples were hydrolysed by heating to 105°C for 2h in the presence of 2M trifluoroacetic acid (total volume 200μl). 10μl of 1mM myoinositol was added as the internal standard. The samples were then dried down using an evaporator (GeneVac EZ-2). To derivatise samples, 20μl of 20 mg ml^{-1} methoxyamine hydrochloride dissolved in pyridine was added to each sample before incubation at 37°C for 2h. 30μl of N-methyl-N-trimethylsilyltrifluoroacetamide (MSTFA) was added and the samples returned to 37°C for a further 30 min. Blanks (TFA only), controls (pectin and calcite) and sugar standards were treated in the same way, along with a derivatisation agent only blank. Sugar standards included D-glucose, D-galactose, D-mannose, D-xylose, D-arabinose, L-fucose, D-galacturonic acid, D-glucuronic acid, L-rhamnose, glycerol, D-fructose, levoglucosan and L-ribose. Derivatising agents and standards were all purchased from Sigma-Aldrich, UK.

4.2.7. Gas Chromatography-Mass Spectrometry (GC-MS)

Derivatised samples were analysed using an Agilent 7200 series accurate mass Q-TOF GC-MS together with a 7890A GC system (Agilent Technologies, Santa Clara, USA), equipped with an EI (electron ionisation) ion source. 0.6μl of each sample was injected into a non-deactivated, baffled glass liner with a 12:1 split ratio (14.448 ml min^{-1} split flow) and the inlet temperature was maintained at 300°C. A 3 ml min^{-1} septum purge flow was applied. A Zebron semi-volatiles (Phenomenex, Torrance, USA) column (30 m x 250μm x 0.25μm) coupled with a 10m guard column, was maintained at a constant helium flow of 1.2 ml min^{-1}. The temperature gradient of the GC was ramped up at a rate of 15°C min^{-1}, from 70°C to 310°C over 16 min, and held at 310°C for a further 6 minutes. The total run time of 22 min, was followed by a 7 min backflush at 310°C to clean the column at the end of every run. The MS emission current and emission voltage were held at 35μA and 70 eV respectively, and the MS was automatically calibrated after every run. The mass range was set from 50 to 600 amu, with an acquisition rate of 5 spectra s^{-1}, and a solvent delay of 5 min. Hexane and extraction solvent blanks were run at the beginning and end of the run. Data were analysed using Agilent technologies MassHunter qualitative

and quantitative software.

GC-MS analysis provided normalised peak areas for each sugar and is a unit-less quantity. The magnitude of the normalised peak area reflects the sugar abundance within samples or blanks. All samples were blank corrected based on measurements for the calcite process blank. Given the low yield of CAPs extracted, repeat measurements could not be conducted nor could the absolute concentration of CAPs be determined. The concentration of monosaccharides per CAP were therefore unable to be determined. In this chapter monosaccharide abundances are presented as a percentage peak area:

$$P_s = \frac{N_s}{\sum_{i=1}^{I} N_i} \times 100 \tag{4.1}$$

Where P_s is the % peak area of monosaccharide s and N_s represents the measured normalised peak area for monosaccharides. i represents individual monosaccharides and $i \in \{1 : I\}$ where I is equal to the total monosaccharides included in the analysis and is equal to 10 (rhamnose, fucose, xylose, arabinose, ribose, glucose, galactose, mannose, galacturonic acid and glucuronic acid). Percentage peak area allows comparison between studies and removes the dependence on the absolute concentration of CAPs in each sample.

4.3. Results

4.3.1. CAP quantification and GC-MS analysis

The phenol-H_2SO_4 assay returned non-zero values for absorbance at 490nm wavelength for all samples and the pectin process blank confirming the presence of polysaccharides. The absorption for the calcite process blank was indistinguishable from the water control. Subsequent GC-MS analysis showed the presence of rhamnose, fucose, xylose, arabinose, ribose, glucose, galactose, mannose, galacturonic acid and glucuronic acid for CAPs extracted from cultures (Fig. 4.3). Glycerol was also detected for modern day culture samples, the pectin and calcite process blanks. Given the two blanks should not contain glycerol, the presence of glycerol was deemed to be anomalous. Given the uncertainty regarding its origin, the presence of glycerol was not included within the % peak area calculations and interpretations (see section 4.4.1 for the discussion of glycerol's presence).

For *C. pelagicus* large increases in monosaccharides rhamnose and galactose were ob-

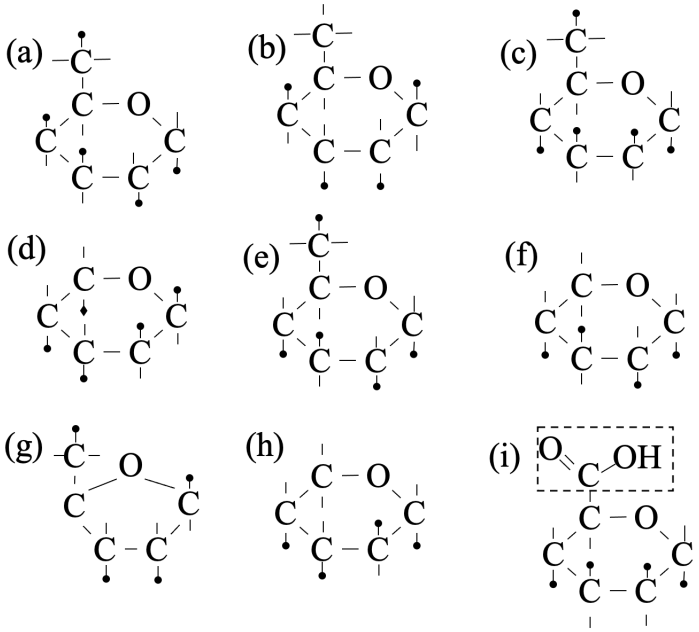

Figure 4.3: Molecular structures are shown for galactose **(a)**, rhamnose **(b)**, mannose **(c)**, fucose **(d)**, glucose **(e)**, xylose **(f)**, ribose **(g)**, arabinose **(h)** and galacturonic acid **(i)**. | indicates a bond to H, whereas | with a • represents a bond to OH. The ♦ in **(d)** represents a downward methyl group not drawn due to space constraints. The dotted box in **(i)** represents a carboxylic group. **(a-e)** contain six carbon atoms, whilst **(e-g)** contain five carbon atoms.

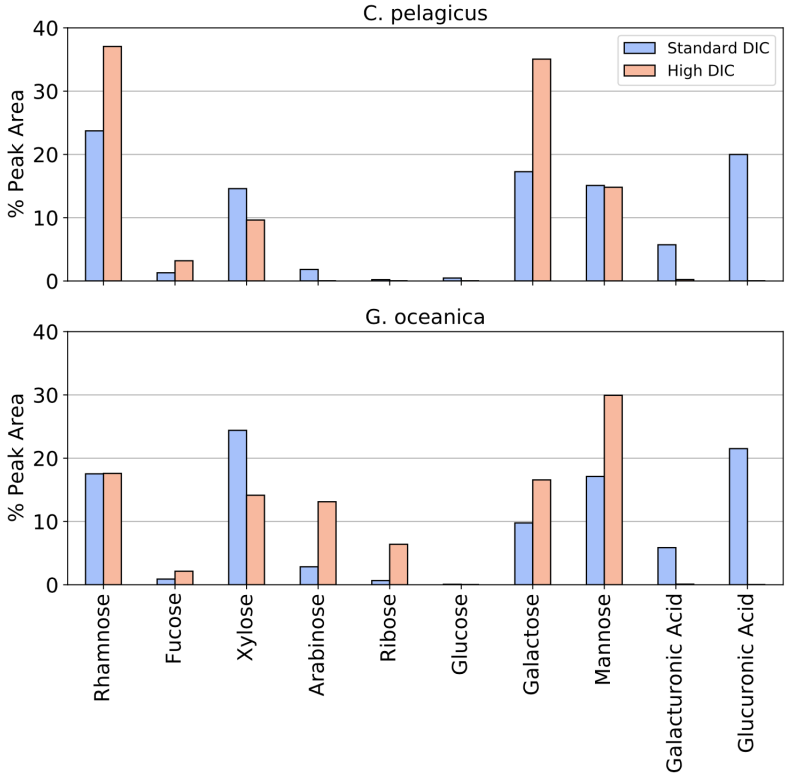

Figure 4.4: Percentage peak area calculated for each monosaccharide for *C. pelagicus* and *G. oceanica*. Data is shown for CAPs extracted from cultures under standard conditions (blue) and high DIC conditions (red).

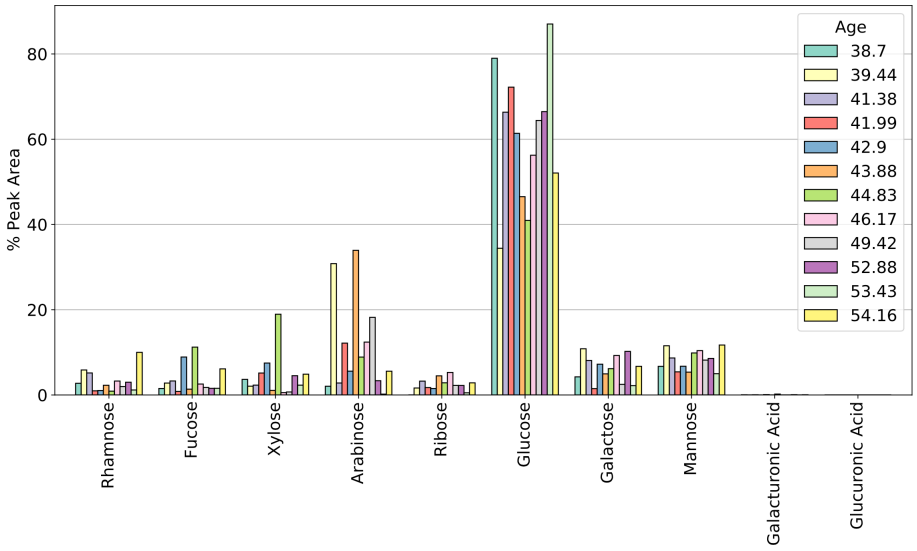

Figure 4.5: The chemical composition for the 12 3-5μm size fractions excluding measured glycerol. The colours of the bars represent the age of each sample (see A.1 for sample names).

served from standard DIC to high DIC conditions (experiment 1 and 2 respectively). Both galacturonic and glucuronic acid were present at standard DIC conditions, but undetectable at high DIC for both species (Fig. 4.4). For *G. oceanica* large increases in the monosaccharides arabinose, galactose and mannose were observed from standard DIC to high DIC conditions whilst the presence of xylose declined.

GC-MS analysis of the sedimentary samples identified the presence of xylose, arabinose, ribose, fucose, rhamnose, glucose, galactose, mannose (Fig. 4.5). Trace levels of galacturonic acid was also detected, however the relative percentage abundance was less than in culture experiments. Sediment samples also showed a large GC-MS normalised peak area with the same retention time and fragment pattern to glycerol. The sediment samples' glycerol normalised peak area was two orders of magnitude greater than in the negative controls and culture samples (Fig. 4.6). When the normalised peak area for glycerol was included in the relative percentage peak area calculations for sediment samples, glycerol accounted for $\geq 95\%$ relative peak area. In addition to the aforementioned monosaccharides 13 unidentifiable monosaccharides were also measured.

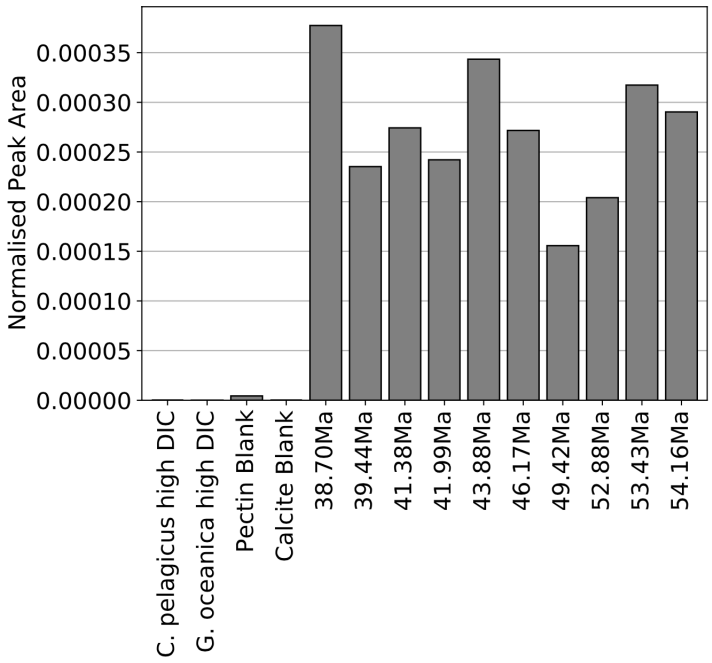

Figure 4.6: The normalised peak area of glycerol is shown for process blanks and samples from a single GC-MS run. The normalised area is a unit-less metric. The samples shown here are a subset of the 12 Eocene sediment samples as multiple runs were performed. Normalised peak area only provides a comparison within and not between runs.

4.4. Discussion

4.4.1. On the presence of glycerol

Previous studies into the chemical composition of CAPs make no mention of glycerol and so its presence here is perplexing [Fichtinger-Schepman et al., 1981, Marsh et al., 1992, Walker et al., 2018]. In order to identify whether glycerol was a true signal or a source of contamination four hypotheses are presented to test: **(1)** glycerol derives from contamination during measurement on the GC-MS; **(2)** glycerol derives from contamination during the CAP extraction procedure; **(3)** glycerol is a true signal preserved within the sediment, but is not associated with the CAP; and **(4)** glycerol derives from the sediment samples, was produced by coccolithophores and is associated with the CAP.

Hypothesis **(1)** was ruled out based on the glycerol normalised peak area being below the detectable limit for the GC-MS derivatising agent process blanks. The derivatising agent blanks were run before and after sample measurements and hence rule out the cross contamination between samples.

In order to test hypothesis **(2)** the calcite and pectin process blanks normalised peak

area was investigated. The calcite process blank contained trace signals of glycerol and, although the pectin blank possessed a larger glycerol normalised peak area than the calcite blank, the signals measured for the sediment samples were orders of magnitude higher (Fig. 4.6). Other monosaccharides compared in this way are of a comparable magnitude, or lower, than the modern day samples and the pectin blank (see appendix A.9). Moreover, all blanks and samples were stored in the same manner suggesting storage did not contribute to the presence of glycerol. Given all samples were processed and stored in the same way, a systematic contamination from the extraction process is difficult to reconcile with the large abundance in sediment samples relative to process blanks and culture samples. Whilst hypothesis **(2)** can not be totally ruled out due to the trace glycerol signature within the process blanks, the difference in absolute magnitudes between the culture samples, process blanks and sediment samples suggests that the dominant source of the glycerol signal is likely associated with the ancient coccolith samples.

Hypothesis **(3)** is more difficult to test. The extraction process removes organic matter from the exterior of the coccolith, thus any organic matter that is measured on the GC-MS likely derives from within the coccoliths crystalline structure. During extraction the organic material released from the dissolved coccoliths is passed through an anion exchange column, which allows the separation of negative and neutral/positively charged molecules. All samples run here derive from the negatively charged fraction. Glycerol, which has no overall charge, is therefore likely forming a more complex macromolecule or compound (e.g. glycoprotein, glycolipid) with an overall net negative charge. The eluted negative fraction is subsequently passed through a 10 kDa filter for buffer exchange to allow for storage in deionised water. The molecule containing glycerol must therefore be strongly associated with a molecule that is $\geq$10 kDa, negatively charged and present within the coccolith crystal lattice.

Possible scenarios in which glycerol may have been incorporated within the crystal lattice, yet not associated with the coccolithophore, are limited, however, may derive from bacterial action. Studies have found complex acidobacteria biomes living on the coccolith surface that potentially utilise CAPs as an energy source [Green et al., 2015]. Multiple acidobacteria result in complex chemical signalling and secondary metabolite production [Green et al., 2015]. Indeed, glycerol is a common product of fermentative metabolism in organisms and could derive from a complex bacterial biome and could

become incorporated within the crystal lattice via intra-crystalline fermentative processes [Catalanotti et al., 2013]. Pure glycerol has no net negative charge and thus would not elute with the negative CAP. Glycerol attached to a polyanionic substance is therefore far more plausible. Polyanionic glycopolymers such as teichoic acid have been found in the cell wall of gram-positive bacteria (e.g. [Edgar et al., 2019]). Teichoic acid provides flexibility to cell walls by attracting cations such as calcium and potassium. Given gram-positive bacteria are present and diverse in marine sediments, it may be possible that such glycopolymers were produced within the coccolith post deposition [Gontang et al., 2007]. Yet, SEM images of the coccoliths prior to CAP extraction show no overgrowth or signs of dissolution, suggesting that coccoliths avoided post burial alteration and that the glycerol containing molecule is likely incorporated into the coccolith during formation either as a molecule assisting with calcification or as a byproduct of ancient coccolithophores life cycle. Alternatively, glycerol could be strongly adsoprbed onto the surface of the coccolith after cleaning, which is then associated with the CAP once the coccolith was dissolved in the EDTA solution.

Recent work has shown that coccolithophores have the ability to take up dissolved organic compounds found in seawater [Godrijan et al., 2020]. In particular, glycerol was shown to be taken up, albeit in small quantities when compared to bicarbonate. Nonetheless, glycerol, could be taken into the cytoplasm to assist with growth during periods of dark. Assuming glycerol is membrane permeable, which is valid given molecules with no net charge can move across membranes by diffusion, glycerol may also pass into the coccolith vesicle, the site of calcification, before being incorporated into the crystal lattice. If the glycerol is combined to form a glycopolymer it could subsequently be both stored within the coccolith and pass through the anion exchange column. However, it seems unlikely that mixotrophy would have resulted in such a large presence of glycerol measured for sediment samples. Moreover, a process by which glycopolymers are made within the CV remain to be identified.

Hypothesis **(4)** is also difficult to test. Nonetheless, it is possible that the CAP involved in calcification during the Eocene was different to modern day species both in terms of composition and function. For example, during the Eocene the now extinct genus of coccolithophore Discoaster was present. Discoaster forms elaborate star shaped coccoliths and no intact coccospheres have ever been found in the sedimentary record. It is possible

that Discoaster used glycerol within its calcification process. Indeed, previous studies have shown that hyperbranched-polyglycerols can affect calcification *in vitro* with the presence of self-assembling monolayers (SAMs) [Balz et al., 2005]. SAMs are chain molecules that possess a functional group at one end and a head group at the other. The head group adsorbs onto molecules with the functional group facing outward. Interaction and control over calcite and aragonite has been shown to depend on the functional group and molecular weight of the polygylcerols [Balz et al., 2005]. SAMs with a carboxyl functional group were shown to control calcite nucleation even when the solution kinetically favoured aragonite precipitation [Balz et al., 2005]. Subsequent work has found that neutral, highly branched polysaccharides could control calcite crystallisation to the same degree as highly charged CAPs [Nielsen et al., 2012]. Discoaster, or other ancient coccolithophores present in the sediments, may be using a hybrid form of CAP whereby the base mannose chain is acting as a SAM and the glycerol is present as a hyperbranched-polyglycerol. Together, the mannose chain and polyglycerol may dictate and inhibit calcification differently than is observed today. Moreover, bound together hyperbranched-polyglycerols and SAMs could make it though the anion exchange columns.

Whilst it is possible to reject hypothesis **(1)** and hypothesis **(2)** is unlikely to be true, it is not possible to reject or accept hypotheses **(3)** and **(4)** with the current data available. Proving or disproving hypotheses **(3)** and **(4)** should be the target of future work. Nonetheless, whilst the source of glycerol remains unclear, it is still possible to investigate the change in % contribution of other monosaccharides within both the culture and sediment samples.

4.4.2. CAP chemistry

Knowledge of CAP chemistry is currently limited to the species *P. carterae* and *E. huxleyi* [Fichtinger-Schepman et al., 1981, Jong et al., 1976, Marsh et al., 1992]. Whilst, *P. carterae* is known to produce three CAPs (PS1, PS2, and PS3), *E. huxleyi* produces one, although it is thought to be functionally similar to PS3 [Marsh et al., 1992, 2002, Ozaki et al., 2004]. The GC-MS analysis conducted as part of this study revealed *C. pelagicus* and *G. oceanica* have a similar chemical fingerprint to CAPs extracted from *E. huxleyi* with mannose, likely the CAP backbone, contributing at least 15% to total CAP peak area ([Fichtinger-Schepman et al., 1981]; Fig. 4.7). The data presented here may therefore

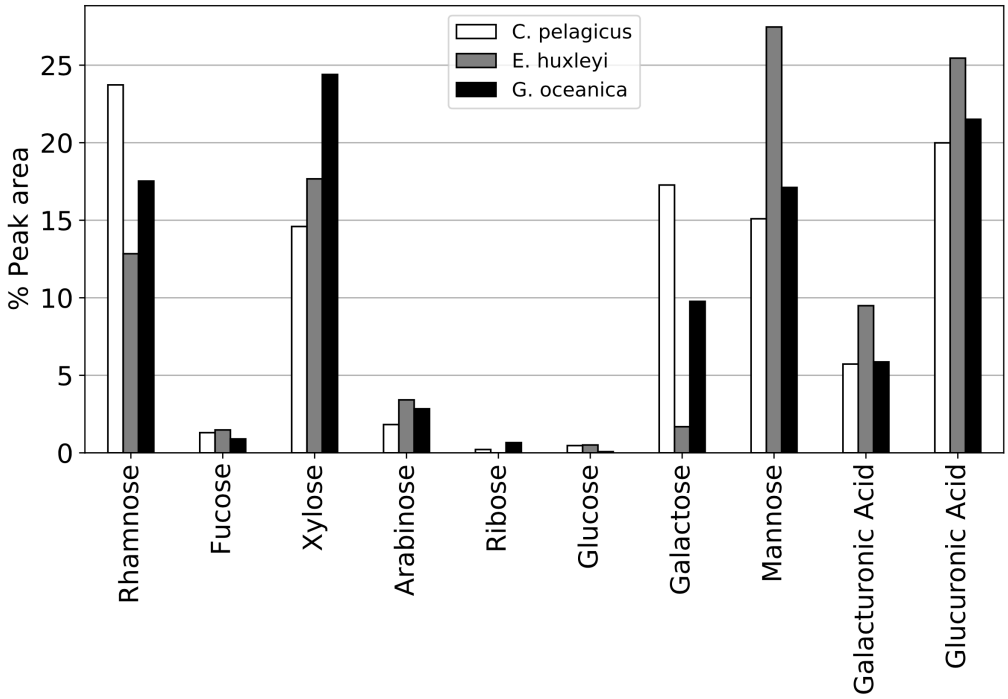

Figure 4.7: The chemical composition is presented for *C. pelagicus* (white), *E. huxleui* (grey) and *G. oceanica* (black) measured under standard DIC conditions. Under standard DIC conditions, there is a large presence of mannose, believed to be the CAP backbone, and galacturonic and glucuronic acid, believed to be involved with controlling calcification. *E. huxleyi* CAP data from culture experiments performed under standard conditions by Renee Lee.

suggest that the CAPs produced by *C. pelagicus* and *G. oceanica* under standard DIC conditions is similar in function to PS3, the coccolith morphology dictating CAP [Marsh et al., 2002].

4.4.3. Response of CAP chemistry to elevated CO_2 in culture

Whilst studies have investigated the interaction of CAPs and calcite with differing external media conditions, there is a lack of data on how, and indeed if, CAP chemistry varies in tandem (e.g. [Borman et al., 1982, Henriksen and Stipp, 2009, Sand et al., 2017]). Although there is a paucity of data for CAPs, comparable studies exist for chemically similar, soluble cell wall polysaccharides and soluble external polysaccharides in green microalgae, Rhodophyta and cyanobacterium [Cheng et al., 2014, Li et al., 2000, Han et al., 2017]. Indeed, algal cells produce cell walls that contain pectin and are polysaccharide rich [Caffall and Mohnen, 2009, Popper and Tuohy, 2010]. Cell wall pectin is both soluble, and given its negative charge deriving from the presence of uronic acids, can bind Ca^{2+} [Caf-

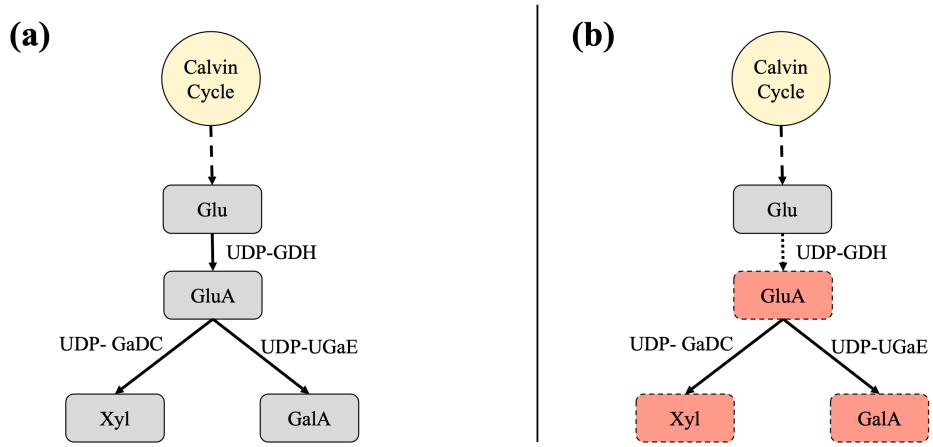

Figure 4.8: A potential pathway for the creation of glucuronic acid (GluA), galactouronic acid (GalA) and xylose (Xyl) downstream of the calvin cycle and glucose (Glu) under standard DIC **(a)** and high DIC **(b)**. Also shown are the potential enzymes that may be dictating monosaccharide expression. UDP-GDH: UDP-glucose dehydrogenase, UDP-UGaE: UDP-galacturonic acid-4-epimerase and UDP-GaDC: UDP-glucuronic acid decarboxylase. Red boxes in **(b)** represent a decrease in measured % peak area (red boxes also have a dashed border). Dotted arrows represent a hypothesised decrease in enzyme activity.

fall and Mohnen, 2009]. Studies into a genus of green microalgae, *Chlorella*, have shown that the UAC of soluble cell wall polysaccharides increased with increasing CO_2 [Cheng et al., 2014]. Cheng et al. [2014] linked the increase in UAC to an increase in the activity of uridine diphosphate (UDP)-glucose dehydrogenase, an enzyme that catalyses the conversion of glucose into glucuronic acid. Han et al. [2017] also finds a significant, positive correlation between UDP-glucose dehydrogenase and the UAC of external polysaccharides produced by the cyanobacteria *Nostoc flagelliforme*. Yet, whilst Cheng et al. [2014] notes UDP-glucose dehydrogenase increases activity under greater carbon availability, Han et al. [2017] observes the opposite, resulting in a decline in UAC with increasing CO_2 availability. Data presented here shows that in a higher DIC environment both *G. oceanica* and *C. pelagicus* reduced their UAC. It is therefore possible that under higher DIC and lower pH conditions a decline in the activity of UDP-glucose dehydrogenase results in a reduced UAC for both species, in line with Han et al. [2017] (Fig. 4.8). We note that, whilst our results show that glucose % peak area remains low under standard and high DIC conditions, its absence within the CAP does not preclude its presence within the wider cell and its availability for conversion to downstream products.

Other enzymes may play an additional role in controlling CAP chemistry. Galacturonic acid is formed from glucuronic acid via the enzyme UDP-galacturonic acid 4-epimerase.

UDP-glucuronic acid decarboxylase meanwhile catalyses the conversion of glucuronic acid into xylose and has been shown to alter the chemical structure of hemicellulose, a matrix, cell wall polysaccharide, in tobacco plants [Bindschedler et al., 2007]. A decline in glucuronic acid and xylose was observed in both *G. oceanica* and *C. pelagicus* and may be linked to the decreased availability of glucuronic acid subsequently available for conversion to xylose via UDP-glucuronic acid decarboxylase (Fig. 4.8). Shifting enzyme activities under greater carbon availability may therefore contribute to the changing abundances of glucuronic acid, galacturonic acid and xylose (Fig. 4.8). Additional cellular pathways and enzymes within the cell may be contributing to other monosaccharide variations.

Enzyme activity is closely linked to enzyme conformation, with optimal conformations and rates occurring under specific conditions, of which pH and temperature are key. Co-factors, such as trace metals and/or co-enzymes may also be important. It may be possible that a rise in the media DIC concentration (and decline in pH) leads to a decline in the internal pH of the CV, assuming the enzymes are localised within the CV, and an alteration to the coccolithophores ability to produce key monosaccharides. Indeed, based on oxygen isotopes the CV pH was suggested to decline at elevated DIC concentrations and lower external pH values (see chapter 3).

Whilst these hypothesised changes in enzyme activity may explain observations, actual pathways within coccolithophores may be more complex in reality. Critically, more research is needed into enzyme activity and CAP monosaccharide expression within coccolithophores. Future studies should elucidate what enzymes are present within coccolithophore cellular compartments and how they respond to changes in specific carbonate parameters. In particular, experiments exploring enzyme gene expression of coccolithophores with varying carbonate conditions are needed.

4.4.4. Implications of a low UAC on calcification

The UAC of the CAP has long been associated with its ability to control calcite nucleation and dictate coccolith morphology [Borman et al., 1982, Fichtinger-Schepman et al., 1981, Giuffre et al., 2013, Sand et al., 2014, 2017]. Whilst uronic acid contributes around 25% to the total peak area for both *C. pelagicus* and *G. oceanica* under standard DIC conditions, at elevated DIC the UAC of both species approaches zero. Having no, or very low, uronic acid is thought to provide a low barrier to nucleation at low Ω_{calcite} at

the site of calcification and results in a faster nucleation rate [Giuffre et al., 2013]. At high $\Omega_{calcite}$, likely achieved at high DIC, having a low UAC would result in uncontrolled, rapid, nucleation, which may be linked to the malformation observed in *C. pelagicus* (see chapter 3). Nonetheless, under elevated DIC, *G. oceanica* was able to produce coccoliths with no signs of malformation with a CAP that had little to no uronic acid. Data presented here therefore alludes to the CAP produced by *G. oceanica* being able to control calcification without glucuronic or galacturonic acid whether on its own or in concert with other molecules.

Previous work has suggested that CAPs have a high affinity for growing crystal surfaces independent of charge [Borman et al., 1982, Henriksen and Stipp, 2009]. More recent *in vitro* experiments found that CAPs extracted from *G. oceanica* promoted greater calcite crystallisation in a solution that favoured aragonite precipitation than the more negatively charged polygalacturonic acid, further highlighting the role of CAP conformation in polymorph selectivity and calcite crystallisation [Walker et al., 2019]. Walker et al. [2019] suggested that additional, unidentified, functional groups may be controlling calcification and that the CAP has a conformational structure that attracts Ca^{2+} and CO_3^{2-} in a geometry similar to that of the existing calcite lattice. The UAC within *G. oceanica* may therefore be a red herring, with conformation more important than the overall charge.

In addition to the monosaccharides identified and discussed here, 13 additional monosaccharides were unable to be matched with any existing reference or standards. An unidentified charged sugar may therefore be contributing to net negative charge and assisting with calcification in the absence of galacturonic and glucuronic acid. Previous studies found evidence of tartaric and glyoxylic acid that contributed to an overall negative charge in CAPS extracted from *P. carterae* [Marsh et al., 1992]. We are unable to assign any of the unidentified peaks to those of tartaric acid. Glyoxlyic acid meanwhile is comparatively small relative to the other monnosaccharides measured and its fragmentation pattern is common in many compounds. We can therefore not rule out the presence of glyoxylic acid.

Whilst the sedimentary CAPs showed a similar chemical fingerprint to modern CAPs, glucose contributed a greater % peak area to total monosaccharide content. Indeed, glucose made up between 30 and 60% of the total peak area for sediment samples (Fig. 4.5). The culture samples investigated here provide only a snapshot of modern CAP chemical

compositions. Extinct species of coccolithophore may possess different chemical compositions and structural arrangements. Moreover, how the chemistry of CAPs respond to elevated temperatures and nutrients in culture is unknown however, work has shown that phytoplankton begin to accumulate and exudate carbohydrates once nutrients become limiting [Hessen and Anderson, 2008].

4.4.5. Chemical composition of CAPs as a DIC proxy

UAC in CAPS and its application to the sedimentary record

In contrast to the calibration performed by Lee et al. [2016], data presented here shows that under high DIC the UAC of CAPs for both *G. oceanica* and *C. pelagicus* decreased below detectable levels (Fig. 4.4). Moreover, the measured UAC for samples dating to the Eocene, thought to have some of the highest atmospheric CO_2 concentrations of the Cenozoic, also possessed low to undetectable levels of galacturonic and glucuronic acid ([Anagnostou et al., 2020, Foster et al., 2017]; Fig. 4.5).

Given we identify no evidence that UAC increases with higher $CO_{2(aq)}$ availability in culture nor across the Eocene, the UAC proxy looks intangible, at least for Cenozoic samples. The GC-MS analysis performed on CAPs from modern day species in this study did not look at a range of DIC conditions, rather, the focus was on the comparison between standard conditions and high DIC. There may be a threshold or upper limit of DIC, or $CO_{2(aq)}$, at which galacturonic and glucuronic acid are no longer produced in certain modern and Eocene species. An experiment over a full range of DIC conditions may show that the CO_2 proxy is tangible. The presence, or lack thereof, of uronic acid may therefore indicate a pCO_2 threshold at which the coccolithophores are no longer able to produce acidic polysaccharides. Such a mechanism resulting in the 'switching off' of uronic acid production could involve the changing activity of enzymes with evolving internal CV conditions as discussed previously (see section 4.4.3).

The ratio of six carbon monosaccharides to five carbon monosaccharides in CAPS

CAP monosaccharides including glucose, galactose, mannose, rhamnose and fucose consist of six carbon atoms ($C_6H_{12}O_5$) whilst the monosaccharides xylose, arabinose and ribose consist of five carbons atoms ($C_5H_{10}O_5$; Fig. 4.3). Six carbon monosaccharides form

a hexose ring consisting of five carbon atoms and a oxygen atom, with a methyl group attached to one of the carbons. Five carbon monosaccharides, meanwhile, form a hexose ring with no methyl group or a pentose ring with an attached methyl group. Here, *C. pelagicus* was observed to increase the ratio of % proportion of six carbon monosaccharides to % proportion of five carbon monosaccharides under elevated DIC (herein referred to as 6C/5C; Fig. 4.9).

Although 6C/5C increased in *C. pelagicus*, changes in 6C/5C were not consistent across species. Culture data shows that the 6C/5C measured for *G. oceanica* was of comparable magnitude under standard and high DIC conditions. Whilst no studies have investigated CAP monosaccharide variation with elevated carbon availability, studies have investigated how components of soluble polysaccharides in other algae vary with CO_2 availability [Li et al., 2000, Han et al., 2017]. Yet, these previous studies paint a complicated picture. Han et al. [2017] found that from the lowest to highest CO_2 conditions, 6C/5C in soluble extracellular polysaccharides produced by *Nostoc flagelliforme* increased, yet the ratio was at its lowest under intermediate CO_2 values. Li et al. [2000] meanwhile found a trend to lower 6C/5C for the soluble component of cell wall polysaccharides produced by *Porphyridium sp.* (rhodophyta) as CO_2 was elevated. Varying 6C/5C may be a complex interaction of enzyme activity and the internal cellular environment in response to changing carbon availability. An increase in 6C/5C with declining carbon availability may represent a mechanism to reduce cellular carbon demand of CAP production. Indeed, there is evidence for similar biochemical shifts to reduce a cells nitrogen budget given limitation in marine microorganisms [Grzymski, 2012].

The ratio of six carbon monosaccharides to five carbon monosaccharides in sedimentary CAPS

Absolute magnitudes of the 6C/5C ratio across the Eocene are generally in line with the magnitudes observed for *C. pelagicus* in culture. Indeed, ten of 12 calculated 6C/5C ratios across the Eocene vary between 1 and 10, however two samples dating to 38.7 Ma and 54.15 Ma have an absolute magnitude of 16 and 32 respectively. Samples dating to 38.7 Ma and 54.15 Ma do not occur during hyperthermals, rapid warming events in the geological past, nor during any rapid turn over of coccolithophore species (Figs. 4.10 and 4.11).

Interpreting variations through time in the CAP chemical composition in the geolog-

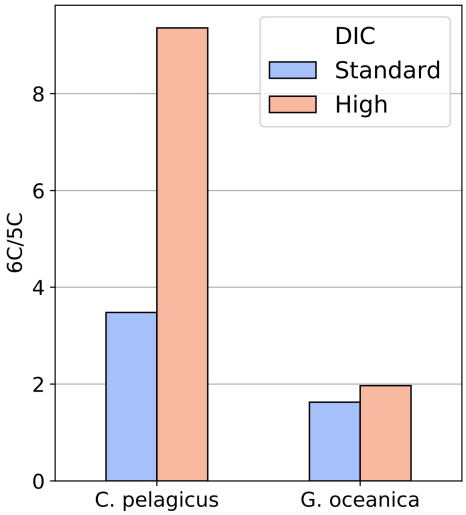

Figure 4.9: 6C/5C shown for standard DIC cultures (blue) and high DIC (red) cultures for *C. pelagicus* and *G. oceanica*. The ratio of six to five carbon monosaccharides was calculated as the % contribution of six carbon monosaccharides over the % contribution of five carbon monosaccharides. The degree of change from six carbon monosaccharides to five carbon monosaccharides appears to be species specific, with *C. pelagicus* displaying a much greater shift than *G. oceanica*.

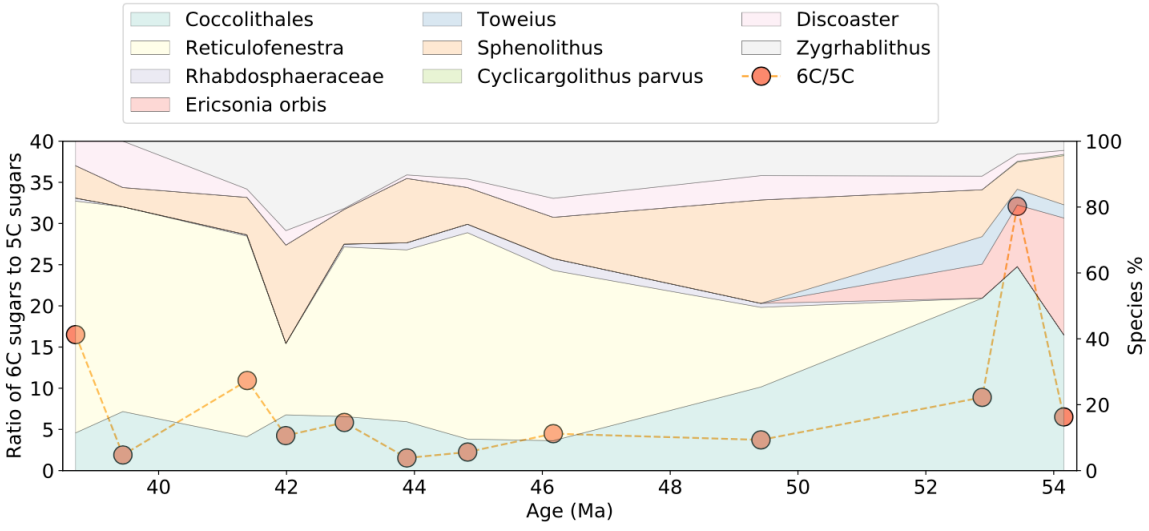

Figure 4.10: The red points represent the change in the ratio of six carbon monosaccharides to five carbon monosaccharides. The overlaid stack plot represents the species percentage distribution through time.

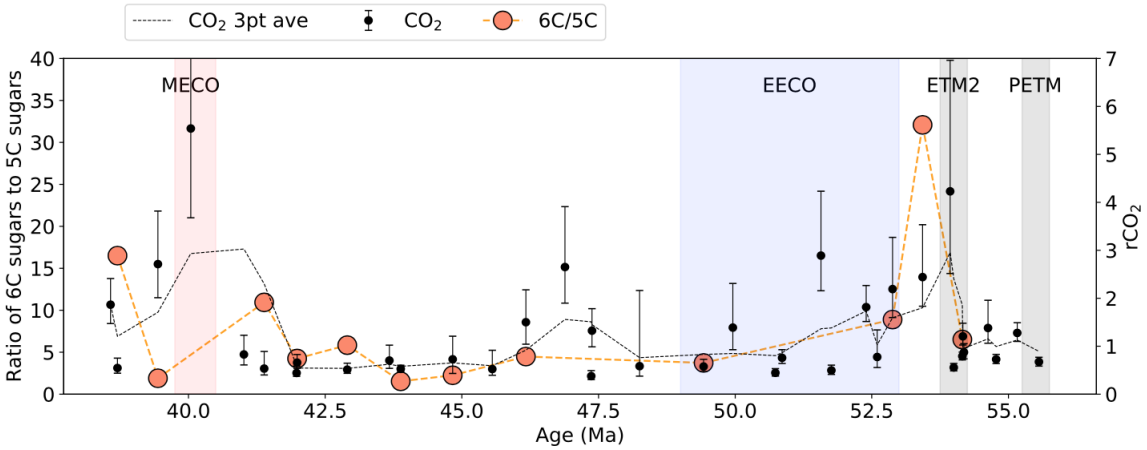

Figure 4.11: The ratio of six carbon monosaccharides to five carbon monosaccharides presented for the 12 3-5μm size fraction samples analysed here are shown in red (left hand y-axis). Also shown is the relative $CO_{2(aq)}$ modelled in chapter 2 (black points) along with the corresponding three-point moving average (dashed black line). The error represents 1-σ of model realisations. Shaded regions represent significant periods of the Eocene and include the MECO, EECO, ETM2 and PETM.

ical past with respect to environmental drivers is more complicated than from modern axenic cultures. From 41.5 Ma to 54 Ma, the variation in 6C/5C is significantly correlated with relative $CO_{2(aq)}$ at the 0.05 significance level ($R^2 = 0.587$,P-value = 0.016, Fig. 4.12). Yet, when all samples measured are included in the regression analysis, 6C/5C shows no correlation with relative $CO_{2(aq)}$. The lack of correlation for samples younger than 41.5Ma may be due to the evolution and radiation of a species of the genus Reticulofenestra that possessed a different 6C/5C sensitivity to changes in carbonate chemistry. Indeed, an ordinary least squares regression model for 6C/5C across all data points based on CO_2, Coccolithale percentage abundance (the order encompassing *C. pelagicus*) and Reticulofenestra percentage abundance increased the adjusted R^2 score to 0.423 from 0.11 based on relative CO_2 alone (P-value = 0.062; for full statistical results see appendix A.4). The multiple-linear regression analysis confirms that species change, in particular the % contribution of the coccolithales, is contributing to variations in 6C/5C. The presence of a different morphotype or strain may contribute to the unexplained variance [Rickaby et al., 2016, Lee et al., 2016]. An unaccounted for strain would be hard to discern from sedimentary coccolith morphology alone, however, may possess a different CAP composition [Rickaby et al., 2016]. Moreover, the presence of an unidentified strain could be causing the large peaks in 6C/5C at 38.7 and 54.15 Ma. Finally, when comparing culture data with data from the sedimentary record, one must note that cultures reflect physiological

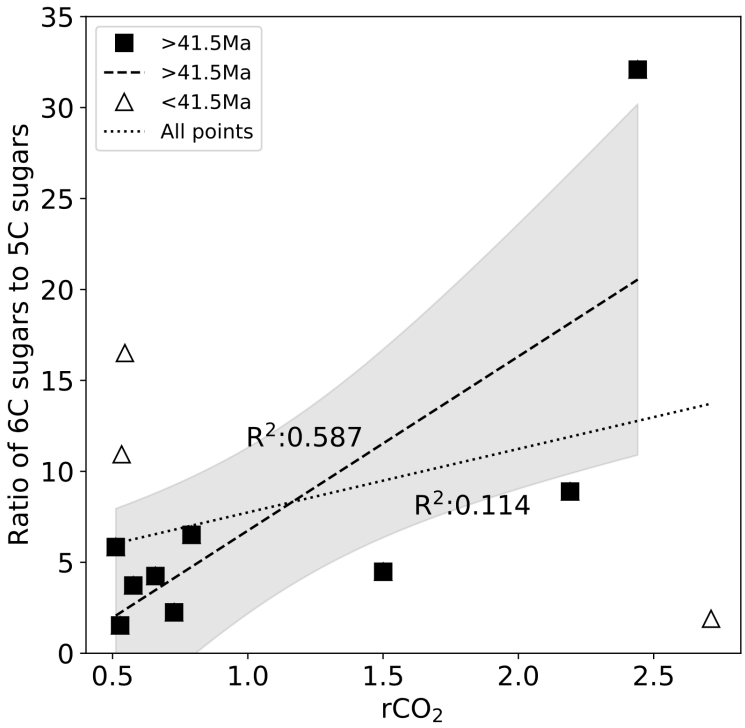

Figure 4.12: A scatter plot of 6C/5C for the sediment samples is plotted against relative $CO_{2(aq)}$ as calculated in chapter 2. The black squares represent the samples older than 41.5Ma, the white triangles are those younger than 41.5Ma. The dashed line represents an ordinary least squares regression analysis for the black squares, the grey shaded region represents the confidence intervals for the dashed line. The R^2 value of 0.587 is associated with the OLS regression on the black sqaures, the corresponding p-value was 0.016. Also show is an OLS regression (dotted line) for all points (black and white) with the associated R^2 value of 0.114. Given the low correlation coefficient and p-value ≥ 0.05 the confidence intervals were not plotted for the dotted line.

change over several generations whereas ancient samples reflect evolutionary change over millions of years.

4.5. Conclusion

Data presented here shows that CAPs from modern species appear to change their composition with elevated DIC concentrations. In particular, both *C. pelagicus* and *G. oceanica* were found to reduce their glucuronic and galacturonic acid content under elevated DIC. Data presented here therefore suggests that the UAC based pCO_2 proxy may be intangible. However, *C. pelagicus* was also found to increase its ratio of six carbon monosaccharides to five carbon monosaccharides within its CAP as carbon availability increased. For samples older than 41.5Ma the ratio of six to five carbon monosaccharides was also found to correlate with relative changes in $CO_{2(aq)}$, however samples younger than 41 Ma suggest

additional work is needed to determine the influence of species variation and carbonate conditions on variations in 6C/5C.

Exactly why coccolithophores alter the chemical composition of the CAP remains to be fully understood, however it may derive from the need to maintain CAP conformation with ongoing changes in carbon availability and pH conditions. With changes in external media composition, changes in the activity of enzymes and monosaccharide production pathways may lead to the alteration in CAP chemistry. Additional *in vitro* enzyme inhibition studies are needed to understand the role of enzyme activity on CAP composition with changes in culture conditions. Coupled gene expression experiments for the presence of specific enzymes with variable environmental conditions should also be conducted.

Whilst this study has demonstrated that CAPs likely record changes in past environmental conditions, several fundamental issues must be addressed before their chemistry can be used to constrain $p\mathrm{CO}_2$. In particular an emphasis should be placed on determining whether glycerol is part of a larger glycopolymer or single molecule. If the latter is confirmed then glycerol is likely a post extraction contaminant. If glycerol is part of a larger glycopolymer, then glycerol likely derives from either bacterial or coccolith production and the mechanism by which calcite is controlled may need to be reconsidered. Finally, a full calibration is needed across several DIC conditions with both the UAC and 6C/5C response investigated for a number of additional species. If these challenges can be overcome then the CAP chemistry based proxy looks promising.

Chapter 5

Exploring the carbon isotopic composition of CAPs as a proxy for pCO_2

Abstract

Coccolith associated polysaccharides (CAPs) are crucial in the production of coccoliths and previous studies have shown that their chemical composition may be sensitive to $p\mathrm{CO}_2$. Additional studies have suggested that the isotopic composition of CAPs may also vary as a function of CO_2 availability. However, isotopic data only currently exists for the modern species *Emiliania huxleyi*, limiting our understanding across coccolithophore species and the geological application of the hypothesised proxy. In this chapter I grow two species of coccolithophore, *Coccolithus pelagicus* and *Gephyrocapsa oceanica*, under varying carbon availability to test the hypothesis that the isotopic composition of CAPs ($\delta^{13}\mathrm{C}_{\mathrm{CAP}}$) varies as a function of carbon availability in a species independent manner. I find that that whilst absolute $\delta^{13}\mathrm{C}_{\mathrm{CAP}}$ values appear species dependent, the offset from organic matter appears to be species independent and decreases with decreasing CO_2 availability and increasing growth rates. If additional measurements of $\delta^{13}\mathrm{C}_{\mathrm{org}}$ can be determined from the fossil record then, in conjunction with coccolith morphometry, future studies may be able to reconstruct $p\mathrm{CO}_2$ with fewer assumptions and requirements than current organic based proxies.

5.1. Introduction

With each year that passes we see more frequent extreme weather events around the globe [Masson-Delmotte et al., 2021]. Whilst it is difficult to undeniably ascribe these events to anthropogenic climate change, we are seeing a corresponding rise in both temperature and $p\mathrm{CO}_2$ as these events become more frequent. Each year the uncertainty on the degree of warming expected given potential increases in $p\mathrm{CO}_2$ is reduced as they both inexorably rise and provide yet more data. However, our understanding of how tightly coupled temperature and $p\mathrm{CO}_2$ are in a world without global ice sheets is lacking. Work is therefore needed to develop methodologies that permit reconstructions of $p\mathrm{CO}_2$ in the geological past where ice sheets are much reduced or non existent. Such understanding will be crucial heading into the second half of the century where we may have ice free summers in the Arctic [Masson-Delmotte et al., 2021].

Geochemists have used signals preserved in molecules extracted from sediments to reconstruct contemporaneous $p\mathrm{CO}_2$ beyond the limit of ice cores for decades. In particular, studies have sought to use alkenones, unsaturated methyl and ethyl ketones produced by the Noëlaerhabdaceae family of coccolithophores, to reconstruct past $p\mathrm{CO}_2$ levels (e.g [Prahl et al., 1989, Laws et al., 2001, Freeman and Pagani, 2005, Zhang et al., 2019]). As discussed in Chapter 1, the $\delta^{13}\mathrm{C}$ of alkenones can be used to infer the $\delta^{13}\mathrm{C}$ of coccolithophore organic matter (alkenones are usually taken to be 4‰ depleted relative to bulk biomass). However, in order to determine $p\mathrm{CO}_2$ from $\delta^{13}\mathrm{C}_{\mathrm{org}}$, assumptions must be made regarding the cells morphometry and growth rate, which both, in addition to $\mathrm{CO}_{2(\mathrm{aq})}$, affect the cells carbon isotopic signature [Popp et al., 1998, Bidigare Robert R. et al., 1997, Laws et al., 2001, 2002]. As alkenones are dissociated from the coccolithophores that produced them within the sediment, cellular parameters are folded into the parameter, b, estimated from contemporaneous ocean phosphate concentrations:

$$C_e = \frac{b}{\varepsilon_f - \varepsilon_p} \tag{5.1}$$

where C_e represents the external concentration of $\mathrm{CO}_{2(\mathrm{aq})}$, ε_f the isotopic fractionation occurring during enzymatic carbon fixation and ε_p the offset of $\delta^{13}\mathrm{C}_{\mathrm{org}}$ from $\delta^{13}\mathrm{C}_{\mathrm{CO2}}$ calculated from $\delta^{13}\mathrm{C}_{\mathrm{DIC}}$ (see Chapter 3; [Bidigare Robert R. et al., 1997, Freeman and Pagani, 2005]). Given a reference $\delta^{13}\mathrm{C}_{\mathrm{CO2}}$ is required, $\delta^{13}\mathrm{C}_{\mathrm{DIC}}$ must be reconstructed.

$\delta^{13}C_{DIC}$ is usually based on the $\delta^{13}C$ of co-eval foraminifera, which adds another layer of uncertainty given assumptions on age tie points, varying ocean habitats and foraminifera specific vital effects. If the requirement to use b and $\delta^{13}C_{DIC}$ can be circumnavigated, or if they can be better constrained, then the uncertainty on pCO_2 can be reduced.

5.1.1. The carbon isotopic signal of CAPS

Recently, the isotopic composition of coccolith associated polysaccharides (CAPs) has been suggested as a novel pCO_2 proxy. Coupled measurements of $\delta^{13}C_{CAP}$ and $\delta^{13}C_{lith}$ from the same coccolithophores were originally proposed as a novel method to reconstruct pCO_2 with the assumption that $\delta^{13}C_{CAP}$ tracked $\delta^{13}C_{org}$ with a constant offset [Hermoso, 2014, McClelland et al., 2017]. However, recent *in vivo* calibrations on *Emiliania huxleyi* suggest that the offset of $\delta^{13}C_{CAP}$ from $\delta^{13}C_{org}$ ($\Delta\delta^{13}C_{CAP\text{-}org}$) varies as a function of carbon utilisation (given as the ratio of carbon used relative to total carbon supply and approximated by $\frac{\mu}{[CO_{2(aq)}]}$, although cellular parameters such as cell size also modulate carbon utilisation; [Wilkes et al., 2018]).

Whilst Wilkes et al. [2018] found that the response of $\delta^{13}C_{CAP}$ was linear, it was less sensitive to changes in $\frac{\mu}{[CO_{2(aq)}]}$ than $\delta^{13}C_{org}$ or $\delta^{13}C_{lith}$ (Fig. 5.1). The linear relationship of $\delta^{13}C_{org}$ was suggested to derive from a purely diffusive supply of $CO_{2(aq)}$ to the cell and internal isotopic distillation of the internal carbon pool from ongoing carbon fixation. The variation in $\Delta\delta^{13}C_{CAP\text{-}org}$ meanwhile was inferred to be derived from isotopically distinct carbon pools contributing changeable allocations of carbon to CAP production over $\frac{\mu}{[CO_{2(aq)}]}$ space. At low $[CO_{2(aq)}]$, more of the cells' total carbon budget was suggested to be devoted to CAP production and was predicted to make up a greater proportion, up to 22%, of total organic matter [Wilkes et al., 2018]. As the carbon contribution of CAP to total biomass increased with increasing carbon utilisation, the two values converged at lower $[CO_{2(aq)}]$. The increase in carbon supplied to CAP production at low CO_2 was suggested to provide a strategy to support calcification as carbon becomes limited. However, given isotopic heterogeneity within monosaccharides, changes to the polysaccharide composition could not be ruled out as driving isotopic variations [Hayes, 2001, Wilkes et al., 2018, Teece and Fogel, 2007].

As discussed in chapter 4, CAPs are extracted directly from coccolithophores and so provide an additional level of information on the morphometry of the coccolithophore

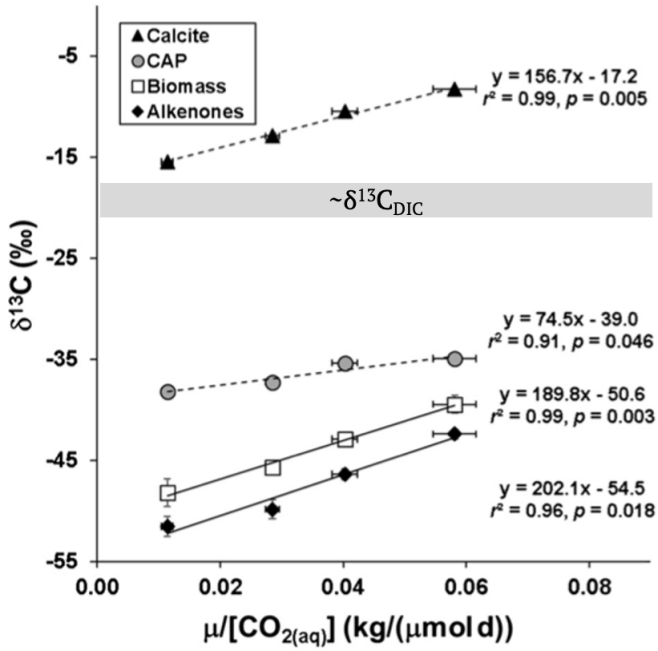

Figure 5.1: δ^{13}C values for *E. huxleyi* cellular material plotted against $\frac{\mu}{[CO_{2(aq)}]}$. Corresponding δ^{13}C values are presented for coccoliths (black triangles), CAPs (grey circles), biomass (white squares) and alkenones (black diamonds). The approximate $\delta^{13}C_{DIC}$ value measured is also shown. Figure modified from Wilkes et al. [2018].

cell, which, for example, can permit estimates of allometric growth rates [Aloisi, 2015]. Coupled measurements on $\delta^{13}C_{CAP}$ and $\delta^{13}C_{lith}$ in the geological record, in addition to constrained cellular morphometry, may therefore circumvent the need to estimate b and reconstruct $\delta^{13}C_{DIC}$. However, additional calibration experiments are needed.

5.1.2. Aims, objectives and hypotheses

To my knowledge only one study exists that investigates the response of $\delta^{13}C_{CAP}$ with changeable carbon availability, thus limiting the data available for comparison [Wilkes et al., 2018]. Moreover, current experimental data on the response of $\delta^{13}C_{CAP}$ to variations in carbon availability is limited to the modern day species *Emiliania huxleyi*. Given the limited presence of *E. huxleyi* in the geological record, a gap in our knowledge of how $\delta^{13}C_{CAP}$ for geologically relevant species varies as a function of $CO_{2(aq)}$ exists, limiting the applicability of the hypothesised proxy.

This study investigates the isotopic response of $\delta^{13}C_{CAP}$ for the species *Coccolithus pelagicus* and *Gephyrocapsa oceanica* with varying $CO_{2(aq)}$, targeted through varying media DIC concentrations and pH. Coupled with existing data, this study then seeks to

answer the question of whether $\delta^{13}C_{CAP}$ responds in a species specific manner or has a universal trend across coccolithophores. The variation in $\delta^{13}C_{CAP}$ relative to the $\delta^{13}C$ values of coccoliths and organic matter as a function of $\frac{\mu}{[CO_{2(aq)}]}$ will also be investigated. In particular, this study will seek to answer whether $\delta^{13}C_{org}$ can be directly reconstructed from $\delta^{13}C_{CAP}$. This study will additionally investigate trends in $\delta^{13}C_{CAP}$ from sediment samples in conjunction with contemporaneous environmental conditions during the Eocene. Ultimately, the aim of this study is to advance our understanding of the response of $\delta^{13}C_{CAP}$ with changing $CO_{2(aq)}$ in an attempt to refine the proposed proxy.

5.2. Methods

5.2.1. Sample selection

Aliquots of coccolithophore pellets were taken from the experimental culture work conducted in chapter 3. To briefly recap, cultures were grown in triplicate across six different target carbonate conditions (see chapter 3, table 3.1 for detailed conditions). Cultures were harvested via centrifugation and aliquots were taken for CAP extraction and analysis once the pellet had been washed with 10ml 1% Triton-X100 in 0.05M $NaHCO_3$ and 6ml 12% NaOCl to remove organic matter. The pellet was then rinsed three times in pH neutral DI water to remove the cleaning solution.

Sediment samples used here are as detailed in chapter 2 and as listed in appendix A.1. Sample preparation, size separation, age model and nannofossil abundance are identical to that listed in chapter 2. In total, CAPs were extracted from 37 sediment samples filtered to 3-5μm and span the Eocene.

5.2.2. CAP extraction

The CAP extraction process was as detailed in chapter 4.

5.2.3. Blanks and Standards

A pectin process blank was run alongside samples to investigate whether the extraction process altered the isotopic composition of the samples. Powdered apple pectin (Sigma, reference number 76282-100G) was dissolved in ultra pure 18mΩ water to target concentrations of 0.1μg pectin μl^{-1}. The pectin process blank was run in parallel from the first

filtration step through the Amicon Ultra-4 centrifugal filter (see chapter 4 for further details). Two additional pure calcite process blanks were run from the initial clean with Triton-X100 and NaOCL (from step one as listed in Chapter 4, Fig. 4.2).

5.2.4. Isotopic analysis of CAPS

Extracted CAP samples were shipped frozen to Harvard University for isotopic analysis within the Pearson Laboratory. CAP isotopic analysis used the moving wire technique on a spooling wire micro-combustion isotope ratio mass spectrometer (SWiM-IRMS; [Sessions et al., 2005]). Briefly, the moving nickel wire was passed through a 950°C cleaning oven to remove any residual organic matter and oxidise the surface. A syringe connected to an auto-sampler takes an aliquot of the sample and places 0.8μL onto the oxidised nickel wire. CAP concentrations of 0.1-0.2μg Carbon/μl de-ionised water were targeted for analysis. The moving wire then passed through a subsequent 150°C oven evaporating any liquid and leaving the organic matter residue on the wire. The wire then passed through a third oven where the organic matter is combusted with the presence of copper and platinum to form CO_2. The CO_2 was passed to a continuous-flow isotope ratio mass spectrometer for isotopic analysis. Additional isotopic measurements on 500μg pectin were made on a SERCON 20/22 Isotope ratio mass spectrometer (IRMS) coupled to a SERCON GSL elemental analyser in the School of Archaeology, University of Oxford. The additional measurements were made to check for consistency between Harvard and Oxford and enable calibration to VPDB via measurements on a known Alanine standard. Pectin was run on the SWiM-IRMS at Harvard via dilution in de-ionised water to target concentrations of 0.02% weight/volume. Repeat measurements (n=7) were made on the pectin standard via the SWiM-IRMS to measure analytical uncertainty. Previous work has shown that the precision is ~1‰ for samples containing 10 ng C [Sessions et al., 2005]. Samples were blank corrected via measurements on 0.8μL milli-Q water after equations presented in Hayes [1983].

5.3. Results

5.3.1. Culture conditions

Measured $CO_{2(aq)}$ and growth rates for cultures were as listed in Chapter 3. Averaged triplicate data is summarised in table 5.1 (For full details see chapter 3, table 3.1, experiment numbers are consistent across chapters).

Table 5.1: Measured media $CO_{2(aq)}$ conditions and cellular growth rate along with cellular $\delta^{13}C$ values. The media $[CO_{2(aq)}]$, cellular growth rate (μ), $\delta^{13}C_{lith}$ and $\delta^{13}C_{org}$ are as measured in chapter 3, however represented here for reference. Also presented is the one sigma error calculated from the standard deviation across triplicate measurements. Missing values for $\delta^{13}C_{CAP}$ data represent no measurement was possible, or measurement not distinguishable from the blank. Missing $\delta^{13}C_{CAP}$ σ values represent only one triplicate measurement was possible.

Species	Experiment	CO_2 μmol $KgSw^{-1}$	μ day^{-1}	μ σ	$\delta^{13}C_{lith}$ ‰	$\delta^{13}C_{lith}$ σ	$\delta^{13}C_{org}$ ‰	$\delta^{13}C_{org}$ σ	$\delta^{13}C_{CAP}$ ‰	$\delta^{13}C_{CAP}$ σ	$\delta^{13}C_{DIC}$ ‰	$\delta^{13}C_{DIC}$ σ
C. pelagicus	1	12.30	0.62	0.10	-5.36	0.10	-30.50	0.18	-23.19	0.03	-3.13	0.05
	2	11.80	0.73	0.17	-5.27	0.12	-30.68	0.82	-24.47	0.17	-3.06	0.18
	3	31.50	0.66	0.04	-2.74	0.30	-29.77	0.70	-23.89		-2.89	0.03
	4	40.80	0.80	0.03	-2.51	0.10	-29.37	1.55	-20.40	0.08	-2.81	0.02
	5	49.00	0.53	0.14	-1.90	0.08	-31.12	0.68	-21.09		-2.72	0.03
	6	59.20	0.54	0.03	-1.85	0.04	-32.12	3.05			-2.69	0.03
G. oceanica	1	11.30	0.51	0.07	-4.12	0.04	-27.51	1.06	-17.78	0.14	-4.14	0.03
	2	19.00	0.53	0.05	-3.89	0.07	-26.25	0.46	-18.68	0.05	-3.98	0.01
	3	30.20	0.67	0.05	-3.57	0.27	-25.72	0.68	-16.96	0.15	-3.88	0.05
	4	30.20	0.74	0.04	-3.83	0.05	-25.27	1.62	-17.51	0.34	-3.89	0.02
	5	44.30	0.61	0.05	-3.75	0.06	-26.10	0.42	-15.91	0.11	-3.83	0.03
	6	56.70	0.57	0.05	-3.57	0.04	-27.30	0.51	-13.30	0.05	-3.81	0.02

5.3.2. CAP quantification

Prior to SWiM-IRMS analysis, polysaccharide presence was confirmed via the use of a phenol-H_2SO_4 assay with a glucose standard as listed in Chapter 4. All samples returned non-zero values for absorbance at 490nm wavelength confirming the presence of acidic polysaccharides extracted from coccoliths.

5.3.3. CAP Carbon isotopes

The $\delta^{13}C$ of the pectin process standards was within error of the unprocessed pectin standard (pectin process blanks: -26.2‰$1\sigma \pm 0.5$ n=3, true pectin standard: -25.4 $\pm$ 0.3 n=7). The extraction procedure was therefore deemed to not affect measured values of $\delta^{13}C_{CAP}$. Isotopic analysis at Harvard University also determined the carbon concentration within each sample. Any CAP samples with a carbon concentration within 1 nmols C ul^{-1} of the blank were discarded due to at least 75% of the measured value deriving from matter other than that of the CAP and hence resulting in a large uncertainty on the final values. The average carbon concentration for *C. pelagicus* was 4.4 nmols C ul^{-1} compared to 3.45 nmols C ul^{-1} for the average of the two calcite blank samples. In total eight of seventeen samples from *C. pelagicus* were therefore discarded. The average concentration for CAP samples deriving from *G. oceanica* cultures was 15.04 nmols C ul^{-1}, with no samples within 1 nmols C ul^{-1} of the blank.

$\delta^{13}C_{CAP}$ values are given relative to $\delta^{13}C_{DIC}$ to allow for comparison across studies and to remove the dependence on the $\delta^{13}C$ value of the carbon source. Measured values of $\delta^{13}C_{CAP}$ for *G. oceanica* trend from more ^{13}C depleted at low $[CO_{2(aq)}]$ to more ^{13}C enriched values at high $[CO_{2(aq)}]$ (Fig. 5.2). The absolute range spans approximately 6‰ from -9‰ to -15‰. Data for *C. pelagicus* shows that $\delta^{13}C_{CAP}$ values trend from approximately -20‰ to -17.5‰ as $[CO_{2(aq)}]$ increases (Fig. 5.2).

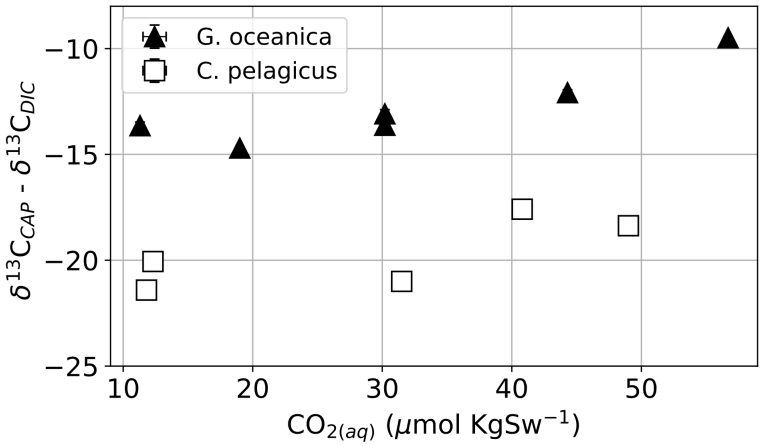

Figure 5.2: $\delta^{13}C_{CAP}$ relative to $\delta^{13}C_{DIC}$ measured for *G. oceanica* and *C. pelagicus* in culture experiments plotted against measured $CO_{2(aq)}$ values. Error bars represent standard deviation across triplicate measurements.

5.3.4. Sediment CAP Carbon isotopes

Sediment samples were run in a randomised order and show that across the Eocene the carbon isotopic composition of CAPs extracted from the 3-5μm sediment size fraction trends from -23.5‰ to -32‰ (Fig. 5.3).

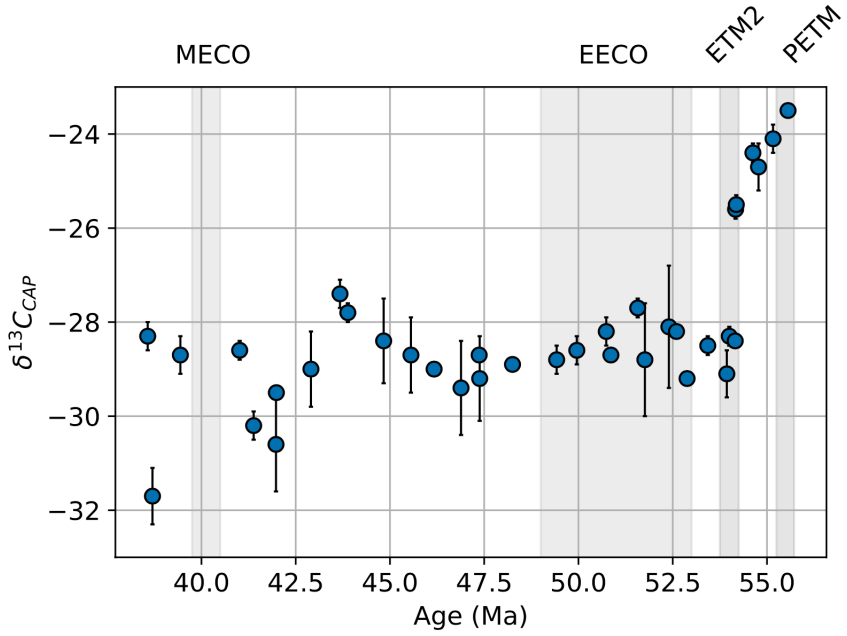

Figure 5.3: $\delta^{13}C_{CAP}$ through the Eocene. Also highlighted are significant climatic periods across the Eocene including the Paleocene Eocene thermal maximum (PETM; 55.25-55.75 Ma), the Eocene thermal maximum 2 (ETM2; 53.75- 54.25 Ma), the Early Eocene climatic optimum (EECO; 53-49 Ma) and the middle Eocene climatic optimum (MECO; 39.75-40.5 Ma).

5.4. Discussion

5.4.1. Culture CAP Isotopes

Measured absolute $\delta^{13}C$ values for both species follow the expected ordering of cellular matter. Relative to $\delta^{13}C_{DIC}$, $\delta^{13}C_{lith}$ is the most ^{13}C enriched, with $\delta^{13}C_{org}$ the most ^{13}C depleted and $\delta^{13}C_{CAP}$ enriched relative to $\delta^{13}C_{org}$ (Table 5.1; [Hayes, 2001, Wilkes et al., 2018]). Absolute values of $\Delta\delta^{13}C_{CAP\text{-}org}$ ranged between 6 and 16‰ for *G. oceanica* and 5 and 10‰ for *C. pelagicus*, encompassing the range of 4-10‰ presented by Wilkes et al. [2018]. Initial studies found the bulk carbohydrate pool is around 4‰ ^{13}C enriched relative to bulk organic matter, with polysaccharides extracted from marine algae up to 9‰ enriched relative to organic matter [Hayes, 2001, Teece and Fogel, 2007]. The general trend of isotopic ordering within coccolithophores derives from reaction pathways in which carbohydrates, including CAPs, are produced early within the biosynthetic pathway [Hayes, 2001]. Downstream organic molecules, such as lipids, are usually more ^{13}C depleted due to ongoing kinetic discrimination against ^{13}C [Hayes, 2001].

Absolute $\delta^{13}C_{CAP}$ values for *C. pelagicus* were approximately 5‰ more negative than values for *G. oceanica*. The difference in $\delta^{13}C_{CAP}$ between species corresponds to overall $\delta^{13}C_{org}$ values being more ^{13}C depleted for *C. pelagicus*. The difference in absolute values likely represents variations in the carbon source (ratio of $CO_{2(aq)}/HCO_3^-$ taken into the cell) and fractionation behaviour within different sized cells with variable ratios of calcification to organic matter fixation rates (see Chapters 2 and 3).

Absolute values for $\delta^{13}C_{CAP}$ presented by Wilkes et al. [2018] trend from ^{13}C-depleted values to more ^{13}C-enriched values with an increase in carbon utilisation, $\frac{\mu}{[CO_{2(aq)}]}$[1], opposite to the corresponding trends measured here (Fig. 5.4). $\delta^{13}C_{DIC}$ was unable to be measured for all experiments by Wilkes et al. [2018] due to machine failure. Differing trends could therefore have derived from Wilkes et al. [2018] not normalising to $\delta^{13}C_{DIC}$, which may have varied across experiments. Although, a similar set up should ensure consistency across experiments. Alternatively, the positive gradients for $\delta^{13}C_{CAP}$ and $\delta^{13}C_{org}$ with $\frac{\mu}{[CO_{2(aq)}]}$ measured for *E. huxleyi* compared to the negative trends for *C. pelagicus* and *G. oceanica* measured here may derive from differences in physiology and intracel-

[1] $\frac{\mu}{[CO_{2(aq)}]}$ represents carbon utilisation for cells that have a fixed cell size, cellular carbon density and membrane permeability

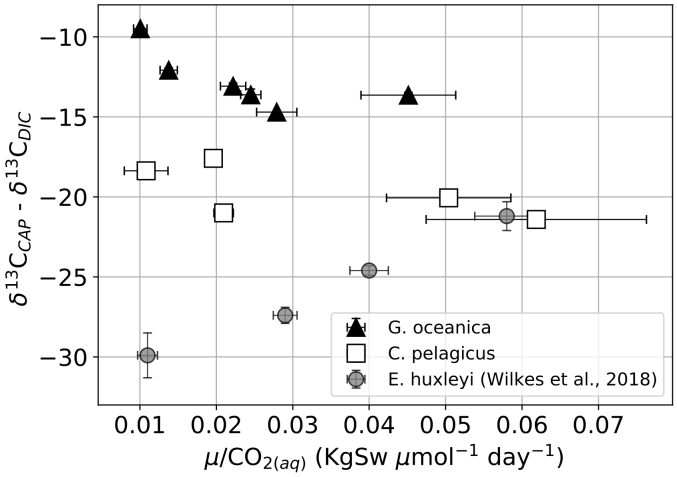

Figure 5.4: $\delta^{13}C_{CAP}$ relative to $\delta^{13}C_{DIC}$ measured in *G. oceanica* and *C. pelagicus* in this study plotted with the data presented by Wilkes et al. [2018] for the species *E. huxleyi*. Isotopic data is plotted against $\frac{\mu}{[CO_{2(aq)}]}$. $\delta^{13}C_{DIC}$ was only available for one experiment in the study by Wilkes et al. [2018], however is inferred here to be constant across experiments, which is reasonable given a similar experimental set up. Error bars represent standard deviation across triplicate measurements.

lular carbon fluxes [McClelland et al., 2017]. Like $\delta^{13}C_{lith}$, $\delta^{13}C_{CAP}$ may be influenced by the rate of calcification relative to the photosynthetic rate (R_{calc}:R_{fix}). Indeed the species *E huxleyi*, *G. oceanica* and *C. pelagicus* all have significantly different R_{calc}:R_{fix} over modern day conditions (p-value ≤ 0.001 based on a one-way ANOVA of particulate inorganic carbon to particulate organic carbon ratios (equivalent to R_{calc}:R_{fix}) for each species from data presented in Aloisi [2015]). Variations in R_{calc}:R_{fix} have been shown to dictate the intracellular flux and distribution of carbon and carbon isotopes within coccolithophores ([McClelland et al., 2017]; Chapters 2 and 3). R_{calc}:R_{fix} may therefore be dictating upstream variations in the $\delta^{13}C$ of the carbon subsequently used for CAP formation. Different species of coccolithophore also dedicate varying proportions of their photosynthetic energy budget to CAP formation [Monteiro et al., 2016]. Coupled with vast morphological differences between coccoliths, how the CAPs belonging to individual species interact with calcification and how coccolithophores control carbon allocation to CAPs appears highly variable between species.

Substantial variations in $\delta^{13}C$ amongst monosaccharide components also exists [van Dongen et al., 2002, Teece and Fogel, 2007]. Teece and Fogel [2007] found the green algae *Ulva lactuca* possessed a monosaccharide, arabinose, 13‰ enriched relative to $\delta^{13}C_{org}$. Changeable allocations of monosaccharides could therefore be contributing to variations in

isotopic compositions with changing carbon utilisation. More positive values of $\delta^{13}C_{CAP}$ at higher $CO_{2(aq)}$ concentrations measured here could reflect a greater (/smaller) contribution of heavier (/lighter) monosaccharides to the CAP composition. Indeed, chemical data presented in Chapter 4 suggests that substantial changes to monosaccharides occur and may be contributing to changes in measured $\delta^{13}C_{CAP}$. For both species the uronic acid content of CAPs decreases at high DIC. Uronic acids are downstream components of glucose and may therefore have a lighter isotopic signature based on ongoing kinetic isotopic discrimination against ^{13}C. At higher $CO_{2(aq)}$ concentrations with less uronic acid within the UAC, the overall $\delta^{13}C_{CAP}$ may therefore drift to heavier values. Other sugar percentage contributions also change. Galactose increases for both species, whilst the percentage contribution of xylose decreases. For *G. oceanica* arabinose increases by around 10%. All else being equal, and assuming arabinose is 13‰ enriched relative to $\delta^{13}C_{CAP}$, the shift in arabinose proportional representation would account for a drift of 1.3‰ of the 6‰ total shift.

5.4.2. Relative changes in isotopic offsets

Although absolute trends in $\delta^{13}C_{CAP}$ vary in a species specific manner, $\delta^{13}C_{CAP}$ for all species appears to adhere to the trend of convergence with $\delta^{13}C_{org}$ at higher carbon utilisation (Fig. 5.5; [Wilkes et al., 2018]). Convergence of $\delta^{13}C_{CAP}$ with $\delta^{13}C_{org}$ was linked to an increase in CAP production relative to total organic matter as carbon utilisation increased. Wilkes et al. [2018] suggested that under high carbon utilisation when the intracellular carbon pool is depleted, elevated CAP concentrations may help to support calcification. Such a proposal opposes the idea that CAPs provide a barrier to nucleation and the greater the concentration of CAPs, or charge, the greater the inhibition of calcification [Borman et al., 1982, Giuffre et al., 2013]. Here, whilst we were unable to determine absolute CAP concentrations the carbon concentration per cell derived from isotopic analysis showed no significant change with $CO_{2(aq)}$ for either species (p-values = 0.53 and 0.1 for *C. pelagicus* and *G. oceanica* respectively. Carbon concentration per cell was derived from the measured nMol of carbon per ul of CAP extract multiplied by total CAP extract volume and divided by total number of cells in each culture). The lack in significant change in carbon concentration may allude to the variation in monosaccharide composition being the main driver in $\delta^{13}C_{CAP}$ variation.

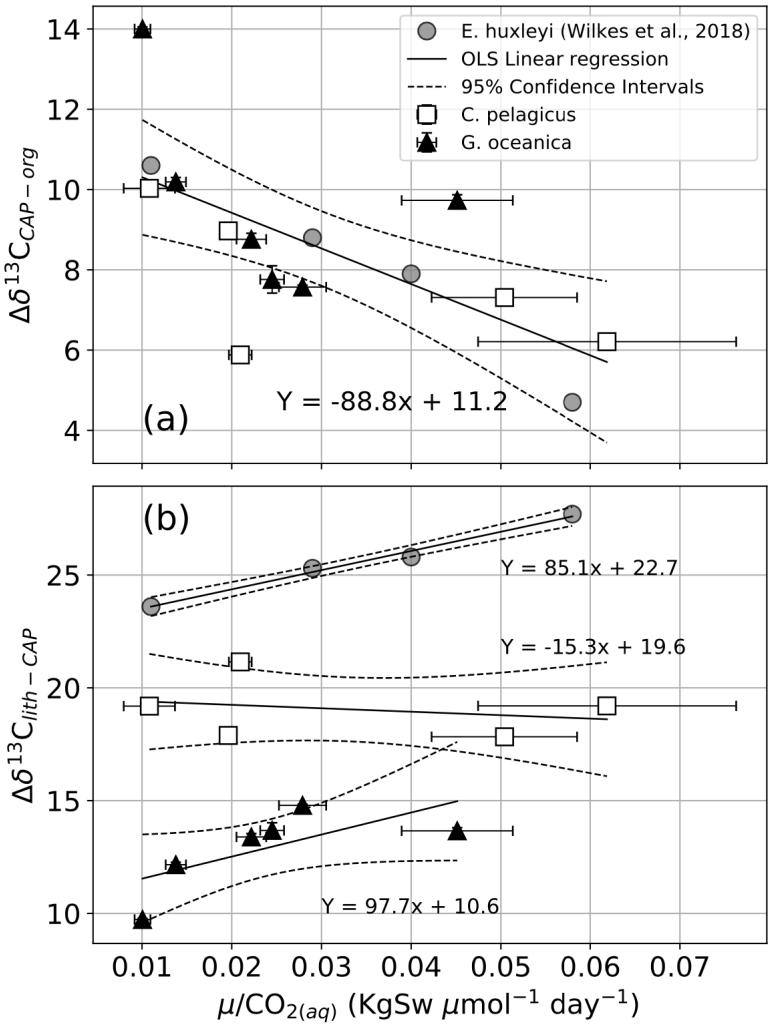

Figure 5.5: **(a)** The offset of $\delta^{13}C_{CAP}$ from $\delta^{13}C_{org}$ ($\Delta\delta^{13}C_{CAP\text{-}org}$) is plotted against $\frac{\mu}{[CO_{2(aq)}]}$ for the species in this study and that previously published by Wilkes et al. [2018]. $\Delta^{13}C_{lith-CAP}$ is also shown **(b)**. The solid lines represent ordinary least squares (OLS) regression with the confidence interval represented by the dashed black lines. Error bars represent standard deviation across triplicate measurements. For plot **(a)** the regression encompasses all species ($r^2 = 0.47$, p-value = 0.005). For plot **(b)** regression analysis was performed for each species (*G. oceanica*: $r^2 = 0.47$, p-value = 0.13, *C. pelagicus*: $r^2 = 0.06$, p-value = 0.67, *E. huxleyi*: $r^2 = 0.98$, p-value = 0.007 (see Wilkes et al. [2018] for full *E. huxleyi* analysis).

Whilst the mechanisms that set the absolute $\delta^{13}C_{org}$ varies across species the mechanisms controlling $\Delta\delta^{13}C_{CAP\text{-}org}$ appears consistent across coccolithophores. This finding confirms that in the geological past $\delta^{13}C_{org}$ cannot be reconstructed directly from $\delta^{13}C_{CAP}$ without additional constraints on $\frac{\mu}{[CO_{2(aq)}]}$. Moreover, given how variable $\Delta\delta^{13}C_{lith\text{-}CAP}$ is across species in terms of absolute magnitude and trend it appears a CAP-lith based pCO_2 proxy will be difficult to employ to a multi-species sediment fraction. Nonetheless, if $\delta^{13}C_{CAP}$ can be determined along with $\delta^{13}C_{org}$, derived from $\delta^{13}C_{alkenones}$, then it will be possible to directly determine $\frac{\mu}{[CO_{2(aq)}]}$. If growth rate can be indirectly determined from coccolith based allometric relationships and cell size from the fossil coccoliths then it may be possible to reconstruct $CO_{2(aq)}$ without the need to determine b or $\delta^{13}C_{DIC}$, thus reducing uncertainty on final pCO_2 estimates. Unfortunately this means that the maximum limit that any CAP based proxy can stretch back into the fossil record is limited by the extent of alkenones.

5.4.3. Sediment $\delta^{13}C_{CAP}$

Measured $\delta^{13}C_{CAP}$ values from the Eocene trended from more ^{13}C enriched values during the early Eocene to more ^{13}C depleted values during the middle to late Eocene (Fig. 5.6). Two steps are also apparent in the $\Delta\delta^{13}C_{lith\text{-}CAP}$ data during the Paleocene-Eocene thermal maximum (PETM; 55.5Ma) and Eocene thermal maximum 2 (ETM2; 53.7 Ma), suggesting that the driver is amplified during hyperthermals. Although, the step during the PETM is likely due to large changes in the associated $\delta^{13}C_{lith}$ rather than $\delta^{13}C_{CAP}$ (Chapter 2; Fig. 5.6). Given the samples were not extracted or analysed in age order, the trend through time would appear to reflect a true signal.

$\Delta\delta^{13}C_{CAP\text{-}org}$ also trends from more positive to less positive values across the Eocene. In culture a smaller $\Delta\delta^{13}C_{CAP\text{-}org}$ suggests higher carbon utilisation. Whilst the relationship between $\Delta\delta^{13}C_{CAP\text{-}org}$ and relative CO_2 in sediment samples was not significant, the general shift to lower $\Delta\delta^{13}C_{CAP\text{-}org}$ across the Eocene as pCO_2 declines is in line with the relationship observed in culture experiments. Other, unaccounted for controls on $\Delta\delta^{13}C_{CAP\text{-}org}$ in the sediment may therefore be controlling variations. Yet, correlations between $\delta^{13}C_{CAP}$ and relative CO_2, oxygen isotopes (a proxy for temperature), percentage species abundance and monosaccharide composition were investigated, with all tests found to be not significant (P-values all $\geq$0.1). Moreover, some sediment $\Delta\delta^{13}C_{CAP\text{-}org}$

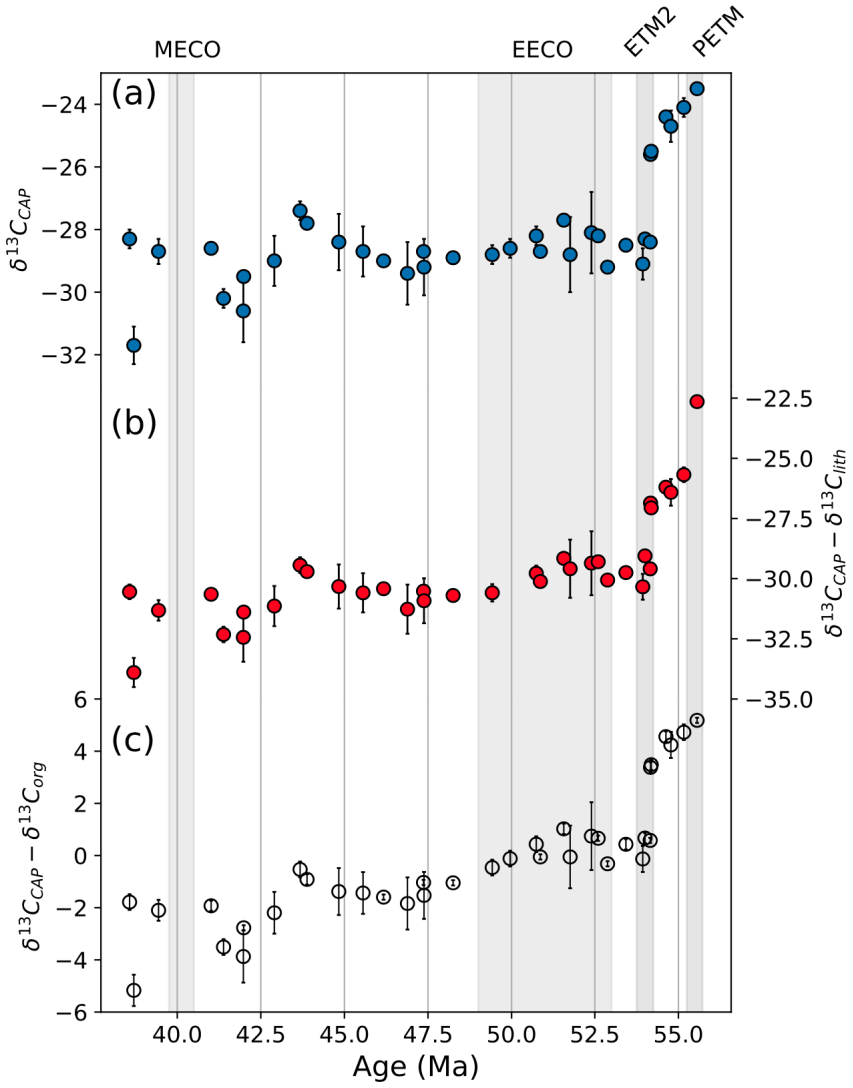

Figure 5.6: Measured $\delta^{13}C_{CAP}$ for sediment samples across the Eocene **(a)** trends from less negative to more negative values through time. The corresponding $\Delta\delta^{13}C_{lith\text{-}CAP}$ values **(b)** shows the inverse trend from a smaller offset during the early Eocene to a greater offset in the middle to late Eocene. Large deviations to the overall negative trend in $\Delta\delta^{13}C_{lith\text{-}CAP}$ occur during the PETM and ETM2 (Fig. 5.3). $\Delta\delta^{13}C_{CAP\text{-}org}$ **(c)** trends from positive values during the Early Eocene to negative values by the late to middle Eocene. $\delta^{13}C_{org}$ values interpolated from from [Hayes et al., 1999].

values are negative whilst culture values are exclusively positive (14-4‰). The negative values in the sediment may result from $\delta^{13}C_{org}$ values derived from global bulk marine sediment rather than associated coccolithophore organic matter [Hayes et al., 1999]. If contemporaneous $\delta^{13}C_{org}$ can be derived from $\delta^{13}C_{alkenone}$, the negative results could be identified as an artefact of the reference $\delta^{13}C_{org}$ value.

Although $\delta^{13}C_{CAP}$ was measured for 37 samples across the Eocene, it was found that the majority of the sample was composed of glycerol (see Chapter 4). Whilst glycerol was found within the pectin process blank, it was orders of magnitude less than that found in the sediment samples. Given glycerol accounts for around 99% of the sediment sample CAP extracts, $\delta^{13}C_{CAP}$ therefore reflects the isotopic composition of the glycerol. The lack of correlation likely derives from the large presence of glycerol within sedimentary CAP samples. Future studies should focus on determining the source of glycerol and whether it affects the isotopic signature measured for sedimentary CAP samples. Given the source of glycerol is not known (see Chapter 4), reaching a conclusion on the driver of evolving isotopic composition is, unfortunately, not possible at this time.

5.5. Conclusion and future directions

The aim of this chapter was to explore variations in $\delta^{13}C_{CAP}$ as a proxy for pCO_2. Data presented here suggests that the response of $\delta^{13}C_{CAP}$ is not uniform across species and processes that contribute to bulk cellular isotopic heterogeneity may also contribute to species specific responses of $\delta^{13}C_{CAP}$. However, whilst absolute values of $\delta^{13}C_{CAP}$ differ between species $\Delta\delta^{13}C_{CAP\text{-}org}$ appeared to show a universal trend to a reduced offset with higher carbon utilisation. The universal trend suggests a common mechanism by which carbon is allocated to CAPs. Further studies should aim to measure the $\delta^{13}C$ of individual monosaccharides and how the $\delta^{13}C$ values, and concentration of, monosaccharides change with changing carbon availability. Moreover, future studies should seek to grow cultures in larger vessels so that larger CAP samples can be extracted and reliable attempts to determine the CAP concentration can be made. Increasing the yield from the CAP extraction method will increase the usefulness of any potential proxy. If the total yield of CAP extracted can be increased, coupled measurements on CAP chemical composition and $\delta^{13}C_{CAP}$ will allow greater constraints to be placed on the carbonate system and may pave the way for a combined 6C/5C - $\delta^{13}C_{CAP}$ pCO_2 proxy. Finally, if a method can be

formulated to digest the glycerol from the sample or separate the mannose backbone of the CAP from the glycerol fraction then the $\delta^{13}C_{CAP}$ proxy may have greater geological relevance.

Chapter 6

Concluding remarks and future directions

This thesis set out to explore the isotopic and chemical composition of coccoliths and coccolith associated polysaccharides as a proxy for pCO_2. Prior to the undertaking of this thesis, coccolithophore cellular models could recreate isotopic behaviour of coccoliths and organic matter observed *in vivo* given constraints on the external carbonate system, cellular morphometry, physiology and growth rate. However, prior studies had yet to invert models to quantitatively recreate pCO_2 variations based on isotopic data from the fossil record. Preliminary studies into CAPs had also been conducted, which led to the suggestion that the isotopic composition and chemistry of CAPs could additionally inform on pCO_2. Yet, existing studies into CAPs were restricted to the modern day species *E. huxleyi*. The work presented in this thesis sought to invert and update model parameters for existing coccolith isotopic flux models to reconstruct past pCO_2 levels. Moreover, this thesis sought to explore how CAPs could be used to supplement the work on coccoliths. Specifically, as listed in the introduction, the aims of the thesis were to:

1. Invert existing coccolith isotopic flux models, and using novel sedimentary data, reconstruct CO_2 levels during the warmest period of the Cenozoic, the Eocene (54 - 34 millions years ago).

2. Increase the granularity of existing coccolith isotopic flux models through the provision of additional culture data in geologically abundant species and to further elucidate individual species carbon acquisition strategies.

3. Investigate the response of $\delta^{13}C_{CAP}$ and CAP chemistry in cultures and in sediments to changes in carbon availability.

6.1. The Isotopic Composition of Coccoliths

Over the past several decades, literature explored the enigmatic carbon isotopic vital effects within the cellular components of coccolithophores. Early work established the control of the external concentration of CO_2, cellular growth rate and cellular morphometry on $\delta^{13}C_{org}$ [Burkhardt et al., 1999, Bidigare Robert R. et al., 1997, Laws et al., 2001]. Ensuing work explored coupled variations in $\delta^{13}C_{lith}$ and $\delta^{13}C_{org}$, before models were developed to recreate the isotopic patterns observed in laboratory culture experiments [Schulz et al., 2007, Rickaby et al., 2010, Hermoso et al., 2016a, McClelland et al., 2017, Holtz et al., 2017]. These models provided insight into coccolithophore physiology and paved the way for the work conducted in Chapter 2.

In Chapter 2 I sought to invert the carbon isotopic flux model first developed by McClelland et al. [2017] to reconstruct past pCO_2 concentrations. Model inversion to reconstruct pCO_2 required measured values of $\delta^{13}C_{lith}$ from size separated coccoliths and assumptions regarding ancient cellular morphometry. Whilst cell size and growth rate could be inferred from morphometric relationships, R_{calc}:R_{fix}, a key control on $\delta^{13}C_{lith}$ magnitude, estimated through existing methods resulted in a poor model fit for Eocene coccolithophores. A procedure whereby pCO_2 and R_{calc}:R_{fix} were simultaneously constrained through minimising the misfit of measured and modelled $\delta^{13}C_{lith}$ values was thus developed. With no prior inputs of pCO_2 or R_{calc}:R_{fix}, the method developed in Chapter 2 provides a truly independent paired reconstruction of Eocene pCO_2 variations and shifts in community calcification to photosynthetic rates.

Coupled with benthic oxygen isotope data, a proxy for deep sea water temperature variations, Chapter 2 supported previous studies that suggested the atmospheric concentration of CO_2 declined contemporaneously with a decline in temperature. The work in Chapter 2 also suggested that Eocene coccolithophores produced some of the largest and most calcified coccoliths of the Cenozoic time period. Moreover, the paradigm that a decline in CO_2 is coupled with a decline in coccolithophore calcification was challenged [Si and Rosenthal, 2019, Bolton et al., 2016, Duchamp-Alphonse et al., 2018, McClelland et al., 2016, Meier et al., 2014]. Greater calcification relative to organic matter fixation

would have sequestered additional alkalinity at depth and may have acted as a negative feedback on the deepening on the carbonate compensation depth, inline with previous studies [Boudreau et al., 2018].

Whilst the work in Chapter 2 was able to recreate relative changes in $CO_{2(aq)}$ inline with previous estimates, cellular parameters constrained for the original model, such as the effective permeability to HCO_3^- and CO_2, were tuned to several species [McClelland et al., 2017]. In order to be more reflective of the extant and extinct species from the Eocene, cellular parameters within the isotopic flux model were re-calibrated to novel isotopic data and cellular morphometry in Chapter 3. Cellular parameters were determined to a species specific level for *Coccolithus pelagicus*, present during the Eocene, and *Gephyrocapsa oceanica*, a close relative of the Cenozoic Reticulofenestra, under varying carbonate conditions.

Data showed that when $\Omega_{calcite}$ was held approximately constant and $[CO_{2(aq)}]$ was increased, coccoliths expressed similar coccolith carbon isotope vital effects as those observed previously [Rickaby et al., 2010]. The expression of carbon isotope vital effects under approximately constant $\Omega_{calcite}$ proves the applicability of the coccolith carbon isotope vital effect proxy to ancient sediments, which saw different $[CO_{2(aq)}]$, but likely similar $\Omega_{calcite}$ values [Tyrrell and Zeebe, 2004].

Recalibration of the isotopic flux model highlighted contrasting carbon acquisition strategies of *C. pelagicus* and *G. oceanica* and improved model granularity for future studies, particularly those that are able to separate sediments into species-specific size fractions. The main finding of Chapter 3 was that whilst *G. oceanica* likely increased its HCO_3^- transporters under limited carbon availability, *C. pelagicus* does not, although *C. pelagicus* possessed enough transporters to provide approximately 10% of its carbon in the form of HCO_3^- under all conditions. Future gene expression studies are needed to confirm the results from this coupled *in vivo* and *in silico* study.

The work completed in chapter 3 can also help shed light on the species distribution observed during the Eocene. In chapter 2 I confirm that the Reticulofenestra order first appeared in the sedimentary record at IODP site 1263 approximately 52 million years ago [Zachos et al., 2004]. After the first appearance, the Reticulofenestra order rapidly increased in size and came to dominate the smallest size fractions by the end of the Eocene. In chapter 3 I found that the *G. oceanica*, descendants of the Reticulofestra order, likely

possess an ability to upregulate HCO_3^- transporters to assist with carbon acquisition under carbon limitation. The ability to upregulate HCO_3^- transporters coupled with their small size may help to explain the radiation of Reticulofestra in the late Eocene as $CO_{2(aq)}$ declined. In contrast, assuming Eocene *C. pelagicus* is similar to modern *C. pelagicus* and does not have the ability to upregulate HCO_3^- transporters, then it may be that the decrease in coccolith size that occurs from the Eocene to modern day may have been in response to carbon limitation as $CO_{2(aq)}$ declined.

Together, Chapters 2 and 3 addressed aims one and two of this thesis through applying existing knowledge to develop a novel method for reconstructing past pCO_2. The novel methodology was applied to sedimentary data and provided independent reconstructions of pCO_2 for the Eocene time period. The reconstructed decline in pCO_2 was further supported through investigating coccolith species abundance, which documented a transition from greenhouse to icehouse world. The work in Chapter 3 permitted the recalibration of the work in Chapter 2 based on culture experiments and derived greater insight into the carbon acquisition strategies of the species *C. pelagicus* and *G. oceanica*. The work in Chapter 2 and 3 has laid the foundations for future studies to reconstruct pCO_2 and/or R_{calc}:R_{fix} back to the Triassic.

Despite the advancements made in this thesis, challenges still remain. Firstly, Chapter 2 focused on the early to middle Eocene, a period with both a high species diversity and giant coccolithophore species [Bown et al., 2004]. The presence of large coccoliths permitted size separation of the sediment into five distinct fractions that could then be isotopically analysed. When compared to an additional reference, the five size fractions provided five degrees of freedom at each time point and thus permitted reasonable constraints to be placed on pCO_2 and R_{calc}:R_{fix}. Periods such as the Cenozoic saw the decline in the size and diversity of coccolithophores [Bown et al., 2004]. During such periods, obtaining five clearly defined size fractions with unique isotopic fractionation behaviours may prove to be difficult, thus limiting the power of the model to constrain both pCO_2 and R_{calc}:R_{fix}. However, if future studies can provide a robust record for pCO_2 in conjunction with size separated $\delta^{13}C_{lith}$ values, then more reliable estimates of R_{calc}:R_{fix} can be made and vice versa. For example, constraining R_{calc}:R_{fix} during glacial-interglacial cycles with pCO_2 derived from ice core measurements should be targeted in future research.

6.2. Coccolithus pelagicus: A comparison of then and now

Through coupled SEM image analysis and isotopic modelling, Eocene *C. pelagicus* was found to be one of the most heavily calcified coccolithophores of the Cenozoic. Although CO_2 was predicted to decline during the Eocene, absolute values were likely higher than modern day [Foster et al., 2017]. Additionally boron isotope proxies suggest that ocean pH during the Eocene was around 7.7; substantially lower than today's value of around 8.1 [Anagnostou et al., 2020]. Sea surface temperatures during this period were also considerably warmer than the modern ocean (e.g. Boscolo Galazzo et al. [2014], Inglis et al. [2020], Lunt et al. [2021]). During the Eocene, *C. pelagicus* therefore produced large, heavily calcified coccoliths during a period of high carbon availability, low pH and warm temperatures.

In Chapter 3 *C. pelagicus* was found to produce malformed coccoliths as pH was reduced and DIC raised to increase $[CO_{2(aq)}]$. Additional studies also found *C. pelagicus* produced malformed coccoliths under elevated carbon availability (see Chapter 3). The contrasting response of *C. pelagicus* in the sediment compared to the lab therefore raises an interesting question: what mechanisms permitted the production of large, heavily calcified coccoliths during the Eocene? Moreover, why is *C. pelagicus* unable to produce normal coccoliths under modern day recreation of Eocene like conditions?

During the Eocene the calcium ion concentration was twice as high compared to the modern ocean whilst the magnesium concentration was approximately 0.6 times lower [Tyrrell and Zeebe, 2004]. The combined effect was that during the Eocene the the Mg/Ca ratio was approximately 0.4 times that of the modern day [Tyrrell and Zeebe, 2004]. Experimental evidence has suggested that a coupled increase in $[Ca^{2+}]$ and lower Mg/Ca may elevate coccolithophore growth and calcification [Stanley, 2006]. Perhaps the combination of lower Mg/Ca and higher $[Ca^{2+}]$ during a period of lower pH and higher CO_2 permitted the production of normal, heavily calcified coccoliths. Future lab experiments should look to raise carbon availability, $[Ca^{2+}]$ and lower the Mg/Ca ratio to determine if this combination permits the production of normal, healthy coccoliths. Work has also shown that Si is important in maintaining normal coccolith morphology in the species *C. pelagicus* whilst the species *G. oceanica* is seemingly insensitive to changes (see [Brownlee et al., 2020] and references therein). Given Si has decreased through the Cenozoic it may

necessary that to form large coccoliths under higher CO_2 levels *C. pelagicus* requires a greater concentration of Si or at least a Si to DIC ratio consistent with Eocene levels [Brownlee et al., 2020].

Alternatively it may be that over the course of the Cenozoic time period, evolutionary pressures resulted in the loss of ability for *C. pelagicus* to survive in Eocene like conditions. It may be that the malformation observed within the culture experiments derives from a short term physiological response rather than a longer term evolutionary adaptation. If modern day *C. pelagicus* existed under conditions similar to the Eocene for several thousand generations rather than the usual 5-10 used in literature, the proportion of malformed coccoliths may decline. Ultimately the reason as to why *C. pelagicus* was able to produced large, typical coccoliths during the Eocene and why it cannot do so under similar conditions today will remain a mystery until we fully understand why coccolithophores calcify. Even if we do elucidate the current role of calcification, it is possible that its role has changed over geological time.

6.3. On the use of coccolith associated polysaccharides (CAPS)

6.3.1. CAP Chemistry

Chapters 4 and 5 contributed to achieving the third aim of this thesis to explore the use of CAPs as a pCO_2 proxy. To this end, both the isotopic and chemical composition of CAPs were investigated under elevated carbon availability. In Chapter 4, CAPs were extracted from *C. pelagicus* and *G. oceanica* under standard and high DIC conditions and from Eocene sediments. The CAPs extracted from high DIC culture experiments and from the Eocene sediment possessed little to no uronic acid. The presence of heavily calcified coccoliths with CAPs possessing little to no UAC during the Eocene complicates the theory that the negative charge associated with CAPs is intrinsically linked with calcification. The conformation of the CAP may therefore play a greater role in calcification than previously thought, or the negative charge associated with the uronic acid content is a recently developed phenomenon that assists with calcification under lower $CO_{2(aq)}$ conditions. It may also be possible that elevated $[Ca^{2+}]$ and lower $[Mg^{2+}]$ during the Eocene led to a different CAP conformation and an increased ability to interact with calcite at higher $CO_{2(aq)}$ and lower pH levels. Indeed modern day *in vitro* experiments have shown that

the ability of CAPs to control calcification is affected by the concentration of Mg^{2+} and Ca^{2+} ions in solution [Sand et al., 2017].

In Chapter 3 it was found that the coccoliths produced by *C. pelagicus* became malformed under higher DIC. The CAPs extracted from these high DIC experiments were found to produce no uronic acid in Chapter 4. In Chapter 3 I suggested that, based on the oxygen isotopes of the coccoliths produced by *C. pelagicus*, the coccolith vesicle pH may be decreasing at higher DIC conditions. In order to explain changes in CAP chemistry I subsequently invoked variations to the activity of intracellular enzymes, which could occur at lower coccolith vesicle pH's. Future studies should investigate whether the CV pH is indeed changing and what the interaction is with coccolith malformation and changes in enzyme expression. Coupled with gene expression experiments to determine the presence of the enzymes discussed in Chapter 4, we may be able to understand why *C. pelagicus* produces malformed coccoliths at elevated DIC conditions.

6.3.2. CAP isotopic signal

Only one existing study has investigated the isotopic response of CAPs with variable carbon availability [Wilkes et al., 2018]. The study by Wilkes et al. [2018] investigated the response of $\delta^{13}C_{CAP}$ with changing carbon availability for the modern day species *E. huxleyi*, which has little relevance to the geological record past approximately 300,000 years ago [Bown et al., 2004]. Work in Chapter 5 therefore sought to investigate variations in $\delta^{13}C_{CAP}$ with changing carbon availability in two geologically relevant species, *C. pelagicus* and *G. oceanica*. Comparison with existing studies suggests that there is likely not a common response of absolute $\delta^{13}C_{CAP}$ values with changing carbon availability amongst species of coccolithophore. However, the offset of $\delta^{13}C_{CAP}$ from $\delta^{13}C_{org}$ as a function of carbon utilisation, for all species follows a common trend of similar magnitude whereby $\delta^{13}C_{CAP}$ converges with $\delta^{13}C_{org}$ at high carbon utilisation. Whilst Wilkes et al. [2018] suggested that an increased proportion of carbon allocated to CAPs at low CO_2 occurred to aid with calcification, no evidence for significant changes in carbon allocation were found. Changes in enzyme activity altering CAP monosaccharide composition was therefore suggested to contribute to changing $\delta^{13}C_{CAP}$. Future studies whereby coupled changes in monosaccharide proportions, isotopic composition and monosaccharide $\delta^{13}C$ are constrained are needed.

The ultimate goal of the CAP based proxy would be to integrate the measurable $\delta^{13}C_{CAP}$ signal into the inverted isotopic flux model to predict $CO_{2(aq)}$ (see chapters 2 and 3; [McClelland et al., 2017]). The incorporation of $\delta^{13}C_{CAP}$, derived from the same coccoliths from which $\delta^{13}C_{lith}$ was measured, into the carbon isotopic flux model would add further constraints on pCO_2. Yet, whilst extensive literature investigating the controls on $\delta^{13}C_{lith}$ and $\delta^{13}C_{org}$ exists, a comprehensive understanding of the drivers of $\delta^{13}C_{CAP}$ are lacking (e.g. [Rickaby et al., 2010, Hermoso, 2014, Burkhardt et al., 1999, Laws et al., 2001]). Modelling $\delta^{13}C_{CAP}$ is therefore likely to prove challenging given the biosynthetic pathway is not known for CAP production, although they are assumed to be produced outside of the CV and transported to the site of calcification via a golgi vesicle transport mechanism (see [Taylor et al., 2017] for review). $\delta^{13}C_{CAP}$ is likely driven by variations to carbon recycling, shifting contributions from distinct isotopic pools and from variable monosaccharide proportions. Furthermore, ongoing isotopic distillation within the chloroplast likely has downstream implications for $\delta^{13}C_{CAP}$. Future work is needed to determine the extent that variable monosaccharide composition contributes to $\delta^{13}C_{CAP}$ through coupled isotopic and GC-MS analysis for individual species over controlled carbonate conditions.

6.4. Concluding Remarks

The work detailed in this thesis has advanced our understanding of the isotopic response of cellular components within coccolithophores. Moreover, it has outlined a methodology whereby an existing isotopic flux model was inverted to reconstruct past periods of pCO_2. Further, the work presented on variations in CAP chemistry and isotopic composition has laid the foundation for future work to build on. The work in this thesis only briefly touched on the oxygen isotopic system within coccolithophores. However, if isotopic flux models can be updated to model the paired oxygen and carbon isotopic system, then the constraints of pCO_2 and R_{calc}:R_{fix} can be doubled.

The main aim of subsequent work should be to ensure the inverted carbon isotopic flux model is easy and fast to apply to future isotopic data from size separated sediment fractions. Work to make a user friendly interface for the model would remove barriers and provide a framework for future studies to utilise the model. Moreover, future work should aim to develop growth rate proxies. Carbon utilisation within coccolithophores is intrinsi-

cally linked with external CO_2 availability and growth rate. If we can reliably reconstruct growth rate via other means, then better estimates can be made for contemporaneous CO_2 concentrations. Additionally, if the mechanistic variation in $\delta^{13}C_{CAP}$ with changes in carbon availability can be fully understood then integration with the existing carbon isotopic flux model will provide further constrains on pCO_2.

The work completed within this thesis has provided novel insight into coccolithophore physiology and advanced the methodology to extract environmental information from their biochemistry. If future studies can address the challenges listed within, we stand to learn more about our past environment and how coccolithophores may respond to future climate perturbation.

Appendix A

Appendix

Table A.1: Sediment Sample List from expedition 208, site 1263. Ages with * are samples used for the low level CAP slice through the Eocene as discussed in chapter 4.

Hole	Core	C-Type	Sec.	Age	Age model reference
C	2	H	6	38.575	Based on [Rivero-Cuesta et al., 2019]
B	7	H	3	38.701*	Based on [Rivero-Cuesta et al., 2019]
C	3	H	4	39.441*	Based on [Rivero-Cuesta et al., 2019]
A	14	H	5	40.043	Based on [Rivero-Cuesta et al., 2019]
B	9	H	6	41.014	Based on [Rivero-Cuesta et al., 2019]
A	15	H	6	41.385*	Based on [Rivero-Cuesta et al., 2019]
B	10	H	5	41.978	Based on [Westerhold et al., 2015]
A	16	H	1	41.987*	Based on [Westerhold et al., 2015]
B	11	H	3	42.904*	Based on [Westerhold et al., 2015]
B	12	H	1	43.675	Based on [Westerhold et al., 2015]
A	17	H	6	43.882*	Based on [Westerhold et al., 2015]
A	18	H	5	44.832*	Based on [Westerhold et al., 2015]
A	19	H	3	45.557	Based on [Westerhold et al., 2015]
B	14	H	3	46.171*	Based on [Westerhold et al., 2015]
A	20	H	5	46.886	Based on [Westerhold et al., 2015]
B	15	H	7	47.366	Based on [Westerhold et al., 2015]
A	21	H	1	47.380	Based on [Westerhold et al., 2015]
B	16	H	7	48.251	Based on [Westerhold et al., 2015]
A	22	H	3	49.421*	Based on [Lauretano et al., 2016]
A	23	H	1	49.956	Based on [Lauretano et al., 2016]
B	20	H	5	50.738	Based on [Lauretano et al., 2016]
A	24	H	3	50.860	Based on [Lauretano et al., 2016]
B	21	H	5	51.572	Based on [Lauretano et al., 2016]
C	7	H	4	51.762	Based on [Lauretano et al., 2016]
A	26	H	7	52.398	Based on [Lauretano et al., 2016]
B	22	H	7	52.600	Based on [Lauretano et al., 2016]
A	27	H	3	52.881*	Based on [Lauretano et al., 2016]
C	9	H	7	53.430*	Based on [Lauretano et al., 2016]
A	28	H	6	53.934	Based on [Lauretano et al., 2016]
B	24	H	6	54.000	Based on [Lauretano et al., 2016]
A	29	H	1	54.157	Based on [Lauretano et al., 2016]
C	10	H	7	54.167*	Based on [Lauretano et al., 2016]
C	11	H	7	54.190	Regression model based on Biostratigraphic Datums
A	30	H	7	54.630	Regression model based on Biostratigraphic Datums
C	12	H	8	54.780	Regression model based on Biostratigraphic Datums
B	27	X	6	55.160	Regression model based on Biostratigraphic Datums
A	34	X	1	55.500	Regression model based on Biostratigraphic Datums

Table A.2: Full isotopic data for culture studies along with analytical errors are presented. Error on $\delta^{13}C_{org}$ derives from standard deviation across all measurements for each experiment. $\delta^{13}C_{CO_{2(aq)}}$ is calculated via the equations presented in chapter 3.

Species	Experiment	$\delta^{13}C_{lith}$	$\delta^{13}C_{lith}$ σ	$\delta^{18}O_{lith}$	$\delta^{18}O_{lith}$ σ	$\delta^{13}C_{org}$	$\delta^{13}C_{org}$ σ	$\delta^{13}C_{DIC_{initial}}$	$\delta^{13}C_{DIC_{final}}$	$\delta^{13}C_{DIC_{mean}}$	$\delta^{13}C_{DIC}$ σ	$\delta^{13}C_{CO_{2(aq)}}$
C. pelagicus	1	-5.37	0.05	-5.07	0.05	-30.40	0.15	-2.85	-3.34	-3.09	0.08	-13.00
		-5.46	0.08	-5.54	0.04	-30.71	0.15	-2.85	-3.53	-3.19	0.04	-13.09
		-5.26	0.08	-6.19	0.08	-30.40	0.15	-2.85	-3.35	-3.10	0.06	-13.00
	2	-5.32	0.07	-5.80	0.03	-30.86	0.67	-2.82	-3.65	-3.23	0.06	-13.08
		-5.13	0.05	-6.09	0.08	-29.78	0.67	-2.82	-2.94	-2.88	0.04	-12.74
		-5.36	0.06	-6.05	0.05	-31.39	0.67	-2.82	-3.34	-3.08	0.04	-12.95
	3	-2.40	0.10	-4.17	0.14	-29.75	0.57	-2.79	-3.07	-2.93	0.02	-12.85
		-2.89	0.08	-4.92	0.03	-29.08	0.57	-2.79	-2.96	-2.88	0.02	-12.80
		-2.93	0.05	-4.62	0.05	-30.47	0.57	-2.79	-2.95	-2.87	0.04	-12.79
	4	-2.60	0.08	-5.05	0.02	-30.99	1.27	-2.74	-2.90	-2.82	0.04	-12.75
		-2.40	0.03	-3.96	0.04	-27.90	1.27	-2.74	-2.85	-2.79	0.03	-12.72
		-2.52	0.06	-4.96	0.02	-29.22	1.27	-2.74	-2.90	-2.82	0.05	-12.75
	5	-1.84	0.07	-3.65	0.06	-30.40	0.55	-2.75	-2.68	-2.72	0.02	-12.65
		-1.99	0.11	-2.47	0.06	-31.75	0.55	-2.75	-2.75	-2.75	0.03	-12.68
		-1.88	0.06	-3.72	0.05	-31.19	0.55	-2.75	-2.65	-2.70	0.02	-12.63
	6	-1.84	0.07	-3.84	0.05	-35.64	0.55	-2.71	-2.62	-2.66	0.03	-12.59
		-1.90	0.07	-3.61	0.10	-30.45	0.16	-2.71	-2.74	-2.72	0.02	-12.65
		-1.82	0.07	-4.28	0.07	-30.26	0.16	-2.71	-2.67	-2.69	0.04	-12.62
G. oceanica	1	-4.14	0.08	-4.15	0.04	-26.49	0.87	-3.91	-4.42	-4.16	0.04	-13.46
		-4.15	0.08	-4.51	0.07	-28.61	0.87	-3.91	-4.31	-4.11	0.07	-13.41
		-4.07	0.07	-4.40	0.05	-27.44	0.87	-3.91	-4.38	-4.14	0.06	-13.44
	2	-3.91	0.06	-4.52	0.03	-26.15	0.37	-3.82	-4.11	-3.97	0.03	-13.28
		-3.80	0.11	-3.84	0.08	-26.75	0.37	-3.82	-4.13	-3.98	0.04	-13.30
		-3.94	0.09	-5.11	0.04	-25.84	0.37	-3.82	-4.14	-3.98	0.05	-13.30
	3	-3.74	0.05	-4.69	0.05	-25.96	0.56	-3.83	-4.00	-3.92	0.03	-13.25
		-3.70	0.08	-4.88	0.05	-24.95	0.56	-3.83	-3.83	-3.83	0.03	-13.16
		-3.25	0.11	-2.38	0.05	-26.24	0.56	-3.83	-4.00	-3.91	0.02	-13.25
	4	-3.78	0.10	-3.69	0.03	-27.12	1.32	-3.75	-4.03	-3.89	0.02	-13.21
		-3.84	0.12	-5.23	0.04	-24.10	1.32	-3.75	-4.01	-3.88	0.02	-13.21
		-3.87	0.10	-4.71	0.05	-24.58	1.32	-3.75	-4.08	-3.91	0.05	-13.24
	5	-3.73	0.06	-4.86	0.05	-25.83	0.34	-3.76	-3.84	-3.80	0.02	-13.15
		-3.71	0.04	-4.98	0.05	-25.90	0.34	-3.76	-3.95	-3.86	0.02	-13.20
		-3.81	0.05	-4.90	0.04	-26.59	0.34	-3.76	-3.93	-3.85	0.03	-13.19
	6	-3.61	0.11	-4.66	0.04	-27.62	0.42	-3.73	-3.89	-3.81	0.02	-13.15
		-3.53	0.07	-4.59	0.03	-27.58	0.42	-3.73	-3.87	-3.80	0.02	-13.14
		-3.56	0.08	-4.61	0.07	-26.71	0.42	-3.73	-3.93	-3.83	0.02	-13.18

Table A.3: Measured Particulate Inorganic Carbon (PIC) and Particulate Organic Carbon (POC). *Denotes PIC determined from change in alkalinity after equation 3.12 due to failed measurements on either TPC or POC or POC values greater than TPC. ** values represent failed measurements.

Species	Experiment	Growth Rate (day^{-1})	TPC pg cell^{-1}	POC pg cell^{-1}	PIC pg cell^{-1}	PIC:POC
C. pelagicus		0.70	532.91	283.94	248.97	0.88
	1	0.51	548.80	285.65	263.15	0.92
		0.66	323.63	277.07	46.57	0.17
		0.82	249.34	144.13	105.21	0.73
	2	0.83	238.37	144.04	94.32	0.65
		0.53	306.78	257.40	49.38	0.19
		0.68	369.33	292.35	76.98	0.26
	3	0.69	324.65	238.62	86.03	0.36
		0.61	355.23	161.41	193.83	1.20
		0.79	187.85	170.99	16.86	0.10
	4	0.77	273.15	160.05	113.09	0.71
		0.83	372.50	274.71	97.79	0.36
		0.50	339.74	284.97	54.77	0.19
	5	0.40	391.92	285.92	106.00	0.37
		0.67	350.77	270.00	80.77	0.30
		0.51	314.85	307.70	7.15	0.02
	6	0.58	492.66	297.79	194.87	0.65
		0.54	513.00	290.12	222.88	0.77
G. oceanica		0.50	84.18	50.99	33.18	0.65
	1	0.59	54.90	47.34	7.57	0.16
		0.45	80.27	54.30	25.97	0.48
		0.59	53.94	54.91	5.09*	0.09*
	2	0.50	83.16	64.27	18.90	0.29
		0.50	**	58.37	16.12*	0.28*
		0.62	74.40	44.00	30.40	0.69
	3	0.72	65.65	51.44	14.21	0.28
		0.67	76.00	59.28	16.72	0.28
		0.76	58.34	36.87	21.46	0.58
	4	0.75	60.23	38.86	21.38	0.55
		0.69	76.21	42.97	33.24	0.77
		0.61	61.08	50.54	10.54	0.21
	5	0.56	78.61	57.29	21.32	0.37
		0.65	64.01	43.52	20.49	0.47
		0.56	57.05	41.69	15.36	0.37
	6	0.62	42.09	36.32	5.77	0.16
		0.53	78.41	49.09	29.32	0.60

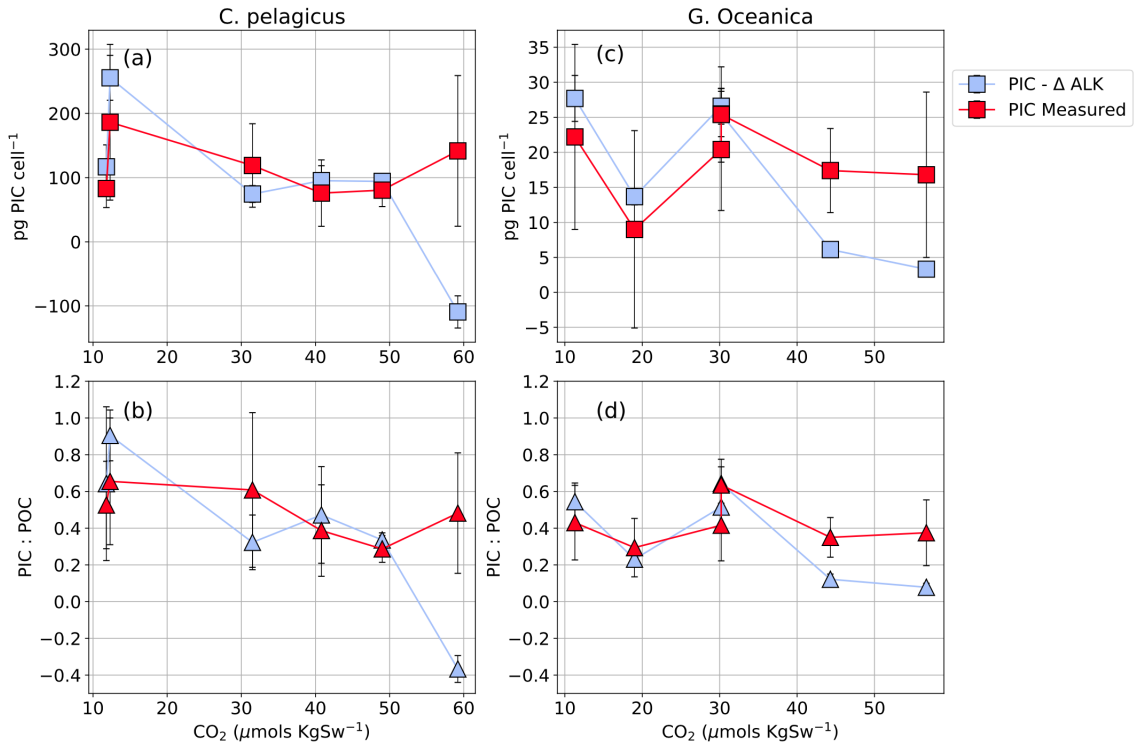

Figure A.1: Measured values of PIC measured on the SERCON mass spectrometer are shown in red for *C. pelagicus* **(a)** and *G. oceanica* **(c)**. Values determined via alkalinity change is shown in blue. The ratio of PIC measured to POC measured is shown in red in **(b)** and **(d)**. The ratio for PIC determined from alkalinity change relatice to measured POC is shown in blue.

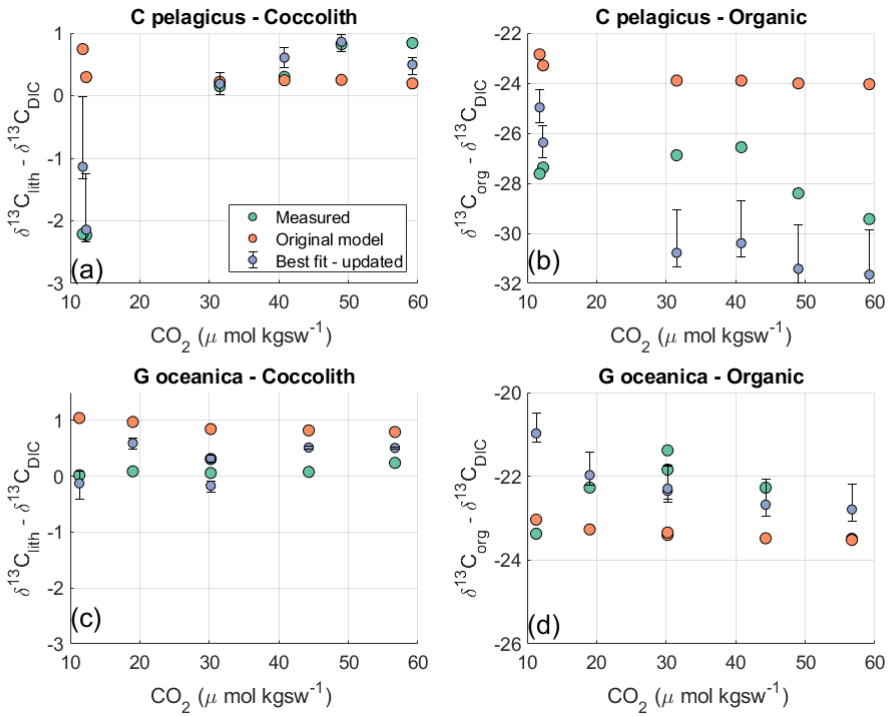

Figure A.2: $\delta^{13}C_{lith}$ relative to $\delta^{13}C_{DIC}$, **(a)**, and $\delta^{13}C_{org}$ relative to $\delta^{13}C_{DIC}$, **(b)**, are presented for *C. pelagicus*. Green markers represent mean $\delta^{13}C$ values across triplicate measurements for each experiment. Error bars on measured values not shown for clarity. Red markers represent modelled $\delta^{13}C$ values using ε_{ef}, T_A, T_B, [CA] P_{Ccell} and G as listed in McClelland et al. [2017]. Blue markers represent modelled $\delta^{13}C$ values derived from the updated values for ε_{ef}, T_A, T_B, [CA] P_{Ccell} as listed in the tables 3.4 and 3.5. Error bars represent the 16th and 84th percentiles from the Monte-carlo sensitivity analysis over 10,000 runs with all input variables varied according to a Gaussian distribution around their mean besides that of PIC:POC. For each run PIC:POC values are assumed exactly as measured and presented in appendix A.3. Corresponding measurements for $\delta^{13}C_{lith}$ relative to $\delta^{13}C_{DIC}$, **(c)**, and $\delta^{13}C_{org}$ relative to $\delta^{13}C_{DIC}$, **(d)**, are show for *G. oceanica*.

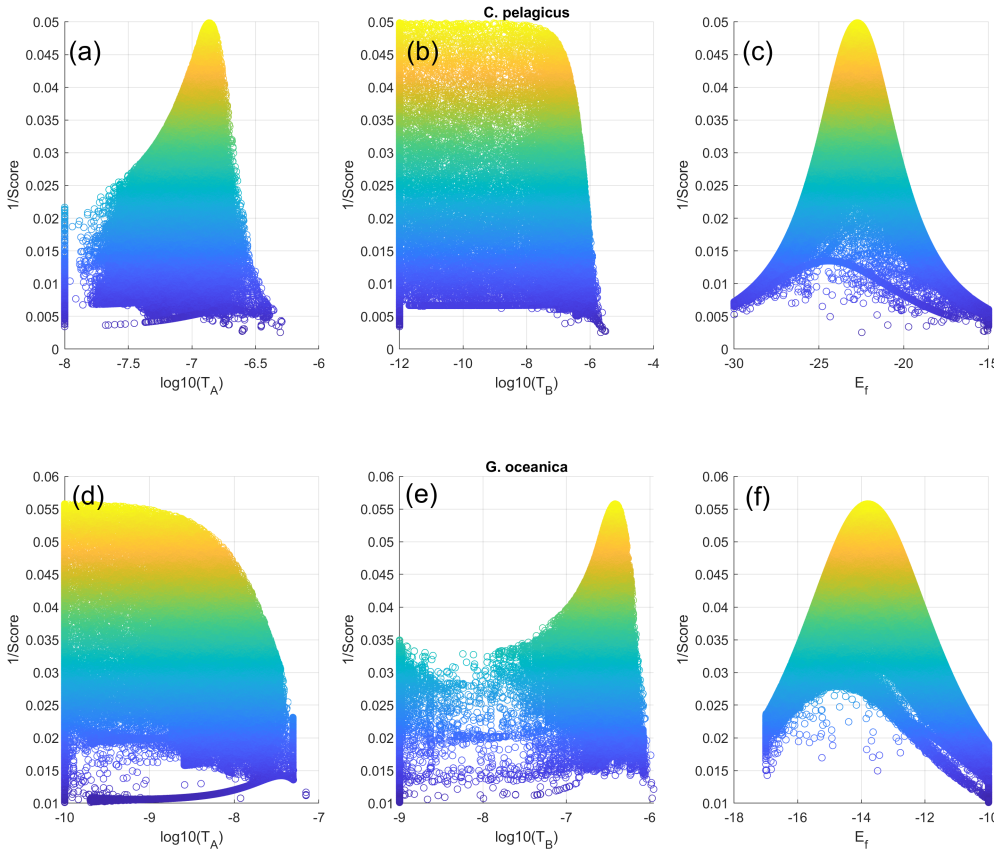

Figure A.3: Inverted scores from the misfit function over 100,000 runs are plotted vs optimised values of T_A, T_B and ε_{ef} for *C. pelagicus* **(a-c)** and *G. oceanica* **(d-f)**. Each point represents a single optimisation run possessing a different initial combination of T_A, T_B and ε_{ef} values. Colour scales with 1/score to highlight optimums. [CA] has been reduced from 0.4 to 0.2 mol m^{-3} all other parameters remain unchanged.

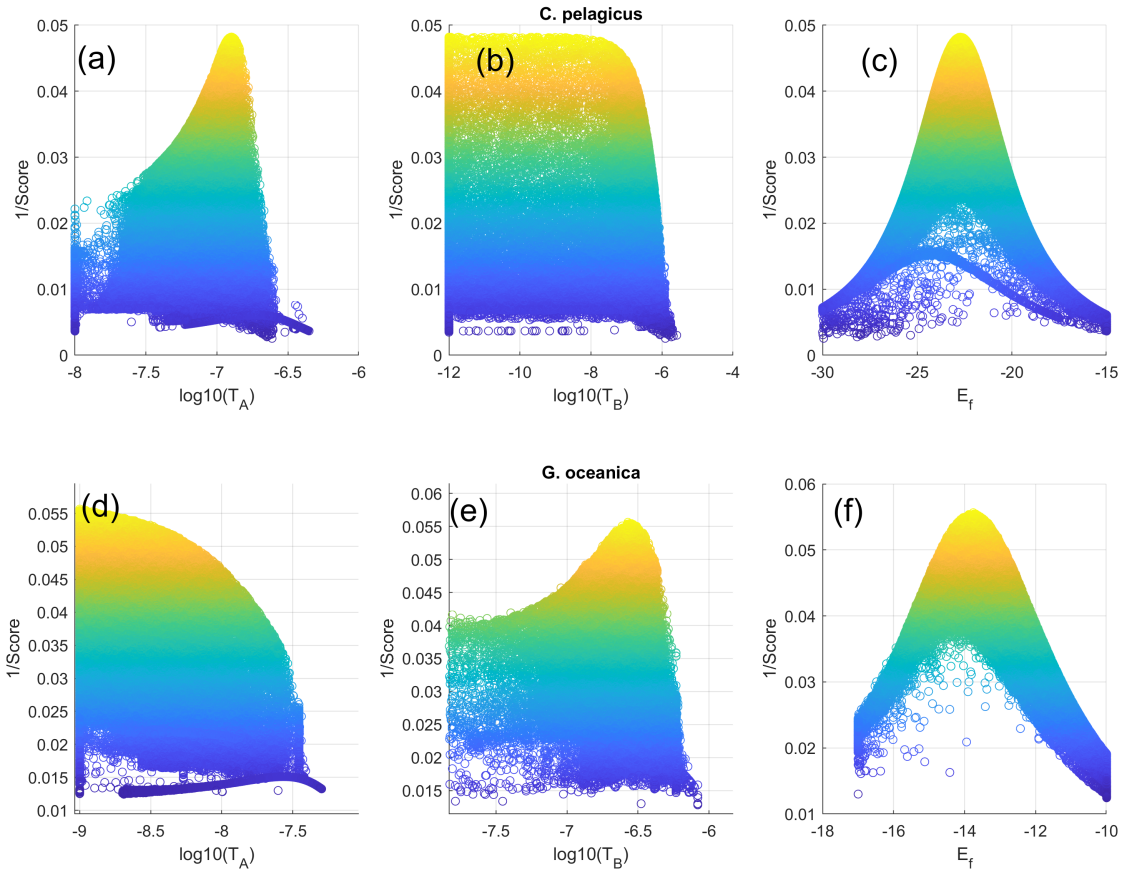

Figure A.4: Inverted scores from the misfit function over 100,000 runs are plotted vs optimised values of T_A, T_B and ε_{ef} for *C. pelagicus* **(a-c)** and *G. oceanica* **(d-f)**. [CA] has been increased from 0.4 to 0.8 mol m^{-3} all other parameters remain unchanged.

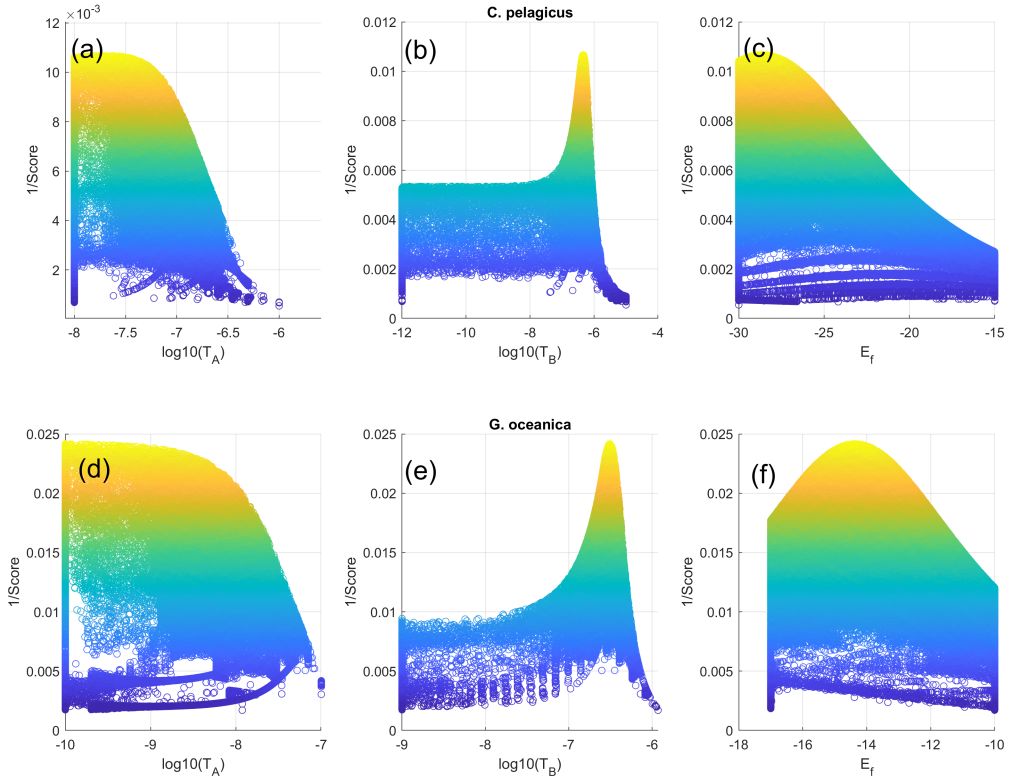

Figure A.5: Inverted scores from the misfit function over 100,000 runs are plotted vs optimised values of T_A, T_B and ε_{ef} for *C. pelagicus* **(a-c)** and *G. oceanica* **(d-f)**. P_{Ccell} has been reduced from 1.2x10^{-4} ms^{-1} to 0.6x10^{-4} ms^{-1} and 1x10^{-4} ms^{-1} to 0.5x10^{-4} ms^{-1} for *C.pelagicus* and *G.oceanica* respectively. All other parameters remain unchanged. A reduced P_{Ccell} results in T_B being non zero for *C. pelagicus* in contrast to the conclusion in the main manuscript. A lower P_{Ccell} results in greater carbon limitation at lower $CO_{2(aq)}$ and thus results in a requirement to upregulate a greater proportion of HCO_3^- to facilitate calcification and photosynthesis. If future studies reveal P_{Ccell} is far lower than previous estimates for *C. pelagicus* and *G. oceanica*, the conclusions in this study regarding T_A and T_B would need to be reconsidered.

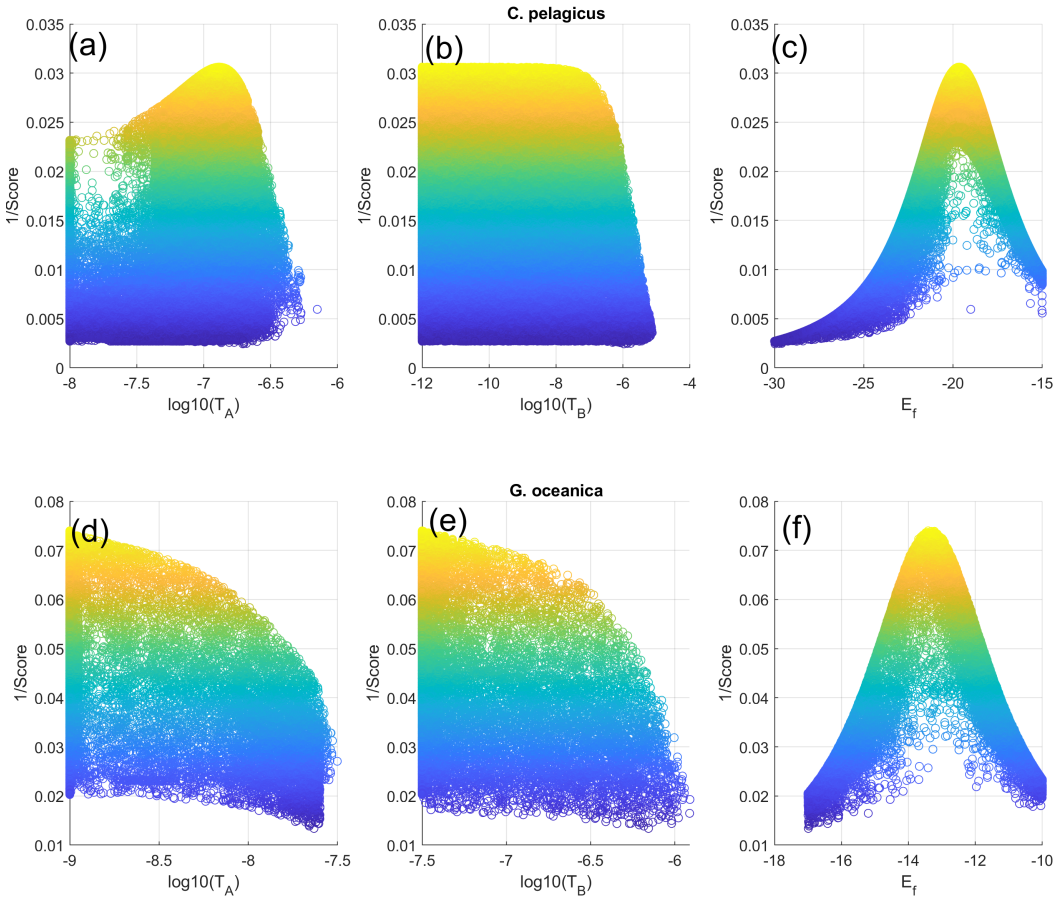

Figure A.6: Inverted scores from the misfit function over 100,000 runs are plotted vs optimised values of T_A, T_B and ε_{ef} for *C. pelagicus* **(a-c)** and *G. oceanica* **(d-f)**. P_{Ccell} has been increased from 1.2x10^{-4} ms^{-1} to 2.4x10^{-4} ms^{-1} and 1x10^{-4} ms^{-1} to 2x10^{-4} ms^{-1} for *C.pelagicus* and *G.oceanica* respectively. All other parameters remain unchanged. For plots *(d-e)* there is no apparent optimum, however the misfit is reduced as T_A and T_B decrease in size. A lack of obvious optimum for T_A and T_B coupled with an increasing fit as the values tend towards 0 suggests that when P_{Ccell} is doubled, *G. oceanica* has no need for an additional upregulation of HCO_3^-.

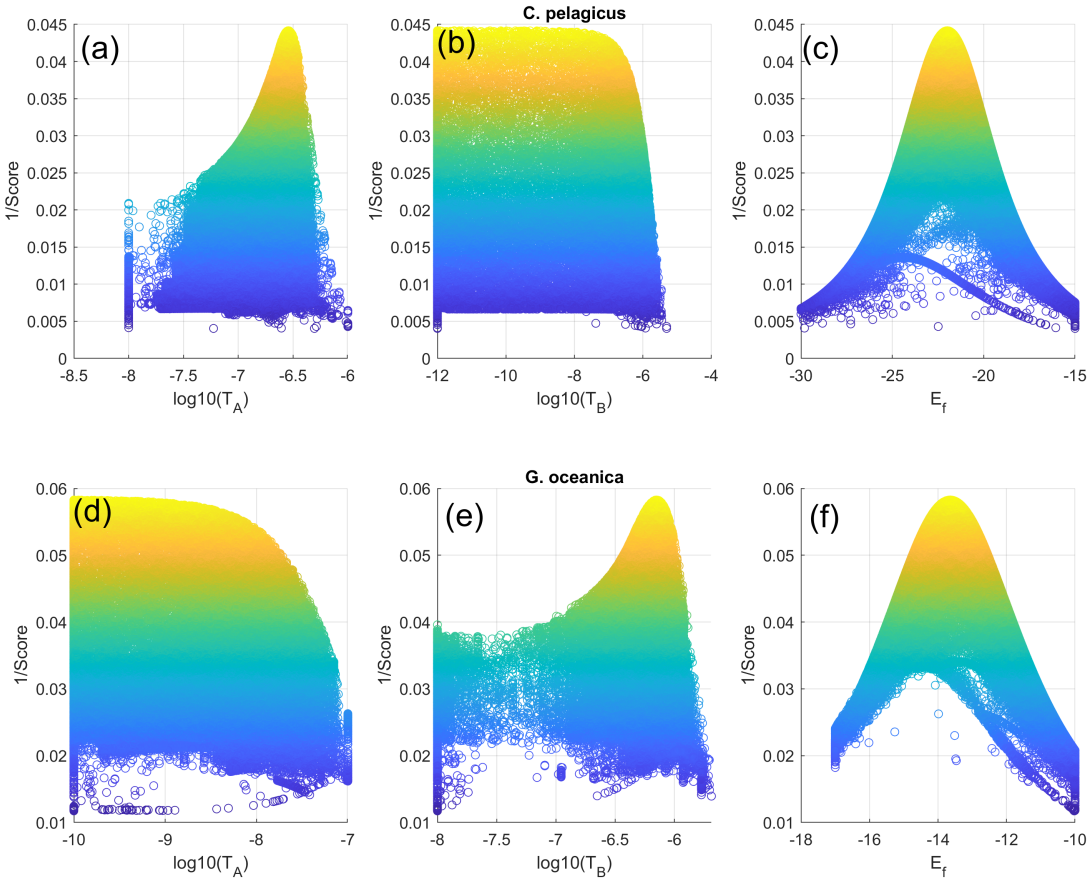

Figure A.7: Inverted scores from the misfit function over 100,000 runs are plotted vs optimised values of T_A, T_B and ε_{ef} for *C. pelagicus* **(a-c)** and *G. oceanica* **(d-f)**. The inferred value of G has been halved from 1 to 0.5 making the cellular membranes more permeable to HCO_3^- efflux than influx. Whilst the model is able to fit data under a G value of 0.5, it remains an unlikely scenario that the efflux effective permeability of membranes would be greater than the influx. All other parameters remain unchanged.

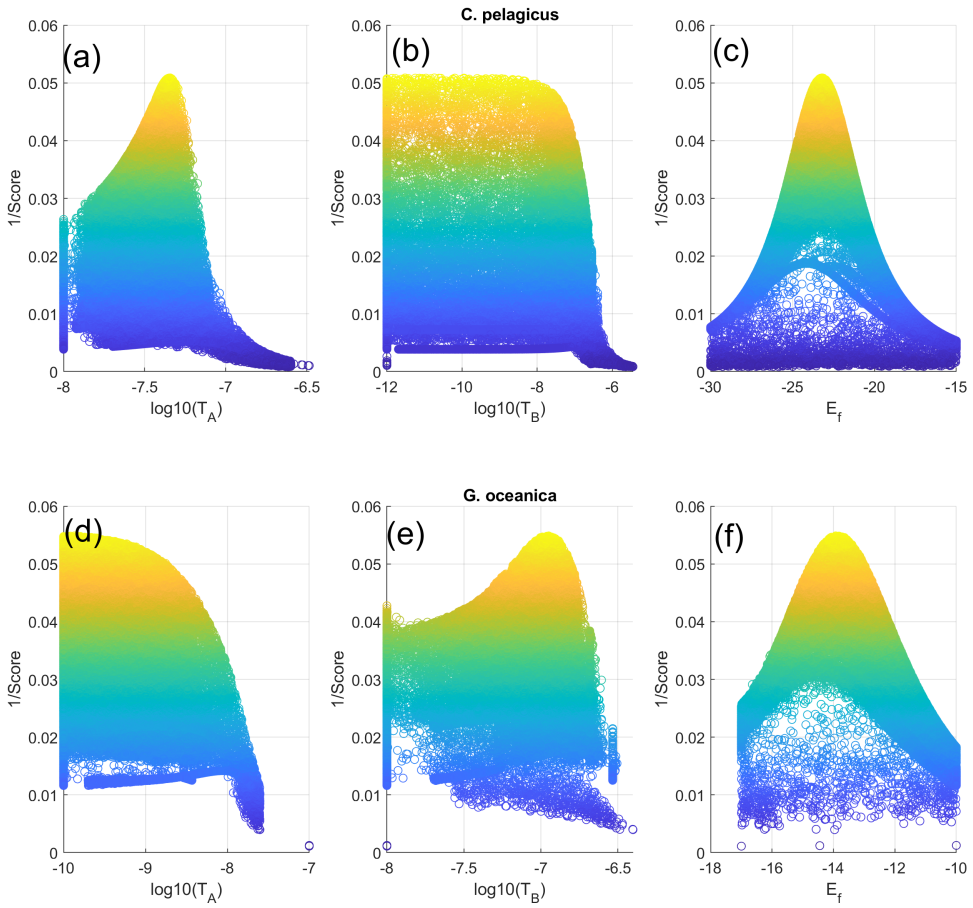

Figure A.8: Inverted scores from the misfit function over 100,000 runs are plotted vs optimised values of T_A, T_B and ε_{ef} for *C. pelagicus* **(a-c)** and *G. oceanica* **(d-f)**. The inferred value of G has been increased from 1 to 2.7, which is the value prescribed in McClelland et al. [2017].

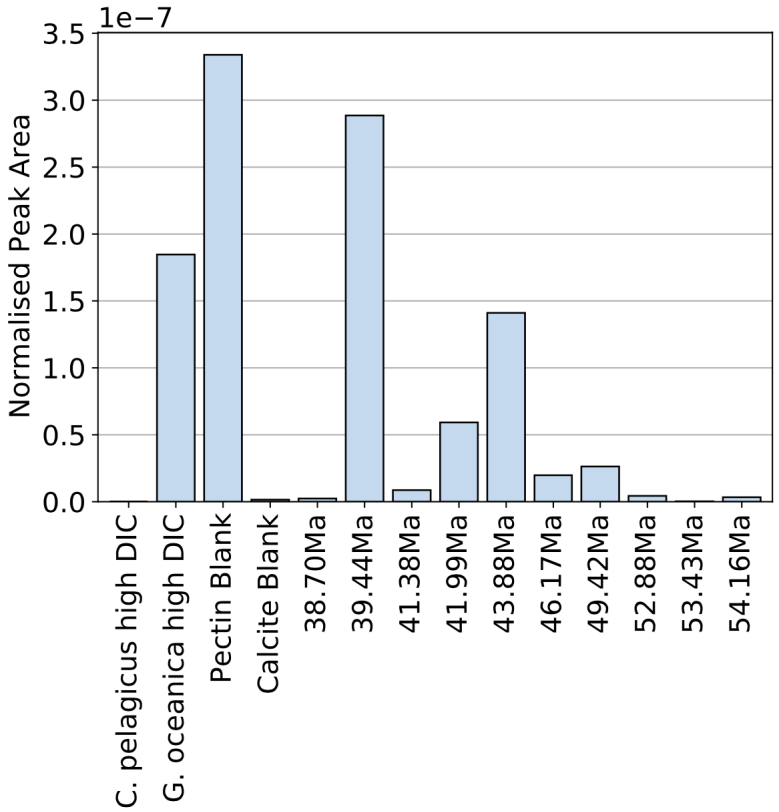

Figure A.9: The normalised peak area of arabinose is shown for process blanks and samples from a single GC-MS run. The normalised area is a unit-less metric. The samples shown here are a subset of the Eocene sediment samples as multiple runs were performed. Normalised peak area only provides a comparison within and not between runs.

Table A.4: OLS CO_2 and species vs 6C/5C statistical summary

Dep. Variable:	6C/5C	**R-squared:**	0.581
Model:	OLS	**Adj. R-squared:**	0.423
Method:	Least Squares	**F-statistic:**	3.691
Df Residuals:	8	**Prob (F-statistic):**	0.0620
Df Model:	3	**Log-Likelihood:**	-37.197
No. Observations:	12	**AIC:**	82.39
		BIC:	84.33

	coef	**std err**	**t**	**P> |t|**	**[0.025**	**0.975]**
Intercept	-22.0353	12.077	-1.825	0.106	-49.885	5.815
rCO_2	-3.1398	3.247	-0.967	0.362	-10.627	4.347
Coccolithales %	0.8495	0.306	2.775	0.024	0.144	1.555
Reticulofenestra %	0.3554	0.176	2.020	0.078	-0.050	0.761

Bibliography

G. Aloisi. Covariation of metabolic rates and cell size in coccolithophores. *Biogeosciences*, 12(15): 6215–6284, 2015.

E. Anagnostou, E. H. John, K. M. Edgar, G. L. Foster, A. Ridgwell, G. N. Inglis, R. D. Pancost, D. J. Lunt, and P. N. Pearson. Changing atmospheric CO2 concentration was the primary driver of early Cenozoic climate. *Nature*, 533(7603):380–384, May 2016. ISSN 0028-0836, 1476-4687. doi: 10.1038/nature17423. URL http://www.nature.com/articles/nature17423.

E. Anagnostou, E. H. John, T. L. Babila, P. F. Sexton, A. Ridgwell, D. J. Lunt, P. N. Pearson, T. B. Chalk, R. D. Pancost, and G. L. Foster. Proxy evidence for state-dependence of climate sensitivity in the Eocene greenhouse. *Nature Communications*, 11(1):4436, Dec. 2020. ISSN 2041-1723. doi: 10.1038/s41467-020-17887-x. URL http://www.nature.com/articles/s41467-020-17887-x.

T. Anning, N. Nimer, M. Merrett, and C. Brownlee. Costs and benefits of calcification in coccolithophorids. *Journal of Marine Systems*, 9(1-2):45–56, Oct. 1996. ISSN 09247963. doi: 10.1016/0924-7963(96)00015-2. URL https://linkinghub.elsevier.com/retrieve/pii/0924796396000152.

D. Archer and E. Maier-Reimer. Effect of deep-sea sedimentary calcite preservation on atmospheric CO2 concentration. *Nature*, 367(6460):260–263, Jan. 1994. ISSN 0028-0836, 1476-4687. doi: 10.1038/367260a0. URL http://www.nature.com/articles/367260a0.

L. T. Bach. Reconsidering the role of carbonate ion concentration in calcification by marine organisms. *Biogeosciences*, 12(16):4939–4951, Aug. 2015. ISSN 1726-4189. doi: 10.5194/bg-12-4939-2015. URL https://www.biogeosciences.net/12/4939/2015/.

L. T. Bach, L. C. M. Mackinder, K. G. Schulz, G. Wheeler, D. C. Schroeder, C. Brownlee, and U. Riebesell. Dissecting the impact of CO $_2$ and pH on the mechanisms of photosynthesis and calcification in the coccolithophore *Emiliania huxleyi*. *New Phytologist*, 199(1):121–134, July 2013. ISSN 0028646X. doi: 10.1111/nph.12225. URL http://doi.wiley.com/10.1111/nph.12225.

L. T. Bach, U. Riebesell, M. A. Gutowska, L. Federwisch, and K. G. Schulz. A unifying concept of coccolithophore sensitivity to changing carbonate chemistry embedded in an ecological framework. *Progress in Oceanography*, 135:125–138, June 2015. ISSN 00796611. doi: 10.1016/j.pocean.2015.04.012. URL https://linkinghub.elsevier.com/retrieve/pii/S0079661115000725.

M. Balz, E. Barriau, V. Istratov, H. Frey, and W. Tremel. Controlled Crystallization of CaCO $_3$ on Hyperbranched Polyglycerol Adsorbed to Self-Assembled Monolayers. *Langmuir*, 21(9): 3987–3991, Apr. 2005. ISSN 0743-7463, 1520-5827. doi: 10.1021/la047977s. URL https://pubs.acs.org/doi/10.1021/la047977s.

Y. M. Bar-On, R. Phillips, and R. Milo. The biomass distribution on Earth. *Proceedings of the National Academy of Sciences*, page 201711842, May 2018. ISSN 0027-8424, 1091-6490. doi: 10.1073/pnas.1711842115. URL http://www.pnas.org/lookup/doi/10.1073/pnas.1711842115.

L. Beaufort, I. Probert, T. de Garidel-Thoron, E. M. Bendif, D. Ruiz-Pino, N. Metzl, C. Goyet, N. Buchet, P. Coupel, M. Grelaud, B. Rost, R. E. M. Rickaby, and C. de Vargas. Sensitivity of coccolithophores to carbonate chemistry and ocean acidification. *Nature*, 476(7358):80–83, Aug.

2011. ISSN 0028-0836, 1476-4687. doi: 10.1038/nature10295. URL http://www.nature.com/articles/nature10295.

D. J. Beerling and D. L. Royer. Convergent Cenozoic CO2 history. *Nature Geoscience*, 4(7):418–420, July 2011. ISSN 1752-0894, 1752-0908. doi: 10.1038/ngeo1186. URL http://www.nature.com/articles/ngeo1186.

D. J. Beerling, J. C. McElwain, and C. P. Osborne. Stomatal responses of the 'living fossil' Ginkgo biloba L. to changes in atmospheric CO2 concentrations. *Journal of Experimental Botany*, 49 (326):1603–1607, 1998.

C. Berger, K. J. S. Meier, H. Kinkel, and K.-H. Baumann. Changes in calcification of coccoliths under stable atmospheric CO2. *Biogeosciences*, 11(4):929–944, Feb. 2014. ISSN 1726-4189. doi: 10.5194/bg-11-929-2014. URL https://bg.copernicus.org/articles/11/929/2014/.

R. A. Berner. The long-term carbon cycle, fossil fuels and atmospheric composition. *Nature*, 426(6964):323–326, Nov. 2003. ISSN 0028-0836, 1476-4687. doi: 10.1038/nature02131. URL http://www.nature.com/articles/nature02131.

K. L. Bice, L. C. Sloan, and E. J. Barron. Comparison of early Eocene isotopic paleotemperatures and three dimensional OGCM temperature field: the potential for use of model-derived surface water 18O. In *Warm Climates in Earth History*, pages 79–129. Cambridge University Press, Cambridge, 2000.

Bidigare Robert R., Fluegge Arnim, Freeman Katherine H., Hanson Kristi L., Hayes John M., Hollander David, Jasper John P., King Linda L., Laws Edward A., Milder Jeffrey, Millero Frank J., Pancost Richard, Popp Brian N., Steinberg Paul A., and Wakeham Stuart G. Consistent fractionation of 13C in nature and in the laboratory: Growth-rate effects in some haptophyte algae. *Global Biogeochemical Cycles*, 11(2):279–292, June 1997. ISSN 0886-6236. doi: 10.1029/96GB03939. URL https://agupubs.onlinelibrary.wiley.com/doi/full/10.1029/96GB03939.

P. K. Bijl, A. J. P. Houben, S. Schouten, S. M. Bohaty, A. Sluijs, G.-J. Reichart, J. S. Sinninghe Damste, and H. Brinkhuis. Transient Middle Eocene Atmospheric CO2 and Temperature Variations. *Science*, 330(6005):819–821, Nov. 2010. ISSN 0036-8075, 1095-9203. doi: 10.1126/science.1193654. URL http://www.sciencemag.org/cgi/doi/10.1126/science.1193654.

K. Billups, R. E. M. Rickaby, and D. P. Schrag. Cenozoic pelagic Sr/Ca records: Exploring a link to paleoproductivity: CENOZOIC PELAGIC SR/CA RECORDS. *Paleoceanography*, 19(3): n/a–n/a, Sept. 2004. ISSN 08838305. doi: 10.1029/2004PA001011. URL http://doi.wiley.com/10.1029/2004PA001011.

L. V. Bindschedler, J. Tuerck, M. Maunders, K. Ruel, M. Petit-Conil, S. Danoun, A.-M. Boudet, J.-P. Joseleau, and G. Paul Bolwell. Modification of hemicellulose content by antisense down-regulation of UDP-glucuronate decarboxylase in tobacco and its consequences for cellulose extractability. *Phytochemistry*, 68(21):2635–2648, Nov. 2007. ISSN 00319422. doi: 10.1016/j.phytochem.2007.08.029. URL https://linkinghub.elsevier.com/retrieve/pii/S0031942207005365.

S. Blanco-Ameijeiras, H. M. Stoll, H. Zhang, and B. M. Hopkinson. Influence of Temperature and CO $_2$ On Plasma-membrane Permeability to CO $_2$ and HCO $_3$ in the Marine Haptophytes *Emiliania huxleyi* and *Calcidiscus leptoporus* (Prymnesiophyceae). *Journal of Phycology*, 56 (5):1283–1294, Oct. 2020. ISSN 0022-3646, 1529-8817. doi: 10.1111/jpy.13017. URL https://onlinelibrary.wiley.com/doi/10.1111/jpy.13017.

S. M. Bohaty and J. C. Zachos. Significant Southern Ocean warming event in the late middle Eocene. *Geology*, 31(11):1017, 2003. ISSN 0091-7613. doi: 10.1130/G19800.1. URL https://pubs.geoscienceworld.org/geology/article/31/11/1017-1020/29164.

A. J. Boller, P. J. Thomas, C. M. Cavanaugh, and K. M. Scott. Low stable carbon isotope fractionation by coccolithophore RubisCO. *Geochimica et Cosmochimica Acta*, 75(22):7200–7207, Nov. 2011. ISSN 00167037. doi: 10.1016/j.gca.2011.08.031. URL http://linkinghub.elsevier.com/retrieve/pii/S001670371100487X.

C. T. Bolton and H. M. Stoll. Late Miocene threshold response of marine algae to carbon dioxide limitation. *Nature*, 500(7464):558–562, Aug. 2013a. ISSN 0028-0836, 1476-4687. doi: 10.1038/nature12448. URL http://www.nature.com/articles/nature12448.

C. T. Bolton and H. M. Stoll. (SUP) Late Miocene threshold response of marine algae to carbon dioxide limitation. *Nature*, 500(7464):558–562, Aug. 2013b. ISSN 0028-0836, 1476-4687. doi: 10.1038/nature12448. URL http://www.nature.com/articles/nature12448.

C. T. Bolton, M. T. Hernández-Sánchez, M.- Fuertes, S. González-Lemos, L. Abrevaya, A. Mendez-Vicente, J.-A. Flores, I. Probert, L. Giosan, J. Johnson, and H. M. Stoll. Decrease in coccolithophore calcification and CO2 since the middle Miocene. *Nature Communications*, 7: 10284, Jan. 2016. ISSN 2041-1723. doi: 10.1038/ncomms10284. URL http://www.nature.com/doifinder/10.1038/ncomms10284.

M. Bordiga, J. Henderiks, F. Tori, S. Monechi, R. Fenero, and E. Thomas. The Eocene–Oligocene transition at ODP Site 1263, Atlantic Ocean: decreases in nannoplankton size and abundance and correlation with benthic foraminiferal assemblages. *Climate of the Past Discussions*, 11(3): 1615–1664, May 2015. ISSN 1814-9359. doi: 10.5194/cpd-11-1615-2015. URL http://www.clim-past-discuss.net/11/1615/2015/.

A. H. Borman, E. W. Jong, M. Huizinga, D. J. Kok, P. Westbroek, and L. Bosch. The Role in CaCO3 Crystallization of an Acid Ca2+-Binding Polysaccharide Associated with Coccoliths of Emiliania huxleyi. *European Journal of Biochemistry*, 129(1):179–183, Dec. 1982. ISSN 0014-2956, 1432-1033. doi: 10.1111/j.1432-1033.1982.tb07037.x. URL http://doi.wiley.com/10.1111/j.1432-1033.1982.tb07037.x.

A. H. Borman, E. W. Jong, R. Thierry, P. Westbroek, L. Bosch, M. Gruter, and J. P. Kamerling. COCCOLITH-ASSOCIATED POLYSACCHARIDES FROM CELLS OF EMILIANIA HUXLEYI (HAPTOPHYCEAE)1. *Journal of Phycology*, 23(2):118–123, 1987. ISSN 00223646. doi: 10.1111/j.1529-8817.1987.tb04433.x. URL http://doi.wiley.com/10.1111/j.1529-8817.1987.tb04433.x.

F. Boscolo Galazzo, E. Thomas, M. Pagani, C. Warren, V. Luciani, and L. Giusberti. The middle Eocene climatic optimum (MECO): A multiproxy record of paleoceanographic changes in the southeast Atlantic (ODP Site 1263, Walvis Ridge): MECO repercussions in the SE Atlantic. *Paleoceanography*, 29(12):1143–1161, Dec. 2014. ISSN 08838305. doi: 10.1002/2014PA002670. URL http://doi.wiley.com/10.1002/2014PA002670.

B. P. Boudreau, J. J. Middelburg, and Y. Luo. The role of calcification in carbonate compensation. *Nature Geoscience*, 11(12):894–900, Dec. 2018. ISSN 1752-0894, 1752-0908. doi: 10.1038/s41561-018-0259-5. URL http://www.nature.com/articles/s41561-018-0259-5.

P. Bown. *Calcareous nannofossil biostratigraphy*. Chapman and Hall; Kluwer Academic, 1998.

P. R. Bown, J. A. Lees, and J. R. Young. Calcareous nannoplankton evolution and diversity through time. In *Coccolithophores*, pages 481–508. Springer, Berlin, Heidelberg, 2004. ISBN 978-3-642-06016-8 978-3-662-06278-4. doi: 10.1007/978-3-662-06278-4_18. URL https://link.springer.com/chapter/10.1007/978-3-662-06278-4_18.

A. L. Bradshaw, P. G. Brewer, D. K. Shafer, and R. T. Williams. Measurements of total carbon dioxide and alkalinity by potentiometric titration in the GEOSECS program. *Earth and Planetary Science Letters*, 55(1):99–115, Sept. 1981. ISSN 0012821X. doi: 10.1016/0012-821X(81)90090-X. URL https://linkinghub.elsevier.com/retrieve/pii/0012821X8190090X.

T. J. Bralower. Evidence of surface water oligotrophy during the Paleocene-Eocene thermal maximum: Nannofossil assemblage data from Ocean Drilling Program Site 690, Maud Rise, Weddell Sea: Evidence for surface water oligotrophy. *Paleoceanography*, 17(2), May 2002. ISSN 08838305. doi: 10.1029/2001PA000662. URL http://doi.wiley.com/10.1029/2001PA000662.

S. C. Brassell, M. Dumitrescu, and the ODP Leg 198 Shipboard Scientific Party. Recognition of alkenones in a lower Aptian porcellanite from the west-central Pacific. *Organic Geochemistry*, 35(2):181–188, Feb. 2004. ISSN 01466380. doi: 10.1016/j.orggeochem.2003.09.003. URL https://linkinghub.elsevier.com/retrieve/pii/S0146638003002031.

W. Broecker and E. Clark. Ratio of coccolith CaCO $_3$ to foraminifera CaCO $_3$ in late Holocene deep sea sediments: COCCOLITH TO FORAMS IN DEEP SEA SEDIMENT. *Paleoceanography*, 24 (3), Sept. 2009. ISSN 08838305. doi: 10.1029/2009PA001731. URL http://doi.wiley.com/10.1029/2009PA001731.

V. Brovkin, J. Bendtsen, M. Claussen, A. Ganopolski, C. Kubatzki, V. Petoukhov, and A. Andreev. Carbon cycle, vegetation, and climate dynamics in the Holocene: Experiments with the CLIMBER-2 model: Carbon cycle, vegatation, and climate dynamics in the Holocene. *Global Biogeochemical Cycles*, 16(4):86–1–86–20, Dec. 2002. ISSN 08866236. doi: 10.1029/2001GB001662. URL http://doi.wiley.com/10.1029/2001GB001662.

C. Brownlee, G. Langer, and G. L. Wheeler. Coccolithophore calcification: Changing paradigms in changing oceans. *Acta Biomaterialia*, page S1742706120304360, Aug. 2020. ISSN 17427061. doi: 10.1016/j.actbio.2020.07.050. URL https://linkinghub.elsevier.com/retrieve/pii/S1742706120304360.

G. Brummer and A. van Eijden. "Blue-ocean" paleoproductivity estimates from pelagic carbonate mass accumulation rates. *Marine Micropaleontology*, 19(1-2):99–117, Apr. 1992. ISSN 03778398. doi: 10.1016/0377-8398(92)90023-D. URL https://linkinghub.elsevier.com/retrieve/pii/037783989290023D.

E. T. Buitenhuis, H. J. W. de Baar, and M. J. W. Veldhuis. PHOTOSYNTHESIS AND CALCIFICATION BY EMILIANIA HUXLEYI (PRYMNESIOPHYCEAE) AS A FUNCTION OF INORGANIC CARBON SPECIES. *Journal of Phycology*, 35(5):949–959, Oct. 1999. ISSN 0022-3646, 1529-8817. doi: 10.1046/j.1529-8817.1999.3550949.x. URL http://doi.wiley.com/10.1046/j.1529-8817.1999.3550949.x.

D. Bukry. Discoaster Evolutionary Trends. *Micropaleontology*, 17(1):43, Jan. 1971. ISSN 00262803. doi: 10.2307/1485036. URL https://www.jstor.org/stable/1485036?origin=crossref.

S. Burkhardt, U. Riebesell, and I. Zondervan. Effects of growth rate, CO2 concentration, and cell size on the stable carbon isotope fractionation in marine phytoplankton. *Geochimica et Cosmochimica Acta*, 63(22):3729–3741, Nov. 1999. ISSN 00167037. doi: 10.1016/S0016-7037(99)00217-3. URL https://linkinghub.elsevier.com/retrieve/pii/S0016703799002173.

K. H. Caffall and D. Mohnen. The structure, function, and biosynthesis of plant cell wall pectic polysaccharides. *Carbohydrate Research*, 344(14):1879–1900, Sept. 2009. ISSN 00086215. doi: 10.1016/j.carres.2009.05.021. URL https://linkinghub.elsevier.com/retrieve/pii/S0008621509002006.

C. Catalanotti, W. Yang, M. C. Posewitz, and A. R. Grossman. Fermentation metabolism and its evolution in algae. *Frontiers in Plant Science*, 4, 2013. ISSN 1664-462X. doi: 10.3389/fpls.2013.00150. URL http://journal.frontiersin.org/article/10.3389/fpls.2013.00150/abstract.

J. K. Caves, A. B. Jost, K. V. Lau, and K. Maher. Cenozoic carbon cycle imbalances and a variable weathering feedback. *Earth and Planetary Science Letters*, 450:152–163, Sept. 2016. ISSN 0012821X. doi: 10.1016/j.epsl.2016.06.035. URL https://linkinghub.elsevier.com/retrieve/pii/S0012821X16303223.

Y. S. Cheng, J. Labavitch, and J. VanderGheynst. Elevated CO2 concentration impacts cell wall polysaccharide composition of green microalgae of the genus Chlorella. *Letters in Applied Microbiology*, page 7, 2014.

C. J. Daniels, A. J. Poulton, W. M. Balch, E. Marañón, T. Adey, B. C. Bowler, P. Cermeño, A. Charalampopoulou, D. W. Crawford, D. Drapeau, Y. Feng, A. Fernández, E. Fernández, G. M. Fragoso, N. González, L. M. Graziano, R. Heslop, P. M. Holligan, J. Hopkins, M. Huete-Ortega, D. A. Hutchins, P. J. Lam, M. S. Lipsen, D. C. López-Sandoval, S. Loucaides, A. Marchetti, K. M. J. Mayers, A. P. Rees, C. Sobrino, E. Tynan, and T. Tyrrell. A global compilation of coccolithophore calcification rates. *Earth System Science Data Discussions*, pages 1–29, May 2018. ISSN 1866-3591. doi: 10.5194/essd-2018-52. URL https://www.earth-syst-sci-data-discuss.net/essd-2018-52/.

R. Dasgupta and M. M. Hirschmann. The deep carbon cycle and melting in Earth's interior. *Earth and Planetary Science Letters*, 298(1-2):1–13, Sept. 2010. ISSN 0012821X. doi: 10.1016/j.epsl.2010.06.039. URL https://linkinghub.elsevier.com/retrieve/pii/S0012821X10004140.

C. De Vargas, M.-P. Aubry, I. Probert, and J. Young. Origin and Evolution of Coccolithophores: From Coastal Hunters to Oceanic Farmers. In *Evolution of Primary Producers in the Sea*, pages 251–285. Elsevier, 2007. ISBN 978-0-12-370518-1. doi: 10.1016/B978-012370518-1/50013-8. URL https://linkinghub.elsevier.com/retrieve/pii/B9780123705181500138.

M. Dedert, H. Stoll, S. Kars, J. R. Young, N. Shimizu, D. Kroon, L. Lourens, and P. Ziveri. Temporally variable diagenetic overgrowth on deep-sea nannofossil carbonates across Palaeogene hyperthermals and implications for isotopic analyses. *Marine Micropaleontology*, 107:18–31, Mar. 2014. ISSN 03778398. doi: 10.1016/j.marmicro.2013.12.004. URL https://linkinghub.elsevier.com/retrieve/pii/S0377839814000036.

S. C. Doney, V. J. Fabry, R. A. Feely, and J. A. Kleypas. Ocean Acidification: The Other CO $_2$ Problem. *Annual Review of Marine Science*, 1(1):169–192, Jan. 2009. ISSN 1941-1405, 1941-0611. doi: 10.1146/annurev.marine.010908.163834. URL http://www.annualreviews.org/doi/10.1146/annurev.marine.010908.163834.

S. Duchamp-Alphonse, G. Siani, E. Michel, L. Beaufort, Y. Gally, and S. L. Jaccard. Enhanced ocean-atmosphere carbon partitioning via the carbonate counter pump during the last deglacial. *Nature Communications*, 9(1):2396, Dec. 2018. ISSN 2041-1723. doi: 10.1038/s41467-018-04625-7. URL http://www.nature.com/articles/s41467-018-04625-7.

R. J. Edgar, V. P. van Hensbergen, A. Ruda, A. G. Turner, P. Deng, Y. Le Breton, N. M. El-Sayed, A. T. Belew, K. S. McIver, A. G. McEwan, A. J. Morris, G. Lambeau, M. J. Walker, J. S. Rush, K. V. Korotkov, G. Widmalm, N. M. van Sorge, and N. Korotkova. Discovery of glycerol phosphate modification on streptococcal rhamnose polysaccharides. *Nature Chemical Biology*, 15(5):463–471, May 2019. ISSN 1552-4450, 1552-4469. doi: 10.1038/s41589-019-0251-4. URL http://www.nature.com/articles/s41589-019-0251-4.

T. L. Edwards, M. Crucifix, and S. P. Harrison. Using the past to constrain the future: how the palaeorecord can improve estimates of global warming. *Progress in Physical Geography*, 31 (5):481–500, Oct. 2007. ISSN 0309-1333, 1477-0296. doi: 10.1177/0309133307083295. URL http://journals.sagepub.com/doi/10.1177/0309133307083295.

D. Ekart, T. E. Cerling, I. P. Montañez, and N. J. Tabor. A 400 million year carbon isotope record of pedogenic carbonate: implications for paleoatmospheric carbon dioxide. *American Journal of Science*, 299(19):805–827, 1999.

P. Falkowski, R. J. Scholes, E. Boyle, J. Canadell, D. Canfield, J. Elser, N. Gruber, and K. Hibbard. The Global Carbon Cycle: A Test of Our Knowledge of Earth as a System. 290:7, 2000.

A. M. J. Fichtinger-Schepman, J. P. Kamerling, C. Versluis, and J. F. G. Vliegenthart. Structural studies of the methylated, acidic polysaccharide associated with coccoliths of Emiliania huxleyi (lohmann) kamptner. *Carbohydrate Research*, 93(1):105–123, June 1981. ISSN 0008-6215. doi: 10.1016/S0008-6215(00)80756-9. URL https://www.sciencedirect.com/science/article/pii/S0008621500807569.

G. L. Foster, C. H. Lear, and J. W. Rae. The evolution of pCO2, ice volume and climate during the middle Miocene. *Earth and Planetary Science Letters*, 341-344:243–254, Aug. 2012. ISSN 0012821X. doi: 10.1016/j.epsl.2012.06.007. URL https://linkinghub.elsevier.com/retrieve/pii/S0012821X12002919.

G. L. Foster, D. L. Royer, and D. J. Lunt. Future climate forcing potentially without precedent in the last 420 million years. *Nature Communications*, 8:14845, Apr. 2017. ISSN 2041-1723. doi: 10.1038/ncomms14845. URL http://www.nature.com/doifinder/10.1038/ncomms14845.

K. H. Freeman and J. M. Hayes. Fractionation of carbon isotopes by phytoplankton and estimates of ancient CO $_2$ levels. *Global Biogeochemical Cycles*, 6(2):185–198, June 1992. ISSN 08866236. doi: 10.1029/92GB00190. URL https://onlinelibrary.wiley.com/doi/10.1029/92GB00190.

K. H. Freeman and M. Pagani. Alkenone-Based Estimates of Past CO2 Levels: A Consideration of Their Utility Based on an Analysis of Uncertainties. In I. Baldwin, M. Caldwell, G. Heldmaier, R. B. Jackson, O. Lange, H. Mooney, E.-D. Schulze, U. Sommer, J. R. Ehleringer, M. Denise Dearing, and T. E. Cerling, editors, *A History of Atmospheric CO2 and Its Effects on Plants, Animals, and Ecosystems*, volume 177, pages 35–61. Springer-Verlag, New York, 2005. ISBN 978-0-387-22069-7. doi: 10.1007/0-387-27048-5_3. URL http://link.springer.com/10.1007/0-387-27048-5_3.

P. Friedlingstein, M. W. Jones, M. O'Sullivan, R. M. Andrew, J. Hauck, G. P. Peters, W. Peters, J. Pongratz, S. Sitch, C. Le Quéré, D. C. E. Bakker, J. G. Canadell, P. Ciais, R. B. Jackson, P. Anthoni, L. Barbero, A. Bastos, V. Bastrikov, M. Becker, L. Bopp, E. Buitenhuis, N. Chandra, F. Chevallier, L. P. Chini, K. I. Currie, R. A. Feely, M. Gehlen, D. Gilfillan, T. Gkritzalis, D. S. Goll, N. Gruber, S. Gutekunst, I. Harris, V. Haverd, R. A. Houghton, G. Hurtt, T. Ilyina, A. K. Jain, E. Joetzjer, J. O. Kaplan, E. Kato, K. Klein Goldewijk, J. I. Korsbakken, P. Landschützer, S. K. Lauvset, N. Lefèvre, A. Lenton, S. Lienert, D. Lombardozzi, G. Marland, P. C. McGuire, J. R. Melton, N. Metzl, D. R. Munro, J. E. M. S. Nabel, S.-I. Nakaoka, C. Neill, A. M. Omar, T. Ono, A. Peregon, D. Pierrot, B. Poulter, G. Rehder, L. Resplandy, E. Robertson, C. Rödenbeck, R. Séférian, J. Schwinger, N. Smith, P. P. Tans, H. Tian, B. Tilbrook, F. N. Tubiello, G. R. van der Werf, A. J. Wiltshire, and S. Zaehle. Global Carbon Budget 2019. *Earth System Science Data*, 11(4):1783–1838, Dec. 2019. ISSN 1866-3516. doi: 10.5194/essd-11-1783-2019. URL https://essd.copernicus.org/articles/11/1783/2019/.

A. Gal, R. Wirth, J. Kopka, P. Fratzl, D. Faivre, and A. Scheffel. Macromolecular recognition directs calcium ions to coccolith mineralization sites. *Science*, 353(6299):590–593, Aug. 2016. ISSN 0036-8075, 1095-9203. doi: 10.1126/science.aaf7889. URL http://www.sciencemag.org/lookup/doi/10.1126/science.aaf7889.

A. Gal, R. Wirth, Z. Barkay, N. Eliaz, A. Scheffel, and D. Faivre. Templated and self-limiting calcite formation directed by coccolith organic macromolecules. *Chemical Communications*, 53 (55):7740–7743, 2017. ISSN 1359-7345, 1364-548X. doi: 10.1039/C7CC03639F. URL http://xlink.rsc.org/?DOI=C7CC03639F.

S. J. Gibbs, P. R. Bown, J. A. Sessa, T. J. Bralower, and P. A. Wilson. Nannoplankton Extinction and Origination Across the Paleocene-Eocene Thermal Maximum. *Science*, 314(5806):1770–1773, Dec. 2006a. ISSN 0036-8075, 1095-9203. doi: 10.1126/science.1133902. URL https://www.sciencemag.org/lookup/doi/10.1126/science.1133902.

S. J. Gibbs, T. J. Bralower, P. R. Bown, J. C. Zachos, and L. M. Bybell. Shelf and open-ocean calcareous phytoplankton assemblages across the Paleocene-Eocene Thermal Maximum: Implications for global productivity gradients. *Geology*, 34(4):233, 2006b. ISSN 0091-7613. doi: 10.1130/G22381.1. URL https://pubs.geoscienceworld.org/geology/article/34/4/233-236/129493.

S. J. Gibbs, R. M. Sheward, P. R. Bown, A. J. Poulton, and S. A. Alvarez. Warm plankton soup and red herrings: calcareous nannoplankton cellular communities and the Palaeocene–Eocene Thermal Maximum. *Philosophical Transactions of the Royal Society A: Mathematical, Physical and Engineering Sciences*, 376(2130):20170075, Oct. 2018. ISSN 1364-503X, 1471-2962. doi: 10.1098/rsta.2017.0075. URL http://rsta.royalsocietypublishing.org/lookup/doi/10.1098/rsta.2017.0075.

A. J. Giuffre, L. M. Hamm, N. Han, J. J. De Yoreo, and P. M. Dove. Polysaccharide chemistry regulates kinetics of calcite nucleation through competition of interfacial energies. *Proceedings of the National Academy of Sciences*, 110(23):9261–9266, June 2013. ISSN 0027-8424, 1091-6490. doi: 10.1073/pnas.1222162110. URL http://www.pnas.org/lookup/doi/10.1073/pnas.1222162110.

J. Godrijan, D. Drapeau, and W. M. Balch. Mixotrophic uptake of organic compounds by coccolithophores. *Limnology and Oceanography*, 65(6):1410–1421, June 2020. ISSN 0024-3590, 1939-5590. doi: 10.1002/lno.11396. URL https://onlinelibrary.wiley.com/doi/abs/10.1002/lno.11396.

E. A. Gontang, W. Fenical, and P. R. Jensen. Phylogenetic Diversity of Gram-Positive Bacteria Cultured from Marine Sediments. *Applied and Environmental Microbiology*, 73(10):3272–3282, May 2007. ISSN 0099-2240, 1098-5336. doi: 10.1128/AEM.02811-06. URL https://journals.asm.org/doi/10.1128/AEM.02811-06.

D. H. Green, V. Echavarri-Bravo, D. Brennan, and M. C. Hart. Bacterial Diversity Associated with the Coccolithophorid Algae *Emiliania huxleyi* and *Coccolithus pelagicus* f. *braarudii*. *BioMed Research International*, 2015:1–15, 2015. ISSN 2314-6133, 2314-6141. doi: 10.1155/2015/194540. URL http://www.hindawi.com/journals/bmri/2015/194540/.

S. E. Greene, A. Ridgwell, S. K. Turner, D. N. Schmidt, H. Pälike, E. Thomas, L. K. Greene, and B. A. A. Hoogakker. Early Cenozoic Decoupling of Climate and Carbonate Compensation Depth Trends. *Paleoceanography and Paleoclimatology*, 34:930–945, 2019.

J. J. Grzymski. The significance of nitrogen cost minimization in proteomes of marine microorganisms. *The ISME Journal*, 6:81–90, 2012.

I. Halevy and A. Bachan. The geologic history of seawater pH. *Science*, 355(6329):1069–1071, Mar. 2017. ISSN 0036-8075, 1095-9203. doi: 10.1126/science.aal4151. URL https://www.sciencemag.org/lookup/doi/10.1126/science.aal4151.

P.-p. Han, S.-y. Yao, R.-j. Guo, S.-g. Shen, R.-r. Yan, Z.-l. Tan, and S.-r. Jia. The relationship between monosaccharide composition of extracellular polysaccharide and activities of related enzymes in Nostoc flagelliforme under different culture conditions. *Carbohydrate Polymers*, 174:111–119, Oct. 2017. ISSN 01448617. doi: 10.1016/j.carbpol.2017.05.093. URL https://linkinghub.elsevier.com/retrieve/pii/S0144861717306185.

I. C. Handoh, G. R. Bigg, and E. W. Jones. Evolution of upwelling in the Atlantic Ocean basin. *Palaeogeography, Palaeoclimatology, Palaeoecology*, 202(1-2):31–58, Dec. 2003. ISSN 00310182. doi: 10.1016/S0031-0182(03)00571-6. URL https://linkinghub.elsevier.com/retrieve/pii/S0031018203005716.

J. M. Hayes. *Practice and Principles of Isotopic Measurements in Organic Geochemistry*. Organic geochemistry of contemporaneous and ancient sediments. Society of Economic Paleontologists and Mineralogists, Bloomington, IN, 1983.

J. M. Hayes. Fractionation of the Isotopes of Carbon and Hydrogen in Biosynthetic Processes. *Reviews in Mineralogy and Geochemistry*, 43:225–277, 2001.

J. M. Hayes, H. Strauss, and A. J. Kaufman. The abundance of 13C in marine organic matter and isotopic fractionation in the global biogeochemical cycle of carbon during the past 800 Ma. *Chemical Geology*, 161(1-3):103–125, Sept. 1999. ISSN 00092541. doi: 10.1016/S0009-2541(99)00083-2. URL https://linkinghub.elsevier.com/retrieve/pii/S0009254199000832.

J. I. Hedges and R. G. Keil. Sedimentary organic matter preservation: an assessment and speculative synthesis. *Marine Chemistry*, page 35, 1995.

N. Hemming and G. Hanson. Boron isotopic composition and concentration in modern marine carbonates. *Geochimica et Cosmochimica Acta*, 56(1):537–543, Jan. 1992. ISSN 00167037. doi: 10.1016/0016-7037(92)90151-8. URL https://linkinghub.elsevier.com/retrieve/pii/0016703792901518.

J. Henderiks. Coccolithophore size rules — Reconstructing ancient cell geometry and cellular calcite quota from fossil coccoliths. *Marine Micropaleontology*, 67(1-2):143–154, Apr. 2008. ISSN 03778398. doi: 10.1016/j.marmicro.2008.01.005. URL http://linkinghub.elsevier.com/retrieve/pii/S037783980800008X.

M. J. Henehan, G. L. Foster, H. C. Bostock, R. Greenop, B. J. Marshall, and P. A. Wilson. A new boron isotope-pH calibration for Orbulina universa, with implications for understanding and accounting for 'vital effects'. *Earth and Planetary Science Letters*, 454:282–292, Nov. 2016. ISSN 0012821X. doi: 10.1016/j.epsl.2016.09.024. URL https://linkinghub.elsevier.com/retrieve/pii/S0012821X16305040.

M. J. Henehan, K. M. Edgar, G. L. Foster, D. E. Penman, P. M. Hull, R. Greenop, E. Anagnostou, and P. N. Pearson. Revisiting the Middle Eocene Climatic Optimum 'Carbon Cycle Conundrum' with new estimates of atmospheric pCO $_2$ from boron isotopes. *Paleoceanography and Paleoclimatology*, Mar. 2020. ISSN 2572-4517, 2572-4525. doi: 10.1029/2019PA003713. URL https://onlinelibrary.wiley.com/doi/abs/10.1029/2019PA003713.

K. Henriksen and S. L. S. Stipp. Controlling Biomineralization: The Effect of Solution Composition on Coccolith Polysaccharide Functionality. *Crystal Growth & Design*, 9(5):2088–2097, May 2009. ISSN 1528-7483, 1528-7505. doi: 10.1021/cg8004272. URL http://pubs.acs.org/doi/abs/10.1021/cg8004272.

K. Henriksen, S. L. S. Stipp, J. R. Young, and M. E. Marsh. Biological control on calcite crystallization: AFM investigation of coccolith polysaccharide function. page 1.

M. Hermoso. Coccolith-Derived Isotopic Proxies in Palaeoceanography: Where Geologists Need Biologists. *Cryptogamie, Algologie*, 35(4):323–351, Nov. 2014. ISSN 0181-1568, 1776-0984. doi: 10.7872/crya.v35.iss4.2014.323. URL http://www.bioone.org/doi/abs/10.7872/crya.v35.iss4.2014.323.

M. Hermoso, T. J. Horner, F. Minoletti, and R. E. Rickaby. Constraints on the vital effect in coccolithophore and dinoflagellate calcite by oxygen isotopic modification of seawater. *Geochimica et Cosmochimica Acta*, 141:612–627, Sept. 2014. ISSN 00167037. doi: 10.1016/j.gca.2014.05.002. URL http://linkinghub.elsevier.com/retrieve/pii/S0016703714003317.

M. Hermoso, I. Z. X. Chan, H. L. O. McClelland, A. M. C. Heureux, and R. E. M. Rickaby. Vanishing coccolith vital effects with alleviated carbon limitation. *Biogeosciences*, 13 (1):301–312, Jan. 2016a. ISSN 1726-4189. doi: 10.5194/bg-13-301-2016. URL https://www.biogeosciences.net/13/301/2016/.

M. Hermoso, F. Minoletti, G. Aloisi, M. Bonifacie, H. McClelland, N. Labourdette, P. Renforth, C. Chaduteau, and R. Rickaby. An explanation for the 18 O excess in Noelaerhabdaceae coccolith calcite. *Geochimica et Cosmochimica Acta*, 189:132–142, Sept. 2016b. ISSN 00167037. doi: 10.1016/j.gca.2016.06.016. URL http://linkinghub.elsevier.com/retrieve/pii/S0016703716303465.

M. Hermoso, H.-L. O. McClelland, J. S. Hirst, F. Minoletti, M. Bonifacie, and R. E. Rickaby. Towards the use of the coccolith vital effects in palaeoceanography: A field investigation during the middle Miocene in the SW Pacific Ocean. *Deep Sea Research Part I: Oceanographic Research Papers*, 160:103262, June 2020. ISSN 09670637. doi: 10.1016/j.dsr.2020.103262. URL https://linkinghub.elsevier.com/retrieve/pii/S0967063720300509.

D. O. Hessen and T. R. Anderson. Excess carbon in aquatic organisms and ecosystems: Physiological, ecological, and evolutionary implications. *Limnology and Oceanography*, 53(4):1685–1696, July 2008. ISSN 00243590. doi: 10.4319/lo.2008.53.4.1685. URL http://doi.wiley.com/10.4319/lo.2008.53.4.1685.

L.-M. Holtz, D. Wolf-Gladrow, and S. Thoms. Simulating the effects of light intensity and carbonate system composition on particulate organic and inorganic carbon production in Emiliania huxleyi. *Journal of Theoretical Biology*, 372:192–204, May 2015. ISSN 00225193. doi: 10.1016/j.jtbi.2015.02.024. URL https://linkinghub.elsevier.com/retrieve/pii/S0022519315000958.

L.-M. Holtz, D. Wolf-Gladrow, and S. Thoms. Stable carbon isotope signals in particulate organic and inorganic carbon of coccolithophores – A numerical model study for Emiliania huxleyi. *Journal of Theoretical Biology*, 420:117–127, May 2017. ISSN 00225193. doi: 10.1016/j.jtbi.2017.01.030. URL https://linkinghub.elsevier.com/retrieve/pii/S0022519317300309.

B. M. Hopkinson. A chloroplast pump model for the CO2 concentrating mechanism in the diatom Phaeodactylum tricornutum. *Photosynth Res*, page 11, 2014.

B. M. Hopkinson, C. L. Dupont, A. E. Allen, and F. M. M. Morel. Efficiency of the CO2-concentrating mechanism of diatoms. *Proceedings of the National Academy of Sciences*, 108 (10):3830–3837, Mar. 2011. ISSN 0027-8424, 1091-6490. doi: 10.1073/pnas.1018062108. URL http://www.pnas.org/cgi/doi/10.1073/pnas.1018062108.

A. Houdan, C. Billard, D. Marie, F. Not, A. G. Sáez, J. R. Young, and I. Probert. Holococcolithophore-heterococcolithophore (Haptophyta) life cycles: Flow cytometric analysis of relative ploidy levels. *Systematics and Biodiversity*, 1(4):453–465, June 2004. ISSN 1477-2000, 1478-0933. doi: 10.1017/S1477200003001270. URL http://www.tandfonline.com/doi/abs/10.1017/S1477200003001270.

G. N. Inglis, F. Bragg, N. J. Burls, M. J. Cramwinckel, D. Evans, G. L. Foster, M. Huber, D. J. Lunt, N. Siler, S. Steinig, J. E. Tierney, R. Wilkinson, E. Anagnostou, A. M. de Boer, T. Dunkley Jones, K. M. Edgar, C. J. Hollis, D. K. Hutchinson, and R. D. Pancost. Global mean surface temperature and climate sensitivity of the early Eocene Climatic Optimum (EECO), Paleocene–Eocene Thermal Maximum (PETM), and latest Paleocene. *Climate of the Past*, 16(5):1953–1968, Oct. 2020. ISSN 1814-9332. doi: 10.5194/cp-16-1953-2020. URL https://cp.copernicus.org/articles/16/1953/2020/.

E. W. Jong, L. Bosch, and P. Westbroek. Isolation and Characterization of a Cat 2+-Binding Polysaccharide Associated with Coccoliths of Emiliania huxleyi (Lohmann) Kamptner. *European Journal of Biochemistry*, 70(2):611–621, Nov. 1976. ISSN 0014-2956, 1432-1033. doi: 10.1111/j.1432-1033.1976.tb11052.x. URL http://doi.wiley.com/10.1111/j.1432-1033.1976.tb11052.x.

M. E. Katz, Z. V. Finkel, D. Grzebyk, A. H. Knoll, and P. G. Falkowski. Evolutionary Trajectories and Biogeochemical Impacts of Marine Eukaryotic Phytoplankton. *Annual Review of Ecology, Evolution, and Systematics*, 35(1):523–556, Dec. 2004. ISSN 1543-592X, 1545-2069. doi: 10.1146/annurev.ecolsys.35.112202.130137. URL http://www.annualreviews.org/doi/10.1146/annurev.ecolsys.35.112202.130137.

K. Kayano, K. Saruwatari, T. Kogure, and Y. Shiraiwa. Effect of Coccolith Polysaccharides Isolated from the Coccolithophorid, Emiliania huxleyi, on Calcite Crystal Formation in In Vitro CaCO3 Crystallization. *Marine Biotechnology*, 13(1):83–92, Feb. 2011. ISSN 1436-2228, 1436-2236. doi: 10.1007/s10126-010-9272-4. URL http://link.springer.com/10.1007/s10126-010-9272-4.

K. Keller and F. Morel. A model of carbon isotopic fractionation and active carbon uptake in phytoplankton. *Marine Ecology Progress Series*, 182:295–298, 1999. ISSN 0171-8630, 1616-1599. doi: 10.3354/meps182295. URL http://www.int-res.com/abstracts/meps/v182/p295-298/.

M. D. Keller, R. C. Selvin, W. Claus, and R. R. L. Guillard. Media for the culture of oceanic ultraphytoplankton. *Journal of Phycology*, 23(4):633–638, Apr. 1987. ISSN 00223646. doi: 10.1111/j.1529-8817.1987.tb04217.x. URL http://doi.wiley.com/10.1111/j.1529-8817.1987.tb04217.x.

C. A. Klausmeier, E. Litchman, T. Daufresne, and S. A. Levin. Optimal nitrogen-to-phosphorus stoichiometry of phytoplankton. *Nature*, 429(6988):171–174, May 2004. ISSN 0028-0836, 1476-4687. doi: 10.1038/nature02454. URL http://www.nature.com/articles/nature02454.

K. Klochko, A. J. Kaufman, W. Yao, R. H. Byrne, and J. A. Tossell. Experimental measurement of boron isotope fractionation in seawater. *Earth and Planetary Science Letters*, 248(1-2):276–285, Aug. 2006. ISSN 0012821X. doi: 10.1016/j.epsl.2006.05.034. URL https://linkinghub.elsevier.com/retrieve/pii/S0012821X06003992.

D. M. Kottmeier, S. D. Rokitta, P. D. Tortell, and B. Rost. Strong shift from HCO3 to CO2 uptake in Emiliania huxleyi with acidification: new approach unravels acclimation versus short-term pH effects. *Photosynthesis Research*, 121(2-3):265–275, Sept. 2014. ISSN 0166-8595, 1573-5079. doi: 10.1007/s11120-014-9984-9. URL http://link.springer.com/10.1007/s11120-014-9984-9.

K. M. Krumhardt, N. S. Lovenduski, M. D. Iglesias-Rodriguez, and J. A. Kleypas. Coccolithophore growth and calcification in a changing ocean. *Progress in Oceanography*, 159:276–295, Dec. 2017. ISSN 00796611. doi: 10.1016/j.pocean.2017.10.007. URL https://linkinghub.elsevier.com/retrieve/pii/S0079661117302148.

G. Langer, M. Geisen, K.-H. Baumann, J. Kläs, U. Riebesell, S. Thoms, and J. R. Young. Species-specific responses of calcifying algae to changing seawater carbonate chemistry: Responses of

calcifying algae. *Geochemistry, Geophysics, Geosystems*, 7(9), Sept. 2006. ISSN 15252027. doi: 10.1029/2005GC001227. URL http://doi.wiley.com/10.1029/2005GC001227.

V. Lauretano, F. Hilgen, J. Zachos, and L. Lourens. Astronomically tuned age model for the early Eocene carbon isotope events: A new high-resolution 13Cbenthic record of ODP Site 1263 between ˜ 49 and ˜ 54 Ma. *Newsletters on Stratigraphy*, 49(2):383–400, Apr. 2016. ISSN 00780421. doi: 10.1127/nos/2016/0077. URL http://openurl.ingenta.com/content/xref?genre=article&issn=0078-0421&volume=49&issue=2&spage=383.

E. A. Laws, B. N. Popp, J. R. R. Bidigare, M. C. Kennicutt, and S. A. Macko. Dependence of phytoplankton carbon isotopic composition on growth rate and [COzlsq : Theoretical considerations and experimental results. *Geochimica Et Cosmochimica Acta*, 59(6):1131–1138, 1995.

E. A. Laws, B. N. Popp, R. R. Bidigare, U. Riebesell, S. Burkhardt, and S. G. Wakeham. Controls on the molecular distribution and carbon isotopic composition of alkenones in certain haptophyte algae: MOLECULAR DISTRIBUTION. *Geochemistry, Geophysics, Geosystems*, 2(1):n/a–n/a, Jan. 2001. ISSN 15252027. doi: 10.1029/2000GC000057. URL http://doi.wiley.com/10.1029/2000GC000057.

E. A. Laws, B. N. Popp, N. Cassar, and J. Tanimoto. 13C discrimination patterns in oceanic phytoplankton: likely influence of CO2 concentrating mechanisms, and implications for palaeoreconstructions. *Functional Plant Biology*, 29(3):323–333, 2002. ISSN 1445-4416. doi: 10.1071/pp01183. URL http://www.publish.csiro.au/FP/PP01183.

C. Lear, H. Elderfield, and P. Wilson. A Cenozoic seawater Sr/Ca record from benthic foraminiferal calcite and its application in determining global weathering fluxes. *Earth and Planetary Science Letters*, 208(1-2):69–84, Mar. 2003. ISSN 0012821X. doi: 10.1016/S0012-821X(02)01156-1. URL https://linkinghub.elsevier.com/retrieve/pii/S0012821X02011561.

R. B. Y. Lee, D. A. I. Mavridou, G. Papadakos, H. L. O. McClelland, and R. E. M. Rickaby. The uronic acid content of coccolith-associated polysaccharides provides insight into coccolithogenesis and past climate. *Nature Communications*, 7:13144, Oct. 2016. ISSN 2041-1723. doi: 10.1038/ncomms13144. URL http://www.nature.com/doifinder/10.1038/ncomms13144.

D. Lemarchand, J. Gaillardet, Lewin, and C. Allègre. Boron isotope systematics in large rivers: implications for the marine boron budget and paleo-pH reconstruction over the Cenozoic. *Chemical Geology*, 190(1-4):123–140, Oct. 2002. ISSN 00092541. doi: 10.1016/S0009-2541(02)00114-6. URL https://linkinghub.elsevier.com/retrieve/pii/S0009254102001146.

E. Lessard and M. Murrell. Microzooplankton herbivory and phytoplankton growth in the northwestern Sargasso Sea. *Aquatic Microbial Ecology*, 16:173–188, 1998. ISSN 0948-3055, 1616-1564. doi: 10.3354/ame016173. URL http://www.int-res.com/abstracts/ame/v16/n2/p173-188/.

S.-Y. Li, Y. Shabtai, and S. (Malis) Arad. Production and composition of the sulphated cell wall polysaccharide of Porphyridium (Rhodophyta) as affected by CO $_2$ concentration. *Phycologia*, 39 (4):332–336, July 2000. ISSN 0031-8884, 2330-2968. doi: 10.2216/i0031-8884-39-4-332.1. URL https://www.tandfonline.com/doi/full/10.2216/i0031-8884-39-4-332.1.

K. Littler, U. Röhl, T. Westerhold, and J. C. Zachos. A high-resolution benthic stable-isotope record for the South Atlantic: Implications for orbital-scale changes in Late Paleocene–Early Eocene climate and carbon cycling. *Earth and Planetary Science Letters*, 401:18–30, Sept. 2014. ISSN 0012821X. doi: 10.1016/j.epsl.2014.05.054. URL https://linkinghub.elsevier.com/retrieve/pii/S0012821X14003641.

L. J. Lourens, A. Sluijs, D. Kroon, J. C. Zachos, E. Thomas, U. Röhl, J. Bowles, and I. Raffi. Astronomical pacing of late Palaeocene to early Eocene global warming events. *Nature*, 435 (7045):1083–1087, June 2005. ISSN 0028-0836, 1476-4687. doi: 10.1038/nature03814. URL http://www.nature.com/articles/nature03814.

V. Luciani, R. D'Onofrio, G. R. Dickens, and B. S. Wade. Did Photosymbiont Bleaching Lead to the Demise of Planktic Foraminifer *Morozovella* at the Early Eocene Climatic Optimum?: Early Eocene Photosymbiont Bleaching. *Paleoceanography*, 32(11):1115–1136, Nov. 2017. ISSN 08838305. doi: 10.1002/2017PA003138. URL http://doi.wiley.com/10.1002/2017PA003138.

T. J. Lueker, A. G. Dickson, and C. D. Keeling. Ocean pCO2 calculated from dissolved inorganic carbon, alkalinity, and equations for K1 and K2: validation based on laboratory measurements of CO2 in gas and seawater at equilibrium. *Marine Chemistry*, 70(1-3):105–119, May 2000. ISSN 03044203. doi: 10.1016/S0304-4203(00)00022-0. URL https://linkinghub.elsevier.com/retrieve/pii/S0304420300000220.

D. J. Lunt, F. Bragg, W.-L. Chan, D. K. Hutchinson, J.-B. Ladant, P. Morozova, I. Niezgodzki, S. Steinig, Z. Zhang, J. Zhu, A. Abe-Ouchi, E. Anagnostou, A. M. de Boer, H. K. Coxall, Y. Donnadieu, G. Foster, G. N. Inglis, G. Knorr, P. M. Langebroek, C. H. Lear, G. Lohmann, C. J. Poulsen, P. Sepulchre, J. E. Tierney, P. J. Valdes, E. M. Volodin, T. D. Jones, C. J. Hollis, M. Huber, and B. L. Otto-Bliesner. DeepMIP: model intercomparison of early Eocene climatic optimum (EECO) large-scale climate features and comparison with proxy data. *Clim. Past*, page 25, 2021.

D. Lüthi, M. Le Floch, B. Bereiter, T. Blunier, J.-M. Barnola, U. Siegenthaler, D. Raynaud, J. Jouzel, H. Fischer, K. Kawamura, and T. F. Stocker. High-resolution carbon dioxide concentration record 650,000–800,000 years before present. *Nature*, 453(7193):379–382, May 2008. ISSN 0028-0836, 1476-4687. doi: 10.1038/nature06949. URL http://www.nature.com/articles/nature06949.

L. Mackinder, G. Wheeler, D. Schroeder, U. Riebesell, and C. Brownlee. Molecular Mechanisms Underlying Calcification in Coccolithophores. *Geomicrobiology Journal*, 27(6-7):585–595, Sept. 2010. ISSN 0149-0451, 1521-0529. doi: 10.1080/01490451003703014. URL http://www.tandfonline.com/doi/abs/10.1080/01490451003703014.

L. Mackinder, G. Wheeler, D. Schroeder, P. von Dassow, U. Riebesell, and C. Brownlee. Expression of biomineralization-related ion transport genes in Emiliania huxleyi: Biomineralization in Emiliania huxleyi. *Environmental Microbiology*, 13(12):3250–3265, Dec. 2011. ISSN 14622912. doi: 10.1111/j.1462-2920.2011.02561.x. URL http://doi.wiley.com/10.1111/j.1462-2920.2011.02561.x.

M. Marsh. Regulation of CaCO3 formation in coccolithophores. *Comparative Biochemistry and Physiology Part B: Biochemistry and Molecular Biology*, 136(4):743–754, Dec. 2003. ISSN 10964959. doi: 10.1016/S1096-4959(03)00180-5. URL http://linkinghub.elsevier.com/retrieve/pii/S1096495903001805.

M. Marsh, A. Ridall, P. Azadi, and P. Duke. Galacturonomannan and Golgi-derived membrane linked to growth and shaping of biogenic calcite. *Journal of Structural Biology*, 139(1):39–45, July 2002. ISSN 10478477. doi: 10.1016/S1047-8477(02)00503-8. URL http://linkinghub.elsevier.com/retrieve/pii/S1047847702005038.

M. E. Marsh, D. K. Chang, and G. C. King. Isolation and Characterization of aNovel Acidic Polysaccharide Containing Tartrate and Glyoxylate Residues from the Mineralized Scales of a Unicellular Coccolithophorid Alga Pleurochrysis curterue. *Journal of Biological Chemistry*, 267(28):20507–20512, May 1992. ISSN 0021-9258, 1083-351X. URL http://www.jbc.org/content/267/28/20507.

V. Masson-Delmotte, P. Zhai, S. Pirani, L. Connors, C. Péan, S. Berger, N. Caud, Y. Chen, L. Goldfard, M. Gomis, M. Huang, K. Leitzell, E. Lonnoy, J. Matthews, T. Maycock, T. Waterfield, O. Yelekçi, R. Yu, and B. Zhou. IPCC, 2021: Summary for Policymakers. Technical report, Cambridge University Press, 2021.

K. Mayers, A. Poulton, C. Daniels, S. Wells, E. Woodward, G. Tarran, C. Widdicombe, D. Mayor, A. Atkinson, and S. Giering. Growth and mortality of coccolithophores during spring in a temperate Shelf Sea (Celtic Sea, April 2015). *Progress in Oceanography*, 177:101928, Oct. 2019. ISSN 00796611. doi: 10.1016/j.pocean.2018.02.024. URL https://linkinghub.elsevier.com/retrieve/pii/S0079661117301593.

J. M. McArthur, R. J. Howarth, and T. R. Bailey. Strontium Isotope Stratigraphy: LOWESS Version 3: Best Fit to the Marine Sr-Isotope Curve for 0–509 Ma and Accompanying Look-up Table for Deriving Numerical Age. *The Journal of Geology*, 109(2):155–170, Mar. 2001. ISSN 0022-1376, 1537-5269. doi: 10.1086/319243. URL https://www.journals.uchicago.edu/doi/10.1086/319243.

H. L. O. McClelland, N. Barbarin, L. Beaufort, M. Hermoso, P. Ferretti, M. Greaves, and R. E. M. Rickaby. Calcification response of a key phytoplankton family to millennial-scale environmental change. *Scientific Reports*, 6(1):34263, Sept. 2016. ISSN 2045-2322. doi: 10.1038/srep34263. URL http://www.nature.com/articles/srep34263.

H. L. O. McClelland, J. Bruggeman, M. Hermoso, and R. E. M. Rickaby. The origin of carbon isotope vital effects in coccolith calcite. *Nature Communications*, 8:14511, Mar. 2017. ISSN 2041-1723. doi: 10.1038/ncomms14511. URL http://www.nature.com/doifinder/10.1038/ncomms14511.

A. McIntyre and A. W. H. Be. Modern Coeeolithophoridae of the Atlantic OeeanmI. Placoliths and Cyrtoliths. *Deep Sea Research*, 14:561–597, 1967.

K. Meier, C. Berger, and H. Kinkel. Increasing coccolith calcification during CO2 rise of the penultimate deglaciation (Termination II). *Marine Micropaleontology*, 112:1–12, Oct. 2014. ISSN 03778398. doi: 10.1016/j.marmicro.2014.07.001. URL https://linkinghub.elsevier.com/retrieve/pii/S0377839814000735.

J. J. Middelburg, K. Soetaert, and M. Hagens. Ocean Alkalinity, Buffering and Biogeochemical Processes. *Reviews of Geophysics*, 58(3), Sept. 2020. ISSN 8755-1209, 1944-9208. doi: 10.1029/2019RG000681. URL https://onlinelibrary.wiley.com/doi/10.1029/2019RG000681.

S. Misra and P. N. Froelich. Lithium Isotope History of Cenozoic Seawater: Changes in Silicate Weathering and Reverse Weathering. *Science*, 335(6070):818–823, Feb. 2012. ISSN 0036-8075, 1095-9203. doi: 10.1126/science.1214697. URL http://www.sciencemag.org/cgi/doi/10.1126/science.1214697.

J. F. B. Mitchell, T. C. Johns, J. M. Gregory, and S. F. B. Tett. Climate response to increasing levels of greenhouse gases and sulphate aerosols. *Nature*, 376(6540):501–504, Aug. 1995. ISSN 0028-0836, 1476-4687. doi: 10.1038/376501a0. URL http://www.nature.com/articles/376501a0.

F. M. Monteiro, L. T. Bach, C. Brownlee, P. Bown, R. E. M. Rickaby, A. J. Poulton, T. Tyrrell, L. Beaufort, S. Dutkiewicz, S. Gibbs, M. A. Gutowska, R. Lee, U. Riebesell, J. Young, and A. Ridgwell. Why marine phytoplankton calcify. *Science Advances*, 2(7):e1501822–e1501822, July 2016. ISSN 2375-2548. doi: 10.1126/sciadv.1501822. URL http://advances.sciencemag.org/cgi/doi/10.1126/sciadv.1501822.

C. M. Moore, M. M. Mills, K. R. Arrigo, I. Berman-Frank, L. Bopp, P. W. Boyd, E. D. Galbraith, R. J. Geider, C. Guieu, S. L. Jaccard, T. D. Jickells, J. La Roche, T. M. Lenton, N. M. Mahowald, E. Marañón, I. Marinov, J. K. Moore, T. Nakatsuka, A. Oschlies, M. A. Saito, T. F. Thingstad, A. Tsuda, and O. Ulloa. Processes and patterns of oceanic nutrient limitation. *Nature Geoscience*, 6(9):701–710, Sept. 2013. ISSN 1752-0894, 1752-0908. doi: 10.1038/ngeo1765. URL http://www.nature.com/articles/ngeo1765.

J. W. Nielsen, K. K. Sand, C. S. Pedersen, L. Z. Lakshtanov, J. R. Winther, M. Willemoës, and S. L. S. Stipp. Polysaccharide Effects on Calcite Growth: The Influence of Composition and Branching. *Crystal Growth & Design*, 12(10):4906–4910, Oct. 2012. ISSN 1528-7483, 1528-7505. doi: 10.1021/cg300772h. URL https://pubs.acs.org/doi/10.1021/cg300772h.

P. D. Nooteboom, P. K. Bijl, E. Sebille, A. S. Heydt, and H. A. Dijkstra. Transport Bias by Ocean Currents in Sedimentary Microplankton Assemblages: Implications for Paleoceanographic Reconstructions. *Paleoceanography and Paleoclimatology*, 34(7):1178–1194, July 2019. ISSN 2572-4517, 2572-4525. doi: 10.1029/2019PA003606. URL https://onlinelibrary.wiley.com/doi/abs/10.1029/2019PA003606.

N. Ozaki, M. Ozakai, T. Kogure, and S. Sakuda. Structural and functional diversity of acidic polysaccharides from various species of coccolithophorid algae. *Thalassas*, 20(1):59–68, 2004.

E. Paasche. Biology and Physiology of Coccolithophorids. *Annual Review of Microbiology*, 22(1): 71–86, Oct. 1968. ISSN 0066-4227, 1545-3251. doi: 10.1146/annurev.mi.22.100168.000443. URL http://www.annualreviews.org/doi/10.1146/annurev.mi.22.100168.000443.

E. Paasche. A review of the coccolithophorid Emiliania huxleyi (Prymnesiophyceae), with particular reference to growth, coccolith formation, and calcification-photosynthesis interactions. *Phycologia*, 40(6):503–529, Nov. 2001. ISSN 0031-8884, 2330-2968. doi: 10.2216/i0031-8884-40-6-503.1. URL https://www.tandfonline.com/doi/full/10.2216/i0031-8884-40-6-503.1.

M. Pagani. The alkenone-CO2 proxy and ancient atmospheric carbon dioxide. *Philosophical Transactions of the Royal Society A: Mathematical, Physical and Engineering Sciences*, 360 (1793):609–632, Apr. 2002. ISSN 1364-503X, 1471-2962. doi: 10.1098/rsta.2001.0959. URL http://rsta.royalsocietypublishing.org/cgi/doi/10.1098/rsta.2001.0959.

D. Paillard and Y. Donnadieu. A 100 Myr history of the carbon cycle based on the 400 kyr cycle in marine ^{13} C benthic records: A 100-million year history of carbon. *Paleoceanography*, 29(12): 1249–1255, Dec. 2014. ISSN 08838305. doi: 10.1002/2014PA002693. URL http://doi.wiley.com/10.1002/2014PA002693.

Palaeosens Project Members. Making sense of palaeoclimate sensitivity. *Nature*, 491(7426):683–691, Nov. 2012. ISSN 0028-0836, 1476-4687. doi: 10.1038/nature11574. URL http://www.nature.com/articles/nature11574.

W. Pegram, S. Krishnaswami, G. Ravizza, and K. Turekian. The record of sea water 1870s/1860s variation through the Cenozoic. *Earth and Planetary Science Letters*, 113(4):569–576, 1992.

B. N. Popp, E. A. Laws, R. R. Bidigare, J. E. Dore, K. L. Hanson, and S. G. Wakeham. Effect of Phytoplankton Cell Geometry on Carbon Isotopic Fractionation. *Geochimica et Cosmochimica Acta*, 62(1):69–77, Jan. 1998. ISSN 0016-7037. doi: 10.1016/S0016-7037(97)00333-5. URL http://www.sciencedirect.com/science/article/pii/S0016703797003335.

Z. A. Popper and M. G. Tuohy. Beyond the Green: Understanding the Evolutionary Puzzle of Plant and Algal Cell Walls. *Plant Physiology*, 153(2):373–383, June 2010. ISSN 1532-2548. doi: 10.1104/pp.110.158055. URL https://academic.oup.com/plphys/article/153/2/373/6109452.

A. J. Poulton, R. Sanders, P. M. Holligan, M. C. Stinchcombe, T. R. Adey, L. Brown, and K. Chamberlain. Phytoplankton mineralization in the tropical and subtropical Atlantic Ocean: PHYTOPLANKTON MINERALIZATION. *Global Biogeochemical Cycles*, 20(4):n/a–n/a, Dec. 2006. ISSN 08866236. doi: 10.1029/2006GB002712. URL http://doi.wiley.com/10.1029/2006GB002712.

A. J. Poulton, T. R. Adey, W. M. Balch, and P. M. Holligan. Relating coccolithophore calcification rates to phytoplankton community dynamics: Regional differences and implications for carbon export. *Deep Sea Research Part II: Topical Studies in Oceanography*, 54(5-7):538–557, Mar. 2007. ISSN 09670645. doi: 10.1016/j.dsr2.2006.12.003. URL https://linkinghub.elsevier.com/retrieve/pii/S0967064507000355.

F. G. Prahl, G. J. de Lange, M. Lyle, and M. A. Sparrow. Post-depositional stability of long-chain alkenones under contrasting redox conditions. *Nature*, 341(6241):434–437, Oct. 1989. ISSN 0028-0836, 1476-4687. doi: 10.1038/341434a0. URL http://www.nature.com/articles/341434a0.

H. Pälike, M. W. Lyle, H. Nishi, I. Raffi, A. Ridgwell, K. Gamage, A. Klaus, G. Acton, L. Anderson, J. Backman, J. Baldauf, C. Beltran, S. M. Bohaty, P. Bown, W. Busch, J. E. T. Channell, C. O. J. Chun, M. Delaney, P. Dewangan, T. Dunkley Jones, K. M. Edgar, H. Evans, P. Fitch, G. L. Foster, N. Gussone, H. Hasegawa, E. C. Hathorne, H. Hayashi, J. O. Herrle, A. Holbourn, S. Hovan, K. Hyeong, K. Iijima, T. Ito, S.-i. Kamikuri, K. Kimoto, J. Kuroda,

L. Leon-Rodriguez, A. Malinverno, T. C. Moore Jr, B. H. Murphy, D. P. Murphy, H. Nakamura, K. Ogane, C. Ohneiser, C. Richter, R. Robinson, E. J. Rohling, O. Romero, K. Sawada, H. Scher, L. Schneider, A. Sluijs, H. Takata, J. Tian, A. Tsujimoto, B. S. Wade, T. Westerhold, R. Wilkens, T. Williams, P. A. Wilson, Y. Yamamoto, S. Yamamoto, T. Yamazaki, and R. E. Zeebe. A Cenozoic record of the equatorial Pacific carbonate compensation depth. *Nature*, 488(7413):609–614, Aug. 2012. ISSN 0028-0836, 1476-4687. doi: 10.1038/nature11360. URL http://www.nature.com/articles/nature11360.

I. Raffi, J. Backman, J. C. Zachos, and A. Sluijs. The response of calcareous nannofossil assemblages to the Paleocene Eocene Thermal Maximum at the Walvis Ridge in the South Atlantic. *Marine Micropaleontology*, 70(3-4):201–212, Mar. 2009. ISSN 03778398. doi: 10.1016/j.marmicro.2008.12.005. URL https://linkinghub.elsevier.com/retrieve/pii/S0377839808001485.

G. Rau, U. Riebesell, and D. Wolf-Gladrow. A model of photosynthetic 13C fractionation by marine phytoplankton based on diffusive molecular CO2 uptake. *Marine Ecology Progress Series*, 133: 275–285, 1996. ISSN 0171-8630, 1616-1599. doi: 10.3354/meps133275. URL http://www.int-res.com/abstracts/meps/v133/p275-285/.

G. E. Ravizza and J. C. Zachos. Records of Cenozoic Ocean Chemistry. In *Treatise on Geochemistry*, volume 6, pages 551–581. Elsevier, 2003.

J. R. Reinfelder. Carbon Concentrating Mechanisms in Eukaryotic Marine Phytoplankton. *Annual Review of Marine Science*, 3(1):291–315, Jan. 2011. ISSN 1941-1405, 1941-0611. doi: 10.1146/annurev-marine-120709-142720. URL http://www.annualreviews.org/doi/10.1146/annurev-marine-120709-142720.

R. Rickaby, M. Hermoso, R. B. Lee, B. D. Rae, A. M. Heureux, C. Balestreri, L. Chakravarti, D. C. Schroeder, and C. Brownlee. Environmental carbonate chemistry selects for phenotype of recently isolated strains of Emiliania huxleyi. *Deep Sea Research Part II: Topical Studies in Oceanography*, 127:28–40, May 2016. ISSN 09670645. doi: 10.1016/j.dsr2.2016.02.010. URL https://linkinghub.elsevier.com/retrieve/pii/S0967064516300194.

R. E. M. Rickaby, J. Henderiks, and J. N. Young. Perturbing phytoplankton: response and isotopic fractionation with changing carbonate chemistry in two coccolithophore species. *Climate of the Past*, 6(6):771–785, Dec. 2010. ISSN 1814-9332. doi: 10.5194/cp-6-771-2010. URL http://www.clim-past.net/6/771/2010/.

A. Ridgwell. A Mid Mesozoic Revolution in the regulation of ocean chemistry. *Marine Geology*, 217(3-4):339–357, June 2005. ISSN 00253227. doi: 10.1016/j.margeo.2004.10.036. URL https://linkinghub.elsevier.com/retrieve/pii/S0025322705000575.

A. Ridgwell and R. Zeebe. The role of the global carbonate cycle in the regulation and evolution of the Earth system. *Earth and Planetary Science Letters*, 234(3-4):299–315, June 2005. ISSN 0012821X. doi: 10.1016/j.epsl.2005.03.006. URL https://linkinghub.elsevier.com/retrieve/pii/S0012821X05001883.

U. Riebesell, I. Zondervan, and R. E. Zeebe. Reduced calcification of marine plankton in response to increased atmospheric CO2. 407:4, 2000.

L. Rivero-Cuesta, T. Westerhold, C. Agnini, E. Dallanave, R. H. Wilkens, and L. Alegret. Paleoenvironmental Changes at ODP Site 702 (South Atlantic): Anatomy of the Middle Eocene Climatic Optimum. *Paleoceanography and Paleoclimatology*, 34(12):2047–2066, Dec. 2019. ISSN 2572-4517, 2572-4525. doi: 10.1029/2019PA003806. URL https://onlinelibrary.wiley.com/doi/abs/10.1029/2019PA003806.

G. H. Roe and M. B. Baker. Why Is Climate Sensitivity So Unpredictable? *Science*, 318(5850): 629–632, Oct. 2007. ISSN 0036-8075, 1095-9203. doi: 10.1126/science.1144735. URL http://www.sciencemag.org/cgi/doi/10.1126/science.1144735.

B. Rost, I. Zondervan, and U. Riebesell. Light-dependent carbon isotope fractionation in the coccolithophorid Emiliania huxleyi. *Limnology and Oceanography*, 47:120–128, 2002.

K. K. Sand, C. S. Pedersen, S. Sjöberg, J. W. Nielsen, E. Makovicky, and S. L. S. Stipp. Biomineralization: Long-Term Effectiveness of Polysaccharides on the Growth and Dissolution of Calcite. *Crystal Growth & Design*, 14(11):5486–5494, Nov. 2014. ISSN 1528-7483, 1528-7505. doi: 10.1021/cg5006743. URL http://pubs.acs.org/doi/10.1021/cg5006743.

K. K. Sand, C. S. Pedersen, J. Matthiesen, S. Dobberschütz, and S. L. S. Stipp. Controlling biomineralisation with cations. *Nanoscale*, 9(35):12925–12933, 2017. ISSN 2040-3364, 2040-3372. doi: 10.1039/C7NR02424J. URL http://xlink.rsc.org/?DOI=C7NR02424J.

K. Schulz, B. Rost, S. Burkhardt, U. Riebesell, S. Thoms, and D. Wolf-Gladrow. The effect of iron availability on the regulation of inorganic carbon acquisition in the coccolithophore Emiliania huxleyi and the significance of cellular compartmentation for stable carbon isotope fractionation. *Geochimica et Cosmochimica Acta*, 71(22):5301–5312, Nov. 2007. ISSN 00167037. doi: 10.1016/j.gca.2007.09.012. URL https://linkinghub.elsevier.com/retrieve/pii/S0016703707005212.

O. Seki, G. L. Foster, D. N. Schmidt, A. Mackensen, K. Kawamura, and R. D. Pancost. Alkenone and boron-based Pliocene pCO2 records. *Earth and Planetary Science Letters*, 292(1-2):201–211, Mar. 2010. ISSN 0012821X. doi: 10.1016/j.epsl.2010.01.037. URL http://linkinghub.elsevier.com/retrieve/pii/S0012821X10000816.

A. L. Sessions, S. P. Sylva, and J. M. Hayes. Moving-Wire Device for Carbon Isotopic Analyses of Nanogram Quantities of Nonvolatile Organic Carbon. *Analytical Chemistry*, 77(20):6519–6527, Oct. 2005. ISSN 0003-2700, 1520-6882. doi: 10.1021/ac051251z. URL https://pubs.acs.org/doi/10.1021/ac051251z.

T. Sharkey and J. Berry. Carbon isotope fractionation of algae as influenced by an inducible CO2 concentrating mechanism. In *Inorganic Carbon Uptake by Aquatic Photosynthetic Organisms*, pages 389–401. Jan. 1985.

R. M. Sheward, A. J. Poulton, S. J. Gibbs, C. J. Daniels, and P. R. Bown. Physiology regulates the relationship between coccosphere geometry and growth phase in coccolithophores. *Biogeosciences*, 14(6):1493–1509, Mar. 2017. ISSN 1726-4189. doi: 10.5194/bg-14-1493-2017. URL https://www.biogeosciences.net/14/1493/2017/.

W. Si and Y. Rosenthal. Reduced continental weathering and marine calcification linked to late Neogene decline in atmospheric CO2. *Nature Geoscience*, 12(10):833–838, Oct. 2019. ISSN 1752-0894, 1752-0908. doi: 10.1038/s41561-019-0450-3. URL http://www.nature.com/articles/s41561-019-0450-3.

A. Sluijs, S. Schouten, T. H. Donders, P. L. Schoon, U. Röhl, G.-J. Reichart, F. Sangiorgi, J.-H. Kim, J. S. Sinninghe Damsté, and H. Brinkhuis. Warm and wet conditions in the Arctic region during Eocene Thermal Maximum 2. *Nature Geoscience*, 2(11):777–780, Nov. 2009. ISSN 1752-0894, 1752-0908. doi: 10.1038/ngeo668. URL http://www.nature.com/articles/ngeo668.

H. J. Spero. Life History and Stable Isotope Geochemistry of Planktonic Foraminifera. *The Paleontological Society Papers*, 4:7–36, 1998.

S. M. Stanley. Influence of seawater chemistry on biomineralization throughout phanerozoic time: Paleontological and experimental evidence. *Palaeogeography, Palaeoclimatology, Palaeoecology*, 232(2-4):214–236, Mar. 2006. ISSN 00310182. doi: 10.1016/j.palaeo.2005.12.010. URL https://linkinghub.elsevier.com/retrieve/pii/S0031018205007182.

L. Stap, A. Sluijs, E. Thomas, and L. Lourens. Patterns and magnitude of deep sea carbonate dissolution during Eocene Thermal Maximum 2 and H2, Walvis Ridge, southeastern Atlantic Ocean: Dissolution Patterns during ETM2. *Paleoceanography*, 24(1), Mar. 2009. ISSN 08838305. doi: 10.1029/2008PA001655. URL http://doi.wiley.com/10.1029/2008PA001655.

L. Stap, L. J. Lourens, E. Thomas, A. Sluijs, S. Bohaty, and J. C. Zachos. High-resolution deep-sea carbon and oxygen isotope records of Eocene Thermal Maximum 2 and H2. *Geology*, 38(7):607–610, July 2010. ISSN 1943-2682, 0091-7613. doi: 10.1130/G30777.1. URL http://pubs.geoscienceworld.org/geology/article/38/7/607/130287/Highresolution-deepsea-carbon-and-oxygen-isotope.

H. M. Stoll and S. Bains. Coccolith Sr/Ca records of productivity during the Paleocene-Eocene thermal maximum from the Weddell Sea: COCCOLITH SR/CA RECORDS OF PRODUCTIVITY. *Paleoceanography*, 18(2):n/a–n/a, June 2003. ISSN 08838305. doi: 10.1029/2002PA000875. URL http://doi.wiley.com/10.1029/2002PA000875.

H. M. Stoll and D. P. Schrag. Coccolith Sr/Ca as a new indicator of coccolithophorid calcification and growth rate: COCCOLITH Sr/Ca. *Geochemistry, Geophysics, Geosystems*, 1(5), May 2000. ISSN 15252027. doi: 10.1029/1999GC000015. URL http://doi.wiley.com/10.1029/1999GC000015.

H. M. Stoll, J. Guitian, I. Hernandez-Almeida, L. M. Mejia, S. Phelps, P. Polissar, Y. Rosenthal, H. Zhang, and P. Ziveri. Upregulation of phytoplankton carbon concentrating mechanisms during low CO2 glacial periods and implications for the phytoplankton pCO2 proxy. *Quaternary Science Reviews*, 208:1–20, Mar. 2019. ISSN 02773791. doi: 10.1016/j.quascirev.2019.01.012. URL https://linkinghub.elsevier.com/retrieve/pii/S0277379118305377.

X. Su, C. Liu, and L. Beaufort. Late Quaternary coccolith weight variations in the northern South China Sea and their environmental controls. *Marine Micropaleontology*, 154:101798, Jan. 2020. ISSN 03778398. doi: 10.1016/j.marmicro.2019.101798. URL https://linkinghub.elsevier.com/retrieve/pii/S037783981930057X.

B. Suchéras-Marx and J. Henderiks. Downsizing the pelagic carbonate factory: Impacts of calcareous nannoplankton evolution on carbonate burial over the past 17 million years. *Global and Planetary Change*, 123:97–109, Dec. 2014. ISSN 09218181. doi: 10.1016/j.gloplacha.2014.10.015. URL https://linkinghub.elsevier.com/retrieve/pii/S0921818114002161.

S. Sviben, A. Gal, M. A. Hood, L. Bertinetti, Y. Politi, M. Bennet, P. Krishnamoorthy, A. Schertel, R. Wirth, A. Sorrentino, E. Pereiro, D. Faivre, and A. Scheffel. A vacuole-like compartment concentrates a disordered calcium phase in a key coccolithophorid alga. *Nature Communications*, 7:11228, Apr. 2016. ISSN 2041-1723. doi: 10.1038/ncomms11228. URL http://www.nature.com/doifinder/10.1038/ncomms11228.

A. R. Taylor, M. A. Russell, G. M. Harper, T. f. T. Collins, and C. Brownlee. Dynamics of formation and secretion of heterococcoliths by ***Coccolithus pelagicus*** ssp. ***braarudii*** . *European Journal of Phycology*, 42(2):125–136, May 2007. ISSN 0967-0262, 1469-4433. doi: 10.1080/09670260601159346. URL https://www.tandfonline.com/doi/full/10.1080/09670260601159346.

A. R. Taylor, A. Chrachri, G. Wheeler, H. Goddard, and C. Brownlee. A Voltage-Gated H+ Channel Underlying pH Homeostasis in Calcifying Coccolithophores. *PLoS Biology*, 9 (6):e1001085, June 2011. ISSN 1545-7885. doi: 10.1371/journal.pbio.1001085. URL http://dx.plos.org/10.1371/journal.pbio.1001085.

A. R. Taylor, C. Brownlee, and G. Wheeler. Coccolithophore Cell Biology: Chalking Up Progress. *Annual Review of Marine Science*, 9(1):283–310, Jan. 2017. ISSN 1941-1405, 1941-0611. doi: 10.1146/annurev-marine-122414-034032. URL http://www.annualreviews.org/doi/10.1146/annurev-marine-122414-034032.

M. A. Teece and M. L. Fogel. Stable carbon isotope biogeochemistry of monosaccharides in aquatic organisms and terrestrial plants. *Organic Geochemistry*, 38(3):458–473, Mar. 2007. ISSN 01466380. doi: 10.1016/j.orggeochem.2006.06.008. URL https://linkinghub.elsevier.com/retrieve/pii/S0146638006001343.

M. Tremblin, M. Hermoso, and F. Minoletti. Equatorial heat accumulation as a long-term trigger of permanent Antarctic ice sheets during the Cenozoic. *Proceedings of the National Academy of Sciences*, 113(42):11782–11787, Oct. 2016. ISSN 0027-8424, 1091-6490. doi: 10.1073/pnas.1608100113. URL http://www.pnas.org/lookup/doi/10.1073/pnas.1608100113.

T. Tyrrell and R. E. Zeebe. History of carbonate ion concentration over the last 100 million years. *Geochimica et Cosmochimica Acta*, 68(17):3521–3530, Sept. 2004. ISSN 00167037. doi: 10.1016/j.gca.2004.02.018. URL http://linkinghub.elsevier.com/retrieve/pii/S0016703704001681.

J. Uchikawa and R. E. Zeebe. The effect of carbonic anhydrase on the kinetics and equilibrium of the oxygen isotope exchange in the CO2–H2O system: Implications for 18O vital effects in biogenic carbonates. *Geochimica et Cosmochimica Acta*, 95:15–34, Oct. 2012. ISSN 00167037. doi: 10.1016/j.gca.2012.07.022. URL https://linkinghub.elsevier.com/retrieve/pii/S0016703712004140.

R. van der Ploeg, D. Selby, M. J. Cramwinckel, Y. Li, S. M. Bohaty, J. J. Middelburg, and A. Sluijs. Middle Eocene greenhouse warming facilitated by diminished weathering feedback. *Nature Communications*, 9(1):2877, Dec. 2018. ISSN 2041-1723. doi: 10.1038/s41467-018-05104-9. URL http://www.nature.com/articles/s41467-018-05104-9.

B. van Dongen, S. Schouten, and J. Sinninghe Damsté. Carbon isotope variability in monosaccharides and lipids of aquatic algae and terrestrial plants. *Marine Ecology Progress Series*, 232:83–92, 2002. ISSN 0171-8630, 1616-1599. doi: 10.3354/meps232083. URL http://www.int-res.com/abstracts/meps/v232/p83-92/.

P. Vervoort, M. Adloff, S. E. Greene, and S. Kirtland Turner. Negative carbon isotope excursions: an interpretive framework. *Environmental Research Letters*, 14(8):085014, Aug. 2019. ISSN 1748-9326. doi: 10.1088/1748-9326/ab3318. URL https://iopscience.iop.org/article/10.1088/1748-9326/ab3318.

G. Villa, C. Fioroni, L. Pea, S. Bohaty, and D. Persico. Middle Eocene–late Oligocene climate variability: Calcareous nannofossil response at Kerguelen Plateau, Site 748. *Marine Micropaleontology*, 69(2):173–192, Oct. 2008. ISSN 03778398. doi: 10.1016/j.marmicro.2008.07.006. URL https://linkinghub.elsevier.com/retrieve/pii/S0377839808000844.

C. E. Walker, S. Heath, D. L. Salmon, N. Smirnoff, G. Langer, A. R. Taylor, C. Brownlee, and G. L. Wheeler. An Extracellular Polysaccharide-Rich Organic Layer Contributes to Organization of the Coccosphere in Coccolithophores. *Frontiers in Marine Science*, 5, Aug. 2018. ISSN 2296-7745. doi: 10.3389/fmars.2018.00306. URL https://www.frontiersin.org/article/10.3389/fmars.2018.00306/full.

J. M. Walker, B. Marzec, R. B. Y. Lee, K. Vodrazkova, S. J. Day, C. C. Tang, R. E. M. Rickaby, and F. Nudelman. Polymorph Selectivity of Coccolith-Associated Polysaccharides from Gephyrocapsa Oceanica on Calcium Carbonate Formation In Vitro. *Advanced Functional Materials*, 29(1):1807168, Jan. 2019. ISSN 1616301X. doi: 10.1002/adfm.201807168. URL http://doi.wiley.com/10.1002/adfm.201807168.

L. M. Walter and J. W. Morse. The dissolution kinetics of shallow marine carbonates in seawater: A laboratory study. *Geochimica et Cosmochimica Acta*, 49(7):1503–1513, July 1985. ISSN 00167037. doi: 10.1016/0016-7037(85)90255-8. URL https://linkinghub.elsevier.com/retrieve/pii/0016703785902558.

W. Wei and S. W. Wise. Biogeographic gradients of middle Eocene-Oligocene calcareous nannoplankton in the South Atlantic Ocean. *Palaeogeography, Palaeoclimatology, Palaeoecology*, 79 (1-2):29–61, July 1990. ISSN 00310182. doi: 10.1016/0031-0182(90)90104-F. URL https://linkinghub.elsevier.com/retrieve/pii/003101829090104F.

T. Westerhold, U. Röhl, T. Frederichs, S. M. Bohaty, and J. C. Zachos. Astronomical calibration of the geological timescale: closing the middle Eocene gap. *Climate of the Past*, 11(9):1181–1195, Sept. 2015. ISSN 1814-9332. doi: 10.5194/cp-11-1181-2015. URL https://www.clim-past.net/11/1181/2015/.

T. Westerhold, U. Röhl, T. Frederichs, C. Agnini, I. Raffi, J. C. Zachos, and R. H. Wilkens. Astronomical Calibration of the Ypresian Time Scale: Implications for Seafloor Spreading Rates and the Chaotic Behaviour of the Solar System? *Climate of the Past Discussions*, pages 1–34, Feb. 2017. ISSN 1814-9359. doi: 10.5194/cp-2017-15. URL https://www.clim-past-discuss.net/cp-2017-15/.

T. Westerhold, N. Marwan, A. J. Drury, D. Liebrand, C. Agnini, E. Anagnostou, J. S. K. Barnet, S. M. Bohaty, D. De Vleeschouwer, F. Florindo, T. Frederichs, D. A. Hodell, A. E. Holbourn,

D. Kroon, V. Lauretano, K. Littler, L. J. Lourens, M. Lyle, H. Pälike, U. Röhl, J. Tian, R. H. Wilkens, P. A. Wilson, and J. C. Zachos. An astronomically dated record of Earth's climate and its predictability over the last 66 million years. *Science*, 369(6509):1383–1387, Sept. 2020. ISSN 0036-8075, 1095-9203. doi: 10.1126/science.aba6853. URL https://www.sciencemag.org/lookup/doi/10.1126/science.aba6853.

E. B. Wilkes and A. Pearson. A general model for carbon isotopes in red-lineage phytoplankton: Interplay between unidirectional processes and fractionation by RubisCO. *Geochimica et Cosmochimica Acta*, 265:163–181, Nov. 2019. ISSN 00167037. doi: 10.1016/j.gca.2019.08.043. URL https://linkinghub.elsevier.com/retrieve/pii/S0016703719305666.

E. B. Wilkes, R. B. Lee, H. L. McClelland, R. E. Rickaby, and A. Pearson. Carbon isotope ratios of coccolith–associated polysaccharides of Emiliania huxleyi as a function of growth rate and CO 2 concentration. *Organic Geochemistry*, 119:1–10, May 2018. ISSN 01466380. doi: 10.1016/j.orggeochem.2018.02.006. URL http://linkinghub.elsevier.com/retrieve/pii/S0146638018300251.

A. Winters, R. Jordan, and P. Roth. Biogeography of living coccolithophorids in ocean waters. In *Coccolithophores*, pages 161–178. Cambridge University Press, 1994.

D. A. Wolf-Gladrow, R. E. Zeebe, C. Klaas, A. Körtzinger, and A. G. Dickson. Total alkalinity: The explicit conservative expression and its application to biogeochemical processes. *Marine Chemistry*, 106(1-2):287–300, July 2007. ISSN 03044203. doi: 10.1016/j.marchem.2007.01.006. URL http://linkinghub.elsevier.com/retrieve/pii/S0304420307000047.

J. R. Young. Biomineralization Within Vesicles: The Calcite of Coccoliths. *Reviews in Mineralogy and Geochemistry*, 54(1):189–215, Jan. 2003. ISSN 1529-6466. doi: 10.2113/0540189. URL https://pubs.geoscienceworld.org/rimg/article/54/1/189-215/87494.

J. R. Young and P. R. Bown. Nannotax3 website, 2020. URL URL:http://www.mikrotax.org/Nannotax3.

J. R. Young and P. Ziveri. Calculation of coccolith volume and its use in calibration of carbonate flux estimates. page 22, 2000.

J. R. Young, S. A. Davis, P. R. Bown, and S. Mann. Coccolith Ultrastructure and Biomineralisation. *Journal of Structural Biology*, 126(3):195–215, June 1999. ISSN 10478477. doi: 10.1006/jsbi.1999.4132. URL https://linkinghub.elsevier.com/retrieve/pii/S1047847799941321.

J. R. Young, M. Geisen, L. Cros, A. Kleijne, C. Sprengel, and I. Probert. A Guide to Extant Coccolithophore Taxonomy. *Journal of Nannoplankton Research Special Issue*, 1(1):1–132, 2003.

J. Zachos, M. Pagani, L. C. Sloan, E. Thomas, and K. Billups. Trends, Rhythms, and Aberrations in Global Climate 65 Ma to Present. *Science*, 292(5517):686–693, Apr. 2001. ISSN 00368075, 10959203. doi: 10.1126/science.1059412. URL http://www.sciencemag.org/cgi/doi/10.1126/science.1059412.

J. Zachos, G. R. Dickens, and R. E. Zeebe. An early Cenozoic perspective on greenhouse warming and carbon-cycle dynamics. *Nature*, 451(7176):279–283, Jan. 2008. ISSN 0028-0836, 1476-4687. doi: 10.1038/nature06588. URL http://www.nature.com/doifinder/10.1038/nature06588.

J. C. Zachos, D. Kroon, P. Blum, and the ODP Leg 208 Shipboard Scientific Party. Early Cenozoic extreme climates: the Walvis Ridge transect. *JOIDES*, 2004. URL http://wwwodp.tamu.edu/publications/208_IR/208ir.htm.

J. C. Zachos, H. McCarren, B. Murphy, U. Röhl, and T. Westerhold. Tempo and scale of late Paleocene and early Eocene carbon isotope cycles: Implications for the origin of hyperthermals. *Earth and Planetary Science Letters*, 299(1-2):242–249, Oct. 2010. ISSN 0012821X. doi: 10.1016/j.epsl.2010.09.004. URL https://linkinghub.elsevier.com/retrieve/pii/S0012821X10005650.

R. E. Zeebe and D. Wolf-Gladrow. *CO2 in Seawater: Equilibrium, Kinetics, Isotopes*. Elsevier, Netherlands, 2001.

H. Zhang, H. Stoll, C. Bolton, X. Jin, and C. Liu. A refinement of coccolith separation methods: Measuring the sinking characters of coccoliths. *Biogeosciences Discussions*, pages 1–30, Feb. 2018. ISSN 1810-6285. doi: 10.5194/bg-2018-82. URL https://www.biogeosciences-discuss.net/bg-2018-82/.

H. Zhang, S. Blanco-Ameijeiras, B. M. Hopkinson, S. M. Bernasconi, L. M. Mejia, C. Liu, and H. Stoll. An isotope label method for empirical detection of carbonic anhydrase in the calcification pathway of the coccolithophore Emiliania huxleyi. *Geochimica et Cosmochimica Acta*, 292:78–93, Jan. 2021. ISSN 00167037. doi: 10.1016/j.gca.2020.09.008. URL https://linkinghub.elsevier.com/retrieve/pii/S0016703720305597.

J. Zhang and P. D. Quay. Carbon isotope fractionation during gas-water exchange and dissolution of CO,. *Geochimica Et Cosmochimica Acta*, 59(1):107–114, 1995.

Y. G. Zhang, A. Pearson, A. Benthien, L. Dong, P. Huybers, X. Liu, and M. Pagani. Refining the alkenone-pCO2 method I: Lessons from the Quaternary glacial cycles. *Geochimica et Cosmochimica Acta*, 260:177–191, Sept. 2019. ISSN 00167037. doi: 10.1016/j.gca.2019.06.032. URL https://linkinghub.elsevier.com/retrieve/pii/S0016703719303813.

P. Ziveri, H. Stoll, I. Probert, C. Klaas, M. Geisen, G. Ganssen, and J. Young. Stable isotope 'vital effects' in coccolith calcite. *Earth and Planetary Science Letters*, 210(1-2):137–149, May 2003. ISSN 0012821X. doi: 10.1016/S0012-821X(03)00101-8. URL http://linkinghub.elsevier.com/retrieve/pii/S0012821X03001018.

I. Zondervan. The effects of light, macronutrients, trace metals and CO2 on the production of calcium carbonate and organic carbon in coccolithophores—A review. *Deep Sea Research Part II: Topical Studies in Oceanography*, 54(5-7):521–537, Mar. 2007. ISSN 09670645. doi: 10.1016/j.dsr2.2006.12.004. URL https://linkinghub.elsevier.com/retrieve/pii/S0967064507000343.